DTU Physics
Department of Physics

Wide-Bandgap Selenium-Based Solar Cells for Tandem Device Applications

Tomas Hugh Youngman

Supervisors:
Professor Peter C. K. Vesborg
Professor Ib Chorkendorff

Ph.D. Thesis
Technical University of Denmark
Department of Physics
Surface Physics and Catalysis
March 2021

Abstract

The work and research conducted during this PhD project was motivated by the concept of a photoelectrochemical water splitting device. A photoelectrochemical device offers the direct conversion of solar energy into stored chemical energy in the form of chemical bonds. This may bridge the gap between intermittent solar power and the requirement for renewable energy storage within one single device. The most promising approach for photo water splitting (photoelectrolysis) is the monolithic tandem that requires two different semiconductor absorbers that may each capture different parts of the solar spectrum. The silicon solar cell dominates the photovoltaics market and is a suitable bottom-cell of the tandem. A suitable top-cell contender is yet to be fully determined. Selenium was the world's first photovoltaic material to be discovered but was, due to its large bandgap of ≈ 1.9 eV, outshone by silicon. The large bandgap of trigonal selenium makes it inefficient as a single-junction solar cell, but highly suitable as a wide-bandgap top-cell absorber. The development of a monolithically grown Se-Si tandem is further motivated by the low melting point of selenium (220 °C) that allows for low temperature fabrication, which both minimises damage to the silicon and potentially allows for cheap and scalable manufacturing.

Thus efforts were made to develop efficient and reproducible top-cell selenium-based heterojunction photovoltaic devices. Following in the footsteps of literature a champion device efficiency of 6.4% was achieved which lies merely 0.1% below the world record of 6.5% from 2017. For incorporation in a tandem Se-Si device, both sides of the top-cell must be transparent so that light with energies below the Se top-cell bandgap is transmitted to the silicon bottom-cell. This requires both sides of the device to be semi-transparent, which was achieved by replacing the typical gold metal contact with an In_2O_3:Sn transparent thin film. This work led to the first reported bifacial selenium single-junction solar cell from which a champion device could demonstrate a state of the art power conversion efficiency of 5.2% when illuminating through the n-type contact and 2.7% when illuminating through the p-type contact. This difference in performance is attributed to present low charge carrier lifetimes and mobilities in selenium which suggest inverting the typical device structure when incorporating it into a tandem device. The few inversion attempts of this work were not successful so further future investigations are highly encouraged. Regardless, an optimum selenium thickness was found to be around 300-500 nm for both illumination directions.

Even without the inversion of the selenium top-cell, attempts were still made to develop Se-Si tandem photovoltaic devices, that culminated in the first ever reported Se-Si tandem with a power conversion efficiency of 2.2%. The main reasons for the rather poor performance are yet to be identified and requires further research.

Finally, various studies were performed on selenium in order to identify and estimate some of its charge carrier transport limitations. Time-resolved terahertz spectroscopy reveals a low photoexcited charge carrier lifetime in the order of 3 ns and a low charge carrier mobility of around 5 $\mathrm{cm^2/Vs}$ that results in a charge carrier diffusion length of around 200 nm. Low photoluminescence signals of selenium were only obtainable below 50 K, that along with the low lifetime are attributed to the existence of defects in its bandgap. From capacitance-voltage profiling of a single-junction device, an acceptor density of selenium is extrapolated to be around 9×10^{15} $\mathrm{cm^{-3}}$ as well as a depletion region width of around 200 nm. These findings coincide well with the measured selenium thickness optimum of around 300-500 nm. Some electronic structure calculations are presented which indicate charge carrier transport limitations due to large effective carrier masses and density of states of selenium. Ultimately, calculations and simulations are performed and compared with the findings of the work to estimate the main present device limitations.

Resumé

Arbejdet udført i dette PhD-projekt var motiveret af konceptet af en fotoelektrokemisk vanddelingsenhed. En fotoelektrokemisk enhed muliggør direkte konvertering fra solenergi til kemisk energi i form af kemiske bindinger. På denne måde kan en enkelt enhed på en og samme tid løse problemet med flukturerende solenergi og kravet om lagring af vedvarende energi. Den mest lovende tilgang til fotoelektrolyse er den monolitiske tandem, der kræver to forskellige halvlederabsorbere, der hver især kan fange forskellige dele af solspektret. Silicium solcellen dominerer solcellemarkedet og er en passende bundcelle i en tandem. En passende topcelle kandidat er endnu ikke entydigt identificeret. Selen var verdens første anvendte solcellemateriale, men grundets dets store båndgab på $\approx$ 1,9 eV, blev den udkonkurreret af silicium. Det store båndgab af trigonalt selen gør det ineffektivt som en enkelt absorber solcelle, men yderst velegnet som en bredbåndgabs absorberende topcelle. Udviklingen af en monolitisk groet Se-Si-tandem er yderligere motiveret af selens lave smeltepunkt (220 °C), der giver mulighed for fremstilling ved lav temperatur, hvilket både minimerer beskadigelse af silicium og potentielt muliggør billig og skalerbar produktion.

Således blev der i dette projekt gjort en indsats for at udvikle effektive og reproducerbare topcelle selen-baserede heterojunction solceller. Med udgangspunkt i litteraturen blev der opnået en solcelle effektivitet på 6,4%, som kun ligger 0,1% under verdensrekorden på 6,5% fra 2017. For at topcellen skal kunne inkorporeres i en Se-Si-tandem, skal begge sider af topcellen være gennemsigtig, således at lys med energi lavere end selens båndgab kan transmitteres til silicium bundcellen. Dette kræver, at begge sider af enheden er semitransparente, hvilket blev opnået ved at erstatte den typiske metalkontakt af guld med en In_2O_3:Sn gennemsigtig tyndfilm. Dette arbejde førte til den første rapporterede bifacial selen solcelle, hvorfra den bedste kunne demonstrere en effektivitet på 5,2%, når den belyses gennem n-type kontakten og 2,7%, når den belyses gennem p-type kontakten. Forskellen i ydeevne tilskrives nuværende lave ladningsbærer levetider og mobiliteter i selen, hvilket antyder, at den typiske enhedsstruktur bør vendes, når den inkorporeres i en tandem enhed. De få inversionsforsøg lavet i løbet af dette projekt var ikke vellykkede, og yderligere fremtidige undersøgelser tilskyndes. En optimal selen tykkelse blev fundet til at være omkring 300-500 nm for begge belysningsretninger.

Det blev fortsat forsøgt at udvikle Se-Si-tandem solceller uden inversion, der kulminerede i den første rapporterede Se-Si-tandem nogensinde med en effektivitet på 2,2%. Hovedårsagerne til den lave ydeevne er endnu ikke identificeret og kræver yderligere forskning.

Endelig blev der udført forskellige undersøgelser af selen for at identificere og estimere nogle af dets ladningsbærer transport begrænsninger. Tidsopløst terahertzspektroskopi afslører en lav ladningsbærer levetid i størrelsesordenen af 3 ns og en lav ladningsbærer mobilitet på omkring 5 $\mathrm{cm}^2/\mathrm{Vs}$, hvilket resulterer i en diffusionslængde på omkring 200 nm. Lav fotoluminescenssignaler fra selen kunne kun opnås under 50 K, der sammen med den lave levetid tilskrives eksistensen af defekter i dens båndgab. Fra kapacitans-spændings-profilering af en selen solcelle ekstraheres en acceptortæthed af selen til at være omkring 9×10^{15} cm^{-3} samt en rumladningsbredde på omkring 200 nm. Disse fund passer godt overens med den målte optimale tykkelse af selen på omkring 300-500 nm. Elektronstrukturberegninger indikerer ladningsbærer transport begrænsninger på grund af store effektive ladningsbærer masser og tilstandsdensiteter i selen. Endeligt udføres beregninger og simuleringer der sammenlignes med resultaterne fra arbejdet af dette projekt for at estimere de primære nuværende begrænsninger.

Preface

This thesis has been written to fulfil the requirements for obtaining a PhD degree at the Technical University of Denmark (DTU). The research was supported by the Villum Foundation V-SUSTAIN grant (9455) to the Villum Center for the Science of Sustainable Fuels and Chemicals. The work was carried out under supervision of Prof. Peter C. K. Vesborg and Prof. Ib Chorkendorff from April 2018 to April 2021 at the Surface Physics and Catalysis (SurfCat) group at the Department of Physics, DTU. I would first of all like to sincerely thank both Peter and Ib for their valuable supervision. Naturally none of this work would have been possible without them and I have been glad to have the freedom to steer the project in the direction that I found most relevant. I appreciate all of our many weekly group meetings that also included Prof. Ole Hansen, Assoc. Prof. Brian Seger, PhD student Choongman Moon and PhD student Rasmus Nielsen, whom I would also like to express my gratitude to. Not many PhD students are so fortunate to receive weekly guidance from a total of four brilliant professors. The work of this project involved many up and down experiences and I am sure that my weekly mood must have felt like a flip of the coin. Without all of your valuable support, this project as well as my mental state would have been doomed to fail. In particular I would like to also acknowledge Peter and Ole for spending time with Rasmus and me during our special course where we went through the book of Peter Würfel that involved fundamental photovoltaics theory. Ole has a seemingly limitless knowledge of solidstate physics (among many other fields) and the fact that Ole continued to show up, even after retiring, to offer guidance during the weekly meetings has been a tremendous honour.

I would also like to thank Andrea Crovetto, who initially peaked my interest in photovoltaics as my supervisor during my bachelor project and later became a postdoc co-worker and "unofficial supervisor" during my PhD. Andrea is an ingenious scientist (who also has an unhealthy fondness for karaoke) and I owe most of my knowledge of photovoltaics and many of the experimental methods used in this work to his teachings. After his time at DTU he went momentarily to work with the group of Thomas Unold at Helmholtz-Zentrum Berlin (HZB), who I was fortunate to visit for a couple of weeks. Even though Covid-19 prevented me from revisiting HZB I managed to obtain some valuable results due to the help of Sergiu Levcenco, Hannes Hempel and Marin Rusu, which I am deeply grateful for. I hope that some of these results can be published in the near future.

During the last year, Rasmus Nielsen joined me in the project as a Master's student and later as a PhD student. During most of my project I have been the only one at SurfCat working on the development of photovoltaics, so it was a relief to finally have someone to discuss with on a daily basis. Rasmus' dedication to photovoltaics is overwhelming to the point where he even willingly pays for his own participation in a photovoltaics summer school in Austria. I have been very fortunate to have you both as a student and as a co-worker and our time in the lab (and at summer school) has been great fun and highly productive. Even though a pandemic tried to get in our way, I still think we did incredibly well.

I have been incredibly fortunate that Alireza Hajijafarassar was finishing his PhD work only a year earlier than me. A big thanks goes out to him and his work on silicon bottom-cells that allowed for the collaboration which led to the world's first Se-Si tandem achieved during this project. If I was to have done this without his help it would have required the work corresponding to doing an extra PhD degree which I truthfully would prefer not to.

I would further like to thank some of my many other amazing undergraduate and postgraduate students Frederik Madsen, Martin Voss, Astrid Erecius, Rikke Andersen and Dan Windfeldt, who I have supervised in the past 2 years. Including the solar cells that I made during my Master's thesis (which this PhD project is a continuation of), I estimate that a total of around 1100 devices have been made. Many of these would not have been fabricated without theirs and Rasmus' valuable efforts during their projects which have led to many important findings.

I am also grateful for the collaboration with the group of Computational Atomic scale Materials Design (CAMD), DTU Physics from whom Hadeel Moustafa, Carsten Wedel Jacobsen and Thomas Olsen provided excellent electronic structure calculations that helped with the identification of fundamental device limitations as well as provided ideas for new functional materials that may improve the device architecture. I regret not being able to publish some of this work yet, but I hope that they together with Rasmus may be able to discover some further important findings.

Dan Shacham and Peder Heise from the DTU Physics workshop have performed some remarkable work that allowed for the fabrication of the solar cells of this project. This included building highly essential parts for the fabrication process as well as fix countless UHV related problems that occurred along the way. I am extremely grateful for all of the quality work that they have done and I probably owe them more cake and ice cream than I can currently afford.

A great thanks also goes out to the floor managers of SurfCat that currently include Brian Knudsen, Patrick Strøm-Hansen and Jakob Ejler Sørensen who have helped troubleshoot a great number of problems throughout the years. SurfCat would simply not be able to function without their tremendous work. A special thanks is attributed to my co-worker PhD student and part-time floor manager Jakob Ejler Sørensen who has been a master of Python software and XPS/ISS analysis. Without his kind and highly valued efforts I find it doubtful that any XPS or ISS measurements would have been included in this work.

Doing a PhD at SurfCat has been an amazing and gratifying experience, both scientifically and personally, due to the many wonderful people that I have had the pleasure to work with. I will miss the fun times during coffee breaks and Friday bar sessions, which were unfortunately somewhat disrupted by the sudden pandemic. In particular I would like to thank Johannes Novak Hansen and Olivia Fjord Sloth for providing a spectacularly fun and fulfilling work environment. You have been the best office mates that one can wish for and I will miss our many daily jokes and laughs.

A big thanks goes out to my family and friends for always supporting and encouraging me throughout these years. I hope that you have not felt totally forgotten due to my lack of time, but I confess that I may have been somewhat busy the past three years. I look forward to having more time to spend with all of you again.

Lastly, I would like to send my love and greatest thanks to my beautiful and brilliant fiancé Julia Dyrnum who has stood by my side the past 8 years. I would never have achieved this without your everlasting support and faith in me. You are the love of my life and I cannot wait to celebrate our wedding together later this year. I am sure you will appreciate me not having to talk about my solar cells anymore and finally have some time to help with the wedding planning instead.

T.H.Youngman

Tomas Hugh Youngman

31st of March 2021

List of Publications

First Author

Paper I: Semi-transparent selenium solar cells as a top-cell for tandem photovoltaics
Tomas H. Youngman, Rasmus Nielsen, Andrea Crovetto, Brian Seger, Ole Hansen, Ib Chorkendorff, Peter C. K. Vesborg
Under review at Solar RRL

Co-Author

Paper II: Selenium thin-film solar cells with cadmium sulfide as a heterojunction partner
Rasmus Nielsen, Tomas H. Youngman, Andrea Crovetto, Brian Seger, Ole Hansen, Ib Chorkendorff, Peter C. K. Vesborg
In preparation

Contents

List of Figures

List of Figures

List of Tables

Nomenclature

Acronyms and Abbreviations

2T	Two-terminal
3T	Three-terminal
4T	Four-terminal
a-Se	Amorphous selenium
AM	Air mass
AM0	Air mass without atmosphere (solar spectrum outside the atmosphere)
AM1.5	Air mass with a zenith angle of 48.2°
AM1.5G	Global standard solar spectrum
c-Se	Crystalline trigonal selenium
CAE	Constant analyser energy
CBM	Conduction band minimum
CV	Capacitance-voltage
CZTS	Cu_2ZnSnS_4
DFT	Density functional theory
DOS	Density of states
EDX-S	Energy-dispersive X-ray spectroscopy
EQE	External quantum efficiency
ERE	External radiative efficiency
ETD	Evarhart-Thornley detector
ETL	Electron-transport layer
FAT	Fixed analyser transmission
FTO	Fluorine doped tin oxide (F doped SnO_2)

Nomenclature

FWHM	Full width half maximum
HER	Hydrogen evolution reaction
HF	Hydrogen fluoride
HTL	Hole-transport layer
IE	Ionisation energy
IR	Infrared
ISS	Ion scattering spectroscopy
ITO	Indium tin oxide (In_2O_3:Sn)
JV	Current-voltage
LCOE	Levelised cost of energy
MI	Monolithically integrated
OER	Oxygen evolution reaction
OTEC	Ocean thermal energy conversion
PCE	Power conversion efficiency
PEC	Photoelectrochemical
PL	Photoluminescence
polySi	Polycrystalline silicon (polysilicon)
pPCE	Pseudo power conversion efficiency
ppm	Parts per million
PV	Photovoltaics
QCM	Quartz crystal microbalance
qRN	Quasi-resonant neutralisation
SCAPS	Solar Cell Capacitance Simulator
SCCM	Standard cubic centimeter per minute
SEM	Scanning electron microscopy
SLG	Sode-lime glass
SQ	Schockley-Queisser
SR	Spectral response
SRH	Shockley-Read-Hall
STH	Solar to hydrogen
TBW	Time bandwidth
TCO	Transparent conductive oxide
TOPCon	Tunnel oxide passivated contact

TRTS	Time-resolved terahertz spectroscopy
UHV	Ultra high vacuum
UPS	Ultraviolet photoelectron spectroscopy
UV	Ultraviolet
UV-Vis	Ultraviolet-visible spectroscopy
VBM	Valence band maximum
XPS	X-ray photoelectron spectroscopy
XRD	X-ray diffraction

Symbols

α	Absorption coefficient
χ_e	Electron affinity
ϵ_0	Permittivity of free space
ϵ_r	Relative permittivity of the material
η	Power conversion efficiency
λ	Wavelength
λ_exc	Excitation wavelength
λ_scatt	Scattered wavelength
μ	Carrier mobility
μ	Material modulus
μ_e	Electron mobility
μ_h	Hole mobility
μ_eh	Chemical potential of the electron-hole pairs
μ_Σ	Sum of electron and hole mobility
ν	Photon frequency
ω	Angular frequency
ω	Wavenumber
ϕ	Work function
$\phi_\mathrm{AM1.5G}$	Spectral photon flux
ρ	Electrical resistivity
ρ	Material density
σ	Electrical conductivity
τ	Carrier lifetime

Nomenclature

$\tau_{\mathrm{non-rad}}$	Non-radiative recombination lifetime
τ_{rad}	Radiative recombination lifetime
τ_{scat}	Carrier scattering time
θ	Diffraction angle
θ	Scattering angle
θ_{z}	Zenith angle
A	Absorbance
A	Area
C	Capacitance
c	Speed of light
D	Diffusion coefficient
d	Absorber thickness
d	Crystal lattice spacing
D_{e}	Electron diffusion coefficient
D_{h}	Hole diffusion coefficient
e	Elementary charge
E_{i}	Incoming ion energy
E_{r}	Reflected ion energy
E_{bin}	Binding energy
E_{C}	Energy level of the conduction band minimum
E_{FC}	Quasi-Fermi energy level for electrons
E_{FV}	Quasi-Fermi energy level for holes
E_{F}	Fermi energy level
E_{g}	Bandgap
E_{kin}	Kinetic energy
E_{V}	Energy level of the valence band minimum
f	Frequency
G	Generation rate
h	Planck constant
I	Current
I_0	Incident light intensity
I_{T}	Transmitted light intensity
I_{ph}	Photogenerated current

J_{mp}	Current density for the maximum power point
J_0	Dark (or reverse) saturation current density
J_{sc}	Short-circuit current density
J_{ph}	Photogenerated current density
k_{B}	Boltzmann constant
l	Optical path length through atmosphere
l_0	Atmosphere thickness
L_{diff}	Diffusion length
L_{e}	Electron diffusion length
L_{h}	Hole diffusion length
m^*	Effective mass
m_0	Electron mass
M_{i}	Incoming ion mass
M_{s}	Surface atom mass
m_{C}	Effective electron DOS mass in the conduction band
m_{e}	Effective electron mass
m_{h}	Effective hole mass
m_{V}	Effective hole DOS mass in the valence band
n	Ideality factor
n	Order of reflection
n	Refractive index
N_{q}	Frequency constant for an AT-cut quartz crystal
n_{i}	Intrinsic carrier concentration
n_{A}	Density of acceptors
n_{CV}	CV density of the lightly doped side of the one-sided p-n junction
N_{C}	Effective DOS in the conduction band
n_{D}	Density of donors
n_{e}	Density of electrons in the conduction band
n_{h}	Density of holes in the valence band
N_{V}	Effective DOS in the valence band
P_{max}	Largest photogenerated power density
Q	Charge
q	Elementary charge

Nomenclature

R	Recombination rate
R_p	Parallel resistance
R_sh	Shunt resistance
R_s	Series resistance
T	Temperature
T	Transmittance
V	Voltage
V_ac	Alternating current (AC) voltage
V_bi	Built-in voltage
V_dc	Direct current (DC) voltage
V_mp	Voltage for the maximum power point
V_oc	Open-circuit voltage
v_oc	Normalised voltage
W	Depletion region width
X	Reactance
$x_{\mathrm{p-n}}$	Distance to the p-n junction interface
Z	Impedance
FF	Fill factor
pη	Pseudo power conversion efficiency
pV_oc	Pseudo open-circuit voltage
pFF	Pseudo fill factor
Z	Z-factor of film material

1 | Introduction

This chapter motivates the research and work performed during my PhD project and will provide an overview of the contents of this thesis. The aim of the project, was as the title of the thesis suggests, to fabricate wide-bandgap selenium-based solar cells for tandem device applications. This chapter will seek to provide the reader with the necessary knowledge required to understand what those words in fact mean and how it connects to the ambition of providing cheap and efficient sustainable and renewable solar energy generation and storage.

1.1 The Global Energy and Climate Crisis

Humans have evolved and developed in the past 1.2 million years. The climate of Earth has through this period of time mainly been affected by slow changes in Earth's orbit and inclination which has kept it in a glacial-interglacial cycle resulting in ice ages around every 100,000 years.[1] The global average temperature of the past 420,000 years has been estimated from ice core drillings at Antarctica to have fluctuated around 10 °C below pre-industrial levels. However, the global average temperature has in the past 11,700 years (also called the Holocene geological epoch) been remarkably stable within 1 °C.[2] This stability allowed Homo sapiens to transition from nomadic hunter-gatherer tribes to sedentary communities that led to the development of agriculture and eventually complex technology driven societies.[1]

Today, the world faces a global energy and climate crisis caused by man-made greenhouse gas emissions, that has since the industrial revolution (ca. year 1850) led to the increase in the average global temperature of around 1 °C.[3] The increase in temperature is presumed quasilinearly correlated with the concentration of CO_2 in the atmosphere, which absorbs the blackbody radiated infrared light (wavelength of about 10 µm) emitted from Earth.[1,4,5] Without CO_2 in the atmosphere, Earth's average temperature would be around -18 °C instead of the present average temperature of ≈ 16 °C.[6] However, in the past 800,000 years the CO_2 concentration has fluctuated in the range of 180-300 parts per million (ppm). Since 1950, this concentration has been steadily increasing above 300 ppm due to man-made emissions (mainly the combustion of fossil fuels) and is at the time of the writing of this thesis at 416 ppm and increasing at an alarming rate of around 3 ppm per year (up to 10 times faster than any sustained rise in CO_2 during the past 800,000 years).[7,8] In turn an increased number and intensity of natural extreme weather phenomenons, such as floods, wildfires, heatwaves and droughts, have been observed in recent years.[9] This signifies an end to the Holocene and the beginning of a new epoch which has unofficialy been coined the Anthropocene that will be heavily affected by the impact of the actions of mankind.[1] Figure 1.1 illustrates the history of the fluctuating atmospheric CO_2 concentration in the past 800,000 years that have correlated with the glacial-interglacial cycle and the correlation between the increasing CO_2 concentration and the average temperature anomaly since 1850.

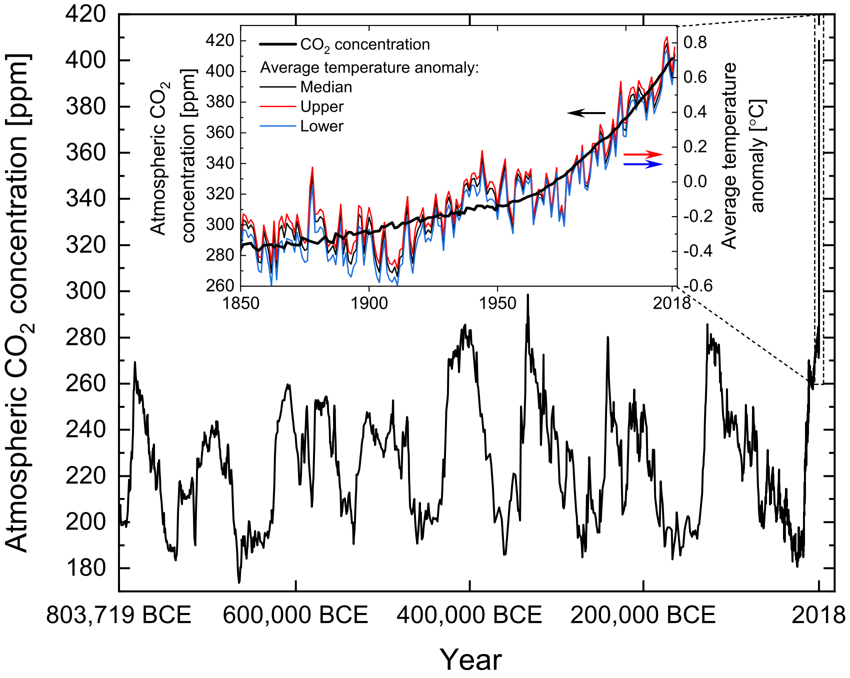

Figure 1.1: Atmospheric CO_2 concentration for the past 800,000 years and the recent increase in the global average temperature anomaly since 1850 and its correlation to the rising CO_2 concentration. Data obtained from [10], which is sourced from [11] and [12].

Thus, the future trajectory of the climate of Earth looks to be headed away from the glacial-interglacial cycle, which is schematically illustrated in Figure 1.2.

Many potential biogeophysical feedbacks have been identified that may further accelerate global warming once a certain temperature threshold is met. Many of

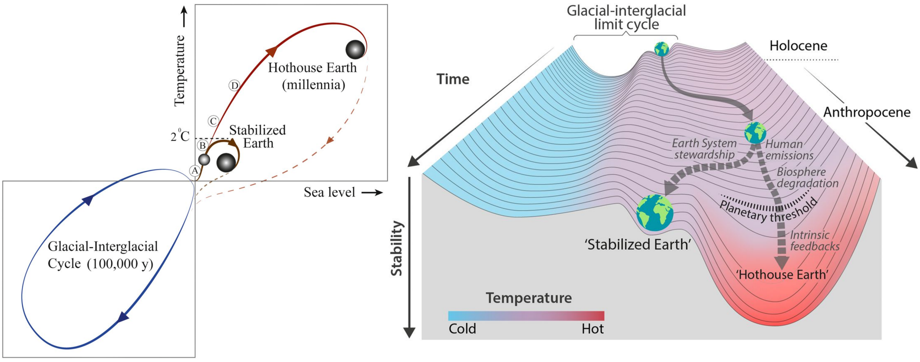

Figure 1.2: Schematic illustrations of the possible future climate pathways versus past typical glacial-interglacial cycles. A proposed stable planetary threshold at ≈ 2 °C above pre-industrial levels is shown. Left: Four recent time periods along the Stabilised/Hothouse Earth pathways are represented: (A) Mid-Holocene, (B) Eemian, (C) Mid-Pliocene and (D) Mid-Miocene. Right: Increasing temperatures above an uncertain planetary threshold (≈ 2 °C) will likely lead to an irreversible pathway towards a 'Hothouse Earth'. The term stability is meant to symbolise the likelihood of the trajectory. Figures reprinted with permission from [1].

these tipping points are estimated to occur between and above temperatures of 1-5 °C compared to pre-industrial levels. Some of these run-away scenarios include the melting of the polar ice sheets, thawing of permafrost and forest dieback of the Amazon and Boreal forests. Some of which are already happening at an alarming rate. Going beyond this planetary threshold will set the climate towards the so called 'Hothouse Earth' trajectory where the global average temperature and sea levels may rise to devastating levels. With the current CO_2 concentration in the atmosphere, this trajectory will in the best case scenario lead to climate conditions similar to those of the Mid-Pliocene (≈ 3-4 million years ago) or with the present trajectory be similar to the Mid-Miocene (≈ 15-17 million years ago), which had atmospheric CO_2 concentrations/global mean surface temperatures of up to 400-450 ppm/2-3 °C and 300-500/4-5 °C, respectively.[1]

The Paris Climate Accord has a goal of limiting global warming well below 2 °C and preferably to 1.5 °C.[13] In order to stay below the 1.5 °C goal, CO_2 emissions must be reduced by ≈ 50% by 2030 (relative to 2010) and to net zero by around 2050.[14] Even if these goals are achieved, the climate trajectory may still pass the planetary threshold, which may ultimately require new technology to capture and permanently store CO_2.[15]

Man-made CO_2 emissions mainly stem from the combustion of fossil fuels, that for the past 100 years have been the primary energy source of mankind and has enabled the exponential growth of the world population, technological advancement and energy consumption. The global primary energy consumption by source is shown in Figure 1.3.

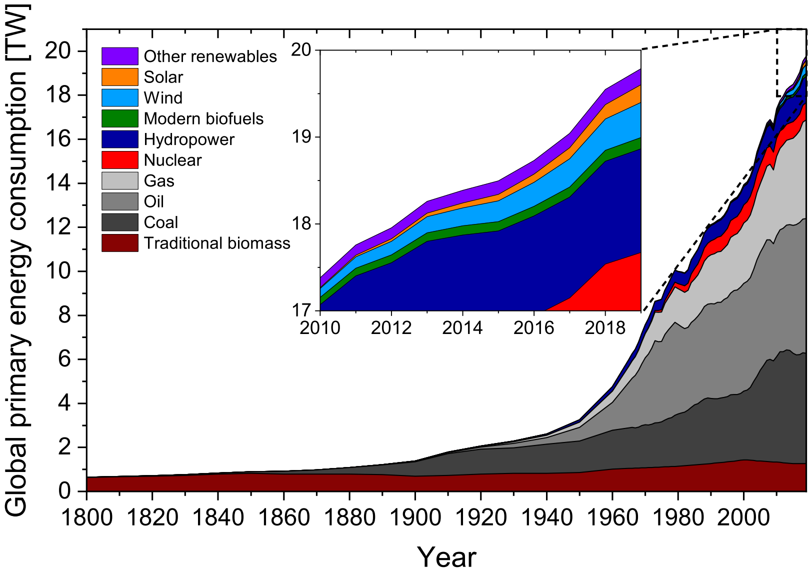

Figure 1.3: Global primary energy consumption by source up until 2019 recalculated from TWh per year to TW. Data obtained from [10], which is sourced from [16] and [17].

The global energy consumption is almost 20 TW, from which only 2.1 TW originate from renewables (2.9 TW if nuclear power is included). It is evident from the data that the global energy consumption is rising and it is estimated that a demand in the order of more than 30 TW is to be expected around 2050.[18,19] In the meantime, all the energy consumption by fossil fuels (gas, oil and coal) and traditional biomass must be eliminated if the goal of reducing CO_2 emissions to net zero is to be met. Since 2010 the share of renewables in the global power consumption has increased from 7.7% to 10.7%, whereas nuclear power has decreased from 4.7% to 4.0%.

Ultimately, this requires the need for the exponential growth of installed renewables on the TW scale if the Paris Climate Accord goals are to be met. There are three renewable energy sources available to us: 1. the radiation from the Sun, 2. the internal heat of Earth and 3. the gravitational pull of the Moon on Earth. All renewable energy sources are either directly or indirectly derived from these.

The most scalable renewables are solar and wind power, both of which derive their energy from the Sun either directly or indirectly. The solar irradiance that hits the surface of the Earth (assuming 65% losses from albedo and atmosphere absorption and reflection) is around 23,000 TW[20], which is more than 700 times our predicted energy consumption in 2050. Wind is a derived energy source of the Sun caused by the variation of absorbed sunlight, which creates atmospheric pressure gradients. A maximum estimation for the possible wind power is around 70-120 TW. The rest of the renewable energy sources are far more finite with accessible geothermal power of around 0.3-2 TW, tidal wave power of around 0.3 TW, hydropower of around 3-4 TW, biomass power of around 2-6 TW and ocean thermal energy conversion (OTEC) power of around 3-11 TW.[20]

Renewable energy primarily generates electricity and therefore requires as much of the total energy consumption to become electrified as possible. The current electricity consumption is at around 3.1 TW (15.6% of the total consumption), from which 62.8% still originates from fossil fuel combustion (mainly coal and natural gas).[17] The levelised cost of energy (LCOE) of both solar and wind power are already lower than fossil fuels and is continuously falling with increased installed capacity.[21] However, even though renewables are now offered at a competitive cost, they still face two major issues. The first being that the electrification of certain sectors is difficult and secondly the fact that solar and wind energy is highly intermittent. Both issues can be potentially be solved if the electricity can be stored efficiently through the conversion into chemical bonds in chemical fuels. To achieve this in a renewable fashion the Earth abundant feedstocks of water, carbon dioxide and nitrogen should be converted electrochemically (or photoelectrochemically) into sustainable fuels such as for instance hydrogen, ethylene or ammonia. This requires the development of new electrocatalysts that goes beyond the scope of this work.[22]

1.2 Harnessing the Power of the Sun

The solar spectrum can be approximated by the radiation from a black body with a temperature of around 5800 K. The solar spectrum ranges from ultraviolet (UV) to infrared (IR) (around 150-4000 nm or 8.0-0.3 eV) with the greatest spectral irradiance within the visible region (around 380-750 nm or 3.3-1.65 eV).[5] The Sun irradiates the outside of Earth's atmosphere with a power density of around 1361 W/m^2.[23] Before reaching the surface of Earth it is partially absorbed by the various gasses of the atmosphere (mainly H_2O and O_3) that decreases the intensity of certain parts of the spectrum. The longer a distance the light has to pass through the atmosphere the more is absorbed. The ratio of this optical path length, l, with respect to the thickness of the atmosphere, l_0, is characterised by an air mass coefficient (AM), which is related to the incident angle with respect to the zenith, θ_z:[5]

$$\mathrm{AM} = \frac{l}{l_0} = \frac{1}{\cos(\theta_\mathrm{z})} \tag{1.1}$$

The spectrum outside of the atmosphere is denoted as AM0 and on the surface of the Earth with the sun directly overhead ($\theta_\mathrm{z} = 0°$), the spectrum has been absorbed by exactly "one atmosphere" denoted as AM1. With a zenith angle of $\theta_\mathrm{z} = 48.2°$, the spectrum power density is 1000 W/m^2 for AM1.5. The AM1.5

spectrum has been chosen as the standard spectrum for measuring the efficiency of terrestrial solar cells (often denoted as AM1.5G for the global standard solar spectrum).[5] The AM0 and AM1.5G solar spectra can be seen in Figure 1.4.

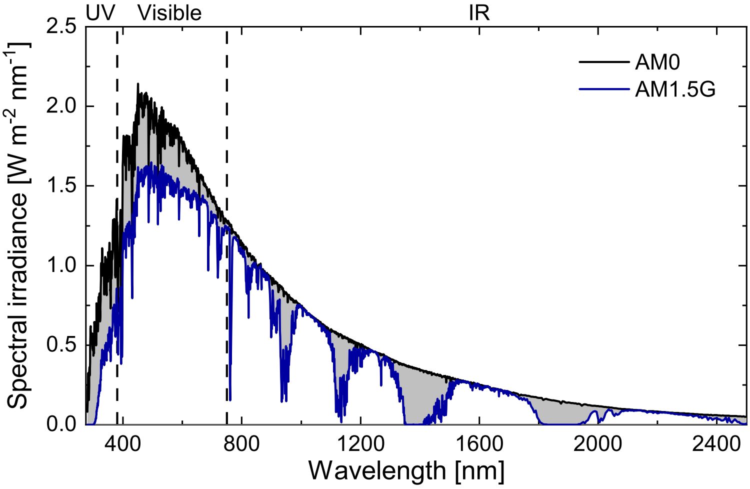

Figure 1.4: AM1.5G and AM0 solar spectra. AM0 is the solar spectrum outside of the atmosphere and AM1.5G is the global standard spectrum at a zenith angle of 48.2°, that includes ambient diffused light. Data obtained from [24].

A solar cell utilises an absorber material, that can absorb light above its bandgap (typically a semiconductor with a bandgap of $E_\mathrm{g} = 0.7$-2.0 eV). The photons with energies above the material bandgap can be absorbed which may generate electron-hole pairs in the valence and conduction band. Within a timescale of about 10^{-12} s, the electrons and holes thermalise to the band edges and reach a thermal and chemical equilibrium with the phonons where they maintain a kinetic energy of $\frac{3}{2}k_\mathrm{B}T$. After thermalisation the distribution of the electrons and holes can be described by two different Fermi-Dirac distributions with the quasi-Fermi energy levels E_FC and E_FV for the electrons and holes, respectively. The thermalisation and splitting of the Fermi levels produces chemical energy and the difference between the quasi-Fermi levels corresponds to the chemical potential, $\mu_\mathrm{eh} = E_\mathrm{FC} - E_\mathrm{FV}$, of the electron-holes pairs. The chemical potential can be converted into electrical power by separating and collecting the photogenerated electrons and holes at different terminals before they recombine. To separate the carriers such that an electrical current can be obtained, a gradient in the electrochemical potential (or the quasi-Fermi levels) must be present, such that the electrons and holes flow naturally in opposite directions.

This can be achieved through a heterojunction structure where the absorber is sandwiched in between n- and p-type materials, with greater bandgaps than the absorber, which act as selective contacts for the electrons and holes, respectively.

Another approach is the p-n homojunction structure, in which the main absorber itself is the less doped side of the junction. The overall efficiency of the solar cell is balanced between losses of the different processes: photon absorption, carrier generation, recombination, separation and transport. [5]

Even for a perfectly designed and fabricated solar cell without any extrinsic losses such as reflection, parasitic absorption, non-radiative recombination and parasitic resistance losses, there is an intrinsic upper theoretical limit for the efficiency of the solar cell. This limit is either called the detailed balance or Schockley-Queisser (SQ) limit, which was first calculated in 1961 by William Schockley and Hans J. Queisser. [25]

The limit originates from the fact that the solar spectrum is broad whereas the absorption of the absorber is determined from its mono-energetic bandgap. In this manner a balance between four energy losses occurs: 1. loss of photons that are not absorbed, 2. loss of kinetic energy from thermalisation, 3. loss by reemission of photons (radiative recombination) and 4. loss during carrier collection (isothermal dissipation). To calculate the largest obtainable power and efficiency of a solar cell as a function of its absorber bandgap, a few assumptions are made: 1. all photons above the bandgap are absorbed, 2. exactly one electron-hole pairs is generated and collected per absorbed photon, 3. after thermalisation, the carriers are in thermal equilibrium with the solar cell and ambient temperature, 4. carrier recombination is only radiative and 5. the contacts are perfectly selective with no ohmic losses. [26] Photons that are reemitted from radiative recombination may be reabsorbed again, which is called photon recycling. [26] Obviously the greatest SQ-efficiency is then obtained when the external radiative efficiency (ERE) is 100%, corresponding to zero non-radiative recombination losses in the solar cell. In other words the absorber should be an equally perfect emitter as it is an absorber of photons above its bandgap. The calculation of the SQ-limit for the AM1.5G spectrum for ERE = 100%, 1% and 0.01% with the experimental efficiency records of various known solar cell absorbers as well as a schematic of the efficiency losses are illustrated in Figure 1.5. [26–28]

For the AM1.5G spectrum (with ERE = 100%) a maximum efficiency of 33.6% and 33.8% is obtained for a bandgap of 1.145 and 1.336 eV, respectively. A direct correlation between the improved external radiative efficiency and the solar cell efficiency of $\mathrm{CuIn}_{1-x}\mathrm{Ga}_x\mathrm{Se}_2$ (CIGS) from 2010 and lead-halide perovskites from 2013 until 2019 are highlighted. [27]

Silicon (c-Si) has a nearly ideal bandgap of 1.12 eV, which has made it a leading photovoltaics (PV) technology with over 95% of the market. The remaining 5% are mainly split between the mature thin film CdTe and CIGS technologies. [29] Since the first silicon solar cell was reported in 1941 [30] many improvements have been made that have culminated in a single-junction record of 26.7%. [31] Mass production has allowed for an annual growth of globally installed solar PV capacity of around 50% from 1996 until 2015. [10] In the meantime, both the improvement in efficiency and advancement in production volume has allowed

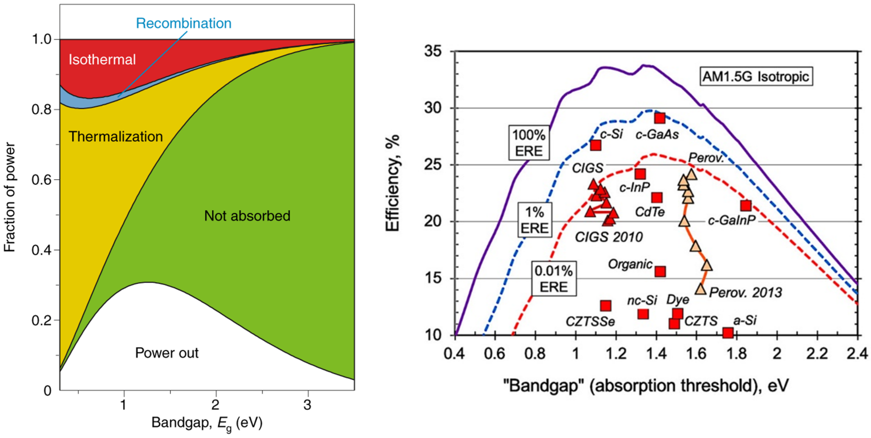

Figure 1.5: Left: Illustration of the Schockley-Queisser limit and the corresponding energy loss origins. Right: The SQ-limit for the AM1.5G spectrum for ERE = 100%, 1% and 0.01% with the greatest experimental efficiency records for various solar cell absorbers. Figures reprinted with permission from [26] and [27].

for a global average PV module price reduction of ≈ 22.6% per doubling of cumulative installed PV capacity since 1976 and ≈ 33.5% since 2006. Similarly the module price has halved around every 6.5 years since 1976 and around every 3.5 years since 2006. This trend is commonly known as Swanson's law. The data is plotted in Figure 1.6 next to the median residential solar PV cost in the US from 2000-2015.

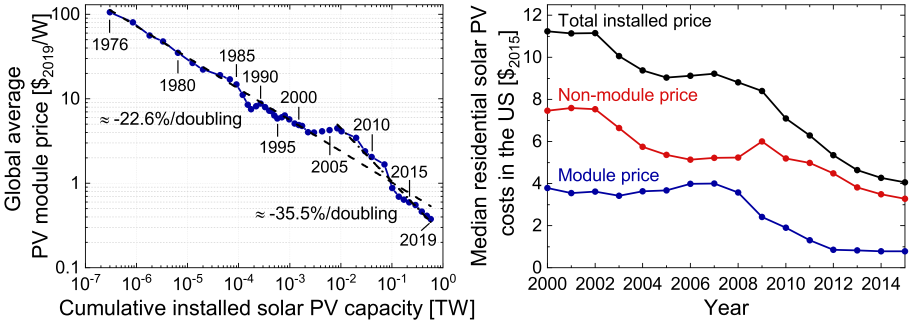

Figure 1.6: Left: Global average silicon PV module price as a function of cumulative installed PV capacity. 1976-2019 trend: Module price is halved every ≈ 6.5 years. 2006-2019 trend: Module price is halved every ≈ 3.5 years. Right: Silicon PV system costs from 2000-2015. Data obtained from [10], which is sourced from [32], [33] and [34].

If the exponential growth in cumulative installed PV capacity from 1976-2019 continues then 30 TW capacity will be reached by 2035. However, an unfortunate linear trend is observed from 2017-2019 where only 97 GW were installed each year. If this linear trend continues then a capacity of 30 TW will be reached by year 2321. The major cost reduction over both time and installed capacity has now resulted in the module price only constituting a fraction of the total installed system price. The non-module system cost (also called the balance of system cost) includes costs from both hardware and labour such as inverters, mounting equipment, land use, electrical wiring, grid connection fees, system design, maintenance and installation labour. [34]

One of the main cost reduction drivers has been the improvement in average module efficiency. [35] However, now silicon modules are reaching their SQ-limit as well as only constituting a fraction of the total installed systems costs. This introduces a new challenge for PV research: Surpassing the SQ-limit while maintaining low costs and complexity. Some of these new technological concepts include hot carrier photovoltaics [36], thermophotovoltaics [37], up-conversion [38], singlet fission [39], impact ionisation [40], intermediate band [41] and multi-junction photovoltaics [42].

The work of this thesis is mainly motivated by tandem photovoltaics, which is multi-junction photovoltaics with two absorbers. Multi-junction photovoltaics introduces multiple absorbers with different bandgaps within one device. In this manner each absorber may more efficiently absorb different parts of the solar spectrum such that the overall losses from non-absorbed light and thermalisation are minimised. Multi-junction PV technology has mainly been developed for aerospace applications using III-V semiconductors (such as GaAs). For this application the key parameter has been to improve the overall efficiency rather than balance it with the fabrication cost and abundance of the materials. Tandem photovoltaics seeks to provide a balance between the overall efficiency and the cost and potential for mass production, which may prove to be more cost-competitive than single-junction silicon solar cells. [43]

1.2.1 Tandem Photovoltaics: Two Absorbers Are Better Than One

There are three different tandem architecture types: 1. mechanically stacked tandem, 2. spectrally split tandem, or 3. monolithically integrated tandem. [44]
The mechanically stacked tandem, which is also known as the 4-terminal (4T) tandem, allows the sub-cells to be mechanically separated on top of each other in which case they can be fabricated independently. This allows for flexible processing and design and allows for a wider independent tuning of their current and voltage. However, this approach requires 3 out of 4 terminal contacts to be transparent.
The spectrally split tandem uses dichroic mirrors to redirect the photons to their respective sub-cells which are also physically separated. The feasibility of upscaling this approach is uncertain as it requires expensive dichroic mirrors and a

more complex and impractical structure.
The monolithically integrated (MI) tandem requires all layers to be sequentially deposited on top of each other. Thereby the sub-cells are physically stacked with a tunnelling junction or recombination layer in between them. This approach requires only the top terminal contact to be transparent, resulting in a practically higher efficiency and fabrication cost potential. The monolithically integrated tandem allows for both a 2-terminal (2T) and 3-terminal (3T) design.[44]

Figure 1.7 shows the theoretical maximum power conversion efficiency (PCE) obtainable for a tandem as a function of its sub-cell bandgaps.

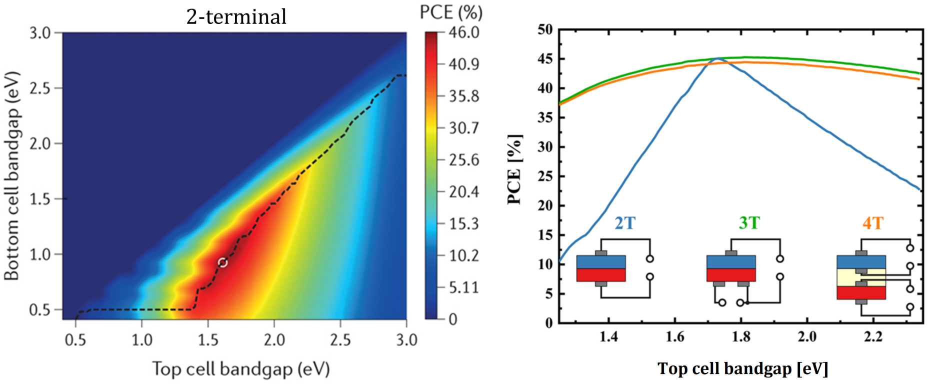

Figure 1.7: The detailed balance limit of a tandem solar cell as a function of its sub-cell bandgaps. Left: 2T monolithically integrated tandem. Right: 2T, 3T and 4T tandem with a silicon bottom-cell. Figures reprinted with permission from [45] and [46].

Silicon PV technology is unlikely to be out-competed in the near future and thereby silicon provides a suitable and cost-efficient bottom-cell with a bandgap of 1.12 eV. A suitable top-cell should in this case have a bandgap of around 1.75 eV, which may maximally achieve an efficiency of 45% (even without concentration). When utilising a 3T or 4T tandem design the bandgap requirement of the top-cell may be widened.
III-V/Si tandems have so far been demonstrated with record efficiencies of 32.8% for GaAs/Si and 32.5% for GaInP/Si. However, techno-economic analysis finds these to be presently infeasible for large scale applications compared to conventional Si solar cells.[47] Another group of suitable top-cell absorbers are organic-inorganic halide perovskites, where a monolithic perovskite-silicon tandem with an efficiency of 29.2% (perovskite top-cell bandgap of 1.68 eV) has already been demonstrated in 2020 by HZB.[48,49] The main challenge for perovskites remains their instability towards prolonged light exposure, moisture and high temperature. Thin film chalcogenides are also potential top-cell candidates from which a CGSe/Si tandem solar cell has been demonstrated with an efficiency of

9.7%.[48,50]

A monolithically integrated 2-terminal (MI-2T) tandem offers another possibility, namely efficient unassisted photo water splitting. Tandem photo water splitting would allow for the direct capture of sun light and storage into solar fuels by one single photoelectrochemical (PEC) device.[18,51,52]

1.2.2 Photoelectrochemical Tandem: Creating Solar Fuels

The collection and storage of solar energy is already demonstrated by nature in the form of photosynthesis. Photosynthesis is a complicated process in which solar light is stored into chemical energy through the conversion of CO_2 and H_2O into carbohydrates and O_2. Plants can survive with a low conversion efficiency in the order of 1%[53], but for the energy needs of mankind this is far from sufficient. Photo water splitting (or photoelectrolysis) provides a simpler chemical process in which solar energy is used to split H_2O into H_2 and O_2. The hydrogen can provide a usable and clean fuel whose only waste product upon use is water. The free energy cost for splitting water is 1.23 eV per electron. Taking the intrinsic losses into account for the PV SQ-limit as well as for the catalytic overpotentials for the hydrogen and oxygen evolutions (HER and OER), a single-junction absorber would require a bandgap of at least 2.3 eV to drive the reaction with a maximum solar to hydrogen (STH) efficiency of 7%.[54,55]

Calculating the detailed balance for a tandem photoelectrolysis device (see Figure 1.8) under standard conditions with photon matching (described in [56]), results in a STH efficiency of 20.8% with a top-cell bandgap of 1.8 eV and a bottom-cell bandgap of 1.1 eV (near optimum for silicon).

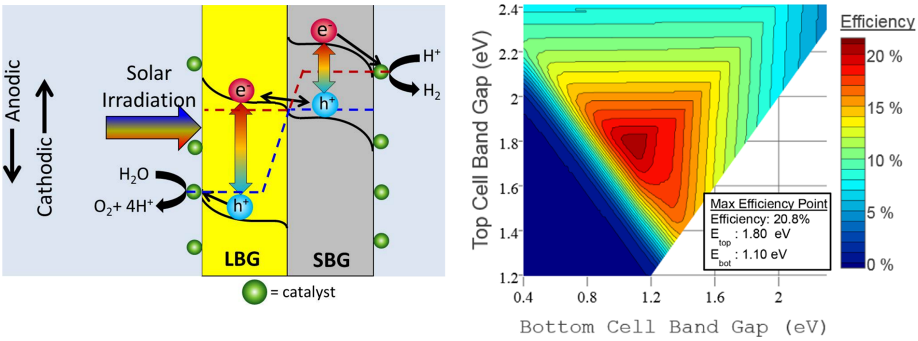

Figure 1.8: Schematic illustration of a monolithic tandem photoelectrolysis device and the detailed balance limit for the STH efficiency. Figures reprinted with permission from [54] and [56].

Two photons photogenerate electron-hole pairs in each sub-cell which are separated by the internal gradients of the electrochemical potential. Suitable catalysts are placed on the surface where the electrons will drive the HER on one side and holes will drive the OER on the other. To complete the circuit, the remaining electron-hole pairs recombine at the tunnelling or recombination layer in between the sub-cells. An electrolyte and an ion permeable gas barrier are used to allow for efficient ion transport. This typically requires the use of protective layers that prevents corrosion.

Notably the bandgap of the top-cell should for a photoelectrolysis tandem be higher than for a photovoltaic tandem. Also it is important to note that increasing the amount of absorbers above two for photoelectrolysis is futile. Increasing the amount of absorbers in a monolithically integrated multijunction device increases the voltage and not the current, since the layers are in series. If the tandem can provide the necessary voltage to run the reaction then it will be the photocurrent of the device that will limit the reaction rate. In an ideal case this makes the monolithically integrated tandem best suited for photoelectrolysis.

A suitable top-cell bandgap material may in fact be the very first discovered PV material, namely selenium (Se).

1.3 Selenium: The Oldest Photovoltaic Material

In 1873, Willoughby Smith discovered that selenium is photoconductive which means that the resistance of selenium changes when exposed to light.[57] Inspired by this discovery William Adams and Richard Day subjected selenium to various experiments. In one of these they contacted selenium with platinum electrodes and discovered in 1877 that selenium could photogenerate currents and internal voltages when illuminated.[58] They had in reality discovered the photoelectric effect which was later understood and explained by Albert Einstein in 1905.[59] He was later awarded the Nobel Prize in Physics for this work in 1921. In 1883 Charles Fritts made the first Se thin film solar cell module of 30 cm^2 with an efficiency of $< 1\%$, by compressing molten selenium in between a metal plate and a thin gold film.[60]

With the emergence and rapid development of the silicon industry, a natural shift away from using selenium as a semiconductor occured. In 1953 Daryl Chapin had attempted the development of selenium solar cells at Bell Labs, but found them too inefficient. He was persuaded by his colleague Gerald Pearson to switch to silicon instead. Together with Calvin Fuller they managed to create the first p-n junction in silicon by introducing gallium and lithium impurities. This resulted in the development of the first silicon solar cell in 1954 with an efficiency of approximately 6%.[61,62]

Selenium continued to be widely used in photosensors, rectifiers and xerographic plates, but in terms of photovoltaics it was outshone by silicon (pun intended). It was only in 1985 that Tokio Nakada and Akio Kunioka demonstrated a selenium solar cell with an efficiency of 5.01%, where a 2 µm thick layer of selenium was sandwiched in between thin layers of TiO_2 (50 nm) and Au.[63]

We now know that one of the main reasons why silicon was found to be more efficient than selenium is due to its more optimal bandgap for single-junction photovoltaics. Crystalline trigonal selenium has a large direct bandgap which has been reported to be between 1.8-2.0 eV.[64–66] This makes selenium a poor choice for a single-junction absorber. However, it is potentially a decent top-cell for tandem photovoltaics and potentially a perfect candidate for tandem photoelectrolysis when combined with a silicon bottom-cell. This work reports a bandgap of selenium of 1.95 eV, which for a Se-Si tandem results in a photovoltaic SQ-limit of $\approx 37\%$ or $\approx 44\%$ for a 2-T or 3T design, respectively.[46] Similarly, a maximum limit for the STH conversion efficiency is $\approx 16.9\%$ for a Se-Si tandem photoelectrolysis device.[56]

1.3.1 The Current State of Selenium

Selenium (Se) is a suitable direct wide-bandgap absorber for tandem applications. Se is an inexpensive single-element semiconductor with a low toxicity and a low melting point (220 °C)[67] that allows for low-temperature deposition methods that are ideal for simple and inexpensive scalability and also offers a compatible sequential monolithic tandem fabrication process on silicon.[68] Although Se is not earth abundant[69], its direct bandgap allows for sufficient absorption with a thin film thickness of 300-500 nm. Assuming that a Se-Si photovoltaics tandem can provide a PCE of 30% for a top-cell Se thickness of 300 nm, then an area of around 3000 km^2 would be required for 1 TW production. Knowing the density of trigonal crystalline selenium (4.81 g/cm^3)[67], around 4329 metric tons would be required. Assuming a STH efficiency of 15% for a tandem photoelectrolysis device, these numbers should be doubled (not taking the fuel efficiency of hydrogen into account).
Selenium is obtained almost exclusively as a by-product of copper mining and currently the world refinery production provides around 2800 metric tons of selenium per year, from which two-thirds is used for metallurgy and glass manufacturing.[19,70]
Thereby Se-Si tandem applications may offer the potential to provide renewable energy generation and storage on the terawatt scale. However, due to limited research and optimisation of Se photovoltaics, the investigation and optimisation of Se single-junction solar cells is still highly relevant.

Most Se single-junction solar cell literature have utilised the same single-junction cell structure of FTO/TiO_2/Se/Au. After almost 3 decades with limited research attention and zero improvements, a new Se single-junction efficiency record of 6.5% was set in 2017 by Todorov et al. from IBM.[68] This was achieved by changing the selective transport contacts of the device with a record device structure consisting of FTO/ZnMgO/Se/MoO_x/Au. Others have since then reported valuable insights into the control and improvement of the selenium crystallisation process[71,72] and alternative device architecture structures have shown to provide a more flexible fabrication approach as well as improve the device stability.[73,74] With a single-junction SQ-limit of $\approx 23.9\%$, there is still much room for improvement.[68]

1.4 Thesis Outline

The ambitious end goal of the project was to make a tandem Se-Si photoelectrolysis device. In order to achieve this goal, the first milestone was to obtain state of the art single-junction efficiencies and reproducibility. Secondly, for selenium to be incorporated in a top-cell it should allow light below its bandgap to be transmitted through to the bottom-cell, which requires both of its contacts to be semitransparent (also called a bifacial device). If the Se top-cell and Si bottom-cell can be monolithically integrated into a tandem photovoltaics device, then attempts could be made to finally introduce protection layers that would allow for the fabrication of a Se-Si photoelectrolysis device.

At the end of the project many of these milestones were achieved which culminated in partially successful tandem Se-Si photovoltaic device fabrication attempts. The structure of this thesis is a reflection of this progress and will try to convey some of the achievements of this work as well as estimate some of the fundamental limitations that selenium photovoltaic devices currently faces. The structure of the thesis is as follows:

Chapter 2 introduces and explains most of the experimental methods used during this thesis in order to understand the fundamental theory behind them. These include both the fabrication and characterisation methods of the Se-based solar cell devices.

Chapter 3 describes the typical architecture of the single-junction selenium solar cell and the role of the individual constituting thin film layers of the device. It further explains the typical fabrication process and the equipment used. Lastly it presents the fundamental measured properties of crystalline trigonal selenium after annealing and the elemental analysis of the thin film layers in the device.

Chapter 4 presents the device characteristics from single-junction to bifacial to Se-Si tandem cells of some of the many fabricated devices during the project. Initially, a brief summary of the best devices reported in literature is provided and finally the chapter summarises the best devices of this project.

Chapter 5 seeks to identify and estimate some of the intrinsic and extrinsic limitations of selenium and how that relates to the present device performances. Measurements, calculations and simulations are presented and compared in order to understand which fundamental properties of selenium and the overall device architecture are mainly to be improved for further device developments.

Chapter 6 concludes the work of this thesis and provides a summary of the main results and conclusions as well as an outlook that details suggestions for future experimental studies.

2 | Experimental Methods

This chapter will introduce the experimental methods used during this work as well as the necessary theory required to understand them. The methods have been split up into two sections that firstly include the thin film fabrication methods and secondly the thin film and device characterisation methods.

2.1 Physical Vapour Deposition

The synthesised thin films of this project were primarily made by use of the physical vapour deposition techniques: thermal evaporation and magnetron sputtering. The basic principle of both methods is the same, in which the ejection of particles from a solid state material travels ballistically in vacuum until it hits and forms an evenly distributed film on the sample.

2.1.1 Thermal Evaporation

Thermal evaporation is performed under vacuum at pressures below $\approx 10^{-6}$ mbar. The deposited material is heated from a resistive source, through the use of an external DC power supply, until a vapour pressure is produced. The lower pressure reduces the vapour pressure of the material, minimises external contamination and oxidation and also allows for a large mean free path of the evaporate material. A schematic of thermal evaporation is shown in Figure 2.1.

The evaporated material is ejected in all directions away from the source. The material that strikes and sticks to the surface of the sample will ideally grow to a uniform thin film.[75]

A thermocouple is used to measure the temperature of the heated crucible and a movable shutter can quickly eliminate further evaporation onto the sample.

A movable quartz crystal microbalance (QCM) is used to measure the deposition rate. A QCM is an extremely sensitive piezoelectric device from which its change in resonant frequency, Δf, can be related to the change in mass, Δm, of the deposited material in accordance with the Sauerbrey Equation (2.1):

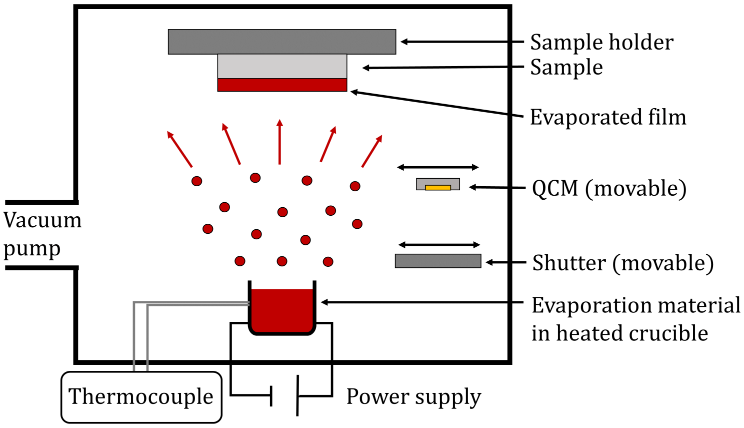

Figure 2.1: Schematic of thermal evaporation.

$$\Delta f = -\frac{2f_0^2}{A\sqrt{\rho_\mathrm{q}\mu_\mathrm{q}}}\Delta m \tag{2.1}$$

where f_0 is the resonant frequency of the QCM crystal, A is the piezoelectric active crystal area, ρ_q is the density of the quartz ($\rho_\mathrm{q} = 2.648$ g/cm^3) and μ_q is the shear modulus of the quartz ($\mu_\mathrm{q} = 2.947 \times 10^{11}$ g/cm·s^2).[76,77]

It is generally accepted that when the change in frequency from an increased material loading meets the conditions $\Delta f / f_0 < 2\%$, then the Sauerbrey equation can be used to accurately estimate the thin film thickness. The Sauerbrey equation can be extended to incorporate the elasticity of the deposited material (see Equation (2.2)):

$$\frac{\Delta m}{A} = \frac{N_\mathrm{q}\rho_\mathrm{q}}{\pi \mathrm{Z} f_\mathrm{L}} \tan^{-1}\left(\mathrm{Z}\tan\left(\pi\frac{f_\mathrm{U} - f_\mathrm{L}}{f_\mathrm{U}}\right)\right) \tag{2.2}$$

where N_q is the frequency constant for an AT-cut quartz crystal ($N_\mathrm{q} = 1.668 \times 10^{13}$ Hz·Å), f_U is the frequency of the unloaded crystal prior to deposition, f_L is the frequency of the loaded crystal and Z is the Z-factor of the film material ($\mathrm{Z} = \sqrt{\frac{\rho_\mathrm{q}\mu_\mathrm{q}}{\rho_\mathrm{f}\mu_\mathrm{f}}}$). The Z-factor is used to match the acoustic properties of the deposited material with the quartz crystal.[77]

The thermally evaporated materials of this project were Se and Te. The respective densities and Z-factors of these are $\rho_\mathrm{Se} = 4.39$ g/cm^3, $\rho_\mathrm{Te} = 6.25$ g/cm^3 and $\mathrm{Z}_\mathrm{Se} = 0.864$ and $\mathrm{Z}_\mathrm{Te} = 0.900$.[78]

2.1.2 Magnetron Sputtering

The magnetron sputtering method replaces the thermal evaporation heat source with a magnetron sputtering source. A schematic of a magnetron sputtering source can be seen in Figure 2.2.

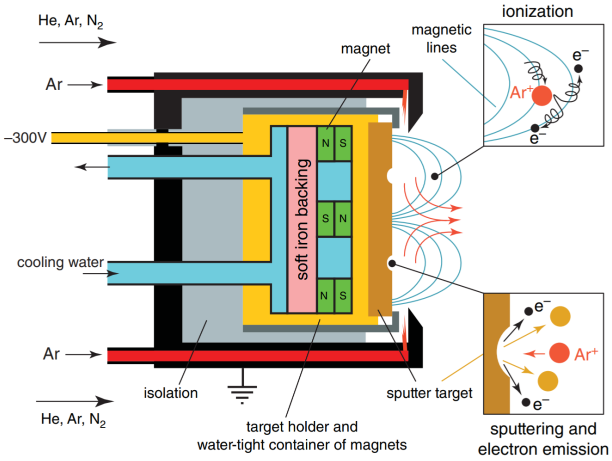

Figure 2.2: Schematic of a magnetron sputtering source. Reprinted with permission from [79].

The target material to be deposited sits inside the magnetron and functions as a cathode. Ar gas is introduced near the target through a flow controller. If the voltage applied to the cathode target reaches the breakdown voltage, then a glow discharge can be ignited. The Ar^+ ions of the formed plasma are accelerated toward the negatively charged cathode target. This collision causes both the ejection of secondary electrons that maintains the plasma as well as the ejection of the target material. Underneath the target sits a ring of magnets that create a magnetic field that confines the electrons near the surface of the target which in turn enhances the ionisation of the plasma. This lowers the required discharge voltage, expands the operational pressure range and leads to higher deposition rates. The Ar^+ ions are similarly affected by the magnetic field lines and collide primarily on the target in a circular pattern that is commonly called the racetrack. The sputtered atoms are neutrally charged and can thereby escape the magnetic field. Most of the energy is dissipated as heat in the target. This effect is diminished through the use of cooling water.[75,79,80]

The sputtered material can travel across the chamber and deposit onto the sample surface. See Figure 2.3. Next to the sample sits a gas inlet that allows the introduction of reactive gasses (e.g. O_2 or N_2) that can react with the newly deposited material.

The sample stage is able to rotate which promotes uniform deposition. On top of

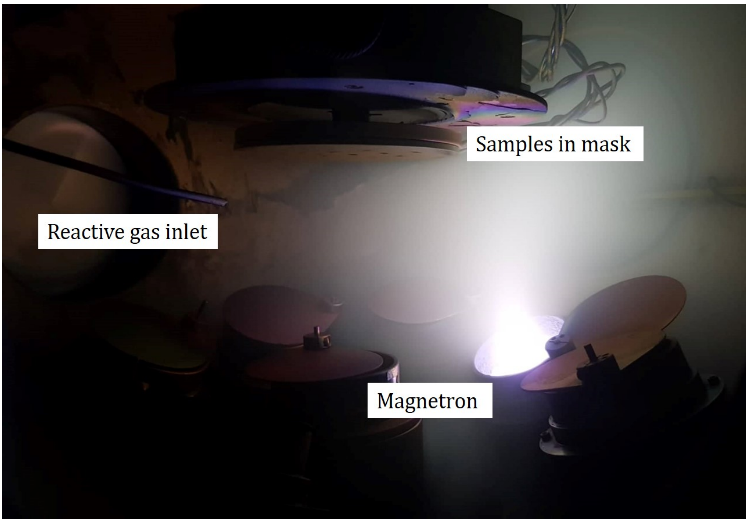

Figure 2.3: Picture of magnetron sputtering.

the samples sits a proportional-integral-derivative (PID) controlled lamp heater that allows for the heating of the sample during deposition.

For insulating materials, the effect of charge accumulation can be detrimental to the sustainability of the plasma. Utilising radio-frequency (RF) magnetron sputtering (commonly 13.56 MHz), this issue can be prevented as the charge accumulation is eliminated from the alternating voltage. However, the deposition rate is typically lower compared to DC-sputtering.[80]

Presputtering was performed with the shutter closed prior to all depositions to remove any potential native oxides or contaminants on the target surfaces. A QCM was used to determine the deposition rate in a similar fashion as for thermal evaporation. The deposition rate is determined by the ion flux onto the target, the sputter yield and the transport of material across the discharge. For metal alloy targets the sputter yield of the different elements will be different, but will with time result in an equilibrium deposition rate such that the ratio of the deposition rates equals the stoichiometry of the target. However, for metal oxide targets (or nitrides), the volatile oxygen or nitrogen may be pumped out of the system before deposition onto the substrate. Therefore reactive sputtering was also often utilised for oxide targets to prevent oxygen deficiency of the deposited thin films.

2.2 Characterisation Methods

Various characterisation methods were utilised to experimentally determine the properties of the materials and devices fabricated in this work. Knowing these properties is essential to understand the performance behaviour of the Se-based devices and to identify which parameters that must be optimised to achieve an optimum solar cell efficiency.

2.2.1 Current-Voltage (JV) Characterisation

The main method of characterising the selenium-based solar cells was to measure the current density, J, as a function of the applied bias, V, under both dark and AM1.5G (100 mW/cm^2) illumination conditions. A solar cell functions like a photodiode. The JV characteristics of a diode are related to the minority carrier currents of its p-n junction. The currents of the minority carriers are related to the gradients of their electrochemical potentials. The combined current is described by the Schockley diode Equation (2.3). For a photodiode, electron-hole pairs are photogenerated, which causes a current, J_{ph}, that runs in the opposite direction.

$$J = J_0 \left(\exp \left(\frac{eV}{nk_{\mathrm{B}}T} \right) - 1 \right) - J_{\mathrm{ph}} \tag{2.3}$$

where n is the diode ideality factor that is related to potential non-ideal non-radiative carrier recombination, which for an ideal diode should be 1 and J_0 is the dark (or reverse) saturation current which relates to the radiative recombination of the minority carriers (see Equation (2.4)). Both depend on the device and material qualities.

$$J_0 = en_{\mathrm{i}}^2 \left(\frac{eD_{\mathrm{e}}}{n_{\mathrm{A}}L_{\mathrm{e}}} + \frac{D_{\mathrm{h}}}{n_{\mathrm{D}}L_{\mathrm{h}}} \right) \tag{2.4}$$

where n_{i} is the intrinsic concentration of electrons and holes ($n_{\mathrm{i}}^2 = n_{\mathrm{e}}n_{\mathrm{h}}$), $D_{\mathrm{e/h}}$ is the diffusion coefficient of the electron/hole, $n_{\mathrm{D/A}}$ is the donor/acceptor density and $L_{\mathrm{e/h}}$ is the diffusion length of the electron/hole. [5,81]

A sketch of an ideal JV characteristic measurement can be seen in Figure 2.4.

Under short-circuit conditions ($V = 0$ V) the short-circuit current, J_{sc}, is obtained which for an ideal device equals the photogenerated current, J_{ph}. The largest photovoltage that can be achieved occurs at open-circuit conditions ($J = 0$ A/m^2) where the open-circuit voltage, V_{oc}, is related to n, J_{ph} and J_0:

$$V_{\mathrm{oc}} = \frac{nk_{\mathrm{B}}T}{q} \ln \left(\frac{J_{\mathrm{ph}}}{J_0} + 1 \right) \tag{2.5}$$

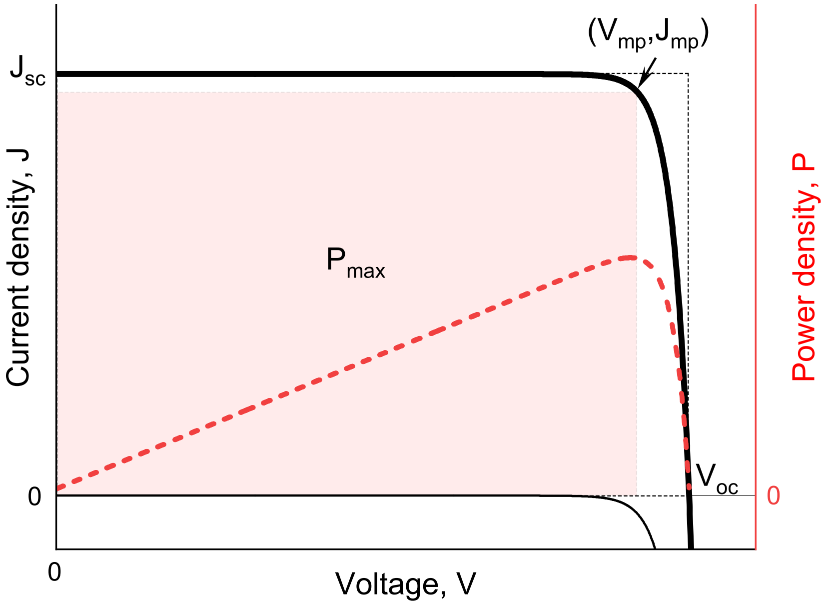

Figure 2.4: Sketch of the JV characteristics.

In a real solar cell, parasitic resistances can reduce its efficiency. Alternate leakage current paths can be described by a shunt resistance R_{sh} and transport ohmic losses can be described by a series resistance R_{s}. The equivalent circuit model can be seen in Figure 2.5.[5]

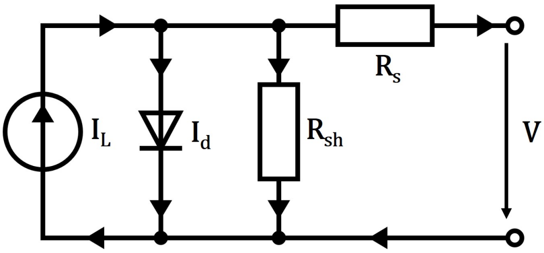

Figure 2.5: Equivalent circuit diagram of a solar cell.

For such a model the one-diode equation becomes:

$$J = J_{\mathrm{L}} - J_0 \left[\exp\left(\frac{q(V + JR_{\mathrm{s}})}{nk_{\mathrm{B}}T} \right) - 1 \right] - \frac{V + JR_{\mathrm{s}}}{R_{\mathrm{sh}}} \tag{2.6}$$

The largest obtainable power density, P_{max}, occurs when the product of the current density and voltage is greatest ($P_{\mathrm{max}} = V_{\mathrm{mp}} J_{\mathrm{mp}}$).

The fill factor, FF, is a measure that describes the relationship between P_{max} and the product of the short-circuit current and open-circuit voltage. In this manner it describes the squareness of the JV curve and is affected negatively by a low shunt resistance, R_{sh}, a high series resistance,R_{s}, and a poor diode behaviour (large carrier recombination resulting in a large diode ideality factor, n). The FF can be defined as:

$$\mathrm{FF} = \frac{J_{\mathrm{mp}} V_{\mathrm{mp}}}{J_{\mathrm{sc}} V_{\mathrm{oc}}} \tag{2.7}$$

Simply explained it is the relationship between the area of the two squares seen in Figure 2.4. Due to a finite radiative recombination limit, the FF can never be 100%. For a diode with an ideality factor, n, an ideal FF can be empirically approximated by:[82]

$$\mathrm{FF} = \frac{v_{\mathrm{oc}} - \ln(0.72 + v_{\mathrm{oc}})}{1 + v_{\mathrm{oc}}}, \quad v_{\mathrm{oc}} = \frac{qV_{\mathrm{oc}}}{nk_{\mathrm{B}}T} \tag{2.8}$$

v_{oc} is the normalised voltage which should be $v_{\mathrm{oc}} > 10$ for an accurate approximation. For $T = 298$ K and $n = 1$ this sets a limit on the open-circuit voltage of $V_{\mathrm{oc}} \gtrapprox 0.26$ V.

Finally the efficiency of the solar cell is described by the maximum electrical power output relative to the optical power of the sunlight ($P_{\mathrm{in}} = 100$ mW/cm^2 for AM1.5G):

$$\eta = \frac{P_{\mathrm{max}}}{P_{\mathrm{in}}} = \frac{J_{\mathrm{mp}} V_{\mathrm{mp}}}{P_{\mathrm{in}}} = \mathrm{FF} \frac{J_{\mathrm{sc}} V_{\mathrm{oc}}}{P_{\mathrm{in}}} \tag{2.9}$$

The JV characteristics of the Se-based solar cell devices were measured using a Keithley 2561A source meter with a 4-terminal sensing setup. A Newport solar simulator was used as a light source with an AM1.5G spectrum that is simulated from the filtering of a xenon arc lamp. A reference silicon solar cell was used to calibrate the light intensity to 1 sun (100 mW/cm^2).

2.2.2 External Quantum Efficiency (EQE)

The external quantum efficiency (EQE) is the measure of the amount of collected carriers of the device relative to the incident number of photons for a given wavelength. This relates to the spectral response (SR) which is defined as the current collected relative to the incident optical power. The SR and EQE relate to each other via:[83]

$$\mathrm{SR} = \frac{J_{\mathrm{sc}}}{P_{\mathrm{in}}} = \frac{e\lambda}{hc}\mathrm{EQE} \Longrightarrow \mathrm{EQE} = \frac{hc}{e\lambda}\mathrm{SR} \tag{2.10}$$

Measuring the SR as a function of the wavelength, λ, and plotting the EQE, one can obtain valuable information about the origin of current collection loss mechanisms in ones solar cell. An example is shown in Figure 2.6 where the potential loss mechanisms at each wavelength of the measured EQE of a single-junction Se-based solar cell is illustrated.

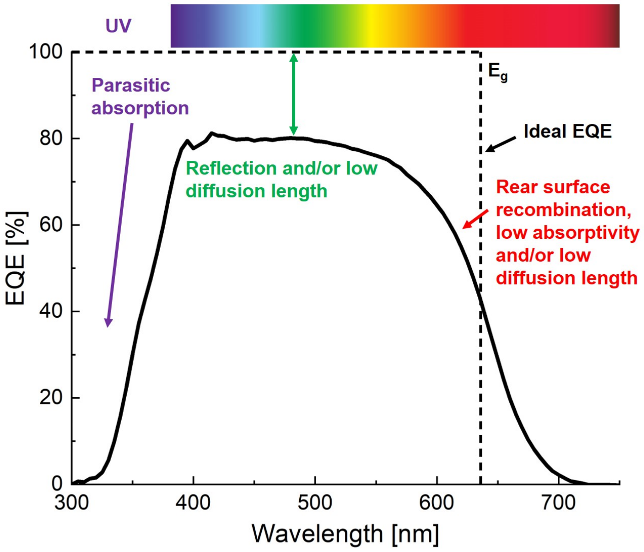

Figure 2.6: Example and sketch of an EQE spectrum of a single-junction Se-based solar cell with the potential current collection loss mechanisms as a function of wavelength.

The measurement is commonly carried out at short-circuit conditions, which allows for the determination of the short-circuit current density J_{sc}. It can be determined from the integration of the product of the EQE and the spectral photon flux, $\phi_{\mathrm{AM1.5G}}$, giving the total number of collected electrons, that when multiplied by the elementary charge, gives the J_{sc}:

$$J_{\mathrm{sc}} = e \int_0^{\lambda_g} \mathrm{EQE}(\lambda)\phi_{\mathrm{AM1.5G}}(\lambda)\mathrm{d}\lambda \tag{2.11}$$

The largest achievable photogenerated current, corresponding to the Schockley-Queisser limit, is obtained when each incident photon with an energy above the bandgap ($E_{\mathrm{ph}} > E_{\mathrm{g}}$) is absorbed, generating an electron-hole pair that are both collected at the terminals of the solar cell. For a bandgap of 1.95 eV, the largest obtainable short-circuit current for the AM1.5G spectrum is 15.7 mA/cm^2.

A QEXL Solar Cell Quantum Efficiency Measurement System was used for the EQE measurements of this work. The setup was calibrated using a reference silicon and germanium photodiode. For measurements on tandem devices a bias flood light was used with suitable optical filters.

The J_{sc} presented in the J-V results of this work were all adjusted to match the value of the J_{sc} measured with EQE to avoid spectral mismatch and internal reflection from outside the active area of the solar cells.

The AM1.5G spectrum used throughout the measurements of this work was retrieved from the American Society of Testing and Materials (ASTM G-173-03). The spectrum was plotted in Figure 1.4 along with AM0 (ASTM E-490-00). It should be noted that standard testing conditions for JV and EQE measurements are useful for the comparison of photovoltaic devices in literature, but real world conditions may vary significantly depending on both where you are on the globe and at what time of the day you are testing your device. For the determination of commercial viability, further field testing is therefore required.

2.2.3 Suns-V_{oc}

The Suns-V_{oc} method (also known as quasi-steady-state V_{oc}) measures the open-circuit voltage, V_{oc}, of the device as a function of illumination intensity. A flash lamp generates a monotonically decaying light pulse which induces a varying photovoltage in the device. The photovoltage is measured by a voltmeter and is related to the illumination intensity which is measured by a reference cell that sits next to the measured device. A pseudo-JV curve can be constructed from the linear relationship between the photogenerated current, I_{ph}, and the short-circuit current density, J_{sc}, (which is determined from either JV or EQE measurements):[84]

$$J = J_{\text{sc}}(1 - I_{\text{ph}}) \tag{2.12}$$

Since no current flows under the open-circuit conditions of the measurement, the pseudo-JV curve neglects the effect of series resistance losses.[84]

Suns-V_{oc} measurements of this work were performed with the Suns-V_{oc} stage for a WCT-120 by Sinton Instruments.

2.2.4 Capacitance-Voltage (CV)

Capacitance-voltage profiling can provide a great deal of information regarding the characteristic nature of the p-n junction of the device. The capacitance is defined as the change in charge as a function of the differential change in the voltage, $C = \mathrm{d}Q/\mathrm{d}V$. The capacitance is measured by applying a small AC voltage while varying the superimposed DC voltage. The current response is characterised by the complex impedance, $Z = \mathrm{Re}(Z) + j\,\mathrm{Im}(Z)$ (or the inverse admittance, Y), such that $V = IZ$, where $\mathrm{Re}(Z)$ is the resistance, R, and $\mathrm{Im}(Z)$ is the reactance, X.[85]

The depletion region width, W, of the p-n junction of the diode is given by (2.13). For a one-side junction where for instance the donor density of the n-type material is much greater than the acceptor density of the p-type material, $n_\mathrm{A} << n_\mathrm{D}$ (e.g. $n_\mathrm{A} = 10^{16}$ cm^{-3} $<< n_\mathrm{D} = 10^{18}$-$10^{20}$ cm^{-3}), the entire depletion region extends into the lower doped p-type region of the junction, which reduces the expression:[81]

$$W = \sqrt{\frac{2\epsilon_\mathrm{r}\epsilon_0(V_\mathrm{bi} - V_\mathrm{dc})}{e}\left(\frac{n_\mathrm{A} + n_\mathrm{D}}{n_\mathrm{A}n_\mathrm{D}}\right)} \approx \sqrt{\frac{2\epsilon_\mathrm{r}\epsilon_0(V_\mathrm{bi} - V_\mathrm{dc})}{en_\mathrm{A}}}, n_\mathrm{A} << n_\mathrm{D} \quad (2.13)$$

where ϵ_r is the relative permittivity of the lightly doped material, ϵ_0 is the permittivity of free space and V_bi is the built-in potential of the junction.

For this approximation the capacitance of the junction, C, is given by:

$$C \approx \sqrt{\frac{e\epsilon_\mathrm{r}\epsilon_0 A n_\mathrm{A}}{2V_\mathrm{bi} - V_\mathrm{dc}}} \quad (2.14)$$

Equation (2.14) can be manipulated to give:

$$C^{-2} = \frac{2(V_\mathrm{bi} + V_\mathrm{dc})}{e\epsilon_\mathrm{r}\epsilon_0 A n_\mathrm{A}} \quad (2.15)$$

Thereby the intercept and slope of the capacitance squared as a function of applied voltage yields the built-in junction voltage, V_bi, and CV density, n_CV, respectively. In an ideal case n_CV is equal to the n_A (or donor density, n_D, for an oppositely doped junction):

$$n_\mathrm{CV} = -\frac{2}{e\epsilon_\mathrm{r}\epsilon_0 A^2}\left(\frac{\mathrm{d}(C^{-2})}{\mathrm{d}V_\mathrm{dc}}\right)^{-1} = \frac{-C^3}{e\epsilon_\mathrm{r}\epsilon_0 A^2 \frac{\mathrm{d}C}{\mathrm{d}V}} \quad (2.16)$$

The capacitance and therefore also the doping density and voltage can be plotted as a function of the distance to the junction interface, $x_\mathrm{p-n}$, which at zero bias equals the depletion region width, W:[85]

$$x_\mathrm{p-n} = \frac{\epsilon_\mathrm{r}\epsilon_0 A}{C} \quad (2.17)$$

2.2.5 X-ray Photoelectron Spectroscopy (XPS)

X-ray photoelectron spectroscopy (XPS) is a surface sensitive UHV technique that can identify the elemental composition of the measured material. Monoenergetic X-rays are are irradiated onto the surface of the sample. The X-rays photogenerate electrons from the material that are emitted with a kinetic energy, E_{kin}, of:

$$E_{\text{kin}} = h\nu - E_{\text{bin}} - \phi \tag{2.18}$$

where $h\nu$ is the X-ray photon energy, E_{bin} is the electron binding energy and ϕ is the analyser work function. [86,87]

By measuring the kinetic energy of the emitted electrons, the binding energy of the atomic orbitals, from where they were ionised, can be determined. The binding energies of all elements are unique and therefore also characteristic. Thus one can determine the chemical composition of the probed surface.

The X-rays can be generated from a metal anode (commonly either Mg or Al) that is bombarded, from a heated filament, with high energy electrons (12 kV and 10 mA used for the XPS spectra of this work). The high energy electrons may ionise the 1s binding state of the metal, which causes higher energy electrons from e.g. the $2p_{1/2}$ or $2p_{3/2}$ orbitals to fill the empty state, that results primarily in the emission of monoenergetic $K_{\alpha12}$ X-rays. For the commonly used metal anodes, Mg or Al, the $K_{\alpha12}$ transition X-rays are $MgK_{\alpha12}$: $h\nu$ = 1253.6 eV with a full width half maximum (FWHM) of 0.7 eV or $AlK_{\alpha12}$: $h\nu$ = 1486.6 eV with a FWHM of 1 eV. [86] A MgKα X-ray source ($h\nu$ = 1253.6 eV) was used for all XPS measurements of this work.

Other less probable X-ray transitions are possible resulting in an emission spectrum that is not trivial. The second most probable transition, $K_{\alpha34}$, occurs due to a double ionisation and for Mg lies around 8.4 eV higher than the $MgK_{\alpha12}$ line with a 9.1% intensity, that results in X-ray satellites. This can be prevented by use of a monochromator. [86,87]

A thin aluminium foil is placed in front of the anode which prevents stray electrons and outgassing.

The emitted X-rays penetrate the bulk of the probed material (in the order of 1-10 µm) and excite electrons throughout. However, the photogenerated electrons have a limited mean free path which is related to their kinetic energy. This relation has been shown to be universally similar across various materials from various experiments (see Figure 2.7).

For an XPS measurement, the measured kinetic energies are typically in the range of 20-1400 eV, which corresponds to an electron mean free path of $\approx$ 1 nm. Thereby the detected electrons can only originate from the surface of the probed material, which makes the technique highly surface sensitive.

The kinetic energy of the photoelectrons is measured by use of hemispherical analyser. A hemispherical analyser consists of two concentric hemispheres with an entrance slit and a detector. A potential difference is applied across the two hemispheres that determines the pass energy that the electrons are allowed to travel through the analyser before being detected by the electron channeltron.

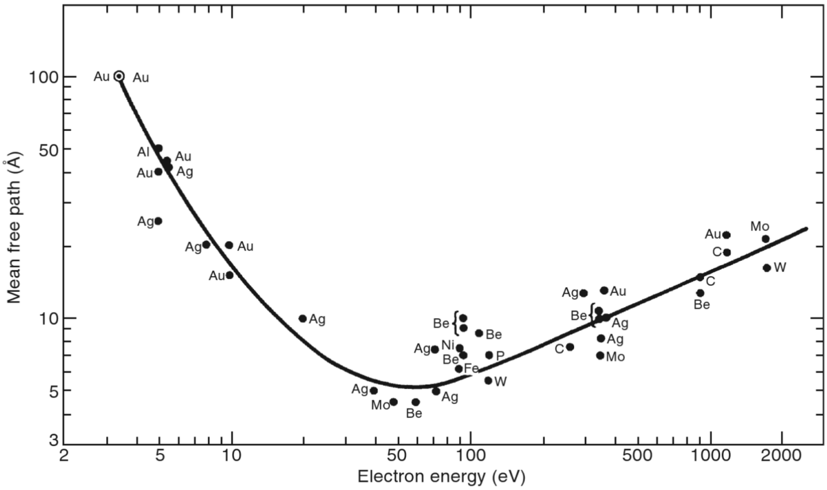

Figure 2.7: The mean free path of electrons at different kinetic energies in various materials. Figure reprinted from [86].

By varying the potential across the hemispheres one is thus able to vary the allowed kinetic energy of the electrons to be detected.[86] A standard mode of operation utilises a grid at the entrance of the analyser that retards the electrons to a specific pass energy (typically 25-125 eV). The resolution of the measured spectra is directly related to the pass energy (around 1%). A low pass energy provides greater resolution and a lower signal to noise ratio and vice versa. This mode is called fixed analyser transmission (FAT) or constant analyser energy (CAE) and results in a constant energy resolution (due to the constant pass energy).

XPS was used to qualitatively confirm the presence and elemental composition of the materials of the deposited thin film layers of this work.

2.2.6 Ultraviolet Photoelectron Spectroscopy (UPS)

Ultraviolet photoelectron spectroscopy (UPS) functions similarly to XPS, but replaces the X-ray source with an ultraviolet (UV) source. The UV emission is typically achieved through the ionisation of He that results in the photoexcitation of singly ionised He^{I} ($h\nu$ = 21.22 eV) or doubly ionised $\mathrm{He}^{\mathrm{II}}$ ($h\nu$ = 40.8 eV) photons that have an energy resolution in the order of meV due to the high lifetime of the ionised atoms. This allows for the efficient probing of the occupied valence levels (where XPS also probes the core levels) of the materials.[86] Thereby the workfunction, ϕ, and valence band with respect to the fermi level $E_{\mathrm{V}} - E_{\mathrm{F}}$ of the material can be determined. The work function of the analyser can be convoluted from the work function of the material by applying a bias to the sample. With the determination of the potential bandgap, E_g, from e.g. UV-Vis spectroscopy, the conduction band minimum energy, E_C, can further be determined providing the total band positions of the material.

2.2.7 Ion Scattering Spectroscopy (ISS)

Ion scattering spectroscopy (ISS), also known as low energy ion scattering spectroscopy (LEIS), is another UHV surface sensitive technique that allows for the determination of the surface elemental composition. The method relies on the binary elastic collision of noble gasses with the surface atoms, from which the surface atomic mass can be determined.

An ion source is used to ionise the noble gas atoms (typically He, Ar or Ne) and accelerate them towards the surface of the sample. Low ion doses and acceleration voltages are used to minimise sputter damage to the surface. Most of the ions that collide with the surface are subject to neutralisation (>99%) through multiple scattering processes. The few ions that survive the interaction have mainly interacted with the top layer primarily through a simple binary elastic collision and can be detected with the bipolar hemispherical analyser. The elastic binary collision conserves both the momentum and energy, from which the relation between the energy of the incoming ion, E_i, and energy of the reflected ion, E_r, is derived from classical mechanics:[86,88,89]

$$E_\mathrm{r} = \left(\frac{\cos\theta + \sqrt{\left(\frac{M_\mathrm{s}}{M_\mathrm{i}}\right)^2 - \sin^2\theta}}{1 + \frac{M_\mathrm{s}}{M_\mathrm{i}}} \right)^2 E_\mathrm{i} \tag{2.19}$$

where θ is the scattering angle between the incoming ion beam and the analyser ($\theta \approx 150^\circ$ for this work), M_s is the surface atom mass and M_i is the incoming ion mass. During the work of this project all ISS measurements were performed using 1 keV He^+ ions and 1 eV kinetic energy scan steps. The kinetic energy of the reflected ions is measured similarly as for XPS with a fixed pass energy, but with reverse polarity due to the positive charge of the ions. Knowing the ion mass and its initial kinetic energy, one can determine the masses of the atoms of the probed surface by scanning the measured kinetic energy. The non-binary collisions that occur lead to a shift in the measured peaks towards lower kinetic energies, so that the foot of the peaks corresponds to the calculated kinetic energy.

Utilising low mass He^+ ions (compared to heavier noble ions such as e.g. Ar^+ or Kr^+ ions) diminishes potential sputter damage significantly. However, the low mass also results in low energy resolution at higher kinetic energies that corresponds to the collision with heavier elements. This can make it difficult to distinguish between heavier elements which instead may be identified through XPS analysis. On the other hand, ISS provides a significant surface sensitivity down to as low as 0.1% of a monolayer. In this manner the ISS and XPS methods can greatly compliment one another. [86]

2.2.8 Scanning Electron Microscopy (SEM)

Scanning electron microscopy (SEM) is a type of electron microscopy that involves the scanning of an electron beam across a sample in vacuum in order to visualise its structure. An electron gun produces a stable beam of electrons with an adjustable energy of typically 0.1-30 keV. The beam of electrons is converged and scanned across the sample with a spot size diameter of less than 10 nm via various electromagnetic condenser/objective lenses and deflection coils. The electrons will penetrate and interact with the sample where they are scattered and absorbed. The scattering and absorption results in various different interactions that primarily results in the generation and/or ejection of primary electrons, secondary electrons and X-rays. This interaction volume relates to the energy of the electrons and the density of the material. Each of these signals can be detected by use of various detectors that can provide information regarding the chemical, elemental or structured nature of the sample. [90] The emitted characteristic X-rays originate from the whole of the interaction volume and can, if detected, provide elemental information about the bulk of the sample. This technique is known as energy dispersive X-ray spectroscopy (EDX-S). The secondary electrons have kinetic energies lower than <50 eV and therefore have a low mean free path in accordance with Figure 2.7. Thereby the topological information of the structure can be obtained through the detection of these.

Primarily the device structures of this work were visualised from the detection of secondary electron signals by use of an Evarhart-Thornley detector (ETD) or an In-lens detector.

2.2.9 X-ray Diffraction (XRD)

X-ray diffraction (XRD) analysis is used to determine the crystal structure of a sample. Monochromatic X-rays are emitted onto the sample from which the interaction may satisfy Bragg's law (see Equation (2.20)) resulting in diffracted X-rays.

$$n\lambda = 2d\sin\theta \tag{2.20}$$

Bragg's law relates the wavelength of the X-rays, λ, with the diffraction angle, θ, and the lattice spacing, d, for a crystalline sample. n is an integer called the order of reflection, which is equal to the number of wavelengths that satisfy the Bragg condition. A schematic of the Bragg condition can be seen in Figure 2.8.

When measuring the reflected X-rays as a function of the diffraction angle, Bragg peaks can be detected that are characteristic of the lattice constants and crystal structure of the sample. [91]

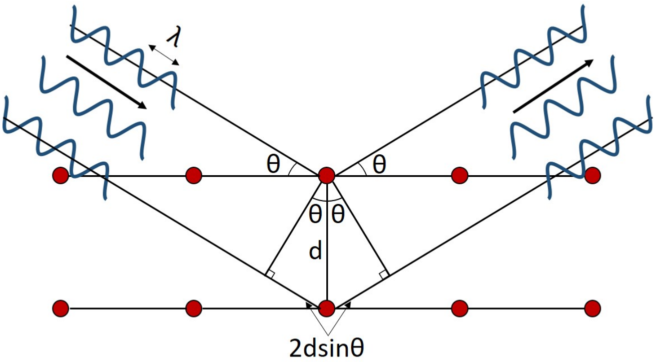

Figure 2.8: Schematic of the Bragg condition for X-ray diffraction of a crystal.

2.2.10 Ultraviolet-Visible Spectroscopy (UV-Vis)

Ultraviolet-visible (UV-Vis) is used to measure the optical transparency of the measured material. A monochromatic light source with a variable wavelength is emitted onto the sample from which the light is either reflected, absorbed or transmitted. The transmittance, T, is measured from the ratio of the transmitted light intensity, I_T, to the incident light intensity, I_0, which is related to the absorbance, A, described by Beer-Lambert's law:

$$T = \frac{I}{I_0} = 10^{-A} = 10^{-\alpha d} \Longrightarrow A = -\log\frac{I}{I_0} = \alpha d \tag{2.21}$$

where A is the absorbance, α is the absorption coefficient and d is the thickness of the sample. If the thickness of the sample is known one is able to determine the absorption coefficient from which the optical bandgap can be determined from a Tauc plot. A Tauc plot shows the quantity $(\alpha h\nu)^{1/r}$ as a function of the photon energy, $h\nu$, where r denotes the nature of the band transition. $r = 1/2$ for direct allowed transitions (corresponding to a direct bandgap) and $r = 2$ for indirect allowed transitions (corresponding to an indirect bandgap). The bandgap can be determined from a linear extrapolation of the Tauc plot. [92]

For the UV-Vis measurements of this project a UV-2600 UV-Vis Spectrophotometer by Shimadzu was used, which provides the emission and measurement of a continuous photon wavelength range of 185-1400 nm through monochromatic filtering of either a deuterium arc lamp or a tungsten halogen lamp.

2.2.11 Raman Spectroscopy

Raman spectroscopy is used to determine the vibrational modes of the atoms or molecules of the measured sample. This is achieved through the inelastic scattering of photons, also known as Raman scattering. Compared to the typical fundamental processes such as transmission, reflection, refraction and absorption, only a small fraction of light (<1%) undergoes light scattering processes (either elastic or inelastic). A monochromatic light source (typically a laser) is used from which the emitted photons may interact with the molecular vibrations or phonons, which results in a shift, called the Raman shift, in the reemitted photon energy. The Raman shift is usually expressed as a wavenumber (inverse wavelength expressed in units of cm^{-1}), which is related to the excitation and scattered wavelengths, λ_{exc}, and λ_{scatt}, respectively:

$$\omega = \frac{1}{\lambda_{\mathrm{scatt}}} - \frac{1}{\lambda_{\mathrm{exc}}} \tag{2.22}$$

The frequency, intensity and bandshape of the Raman bands are related to the chemical composition and crystalline structure of the probed material.[83]

2.2.12 Time-Resolved Terahertz Spectroscopy (TRTS)

Time-resolved terahertz spectroscopy (TRTS) measures both the sum of the photoexcited electron and hole mobility, μ_{Σ}, at THz frequencies as well as the photoconductivity decay from timescales of femtoseconds to nanoseconds. The method utilises an optical pump pulse, a THz probe pulse and a sampling pulse. After photoexciting the carriers with the pump pulse, the THz pulse probes the carrier mobility, μ, and concentration of the excited charge carriers, Δn, via a change in the THz transmission, ΔT. The sampling pulse samples the electric field of the THz pulse by electrooptical sampling in a ZnTe crystal in order to detect the THz pulse and transmission through the sample.[93]

The delay time between the optical pump and the THz probe pulse defines the sampled part of the THz pulse. When this delay time is varied, the whole transmitted THz pulse can be revealed which is then Fourier transformed to obtain $T(f)$ and $\Delta T(f)$. From these, the photoinduced conductivity, $\Delta\sigma$, and mobility can be determined from the thin film approximation:[93,94]

$$\Delta\sigma(t,f) = e\mu_{\Sigma}(t,f)\Delta n(t) = \epsilon_0 c(n_0 + n_2)\frac{\Delta T(t,f)}{T + \Delta T} \tag{2.23}$$

where n_0 and n_2 are the refractive indices of the surrounding medium and substrate of the excited film, respectively. The approximation requires the carrier concentration and conductivity to be assumed homogeneously distributed over the thin film thickness, d. The mobility, μ, can be derived when both T and ΔT are measured shortly after excitation (20 ps) and the initial sheet carrier concentration is calculated from the flux of the pump photons minus the transmission and reflection of the sample.[93]

From the Drude model the DC-mobility at zero frequency can be obtained which relates to the effective carrier mass, m^*, and the carrier scattering time, τ_{scat}:[95]

$$\mu(f) = \frac{q\tau_{\text{scat}}}{m^*}\frac{1}{1+2\pi i f\tau_{\text{scat}}} \tag{2.24}$$

The interaction between the THz field and the charge carriers occurs on the nm-scale. For mobilities below $\mu < 1000$ cm^2/Vs this interaction length is of the order of < 50 nm, which is typically far below the grain size of the thin film absorber.[95] These grain boundaries are likely to further minimise the actual mobility of the carriers over longer distances.

2.2.13 Photoluminescence Spectroscopy

Photoluminescence spectroscopy measures the reemission of photons from a material subsequently to its photoabsorption. An efficient solar cell absorber material should ideally be as good at emitting light as it is at absorbing. In this case, the lifetime of the carriers is only dominated by a radiative recombination, τ_{rad}, and zero non-radiative recombination, $\tau_{\text{non-rad}}$. Non-radiative recombination typically occurs via deep defects situated in the bandgap, which will significantly limit the total recombination lifetime: $\tau_{\text{tot}}^{-1} = \tau_{\text{rad}}^{-1} + \tau_{\text{non-rad}}^{-1}$. In this manner the external radiative efficiency (ERE), which relates to the ratio of amount of photons reemitted over the amount of photons absorbed by the material, is directly related to the lifetimes: ERE $= \tau_{\text{tot}}/\tau_{\text{rad}}$. Both the open-circuit voltage, V_{oc}, and the fill factor, FF, of the device are heavily affected by the lifetime since the dark saturation current, J_0, of the device is inversely proportional to the carrier diffusion lengths, which in turn are proportional to the squareroot of the lifetime, $L_{\text{diff}} = \sqrt{D\tau}$ (see Equations (2.4), (2.5) and (2.8)).[83]

3 | The Single-Junction Selenium Solar Cell

This chapter presents the typical device architecture of the single-junction monofacial selenium solar cell. The thin film layers of the architecture will be introduced and their individual functional purpose within the solar cell structure will be discussed.

The fabrication process of the selenium solar cell will be presented later in the chapter. Fabrication of the Se-based solar cell required the repurposing of a UHV characterisation chamber, which was adapted to thermally evaporate tellurium and selenium, while maintaining XPS and ISS capabilities. XPS and ISS results will be presented to validate the elements of the deposited thin film materials.

3.1 The Device Architecture and Thin Film Functions

The following section will introduce the general architecture of the Se-based *monofacial heterostructure superstrate single-junction* solar cell. That is a lot of words for a seemingly simple structure and therefore deserves some explanation. A *heterostructure* consists of several *heterojunctions*, which is simply the combination of two different semiconductors, which usually have unequal bandgaps. For an ideal heterostructure, the conduction band minimum (CBM) and valence band minimum (VBM) of the transport layers must match up with the photoabsorber of the device, and the doping level of the transport layers must be sufficiently high to introduce proper band bending at the junctions. Further explanation of how such a device architecture functions will follow. *Monofacial* refers to the solar cell allowing light to be transmitted through only one side of the device. In order to do so, a transparent conductive oxide (TCO) is used on one side of the device as a transparent contact. This structure will simply be referred to as a *single-junction* device due to its main collection originating from its p-n junction. For all fabricated single-junction devices of this project, a layer of F doped SnO_2 (FTO) on soda-lime glass (SLG) was used as a substrate. The contact on the other side of the device would for a monofacial device be metallic and for a bifacial device also be a TCO. The work functions of both contacts should ideally match the CBM or VBM of the transport layers. The term *superstrate* refers to a configuration where the solar cell substrate not only functions as a supporting structure for the growth of the solar cell, but also works as a transparent contact.

An example of the general device heterostructure architecture of the Se-based single-junction solar cell consists of the following structure (from the bottom and up):
A SLG substrate with FTO as the transparent front contact, anatase titanium dioxide (TiO_2) as the n-type electron-transport layer (ETL), tellurium (Te) as a nucleation layer, a selenium (Se) p-type absorber layer, molybdenum oxide (MoO_x) as the p-type hole-transport layer (HTL) and gold (Au) as the metallic back contact. This particular architecture resulted in the champion device of this project and is therefore chosen as an example to explain the working principles of the Se solar cell device. A schematic of the device architecture, a cross-sectional SEM image and a corresponding simplistic illustration of the flat band energy diagram can be seen in Figures 3.1, 3.2 and 3.3.

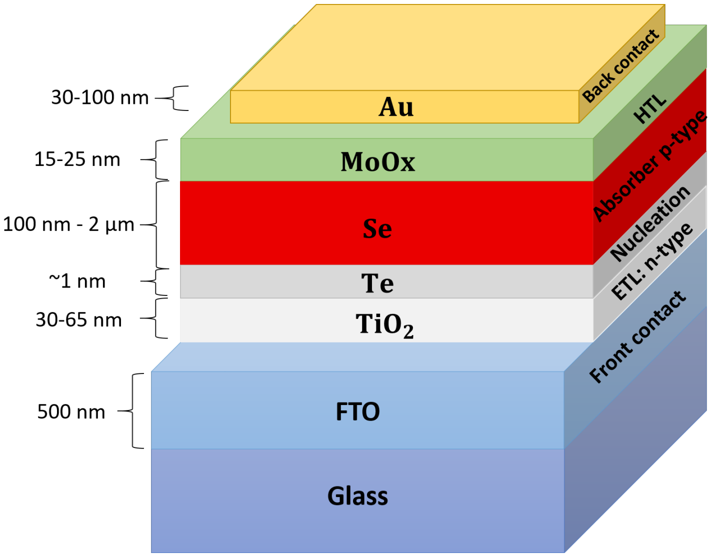

Figure 3.1: Schematic of the champion Se-based monofacial single-junction solar cell architecture: SLG/FTO/TiO_2/Te/Se/MoO_x/Au.

The flat band energy diagram has been illustrated from values found in literature (see Tables A.1, A.2 and A.3). The bandgap of selenium has been measured with UV-Vis (see Section 3.5) and the electron affinity has been measured with UPS

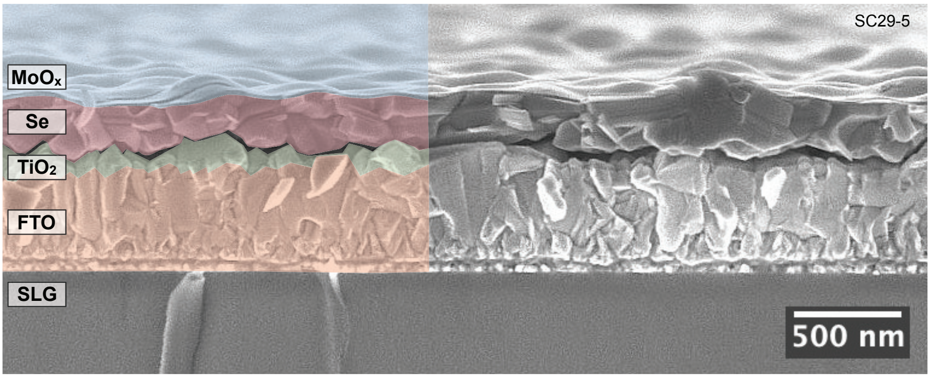

Figure 3.2: SEM cross-section image of a Se-based monofacial single-junction solar cell. The Au back contact is not present in this particular area of the device. Reprinted with kind permission of Rasmus Nielsen.[96]

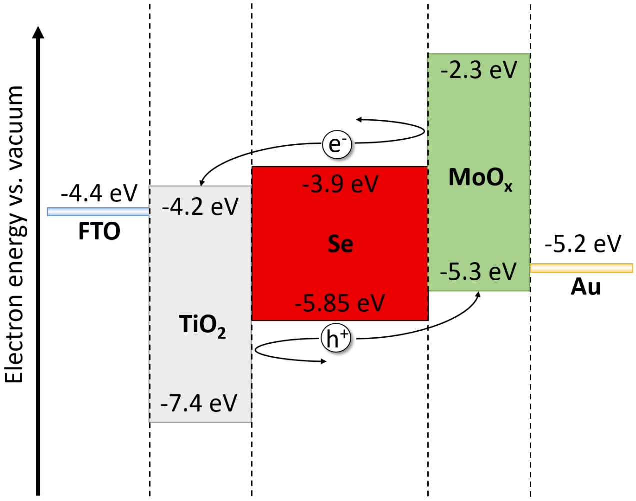

Figure 3.3: Sketch of the flat band energy diagram of the layers of the device seen in Figure 3.1. The bandgaps of the photoabsorber Se and the transport layers TiO_2 and MoO_x are coloured, illustrating the top and bottom of each area as the CBM and VBM of each layer, respectively. The values used have either been measured or found from literature (see Tables A.1, A.2 and A.3 for further details). The work functions of the contacts, FTO ($\phi = 4.4$ eV[97]) and Au ($\phi = 5.2$ eV[98]), are also illustrated.

(see Section 3.6). Be aware that the flat band energy diagram is a highly simplified model. The band positions of each layer can vary with both fabrication and characterisation methods and conditions. Furthermore, the values are derived from measured bulk properties which may likely be different from the thin film properties as well as the properties within or near the interfaces and surfaces. The schematic is included mainly to illustrate the working principles of how a generated electron-hole pair is efficiently collected within the device.

In this section the working principle of the Se-based solar cell will be described. Solar spectrum light enters and passes through both the front contact and the electron-transport layer. This requires the bandgaps of the contact and the electron-transport layer to be sufficiently large in order for them to not parasitically absorb the light that could otherwise have been absorbed by the photoabsorber of the device. The light that reaches the Se photoabsorber is ideally all to be absorbed above the selenium bandgap generating an equal amount of electron-hole pairs as absorbed photons. The generated electron-hole pairs are then ideally all to be both separated to avoid any recombination and collected as efficiently as possible. The reason for this separation is mainly due to the p-n junction formed in the interface between the n-type ETL and the p-type selenium absorber where the greatest band bending will occur within the device. To further increase the collection efficiency, the band positions of the transport layers with respect to the photoabsorber must be aligned as efficiently as possible. The band diagram seen in Figure 3.3 is in this way imperfect. However, the roles and requirements of the ETL and HTL become apparent. The electron-hole pair must be both efficiently collected and blocked by the ETL and the HTL. For efficient collection the CBM (or electron affinity, χ_e) and the VBM (or ionisation energy, IE) of the Se absorber must be well aligned with the CBM and VBM of the ETL and HTL, respectively. Simultaneously, the bandgaps of the ETL and HTL must function as forbidden energy bands in which neither the electrons nor the holes are able to travel or tunnel through.

In the illustration shown in Figure 3.3 the transport layers supply sufficient blocking of the respective carriers, but neither the CBM of the ETL nor the VBM of the HTL align perfectly with the CBM and the VBM of the Se absorber. It should also be noted that the work functions of the non-selective contacts should be well aligned with the respective CBM and HTL of the transport layers to facilitate an efficient ohmic contact. These improvements are necessary to achieve an optimal device performance.

Unfortunately there are more restrictions on the selection criteria of the used transport layers than shown thus far. The selection criteria are as follows: 1) A well aligned CBM/VBM. 2) A sufficiently large bandgap (or equivalent forbidden band) to prevent electron/hole-transport or tunnelling. 3) Large carrier mobility, diffusion length and lifetime to prevent carrier recombination during transport. 4) Stability and durability during fabrication processing. This includes exposure to increased temperature, UV-light, moisture and oxygen. 5) Low material and processing cost.

Both the successful and unsuccessful transport layers utilised during this project will be introduced and explained accordingly in the respective sections.

3.1.1 Selenium Photoabsorber

Elemental selenium is known to exist as six different allotropic crystalline phases. The crystalline allotropes include α-monoclinic, β-monoclinic, orthorombic, rhombohedral and trigonal (or hexagonal) phases. Trigonal Se is the only thermodynamically stable form under ambient conditions and will be refered to as crystalline selenium (c-Se).[67,99–103] The α- and β-monoclinic forms have a ring-like Se_8 structure. Trigonal c-Se consists of helical close packed polymeric chains (space group $P3_121$ or $P3_221$) where each atom has two nearest chain neighbours and four neighbours from adjacent chains (see Figure 3.4). The lattice constants are $a = b = 4.37$ Å and $c = 4.95$ Å at 300 K.[67,99] Se has an electronic valence structure of $4s^2$ $4p^4$. In the crystal structures the 4p electrons form two covalent bonds that hold the chains or rings together and two lone-pair orbitals per atom. The lone-pair orbitals form Van der Waals bonds that holds the chains or rings together.[102]

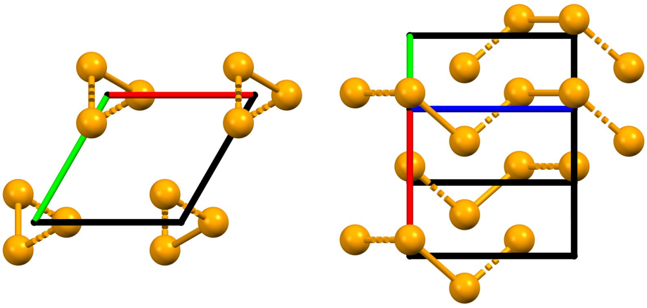

Figure 3.4: Crystal structure of trigonal selenium visualised with Mercury.

The melting point of Se is 220 °C which allows for easy vacuum fabrication.[67] Annealing of amorphous selenium has been reported to crystallise it into the trigonal form near the melting point which lowers the direct bandgap from $E_g = 2.17$ eV[68] down to $E_g = 1.80$ eV.[66] The indirect bandgap has also been reported to be ≈ 0.1 eV lower than the direct ($E_g = 1.85$ eV compared to $E_g = 1.95$ eV).[67] Trigonal Se has a high absorption coefficient greater than 10^4 cm^{-1} above its bandgap which makes it a suitable photovoltaic wide-bandgap photoabsorber.

c-Se exhibits an intrinsic p-type nature which is caused by the prevailing hypothesis that dangling bonds, due to vacancies or free chain ends, act as shallow acceptors. This density has been reported to be around 10^{13}-10^{15} cm^{-3}. The acceptors are completly ionised at 77 K causing a dark electrical conductivity of $\sigma \approx 10^{-6}$-10^{-5} Ω^{-1} cm^{-1}.[67,104,105]

3.1.2 Tellurium Nucleation Layer

An obvious difference between the layers shown in Figure 3.1 compared to Figures 3.2 and 3.3 is the exemption of the very thin layer of Te. This is because Te has for the theoretical principles of the device no optoelectronic role to play. Following the footsteps of the Se-based solar cell literature, Te has always been used as an "adhesion" or "wetting" layer for the growth of trigonal Se. We believe similarly to the recently published work in 2019 by Hadar et al.[71] that the Te hexagonal crystal structure in fact works as nucleation sites for the hexagonal Se growth. In other words, trigonal Se is isomorphic with Te.[67] Te has a melting point of 450 °C where the melting point of Se is only 220 °C.[67] For annealing temperatures of around 200 °C the Se becomes mobile, but the Te remains solid facilitating the growth of crystalline trigonal c-Se. Therefore I have chosen to name Te a nucleation layer. In the same work of Hadar et al. it has been shown that a Se-based device can be made without Te, but with significantly worse performance. Similarly, it was shown that using 5 nm of Te was almost equally detrimental.[71] Alloying of $Se_{1-x}Te_x$ has been shown to reduce the bandgap from 1.8 eV down to the bandgap of 0.3 eV for Te for $x = 1$.[66] This also changes the positions of the CBM and VBM which could attribute the worse performance for a higher fraction of Te.

The attempts of excluding Te have been unsuccessful as Se simply does not grow uniformly and therefore no Se thin film is formed. Attempts of increasing Te thickness have been equally detrimental as reported in literature.[71] The Te layer must therefore be present to secure proper Se growth, but also be as thin as possible in order to avoid interfering with the band alignment in the p-n junction. The results showing the importance of Te will be shown later after introducing the fabrication process of the Se solar cell device.

Whether Te plays some other important or potentially detrimental role in the p-n junction of the Se-based device is still unknown and has not been fully investigated. It can be noted that for the absorber Sb_2Se_3 ($E_g \approx 1.1$ eV), Te has been shown in literature to improve performance by reducing the deep level defects of the absorber.[106] Interestingly, in many reports of Sb_2Se_3 solar cell devices, Te is not required for the absorber crystal growth.[107–110] The crystal structure of Sb_2Se_3 is orthorhombic unlike pure c-Se which is hexagonal and the melting point of Sb_2Se_3 is higher than for c-Se (612 °C compared to 220 °C).[67,108] Potentially Sb_2Se_3 could function as a nucleation layer instead of Te, but only a brief experiment was attempted in this project without success. Further investigations of the role of Te or its possible replacement are encouraged for further understanding of the Se-based device.

It is important to note that for thinner layers of Se, the same Te layer of ≈ 1 nm used for nucleation will contribute to a larger fraction of the total Se/Te ratio.

Successful epitaxial growth of monocrystalline trigonal Se in both the $(10\bar{1}0)$ and (0001) planes on $(10\bar{1}0)$ and (0001) Czochralski grown Te surfaces has previously been reported.[111] This was achieved through either substrate heating of 95-135 °C during thermal evaporation of Se with a rate of 100 nm/min or subsequent melting of selenium on the Te substrate followed by slow cooling. The Te substrates could be removed through dissolution in 20% nitric acid.

I encourage future work to investigate whether similar monocrystalline epitaxial growth of Se can be replicated for the selenium-based device.

3.1.3 Carrier-Selective Transport Layers

A variety of different transport layers were attempted fabricated for Se-based devices with varying success. This section will briefly explain the most successfully implemented transport layers (ETL: TiO_2, ZnO, ZnMgO and CdS - HTL: MoO_x). The unsuccessfully or partially successful implemented layers (ETL: CdS and $SrTiO_3$ - HTL: NiO_x, Spiro-MeOTAD, BaO and YN) will be briefly mentioned later in Chapter 4.

TiO_2 was the most successful ETL of this project with a record device efficiency of 6.4% for a FTO/TiO_2/Se/MoO_x/Au device. TiO_2 is one of the most studied ETL in the field of perovskite photovoltaics [112] and has been the most commonly used ETL for Se-based solar cells. [63,66,68,71,113–118] Thin film TiO_2 can be synthesised from various fabrication methods such as sputter deposition, solution processing and atomic layer deposition (ALD). Sputter deposition of TiO_2 at 400 °C was the main fabrication method used during this project. This high processing temperature is higher than the melting point of Se (220 °C) which prevents its deposition on top of it. ALD fabrication of TiO_2 was briefly attempted but without any initial success. This is believed to be caused be a less ideal band alignment or intrinsic doping related to a different oxygen vacancy concentration. TiO_2 has been reported to have a non-ideal low electron mobility of $\mu_e = 0.1 - 4$ cm^2/Vs [119], that inhibits electron transport and increases the chance for carrier recombination.

The replacement of TiO_2 with ZnO sputtered at room temperature achieved an improved reproducibility of the fabricated devices. However, this resulted in an open-circuit voltage loss of around $\Delta V_{oc} \approx 100$ mV, consistent with reported conduction band offsets of the two ETL compared to Se. [112] ZnO provides a greater mobility of $\mu_e = 200 - 300$ cm^2/Vs [119] as well as lower processing temperatures.

$Zn_{1-x}Mg_xO$ has been successfully implemented by Todorov et al. as a superior ETL over TiO_2, which has in a FTO/$Zn_{0.9}Mg_{0.1}O$/Se/MoO_x/Au device structure achieved the current world record PCE of 6.5% for a Se-based solar cell. [68] By varying the Mg content the position of the conduction band can be modified which also increases the bandgap from $E_g = 3.2 - 3.7$ eV (for $x = 0 - 0.6$). [120] An increase in Mg introduces an increased series resistance resulting in a device performance trade-off between the FF and V_{oc}. Todorov et al. found an optimal composition for the greatest PCE of Mg/(Zn+Mg) to be 0.1. [68] During this project, a stoichiometric $Zn_{0.85}Mg_{0.15}O$ target was used for sputtering which resulted in an improved device reproducibility and V_{oc} compared to ZnO, but a lower record PCE compared to TiO_2 of 5.4%.

MoO_x was successfully implemented as a HTL as similarly reported by Todorov et al. MoO_x has a reported work function of up to 6.9 eV [121–124], but has a high density of states within the bandgap which gives rise to its hole transport nature. The charge transfer mechanism has been reported to be related to tunneling at low voltages and similar to a high barrier Schottky junction at higher voltages.[121]

3.1.4 Transparent Contacts

A transparent contact is required to be both optically transparent and electrically conductive. Transparent conductive oxides (TCO) are commonly used for this purpose as they have bandgaps greater than 3 eV resulting in an optical transmittance greater than 80% in the visible range as well as a resistivity in the order of $10^{-3}\,\Omega\,\mathrm{cm}$. The low resistivity of the TCOs is achieved through degenerately doping of n-type or p-type semiconductors which are most commonly SnO_2, In_2O_3 and ZnO.[125]

FTO (SnO_2:F) and ITO (In_2O_3:Sn) were used as TCOs during this project. FTO has the advantage of being inexpensive as it can be grown using chemical methods such as spray pyrolysis from chlorides or organometallic precursors. FTO has a bandgap of up to 4.1 eV and a low resistivity in the order of $10^{-4}\,\Omega\,\mathrm{cm}$.[125,126] Substrates of 500 nm thick FTO with a sheet resistivity of $\approx 7\ \Omega$/sq (bulk resistivity of $\approx 3.5 \times 10^{-4}\,\Omega\,\mathrm{cm}$) and 80-82% visible transmission on soda-lime glass from Sigma Aldrich were used for all single-junction Se devices of this project. ITO is commonly deposited via magnetron sputter deposition which during heating at 250-350 °C offers the lowest resistivity in the order of $10^{-4}\,\Omega\,\mathrm{cm}$ while maintaining a wide bandgap of $E_\mathrm{g} \geq 3.5$ eV.[126,127] The main consituent of ITO is the scarce element indium (mass ratio of ≈ 9:1 In/Sn)[128] which makes ITO very expensive.

The three major differences between FTO and ITO are the price, surface roughness and typical deposition technique. FTO is far cheaper, but also has a large surface roughness. ITO is expensive, but offers a more planar thin film deposition via magnetron sputtering, which was a readily available technique during this project.

3.2 Adapting an Ultra High Vacuum Characterisation Chamber for Thermal Evaporation

In order to fabricate selenium devices, thermal evaporation of both Te and Se was required. An old ultra high vacuum (UHV) characterisation chamber, named the Volvo, had the main characterisation capabilities of doing both XPS and ISS. When I started the project, selenium evaporation was possible in the loadlock of the chamber, but it was highly uncontrollable yielding an unknown evaporation rate and Se thin film thickness. Te could not yet be evaporated and was at this point in time electrochemically deposited prior to the Se thermal evaporation. The thickness of the Te was determined from the perceived colour of the deposited layer. The main priority at the start of this project was therefore to adapt the Volvo in order to thermally evaporate both Te and Se consecutively under the same vacuum while being able to control both the deposition rate and the total deposited thickness more effectively.

One of the benefits of adapting the Volvo was that it could be possible to do in-situ characterisation of the deposited layers both during and after the deposition of the layers with both XPS and ISS. The hemispherical ion/electron energy analyser in the main chamber and its corresponding electronics and software were defect and required repair before XPS or ISS could be performed. This was initially the second priority of the project.

During the project a Te evaporation design was implemented which included a new Te gun and a movable QCM and horizontal shutter. The design of the Se gun was changed to include a shutter and the size of the Se pellet holder was changed to obtain more uniform heating. The old design of the Se gun had nonuniform heating of the gun which resulted in a volcano-like behaviour which was highly unpredictable and yielded uncertain Se thicknesses. Both the Se and Te guns are heated in the same way by flowing a current through an adjacent tungsten filament. A picture of the final adaptation of the Volvo of this project can be seen in Figure 3.5.

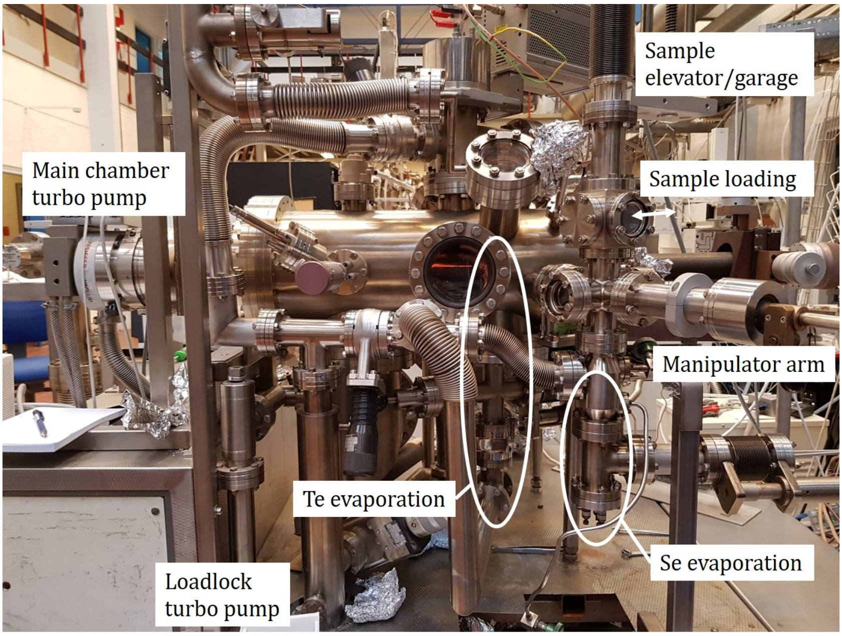

Figure 3.5: Picture of the Volvo with illustrations of the Se and Te deposition capabilities.

The samples to be deposited or characterised are inserted through the sample loading window. The samples are mounted on small custom made sample holders which can be loaded into a "garage" capable of holding 13 samples. The garage is mounted to a linear motion which allows it to function as an elevator. The design of the garage and sample holders was altered with help from the DTU Physics workshop in order to prevent samples from falling out or getting stuck. The end of the manipulator arm has a small flexible hook which can be used to grab the sample holders from the elevator. The samples can in this manner be moved in and out of the slots of the elevator and also be transported to and from the main chamber. The bottom sample position of the elevator is exposed underneath which allows the deposition of Se onto the sample which points downwards towards the Se thermal evaporation gun. Thereby, only one sample can be deposited on at a time. Pictures of the Se gun and its point of view of the QCM and sample can be seen in Figure 3.6.

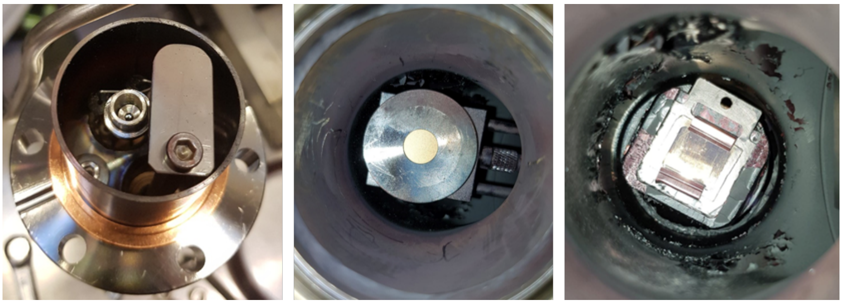

Figure 3.6: Pictures of the Se thermal evaporation gun and its point of view of the QCM and sample.

The sample which sits in the bottom position of the elevator is moved down to a fixed position of ≈ 20 cm away from the Se evaporation gun. In between the sample and the Se gun a QCM attached to a linear motion is situated. The QCM is used to determine the rate of the Se evaporation and once a desired rate is achieved (usually $\approx 8-12$ Å/s), the QCM is moved away to allow deposition for a certain amount of time. The deposition rate is again checked after deposition to approximate the deposited Se thickness. The rotatable shutter seen next to the Se gun in the left image of Figure 3.6 is used to cover the evaporation when the QCM is moved. A typical Se gun temperature required for 1 Å/s deposition was ≈ 90 °C.

Since the QCM is situated closer to the evaporation source, more Se is deposited on it compared to the actual sample. The evaporation area scales inversely with the distance squared and therefore one has to approximate the actual deposited thickness on the sample. In order to quantify this difference a batch of 6 samples was made with the aim of depositing 150-1000 nm amorphous Se approximated from the measured rate and time with the QCM. The thickness of the deposited Se on the samples was measured by ellipsometry yielding an average thickness approximately half of the Se deposited directly on the QCM. This correlates well with the fact that the QCM is situated at a distance of around two-thirds closer than the sample. A cross-sectional SEM image of 350 nm amorphous selenium is seen in Figure 3.7.

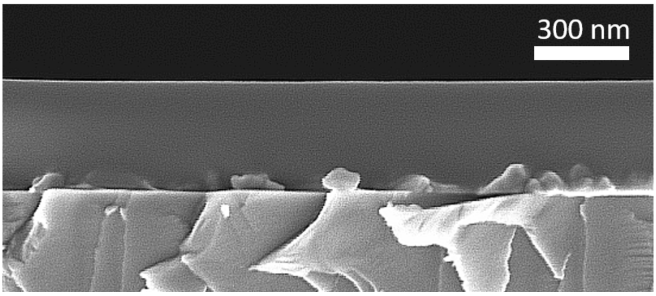

Figure 3.7: Cross-sectional SEM image of 350 nm amorphous selenium on silicon.

Se needs to be crystallised to obtain the desired wide-bandgap and large absorption coefficient. As previously explained, Te is required for this crystal growth and therefore needs to be deposited onto the substrate before the deposition of Se. The samples are moved into the main chamber by the use of the manipulator arm. From this position Te can be deposited from the bottom of the chamber as illustrated in Figure 3.8.

A gate valve separates the Te gun in the load lock from the main chamber in order to more easily access the gun and refill it with new Te pellets without venting the main chamber. The Te is evaporated onto the QCM until a fixed deposition rate is achieved (usually ≈ 1 Å/s). When the rate is deemed stable, the QCM is moved away with the shutter still closed in place. The time is noted when the shutter is opened and once the calculated time is reached, the shutter is closed off again. Since the sample is situated twice the distance away from the evaporation gun compared to the QCM, around 4 times less Te is deposited on the sample. For a deposition rate of ≈ 1 Å/s, 40 seconds are required to achieve a Te thickness of ≈ 1 nm. A typical Te gun temperature required for 1 Å/s deposition was ≈ 400 °C.

The Te is evaporated into the main chamber where the sample sits on a rotatable and movable sample holder. This is illustrated in Figure 3.9.

The sample holder is able to turn 360 degrees and moved in all three dimensions. The sample surface can thereby be situated in optimal positions for Te deposition, XPS and ISS analysis, respectively. A FTO/Au sample with a ≈ 0.1 cm^2 Au square in the center of the sample was used to optimise the positions yielding the maximum XPS and ISS signals. XPS and ISS can be performed both before and after the deposition of the layers to characterise the elements of the layers in the device.

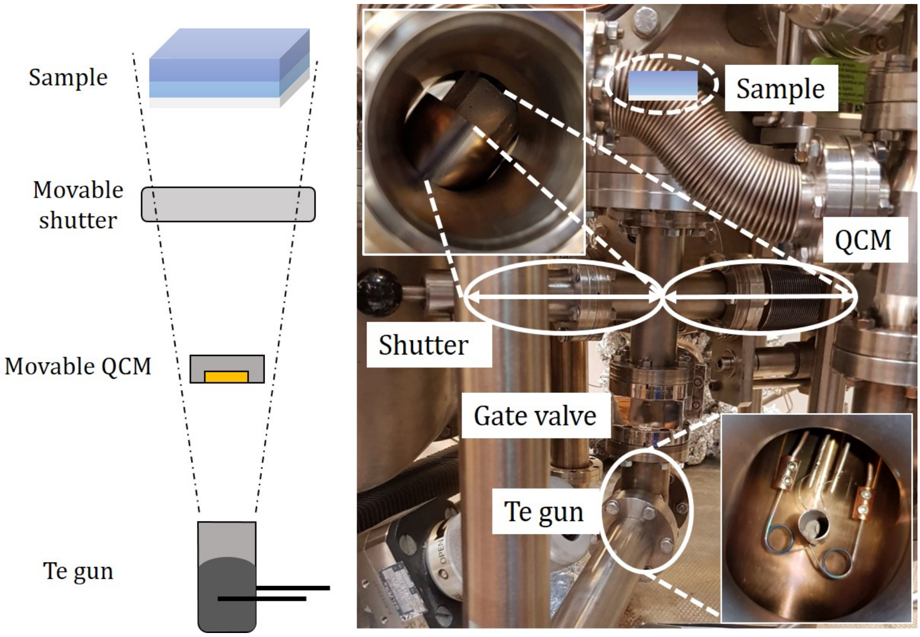

Figure 3.8: Pictures and schematic of the Te thermal evaporation part of the Volvo.

Around 1000 samples were made with the Te gun shown in Figure 3.8. With a thickness of around 1 nm per sample an estimated deposited Te thickness of around 1 µm is to be expected around 40 cm away from the Te source. I happened to have taken a picture before and after around 3 years of use. These pictures can be seen in Figure 3.10, where a thick layer of Te is clearly visible for the picture taken after 3 years of intense use. It is not surprising that some Te contamination may be present in the Volvo.

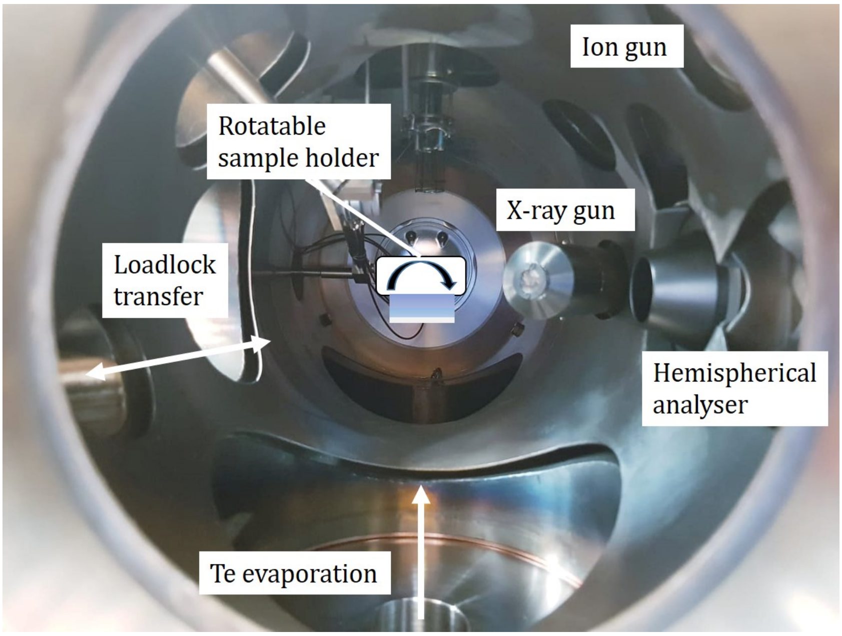

Figure 3.9: Picture of the inside of the Volvo.

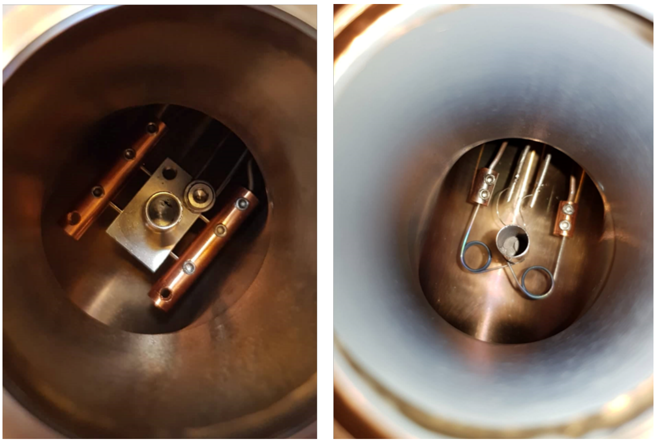

Figure 3.10: Pictures of Te gun before and after 3 years of use. Left: Old and non-working Te gun design. Right: Te gun used for most of the project. A thick layer of Te is clearly visible.

3.3 Typical Fabrication Process

The typical fabrication process of the Se-based monofacial single-junction solar cell as seen in Figure 3.1 is as follows:

1. Commercial $\approx$ 7 ohm/sq FTO(500 nm)/SLG from Sigma Aldrich are cut into 14x16 mm substrate sizes. Blue tape is used to prevent cut FTO and glass shards and residues from contaminating the surface of the FTO.
2. The samples are cleaned by ultrasonication with Triton-X in milli-Q water, acetone and isopropanol for 15 minutes each. The samples are subsequently dried in N_2 gas to prevent residues forming on the FTO surface.
3. The ETL is deposited on the cleaned FTO/SLG substrates by use of DC or RF magnetron sputtering in a dedicated sputter chamber. Example: $\approx$ 50 nm TiO_2 is deposited with DC magnetron sputtering during substrate heating of 400 °C from a Ti target with a power of 160 W in a 5 mTorr 3/30 SCCM O_2/Ar atmosphere for $\approx$ 15 minutes.
4. $\approx$ 1 nm Te is deposited by thermal evaporation from Te(99.9999%) pellets (from Sigma-Aldrich) in the Volvo main chamber at room temperature for 40 seconds (rate of $\approx$ 25 Å/s) at a pressure of $\approx 10^{-8}$ mTorr and a resitively heated gun temperature of $\approx$ 390-400 °C.
5. Se (typically 300-500 nm) is thermally evaporated from Se(99.999+%) pellets (from Sigma-Aldrich) in the Volvo loadlock at room temperature at a rate of $\approx 20-30$ nm/min at a pressure of $\approx 10^{-7}$ mTorr.
6. The samples are annealed in a dedicated home-made aluminium mini-oven for $\approx$ 190-200 °C for 4 minutes in order to crystallise Se.
7. The HTL is deposited by DC or RF magnetron sputtering in the former sputter chamber. Example: $\approx$ 15 nm MoO_x is deposited by DC magnetron sputtering from a Mo target with a power of 50 W in a 5 mTorr 5/30 SCCM O_2/Ar atmosphere for $\approx$ 6 minutes.
8. Annealing again at $\approx$ 190 °C for 4 minutes.
9. The Au back contact (typically $\approx$ 30 nm) is deposited with DC magnetron sputtering from a Au target with a power of 50 W in a 5 mTorr Ar atmosphere for $\approx$ 6 minutes. The deposited contact area was typically 0.4-0.5 cm^2.
10. Final annealing at $\approx$ 190 °C for 4 minutes.

The deposited thickness of the oxide layers were measured with a spectroscopic ellipsometer VASE (J.A. Woollam) on the samples deposited on silicon substrates. The models used for the ellipsometry data fitting were chosen and developed with kind help from postdoc Andrea Crovetto. The thickness of the layers were confirmed by cross-section SEM images as seen in Figure 3.2.

Ideally all the fabricated layers of the Se-based device should be fabricated under the same vacuum to prevent potential contamination while moving the devices from chamber to chamber during the fabrication process.

Results have shown that annealing after sputtering increases device performance. It is believed that each annealing step helps to alleviate potential sputter damage of the Se absorber. For future studies it would be beneficial to replace the sputtering of the layers on the Se absorber with thermal evaporation or similar gentle deposition techniques.

3.4 Crystallisation of Thin Film Selenium

The first aim of this project was to try to replicate the work of Todorov from 2017 who obtained a record PCE of 6.5%.[68] This was achieved by rapid annealing of thin film Se on a hotplate at 200 °C in air. As a first attempt at achieving a reproducible rapid annealing process a home-made aluminium mini-oven with in-built thermocouples was made by the workshop at DTU Physics. The mini-oven is placed on a hotplate and once a stable measured temperature is achieved the sample is placed inside it. The mini-oven allows room for the annealing of one sample at a time and after a time period of typically 4 minutes, the sample is taken out and left to cool at room temperature.

3.4.1 Effect of Annealing Temperature on Se Crystal Grain Size and Pinholes

The optimal annealing temperature for the crystal growth of Se has been reported by various groups to be around 200 °C for around 2-4 minutes.[68,71,117] Various annealing conditions were tested during this project, but ultimately a standard set of annealing conditions were settled at 190 °C for 4 minutes. Overall these conditions yielded the best device performance as well as reproducibility. A simple experiment was carried out to show the difference in Se crystal grain sizes with respect to the annealing temperature. Si/ZnMgO/Te/Se cells were annealed at 180 °C, 190 °C and 200 °C for 4 minutes. SEM images of the Se crystal grain morphology taken with different secondary electron detectors can be seen in Figure 3.11.

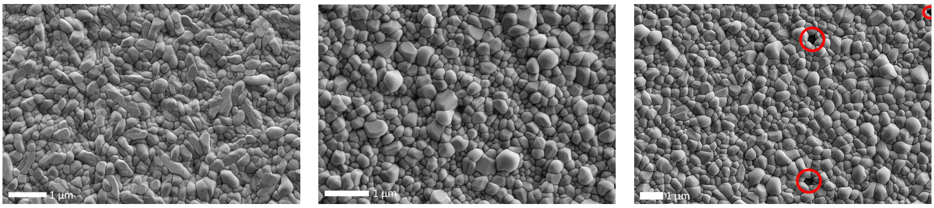

(a) 180 °C. ETD. (b) 190 °C. ETD. (c) 200 °C. ETD.

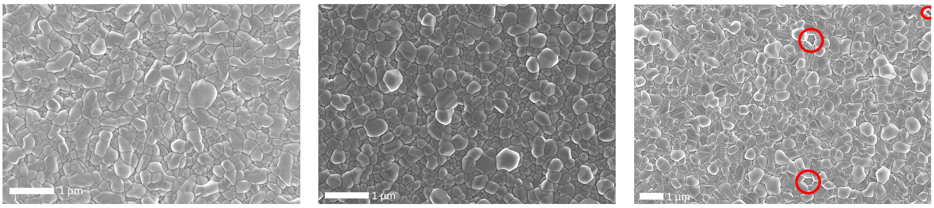

(d) 180 °C. In-lens. (e) 190 °C. In-lens. (f) 200 °C. In-lens.

Figure 3.11: SEM images of the surface of Si/ZnMgO(60 nm)/Te(1 nm)/Se(300 nm) annealed for 4 minutes at 180 °C, 190 °C and 200 °C. Scale bar is 1 µm for all images. Images taken with an Everhart-Thornley detector (ETD) and an In-lens detector to show different contrasts in the Se crystal morphology. The contrast clearly indicates observed pinholes for the 200 °C annealed sample, which have been highlighted with red circles.

From the images a clear trend in the increase of Se grain size can be seen with increasing annealing temperature. If one looks closer at the Se film one can spot a couple of pinholes in the film for the 200 °C annealed sample (highlighted with red circles). This is clearly shown when comparing the ETD and the In-lens images where the ZnMgO surface is especially apparent from the In-lens image. For the 190 °C images no pinholes are observed. Increasing the annealing time resulted in more pinholes for the > 200 °C annealed samples and also thinner Se films as some Se evaporates from the surface during annealing, which has also been reported in the literature.[71] Further reducing both the annealing time and temperature resulted in smaller grain sizes. Increasing the Se crystal grain sizes while avoiding pinholes is crucial for optimal device performance. Increasing the grain size should increase the carrier lifetime and diffusion length by reducing the chance of surface recombination. Simultaneously, by avoiding pinholes, less shunting paths are introduced which will increase the shunt resistance of the device. The size of the crystal grains will likely influence the optimal Se thin film thickness as the carriers ideally should only travel vertically within one single crystal grain, thereby avoiding the transport across different grains. For 190 °C annealing, crystal grains of $\approx$ 100-500 nm in diameter are observed. Thereby an optimum Se thickness is also to be expected within this thickness range. From the results that we reported in Paper I (see Appendix B) an optimum Se thickness was found for ≈ 300-500 nm which is consistent with the observed grain size diameter. A cross-section of the ≈ 300 nm Se thin film is shown in Figure 3.12.

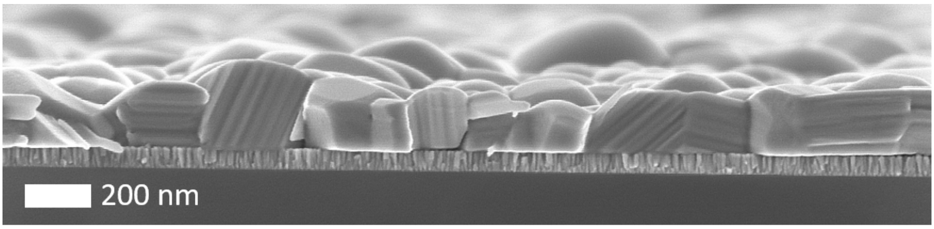

Figure 3.12: Cross-sectional SEM image of Se thin film annealed at 190 °C for 4 minutes. Sample structure: Si/ZnMgO(60 nm)/Te(1 nm)/Se(300 nm).

From the cross-section it is observed that the potential carriers photogenerated in the Se thin film can travel vertically without having to cross between grain boundaries. Even though the substrate is flat, the Se thin film has a large variation in thickness varying from around 100-300 nm. This naturally introduces a lower thickness level before pinholes or shunt paths are introduced to the device. In general this meant that it was difficult to obtain reproducible performance for devices with a Se thickness below around 250 nm. This roughness effect is only further amplified when using a rough FTO substrate.

3.4.2 Importance of Te for Nucleation and Growth of Se

To show the importance of the Te layer for the crystal growth of Se, a simple experiment was previously carried out during my Master project.[129] A sample of FTO/TiO_2/Se(250 nm) is made with and without a layer of Te. Both samples are annealed at ≈ 190 °C for 2 minutes. Within 5 seconds a change in crystallisation occurs indicated by an immediate change in colour. Pictures and SEM images of the samples with and without Te before and after crystallisation can be seen in Figure 3.13.

Without Te the Se becomes highly mobile and in order to minimise its surface energy, it forms large islands of ≈ 10-20 µm in diameter that seem to remain amorphous. However, with a layer of Te, a thin film of crystalline Se layer is formed with grain sizes of $\approx 100 - 500$ nm in diameter. Our hypothesis on this phenomenon is that Te functions as a nucleation layer, which Se can grow from. Both Se and Te are hexagonal at low pressures and temperatures. However, the melting points are different being 220 °C for Se and 450 °C for Te.[130] During the annealing of Se, the Se does not fully melt but becomes highly mobile. Since the Te has a much higher melting point it is less mobile and can thereby introduce stable and energetically favourable sites from which the Se can nucleate at and grow from. This effect seems to be largely unaffected by the substrate. During this project crystalline Se has with a layer of Te been successfully grown on FTO, SLG, fused quartz, Si, TiO_2, ZnO, ZnMgO, MoOx, CdS and $SrTiO_3$.

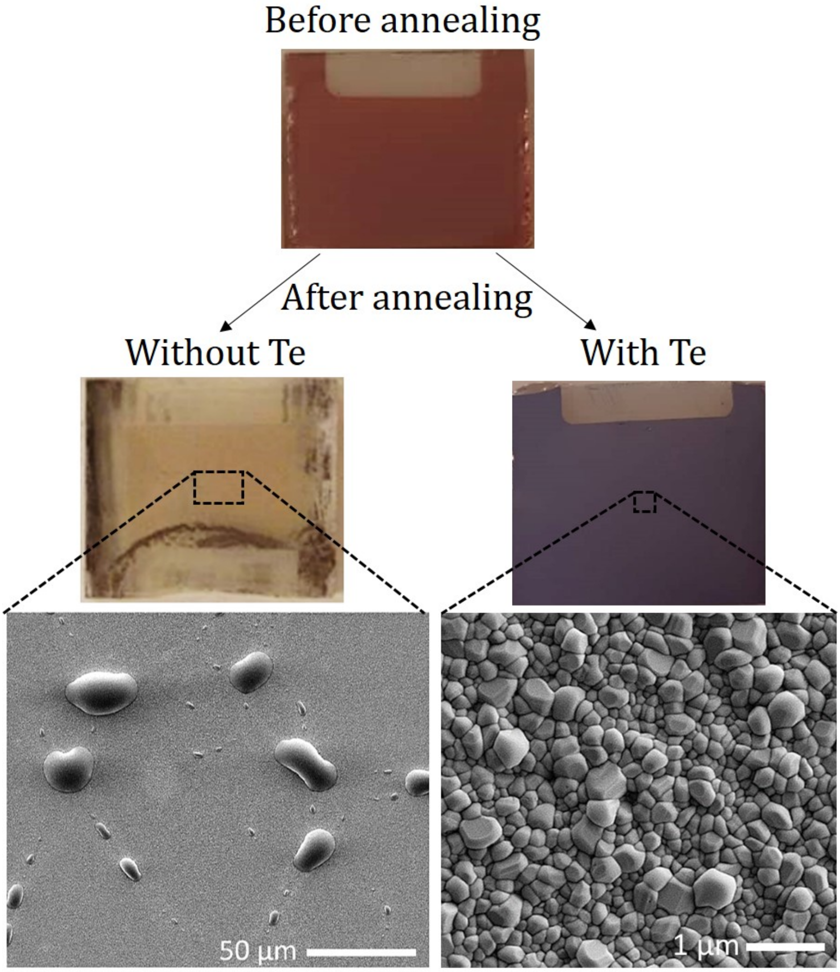

Figure 3.13: Se annealed at 190 °C for 4 minutes with and without ≈ 1 nm Te.

3.4.3 XRD and Raman Spectroscopy of Crystalline Se

To verify that the crystal structure of selenium matches that of the literature, c-Se thin films were investigated by XRD and Raman spectroscopy. An FTO/TiO_2/Se(300 nm) sample was made and annealed at 190 °C for 4 minutes. Grazing incidence X-ray diffraction (GIXRD) was performed with a Panalaytical Empyrean XRD using a parallel plate collimator to measure the Bragg peaks of the crystalline layers of the stack. The results can be seen in Figure 3.14.

The XRD measurements show that trigonal c-Se is formed after annealing with preferred growth along the (101) orientation. The obtained Bragg peaks match

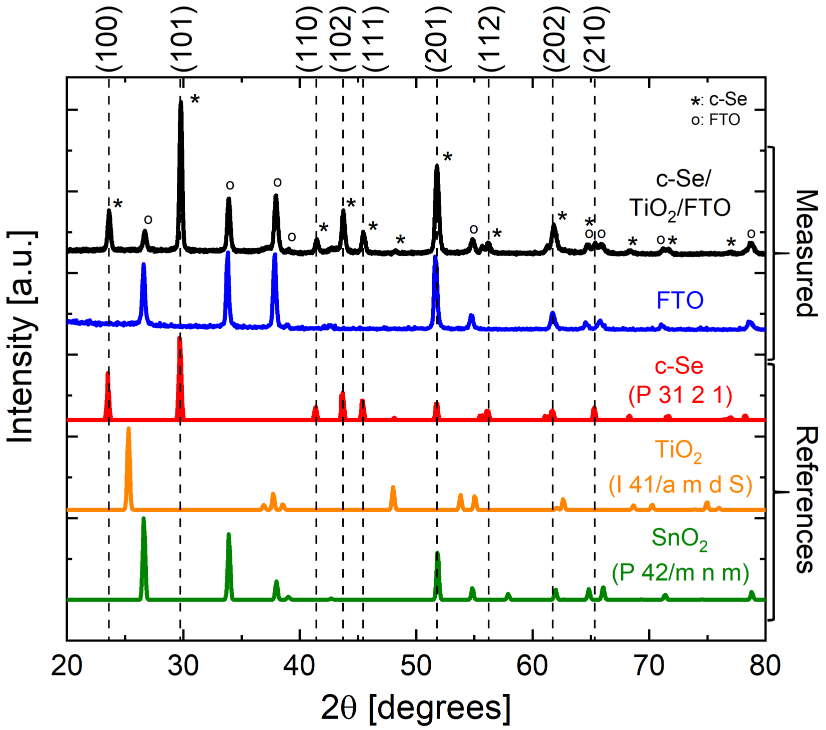

Figure 3.14: XRD spectra of c-Se on SLG/FTO/TiO_2 after annealing at 190 °C for 4 minutes and FTO/SLG. The crystal orientations for trigonal Se are highlighted with dashed lines.[131] XRD reference spectra of trigonal Se, anatase TiO_2 and tetragonal SnO_2 are found from the Inorganic Crystal Structure Database.[132]

the c-Se of recent studies[71] for rapid annealing conditions, where it was shown that the (100)/(101) peak ratio and (100) peak width changes with the annealing temperature and heating rate. In the study it was reported that there is a preferred growth orientation below 180 °C, but that the crystal grain size increases for higher temperature. An optimum device performance was obtained for devices annealed at $\approx$ 185-190 °C. Their results also suggested that a rapid crystallisation tends to fix the crystals in a random orientation while slow crystallisation allows the grains to orient and grow more homogeneously. An optimum annealing resulting in a homogeneous crystal orientation and large grain sizes is therefore expected to be obtained at high annealing temperatures with slow ramp rates. It was also reported that illumination during the crystallisation process increases the Se grain growth.

The annealing setup made and used during the work of this PhD project does not allow us to properly control the heating rate. For future studies it is highly encouraged to further investigate the benefits of performing slow annealing with a slow ramp up time in order to gain a more homogeneous crystal growth. Our attempts of illuminating the devices during annealing yielded no significant or reproducible increase in device performance.

The reason for not seeing the anatase TiO_2 Bragg peaks in the XRD measurement is believed to either be due incomplete crystallisation or simply due to being too thin ($\approx$ 25 nm) for detection.

Raman spectroscopy measurements were also carried out. This was done at Helmholtz-Zentrum Berlin (HZB), Germany with help from Sergiu Levcenco using a Horiba HR800 setup with a 632.8 nm He-Ne laser. A laser power of 0.3 mW was used with a spot size of around 1.6 µm in diameter corresponding to around 150k suns with an acquisition time of 30 seconds. The measurements were carried out on an as-deposited amorphous and a crystalline thin film Se sample. A commercial c-Se wafer bought from American Elements (99.999%) was also measured for comparison with our own c-Se. The results can be seen Figure 3.15.

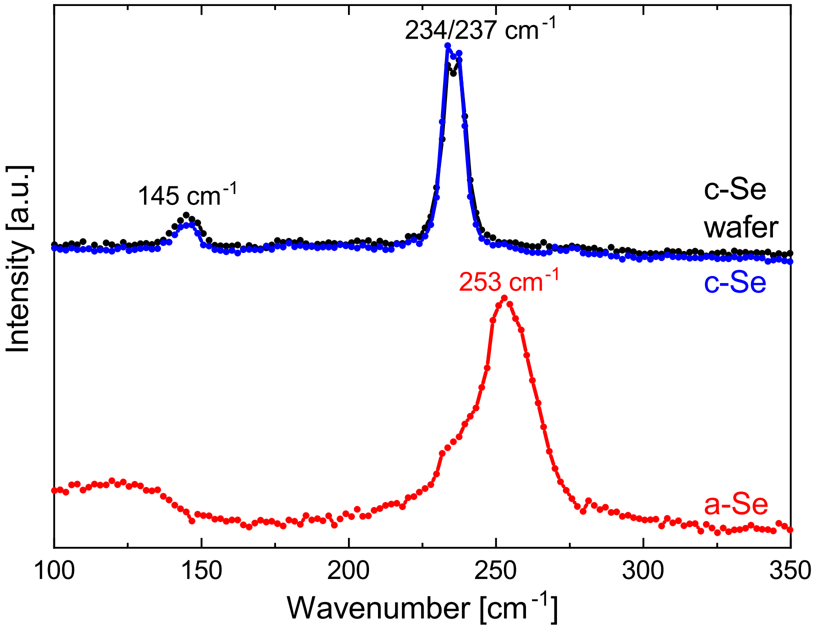

Figure 3.15: Raman spectra of a-Se and c-Se. A commercial c-Se wafer bought from American Elements was also measured for comparison.

The measured Raman spectra match the literature of both amorphous and trigonal selenium. The crystalline Se shows a convoluted peak at 234 and 237 cm^{-1} which is in accordance to literature.[68,133] Both the spectra of the fabricated c-Se and the commercially bought c-Se wafer coincide well. Most importantly, when comparing our Raman spectra with those of c-Se used for the current world record PCE of 6.5%[68], both our a-Se and c-Se peaks match theirs.

3.5 Photoabsorption of Se

Since Se is to function as our wide-bandgap photoabsorber it is highly relevant to measure its photoabsorption. The photoabsorption was measured before and after annealing by use of UV-Vis direct transmission measured with a UV-2600 spectrophotometer from Shimadzu. The c-Se sample scatters too much light in order to realistically calculate its absorption coefficient only from the direct transmission. Therefore Andrea Crovetto was kind enough to measure the c-Se sample at NREL, Colorado USA, using a double-beam Cary 7000 spectrophotometer. The total transmission (the sum of direct and diffuse transmission) was measured by collecting the light transmitted over a ≈ 2π sr solid angle using an integrating sphere. The total reflection was similarly measured with an incidence angle close to normal. The absorption coefficient of c-Se was calculated from $T_{\text{total}}/(1\text{-}R)$ knowing the thickness (≈ 300 nm) which was measured by ellipsometry. The resulting absorption coefficients and corresponding tauc plots for c-Se and a-Se can be seen in Figure 3.16.

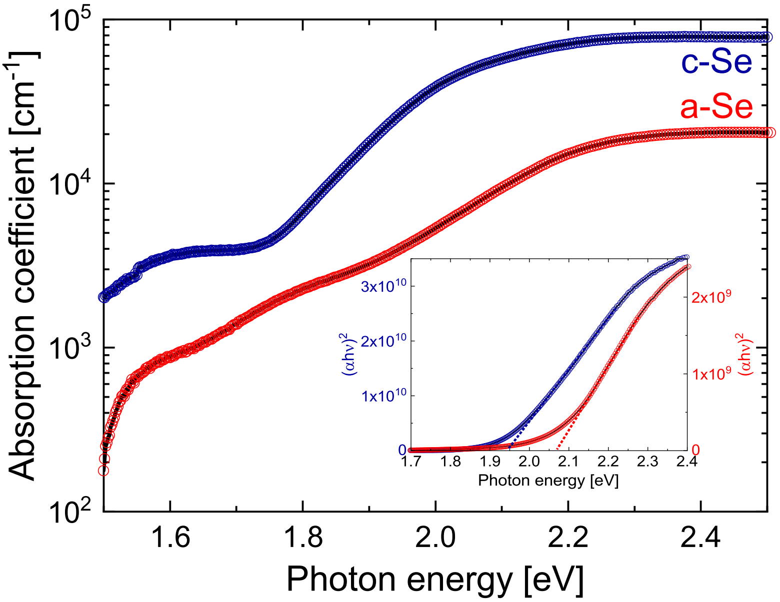

Figure 3.16: Absorption coefficient and Tauc plots of c-Se and a-Se with extrapolated bandgaps measured by UV-Vis. The bandgap of selenium changes from ≈ 2.07 eV for a-Se to ≈ 1.95 eV for c-Se after annealing.

Above its bandgap, selenium absorbs around 5 times as much of the light in its crystalline form compared to being amorphous. The bandgap of Se is, as expected from literature, reduced during crystallisation. Our resulting bandgap of around 1.95 eV for c-Se matches that obtained by Todorov[68] which coincides well with a similar annealing technique. Investigating and optimising the annealing conditions further might yield a lower bandgap down to $\approx$ 1.8 eV as has also been reported.[66]

For a bandgap of 1.95 eV, one can expect a maximum current density of around 15.7 mA/cm^2 from the AM1.5G solar spectrum, if perfect collection of carriers is assumed. For an absorption coefficient similar to the one measured and calculated in Figure 3.16, a Se thickness of 300-500 nm should be sufficient to absorb most of the light above the bandgap (see Appendix B, Figure 2 (a)).

For future studies it is recommended and encouraged to develop an annealing setup that allows the control of a variety of parameters. Parameters that have already been shown or are expected to affect the crystal growth during annealing are as follows: absolute temperature, heating and cooling rate, encapsulation (to avoid reevaporation of Se from the surface and reduce Se thickness variation), pressure, selective gas flow (e.g. Ar, N_2 and/or O_2), moisture and illumination (e.g. laser annealing). The annealing of this project has had limited control of most of these parameters. During the project, small attempts of changing the heating and cooling rate as well as encapsulation of devices during annealing have yielded non-reproducible and unsuccessful results. If increased control of these parameters can be achieved, an expected large increase in c-Se crystal quality and thereby also device performance could potentially be obtained.

3.6 Band Positions of Se Measured by UPS

Near the end of the project it became possible to use the equipment Nexsa by ThermoFisher Scientific that allowed for the combined characterisation techniques of XPS, ISS, Raman and UPS analysis. Due to my limited time left, Rasmus Nielsen who had just started as a PhD student received training on it which allowed for the UPS measurements in order to investigate the band position of our fabricated c-Se. A He I (21.22 eV photon energy) source was used and the measurements were performed with a -5 V bias to the sample to deconvolute the work function of the Se surface from the work function of the spectrometer. A pass energy of 2k eV was used with a step size of 0.05 eV and a dwell time of 50 ms averaged over 20 scans. The results can be seen in Figure 3.17.

From the measurements a work function of $\phi = 5.05$ eV is determined from the extrapolation of the low kinetic energy cutoff of the spectrum which is subtracted from the incident photon energy of 21.22 eV. The valence band energy, E_V with respect to the fermi level, E_F, is found to be $E_\mathrm{V} - E_\mathrm{F} = 0.74$ eV, proving that c-Se is intrinsically a p-type material. This is in accordance with most literature.[67,104,105] Comparing this value with that calculated from the measured

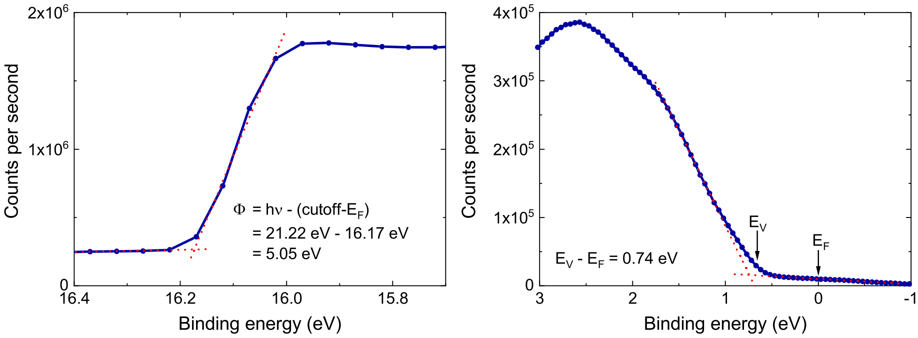

Figure 3.17: UPS measurement of c-Se. Data used with kind permission from Rasmus Nielsen.

acceptor density determined from capacitance-voltage measurements and the effective density of states calculated by DFT (see Chapter **??**), there is a ≈ 0.5 eV discrepancy. It is believed that this discrepancy is related to Fermi level pinning to the surface during the UPS measurement. [134]

3.7 Elemental Analysis of the Thin Film Elements

The XPS and ISS systems of the Volvo were during the project repaired to a certain extent. I would like to thank my colleague PhD student Jakob Ejler Sørensen who helped me out with the home-made software of the system which connected a Python script with the HAC100 hemispherical analyser and the HAC5000 electronics box through a Keysight 34972A data acquisition/data logger switch unit. No XPS or ISS measurements would have been possible without his valuable help. An unknown drift in the peak positions is still to be solved which yields an uncertainty of the absolute peak positions of around 1-2 eV. For this reason the XPS and ISS results were mainly made for qualitative purposes. Unfortunately, the controls for the pass energy remained defective until near the end of the project. This meant that the pass energy was fixed to its a value of 25 eV which results in low signal to noise ratios, but a high resolution of the XPS peaks. This was fixed near the end of the project, but unfortunately the amount of Te and Se deposited in the chamber at this point in time yielded a background contamination that was apparent from all XPS measurements regardless of Ar sputter cleaning.

For this reason I have chosen to show some of the initial XPS spectra measured of the different deposited thin films of the device to confirm the existence of the elements and also show that no large apparent contamination is present in the surfaces of the interfaces.

3.7.1 XPS Characterisation

An XPS spectrum of TiO_2 on FTO inserted into the Volvo directly after sputter deposition can be seen in Figure 3.18.

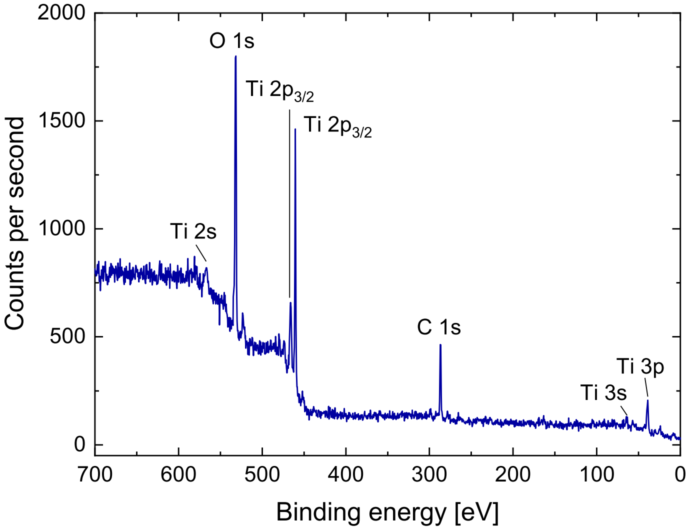

Figure 3.18: XPS spectrum of TiO_2 on FTO.

Carbon contamination is clearly apparent from the spectrum which originates from non-ideal transport between the sputter chamber and the Volvo. No other contaminations are observed. The sample is sputtered with 1 keV Ar^+ for 2 minutes and 1 nm Te is deposited onto the sample. The subsequently made XPS spectrum can be seen in Figure 3.19.

The C 1s peak is diminished significantly, which is attributed to the Ar sputtering of the TiO_2 surface prior to Te deposition. Clear Te 3d peaks are observed after 1 nm Te deposition with reduced, yet still visible TiO_2 peaks. If it is assumed that the Te is deposited uniformly, then it signifies that the mean free path of the electrons excited from TiO_2 is still greater than the thickness of the Te, which according to Figure 2.7 would mean that the Te is thinner than 1-2 nm. After depositing Se on the surface of the device only Se is observed with XPS. It was investigated whether any foreign contaminations are introduced after subsequent annealing steps and deposition of Au on Se. The sample was annealed to crystallise the Se and Au was sputter deposited onto the Se in a grid. The sample was again placed inside the Volvo for XPS analysis (see Figure 3.20).

From the spectrum both Se and Au peaks are observed. No significant quantity of foreign elements looks to be introduced. Carbon contamination is again introduced and an oxidated Se surface is introduced from the annealing in air which is in accordance to my prior work during my Master's Thesis.[129] Once again

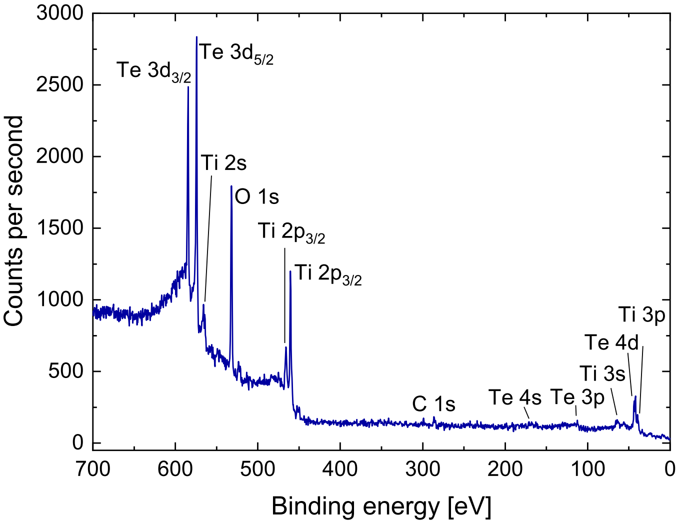

Figure 3.19: XPS spectrum of 1 nm Te on TiO_2/FTO after 2 minutes of 1 keV Ar^+ sputtering.

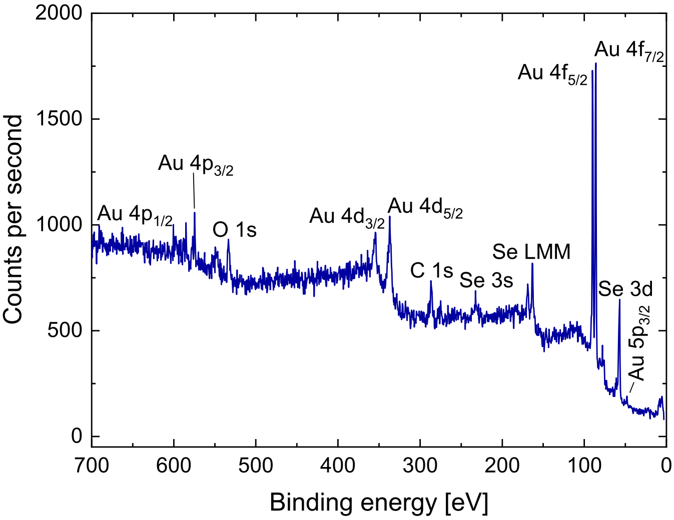

Figure 3.20: XPS spectrum of Au grids on Se(300 nm) on Te/TiO_2/FTO.

these results encourage future work on limiting air exposure during the fabrication process as well as controlling the annealing conditions to avoid oxidation in the Se/HTL interface.

3.7.2 ISS Characterisation

ISS measurements became possible near the end of the project after physical and electronic repairs and software updates. At this stage in the project TiO_2 had been replaced with ZnMgO in accordance to the architecture used by Todorov et al.[68] Results of these device architectures will be further explained in Chapter 4. A sample of FTO/ZnMgO was measured with XPS and ISS before and after Ar sputtering and Te/Se deposition. Due to Se and Te contaminations I have chosen not to include the XPS spectra here as I believe that the XPS spectra shown in Figures 3.18, 3.19 and 3.20 paint a clearer picture. The ISS spectra made with 1 keV He^+ ions at a scattering angle of 150 degree can be seen in Figure 3.21. Note that the peak energies shown roughly correspond to the high-energy "foot" of the peak due to inelastic processes. Therefore the actual ISS peaks are lower than the calculated values.

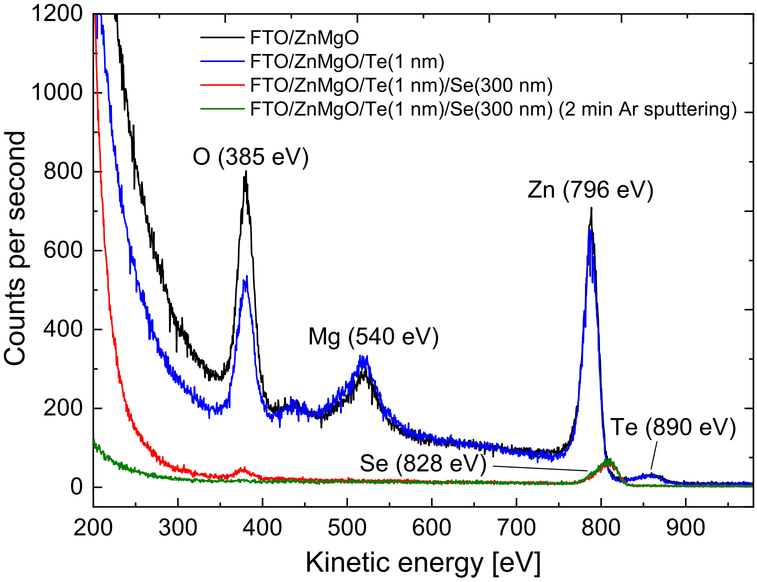

Figure 3.21: ISS spectra of FTO/ZnMgO/Te(1 nm)/Se(300 nm) before and after 2 minutes of 1 keV Ar^+ sputtering and Te/Se deposition.

Zn, Mg and O peaks are clearly observed from the ZnMgO surface. A small peak at 890 eV is attributed to Te contamination. After depositing 1 nm Te, the background signal below 300 eV (typically originating from carbon contamination) is diminished. The oxygen peak at 385 eV is also slightly reduced. The Te peak at 890 eV does not increase even though an increase in Te signal is detected with XPS (similar to the increase in Te 3d peaks in Figure 3.19). The reason for this was later realised to be due to long ISS scan times (dwell time of 3 seconds per eV) that are scanned from low to high kinetic energies. The 1 keV He^+ ions will in this time manage to remove the Te within this time frame. The subsequent investigations have all been made with lower dwell times of 0.2 seconds per eV to diminish this issue. After the deposition of Se, a Se peak at 828 eV arises. From the presence of the small O peak it can be concluded that the surface of Se becomes slightly oxidised even without breaking the vacuum of the Volvo. After Ar sputtering the surface for 2 minutes, the background signal below 300 eV as well as the oxygen peak is reduced which is attributed to the removal of both carbon and an oxidised Se surface. The disappearance of the Te peak after the Se deposition can be attributed to the Te contamination being present on either the sample or the sample holder prior to the Se deposition.

Curiously both the Se and Te peak signals are very low. The current hypothesis for this phenomenon is that more He^+ ions are neutralised by these elements due to a neutralisation process called quasi-resonant neutralisation (qRN). This effect has been observed for elements with d-band energy levels within around 10 eV of the first ionisation energy of He (24.6 eV). This effect has been reported for Ga, Ge, In, Sn, Sb, Pb and Bi.[88,135–138] When the He^+ ion approaches the surface atom a quasi-resonant charge exchange can occur between the d-band and the first ionisation energy of He. This process is more likely to occur the closer the two energy states are aligned. Looking again at the XPS spectra of Figures 3.19 and 3.20, d-states of Te and Se can be seen to be near the 24.6 eV 1s state of He. The 3d peak of Se is situated at 68 eV, which is 44 eV higher than the 1s state of He. Te has a 4d state at 40 eV which is 15 eV higher. Even though these d-states of the Se and Te are not within the 10 eV range, which has typically been reported to cause the qRN effect, it is still believed that this process leads to a larger probability of neutralisation which leads to less intense ISS peak. Low scattered ion yields have already been reported for Te due to this process.[139] Whether other neutralisation processes play a significant role is not certain. The only literature found for ISS analysis on Se was in a study of CdSe by use of 1 keV Ne^+ ions.[140] Further investigations could be made where different ion sources rather than He^+ were used.

Investigation of Te Thickness and Coverage with ISS and XPS

An experiment was carried out to investigate the potential growth mechanics of the Te deposition. Te was deposited gradually with increasing thickness from 0 to 20 nm on a silicon sample where XPS and ISS was measured of the surface before and after each subsequent deposition. The silicon sample was Ar sputter cleaned at 1 keV for 30 minutes prior to the Te deposition to remove carbon and other potential contamination (at this point in time around $\approx$ 1000 samples had been made with Te deposition in the Volvo, which had naturally introduced some Te and Se contamination). The resulting XPS spectra measured with a fixed pass energy of 50 eV can be seen in Figure 3.22.

As expected, the Te signal increases and the Si and O signals decrease with increased Te thickness. Te contamination is clearly observed even at "0 nm"

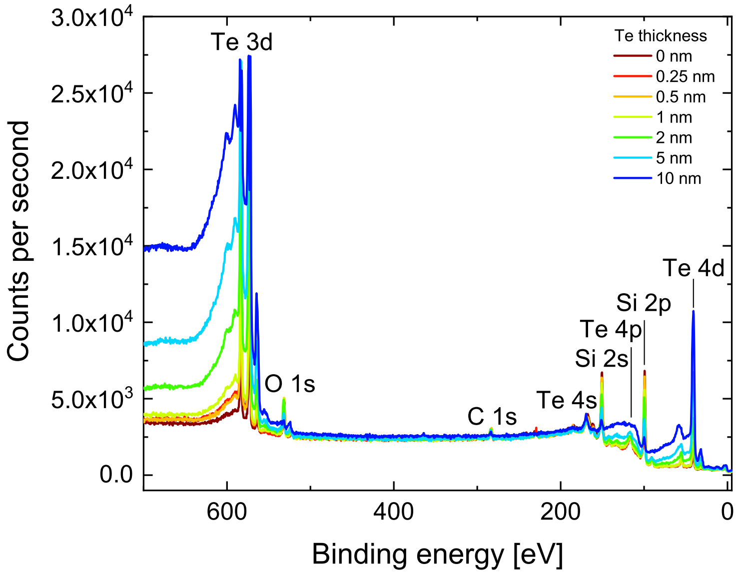

Figure 3.22: XPS spectra of Si/Te(0-10 nm) at a fixed pass energy of 50 eV.

Te, regardless of the Ar sputtering. The presence of Se contamination was not distinguishable from these XPS spectra, but was observed for ISS. Above 5 nm Te the Te 3d peaks reach an intensity of ≈ 2.75×10^4 counts per second which saturated the analyser at this fixed pass energy of 50 eV. For 10 nm and 20 nm Te, XPS spectra were also made with a fixed pass energy of 25 eV. Si could no longer be detected above 20 nm Te indicating full coverage of around >2 nm (see Figure 3.23).

The ISS spectra were made with 1 keV He^+ ions at a scattering angle of 150° (see Figure 3.24).

Similarly as for the XPS spectra, the Si and O signals disappear above 20 nm Te indicating full coverage of at least 1 monolayer of Te. Both Te and Se peaks are also observed as seen previously before the Te deposition. Plotting the integrated areas of both the ISS and XPS peaks (see Figure 3.25) clearly visualises an exponential decay of the Si and O signals which indicates that the Te after deposition does not fully cover the surface homogeneously.

With a lattice constant of around 4-6 Å,[141] one would expect ≈ 0.5-1 nm Te deposition to fully cover a flat surface. For a layer by layer deposition growth (also called a Frank-Van der Merwe thin film growth mechanism) the peak intensity of Te should increase linearly with increasing thickness. Since we do not observe such a linear trend, it indicates that the thin film growth mode is either island formation (Volmer-Weber mechanism) or layer-plus-island (Stranski-Krastanov mechanism).[142] This is affected by the mobility of the Te atoms on the surface

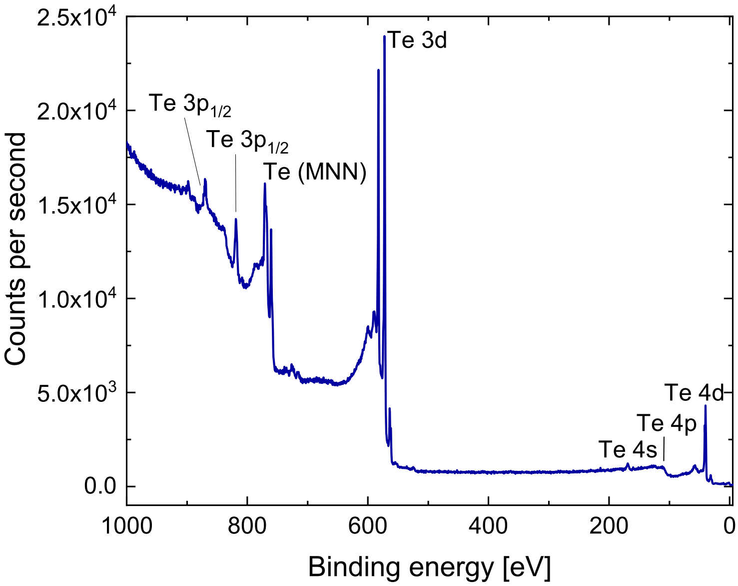

Figure 3.23: XPS spectrum Si/Te(20 nm) at a fixed pass energy of 25 eV.

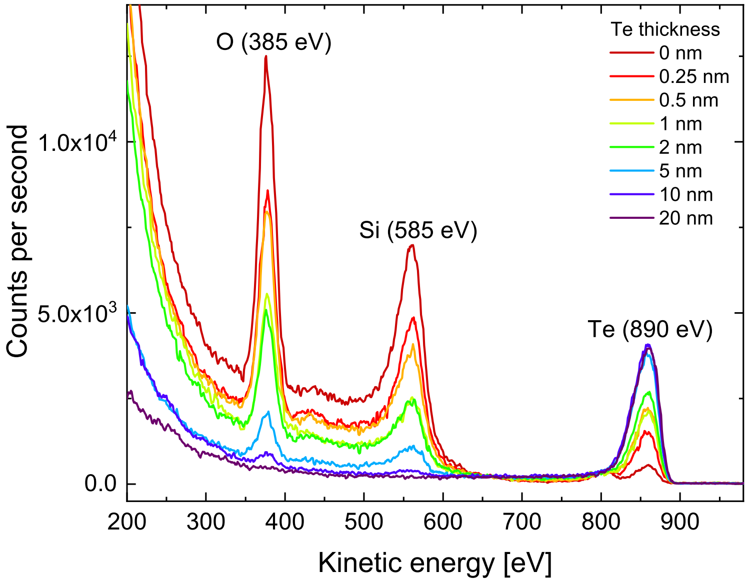

Figure 3.24: ISS spectra of Si/Te(0-20 nm).

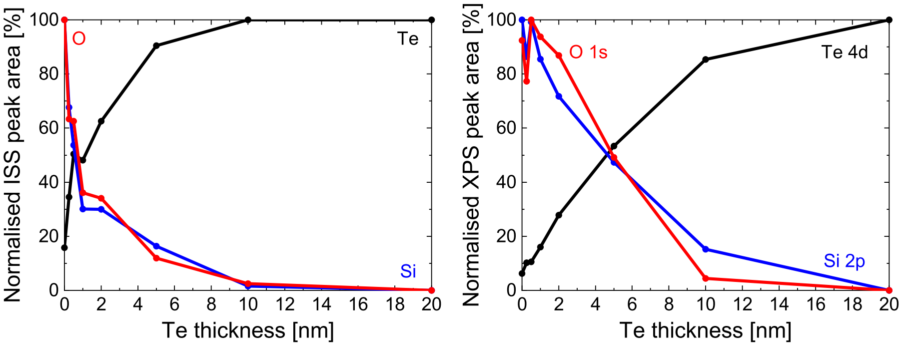

Figure 3.25: Normalised ISS and XPS peak areas of Te, Si and O.

as well as the surface energy of the substrate which is also affected by the temperature. How this relates to the device performance of the Se-based device is yet uncertain. In literature a Te layer of 0.5-1 nm is required for optimal performance and we observe the same tendency. However, it is shown that 20 nm of Te is required to fully cover the surface which does not even take roughness into account. FTO is a much rougher surface than Si and therefore the Te is expected to cover even less. If this is the case then Te acts, as expected, more like a nucleation layer which introduces nucleation sites to the Se to grow from. However, since the optoelectronic properties of Te are non-ideal for the middle of the p-n junction of the device, further increasing the thickness only enhances this effect which could explain worse device performance. Somehow improving the homogeneity of the deposition may improve the Se crystallisation which may achieve improved device performance. It would be interesting to repeat this experiment while changing a few parameters such as the substrate temperature, roughness and material. If it is possible to make the deposited Te mobile during deposition while keeping the surface adhesive force greater than the cohesive forces of the Te atoms, it may allow full coverage at a lower thickness and thereby a more homogeneous deposition. It could be interesting to learn whether this could improve the homogeneity of the Se growth and as a result also the device performance. Performing corresponding XRD measurements would be relevant. Furthermore, it would be desirable to investigate the ISS and XPS signals of the Te and substrate with more datapoints between 0-2 nm to better estimate a linear trend corresponding to the thickness required to deposit a monolayer of Te. Here it would be necessary to further reduce the chamber pressure from $\approx 10^{-8}$ mbar to $\approx 10^{-10}$ mbar to reduce the potential oxidation of the surface between each measurement. The non-linear XPS intensity difference of the O 1s and Si 2p signals for 0-1 nm Te is suspected to be due to reoxidation of the surface.

Ultimately, it would be beneficial to continue a similar experiment of a Se deposition on top of Te to further understand the growth mechanisms of Se on Te.

4 | From Single-Junction to Tandem

This chapter will present results on the development and progression on the device architecture towards the ambitious goal of making a Se-Si tandem device. When I started working on my Master's project in 2017 the Se-based single-junction solar cell PCE record of 5.01% was still held by Nakada and Kunioka from 1985.[63] Their simple device structure consisted of ITO/TiO_2/Te/Se/Au. Comparing this structure to the device structure presented in Section 3.1 a HTL is missing. Since 2017 three new reports show Se-based solar cell devices with HTL (MoO_x, P3HT and PEDOT:PSS).[68,73,74] A HTL should, if introduced properly into the structure, improve the collection of carriers which in turn should improve the PCE. This was achieved by Todorov et al. in 2017 with a PCE of 6.5% for a structure of FTO/ZnMgO/Te/Se/MoO_x/Au.[68]

Naturally these findings influenced this project and inspired us to progress towards certain milestones working towards a tandem device. Initially the Se top-cell was to be improved both in terms of device performance and reproducibility before combining it with a Si bottom-cell. The main milestones were as follows:

1. Simple single-junction without HTL: FTO/TiO_2/Se/Au
2. Introduce a HTL: FTO/TiO_2/Se/MoO_x/Au
3. Replace TiO_2 as an ETL: FTO/ZnMgO/Se/MoO_x/Au
4. Bifacial device: FTO/ZnMgO/Se/MoO_x/ITO
5. Tandem device: Si bottom-cell/ZnMgO/Se/MoO_x/ITO

These milestones will be presented in this chapter as well as a discussion of how to further progress towards a water splitting tandem device.

I estimate that I, along with many of my Bachelor's and Master's students have fabricated around 1100 devices in total during the last 3.5 years. Many of these devices and findings would not have been possible without their help. So I would like to again thank Rasmus Nielsen, Frederik Madsen, Martin Voss, Astrid Erecius, Rikke Andersen and Dan Windfeldt for their valuable help. I have chosen not to show the results of all of these devices as this chapter will otherwise become too long and tedious. I have instead chosen to show the results that I have found most important and interesting.

4.1 Chasing the Single-Junction World Record

Currently the best reported Se-based solar cells with PCEs above 5% are from the work of Nakada and Kunioka in 1985, Hadar et al. in 2019 and Todorov et al. in 2017.[63,68,71] The former two made simple architectures without a HTL and with a TiO_2 as an ETL. The latter reported a similar simple architecture without a HTL but also introduced MoO_x and replaced TiO_2 with ZnMgO. Both implementations yielded large performance benefits as seen from their measured JV and EQE results which have been presented together for comparison (see Figures 4.1 and 4.2).

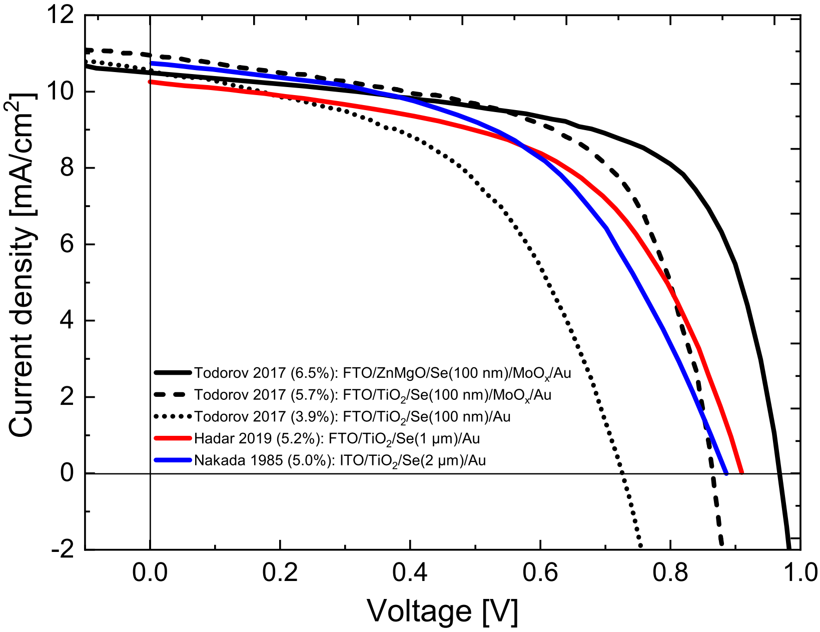

Figure 4.1: JV curves of the best reported Se-based solar cells reproduced from literature by use of Plot Digitizer.[63,68,71]

The goal was to try to achieve and reproduce similar single-junction device performance before attempting to fabricate a Se-Si tandem device.

The device performance of all reported champion devices within recent years has been collected in Table 4.1.

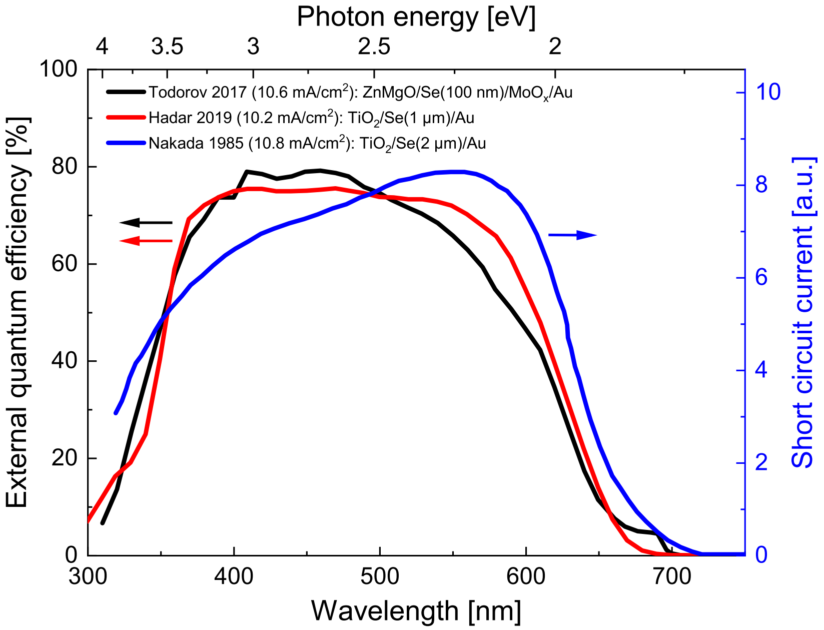

Figure 4.2: EQE curves of the best reported Se-based solar cells reproduced from literature by use of Plot Digitizer.[63,68,71] The photocurrent spectral response measured by Nakada 1985[63] was not calibrated with respect to the power of the light source and therefore only the short circuit current was measured which gives no specific quantitative information.

Table 4.1: Champion Se-based single-junction solar cells reported in literature. Table design was inspired by [103]. VDP: Vapour deposition, ECD: Electro chemical deposition, SP: Spin-coating, TSMP: Two-stage melting processing.

Device architecture	**Method**	**V_{oc} (V)**	**J_{sc} (mA/cm^2)**	**FF (%)**	**η (%)**	**Pub. date ref.**
ITO/Te(0.5nm)/Se(1 µm)/Au	VDP	0.54	10.9	56	3.3	1984 [143]
SnO_2/CdSe/Se(0.5∼0.6 µm)/Au	VDP	0.65	**13.5**	52	4.6	1984 [144]
ITO/TiO_2/Se(2 µm)/Au	VDP	0.884	10.8	52.5	5.01	1985 [63]
TiO_2/Se/CuCNS	ECD	0.60	3.0	-	0.13	1998 [113]
FTO/cp-TiO_2/mp-TiO_2/Se/Au	ECD	0.65	8.7	53	3.0	2013 [114]
FTO/cp-TiO_2/mp-TiO_2/Se(350nm) /P3HT/PEDOT:PSS/Ag	VDP & SC	0.71	9.71	38	2.63	2014 [115]
FTO/cp-TiO_2/mp-TiO_2/Se(350nm) /Spiro-OMeTAD/PEDOT:PSS/Ag	VDP & SC	0.69	8.10	33	1.83	2014 [115]
FTO/TiO_2/Te/Se(100nm)/Au	ECD	0.50	6.4	36	1.17	2014 [116]
FTO/bl-TiO_2/mp-TiO_2/Se/PTAA/Au	SC	0.66	9.1	57	3.52	2016 [117]
FTO/ZnMgO/Te/Se(100nm)/MoO_x/Au	VDP	**0.969**	10.6	**63.4**	**6.51**	2017 [68]
FTO/TiO_2/Te/Se(100nm)/MoO_x/Au	VDP	0.866	10.9	60.6	5.73	2017 [68]
FTO/TiO_2/Te/Se(100nm)/Au	VDP	0.728	10.5	50.5	3.88	2017 [68]
FTO/TiO_2/Se/Spiro-MeOTAD/Au	SC	0.52	6.39	37	1.23	2018 [118]
FTO/TiO_2/Se/PTAA/Au	SC	0.59	4.71	39	1.08	2018 [118]
FTO/TiO_2/Se/P3HT/Au	SC	0.45	3.50	39	0.62	2018 [118]
FTO/TiO_2/Te/Se(1 µm)/Au	VDP & SC	0.911	10.2	55	5.2	2019 [66,71]
FTO/c-TiO_2/mp-TiO_2/ZrO_2/Se/carbon	TSMP	0.67	4.59	65	2.00	2019 [72]
ITO/SnO_2/Te/Se(200nm)/P3HT/Ag	VDP & SC	0.758	8.43	57.5	3.70	2020 [74]
ITO/SnO_2/Te/Se(200nm)/PTAA/Ag	VDP & SC	0.474	8.08	50.1	1.9	2020 [74]
ITO/PEDOT:PSS/Te(0.5nm)/Se(200nm) /PCBM/Ag	VDP & SC	0.839	9.61	47.8	3.9	2020 [73]

4.1. Chasing the Single-Junction World Record

4.1.1 The Simple Architecture

Once it was possible to reproducibly deposit Te and Se by use of thermal evaporation, attempts of fabricating the simple FTO/TiO_2/Se/Au structure became increasingly more successful. Reproducibility was still an issue at this point in time whose origins were difficult to pinpoint. One major increase in performance was obtained by reducing the amount of contacts on each device from 8 down to 1 large contact of ≈ 0.4 cm^2 as illustrated previously in Figure 3.1. The JV-equipment used did not allow for the contacting of all contacts simultaneously nor the shadowing of the non-measured contacts, which resulted in poor device performance due to light induced transport losses.

Reproducibility was an issue for a long time and remained somewhat of a mystery until the TiO_2 was replaced with other ETL such as ZnO or ZnMgO. These results will be shown later in this chapter. The reason most likely stems from the fact that the anatase TiO_2 was sputtered from a Ti target and an inlet flow of oxygen was added during the process at around 400 °C. Both the work function and the Fermi level positions are known to vary up to 1 eV depending on the sputtering conditions.[145] Such a variation can be extremely detrimental to the charge separation of the p-n junction and thereby also the overall device performance. Many parameters can therefore potentially reduce reproducibility from this process. First of all, the Ti target is very easily oxidised and since other users also used the Ti target with varying oxygen flows, the amount of surface oxide is expected to change affecting the rate and oxygen content of the resulting deposited film. This effect was diminished later in the project by pre-sputtering the target for a certain amount of time before the actual deposition. The inlet to the oxygen flow is also not strictly fixed in position and may have moved over time. Since the deposition time for the TiO_2 was rather short due to a high power DC sputtering, this may have affected the amount of O_2 being able to react with the sputtered Ti film. Furthermore, the infrared window allowing the lamp to heat the sample holder in the sputter chamber became over time increasingly covered with different sputtered materials. The thermocouple that reads the deposition temperature sits above this window. Therefore an increased discrepancy between the measured temperature and the actual temperature is to be expected over time. In hindsight it would have been beneficial to measure XRD, UV-Vis and UPS on the TiO_2 on an ongoing basis to monitor whether the crystal structure, absorption or band alignment and doping may have changed over time. Unfortunately UPS was not available for most of my project time.

Regardless, after a long time of trial and error, a record device was obtained with a PCE of 5.4% making it the best reported device with this particular simple device architecture (see Table 4.1). The layers of the device were fabricated in the same manner as explained in section 3.3. A J_{sc} record of 12.0 mA/cm^2 was also measured on a similar device. The JV and EQE results of the 2 devices can be seen in Figure 4.3.

Comparing this device performance with the published results shown in Figures

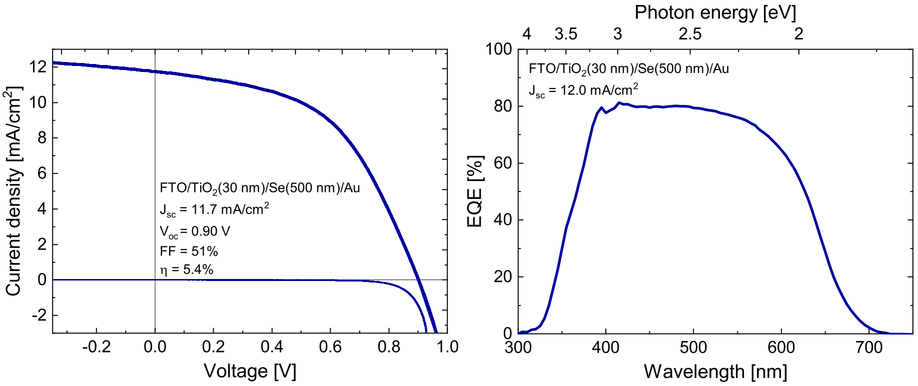

Figure 4.3: JV and EQE results of the 2 champion FTO/TiO_2(30 nm)/Te(1 nm)/Se(500 nm)/Au devices.

4.1 and 4.2, the main performance improvement is related to a higher J_{sc} measured with EQE showing a wide collection efficiency of $\approx$ 80% from 400-550 nm. In fact 12.0 mA/cm^2 was the greatest J_{sc} obtained out of all the different 1100 Se-based devices fabricated during this project and it outperforms most short-circuit currents reported in literature (see Table 4.1). It is believed that the large J_{sc} is mainly a result of a large rear surface reflection from the Au where there is no parasitic absorption from the HTL. Furthermore, without a HTL a thick Se layer is beneficial to the performance since the surface recombination velocity of the Au is expected to be large. With an increased Se thickness as well as large back surface reflection, a large absorption is to be expected. Both the V_{oc} and FF are similar to those reported by Hadar and Nakada. To further improve the J_{sc}, the front surface reflection could be reduced by use of anti-reflective coating. Furthermore the non-ideal EQE shoulder at around 600 nm prevents the collection of much of the solar spectrum light above the 1.95 eV bandgap of selenium (see Figure 4.4).

The long-wavelength photons penetrate further into the selenium and are therefore absorbed further away from the charge separating p-n junction (at the Se and ETL interface). To improve this long-wavelength collection there are a few architectural changes or material improvements that could potentially be made. One could try to improve the carrier lifetime and diffusion length in the selenium in order for the generated carriers to reach the p-n junction before recombining. Introducing a HTL should also reduce the recombination of carriers at the back contact by reducing the surface recombination velocity as well as ideally introducing a back surface field which promotes selective hole collection as well as electron rejection. Improvements to the collection should also be achievable if one could somehow increase the depletion region width by doping the materials accordingly. Lastly improved current collection should be obtainable by

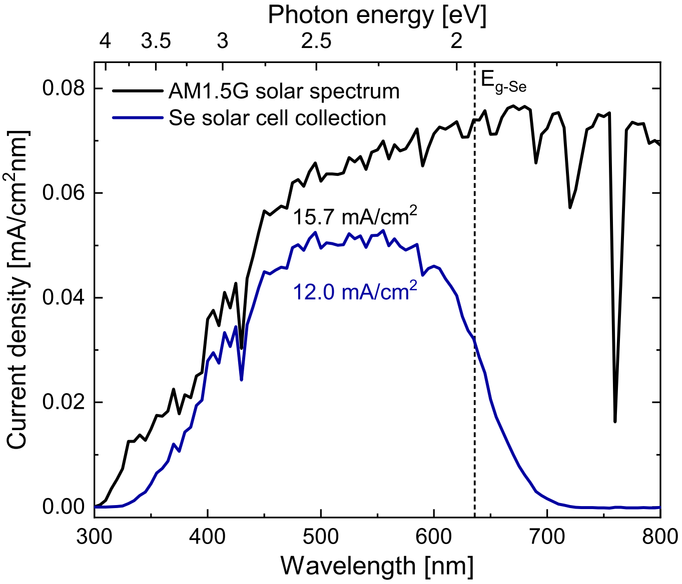

Figure 4.4: EQE converted into collected current from AM1.5G spectrum of a FTO/TiO_2(30 nm)/Te(1 nm)/Se(500 nm)/Au device.

introducing some light trapping from surface texturing and greater back surface reflection.[146,147]

Varying the bias of the device during the EQE measurement one obtains the plot seen in Figure 4.5. Here the change in the measured current from the EQE at each bias matches that of the JV curve seen in Figure 4.3 that is highly collection dependent for positive bias and saturates towards a maximum current for a large negative bias. The shape remains the same for all biasses indicating a wavelength independent collection related to the change in bias.

Reflection measurements were in fact made for most champion cells of this project in order to plot the IQE of the devices, but unfortunately it was realised too late that the reference used for the calibrations of the measurements was not ideal and therefore all reflection measurements were discarded. Regardless, the fact that an EQE of $\approx 80\%$ can be obtained without the inclusion of an anti-reflective coating or light trapping points towards an IQE close to unity.

The fact that we had fabricated a simple architecture FTO/TiO_2/Te/Se/Au device with better performance than the similar device structures previously reported, indicated that our device fabrication process and particularly the Se fabrication and crystal growth had state-of-the-art capabilities. Naturally, the next milestone became to try to include a HTL to further improve performance. The goal was to try to achieve a new efficiency world record beating the 6.5% reported by Todorov et al.

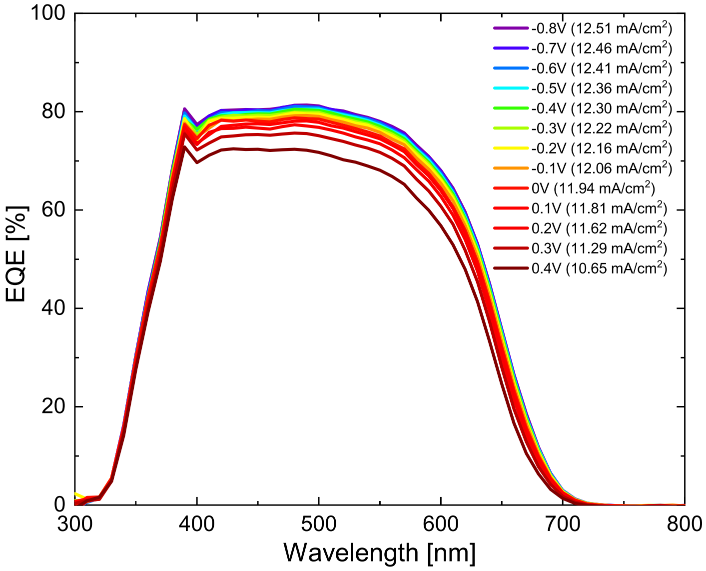

Figure 4.5: EQE of a FTO/TiO_2/Te/Se/Au device as a function of bias voltage.

4.1.2 Introducing MoO_x as a Hole-Transport Layer

Intially NiO_x was attempted as a HTL by sputtering with limited success. NiO_x has been reported to both function as a successful HTL layer for both organic polymer and perovskite photovoltaics. [148,149] Simultanously NiO_x is able to function as both an efficient protective layer and catalyst for the oxygen evolution reaction (OER) in alkaline when incorporated with Fe impurities. [150,151] Potentially this could allow our Se device to function as a photoanode for alkaline OER while simultaneously facilitating better collection of carriers. Many attempts were made to include NiO_x as a HTL, but ultimately the device performance only became worse in terms of the series resistance indicating that the NiO_x acts as an insulator and only increases the series resistance of the device. However, it was possible to obtain a champion PCE of 4.0% (the details for all unique champion devices of this project are included in Figure 4.25 and Table 4.2), which should allow the investigations of these devices as photoanodes for alkaline OER. I still encourage further investigations into optimising NiO_x as a potential HTL and catalytic protective layer for alkaline OER. I would suggest to alter the fabrication technique to either thermally evaporate the NiO_x or to electrochemically deposit it. However, it should be noted that even though NiO_x is semi-transparent allowing illumination through this side of the device, a worse device performance is to be expected! The reason for this is that the carrier-separating p-n junction sits at the ETL/Se interface (since Se is intrinsically p-type) and since the lifetime and diffusion length of the carriers in Se are very short, the illumination direction matters tremendously. Further explanations will follow later in this Chapter (see Section 4.2) and can be also be read from Paper I (see Appendix B). For a single-junction photoanode device this effect can be avoided if one continues to illuminate through the FTO. Yet, for a tandem photocatalytic device this will not be possible. Ultimately, I would therefore encourage to either strive for somehow improving the Se carrier transport properties so that the illumination side matters less or I believe it to be mandatory to strive for an inverted fabricated design with an ETL that can also facilitate HER at the surface (e.g. TiO_2 with Pt[152–154]).

Regardless, the priority remained to strive for single-junction PV PCE superiority as well as to attempt to fabricate a tandem Se-Si PV device. For this purpose NiO_x was replaced with MoO_x as already successfully reported by Todorov et al.[68] They fabricated oxygen deficient MoO_x ($x < 3$) by use of thermal evaporation and an improvement in device performance was observed after long-term air exposure. It is believed that the oxygen deficiency introduces bandgap states into the bandgap of the MoO_3 and that these defect states enable the selective hole-transport. Furthermore, the work function has been reported to vary from 5.4 eV to 6.9 eV depending on the oxygen content.[121–124] Fernandes et al. investigates the properties of sputtered MoO_x[155] as a function of oxygen partial pressure and finds that $MoO_{2.57}$ has high conductivity but also a high and unwanted absorption coefficient from 0.6-3.0 eV. For $MoO_{3.00}$ and $MoO_{3.16}$ the absorption coefficient drops but so does the conductivity giving it insulator rather than hole-transport properties. The goal was therefore to try to synthesise MoO_x with $2.5 < x < 3.0$ via reactive sputtering. This was done during the Master's project of Rasmus Nielsen.[96] Rasmus deposited MoO_x on silicon under various oxygen flow conditions during reactive sputtering of a Mo metallic target. EDX-S was used to determine the relative O/Mo-ratios. A maximum O/Mo-ratio of 2.38 was reached at an O/Ar inlet flow of 0.167 (30/5 SCCM Ar/O_2 at 5 mTorr and room temperature). Further increasing the oxygen flow yielded no greater O/Mo-ratio. Annealing the $MoO_{2.38}$ at 190 °C for 10 minutes increased the O/Mo-ratio to 2.41. However, this should only be interpreted qualitatively as a gradient in the oxygen content towards the surface is to be expected which cannot be properly determined from EDX-S alone. The O/Mo-ratio is lower than the 2.57 reported by Fernandes et al.[155] who reported low transmission for this ratio. However, the transmission for our synthesised MoO_x is high below photon energies of 3.5 eV (see Figure S8 in Appendix B). Further investigations of the composition and properties of the thin film are yet to be made. It is recommended that the sputtering synthesis method is replaced by thermal evaporation as this technique is more gentle towards the deposition on the Se, which will likely reduce the probability for interface defects in the Se/MoO_x interface. The film properties could also potentially be further optimised by varying the deposition pressure and deposition/annealing temperature.[155–157]

Introducing the MoO_x as a HTL to our architecture proved to improve the device performance. A batch was made with an introduced layer of 15 nm MoO_x and a varying selenium thickness between 200 nm (cells 1, 2, 3 and 8), 300 nm (cells 4 and 6) and 500 nm (cell 7). The devices were annealed after each subsequent step after the selenium deposition to diminish sputter damage as well increase the oxygen-content of the MoO_x film. The effect of the final annealing step was investigated by measuring the JV and EQE response of the devices before and after (see Figures 4.6 and 4.7). The device SEM cross-section was previously shown in Figure 3.2.

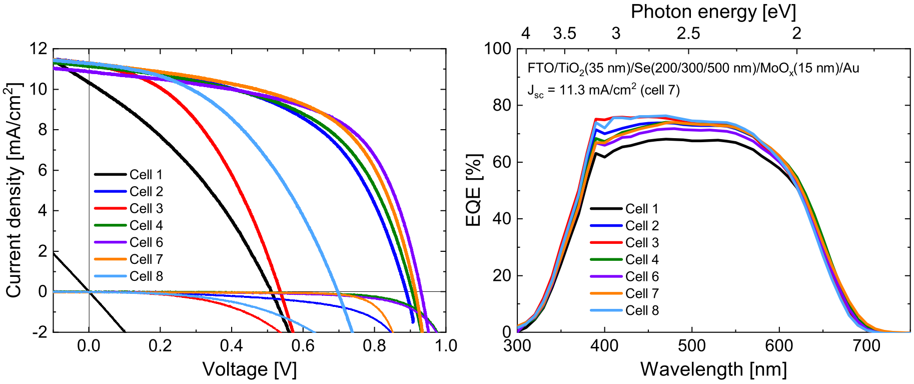

Figure 4.6: FTO/TiO_2(35 nm)/Te(1 nm)/Se(200/300/500 nm)/MoO_x(15 nm)/Au devices before the final annealing step at 190 °C for 4 minutes.

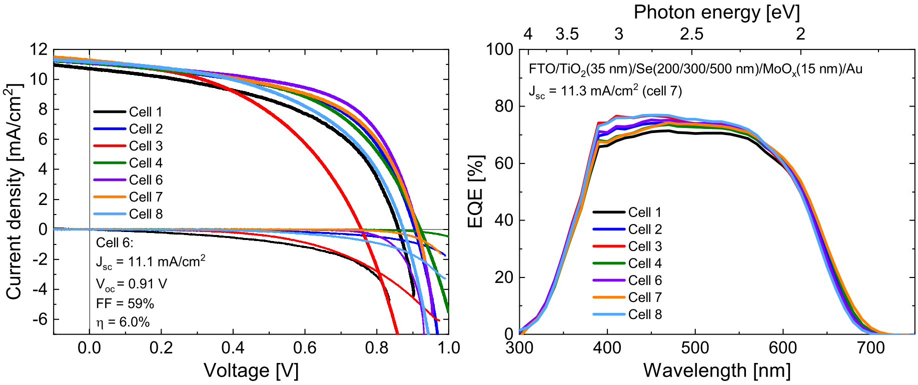

Figure 4.7: FTO/TiO_2(35 nm)/Te(1 nm)/Se(200/300/500 nm)/MoO_x(15 nm)/Au devices after the final annealing step at 190 °C for 4 minutes.

Cells 1, 3, and 8 were all made with 200 nm Se and showed poor performance before the final annealing step. After annealing at 190 °C for 4 minutes they obtained a significant improvement in both FF and V_{oc} resulting in a reasonable batch reproducibility regardless of Se thickness. No devices obtained worse

device performance after the final annealing step. Why a major increase in performance was achieved mainly for the thinnest samples is still uncertain. Perhaps the selenium becomes mobile enough during the annealing to eliminate shunting paths that are more likely to occur for thinner samples.
A new champion device was obtained (cell 6) with a PCE of 6.0% outperforming the PCE of 5.7% of the similar device architecture obtained by Todorov et al.[68] Introducing MoO_x as a HTL into our device architecture was thereby deemed a success which improves both the FF and V_{oc} of the device.

Todorov et al. propose that their improved device performance from ageing stems from a change in the properties of their MoO_x due to air exposure. Our champion device was therefore measured over time to investigate whether this effect could be benefiting our devices as well. The results of ageing of the champion device can be seen in Figure 4.8.

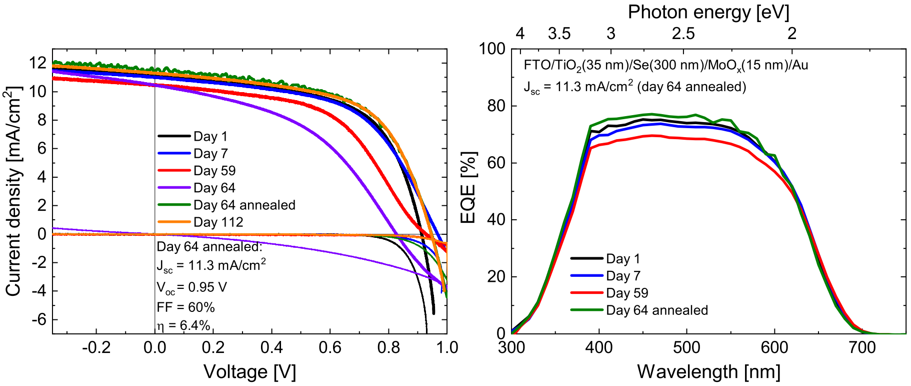

Figure 4.8: The champion FTO/TiO_2(35 nm)/Te(1 nm)/Se(300 nm)/MoO_x(15 nm)/Au device measured as a function of time. After 64 days the device is measured before and after annealing again at 190 °C for 4 minutes.

Over time all the device performance properties decrease. A clear "rollover" effect becomes apparent after day 59 which distorts the J-V curve to an S-shape resulting in a significant reduction in the FF. This rollover effect has previously been reported for non-optimal solar cells when one or more current extraction barriers are present under illumination which results in a charge transport bottleneck.[158] For the single-junction devices fabricated during this project, this effect was only observed for devices made with a TiO_2 ETL. It could be attributed to the change in oxygen content which could change both the doping level (and thereby also the fermi level position) and/or the conduction band position, which could introduce a non-ideal Schottky barrier in the TiO_2/Se p-n junction interface. A Schottky barrier would lead to a voltage-dependent current blocking behaviour that could potentially explain the S-curve behaviour. Alternatively the TiO_2 may change its surface adhesion capabilities of the Se over time which could cause some delamination that would be a possible explanation for current blocking. This could also potentially explain why the device performance was not only retained but also improved after annealing again on day 64 obtaining a new record PCE of 6.4%! During annealing the Se may become mobile enough to restructure and eliminate such a delamination. After day 112 the device retained a similar performance. Unlike the device performance reported by Todorov et al. our devices do not seem to achieve higher PCE performance from long-term air exposure.

Similarly to the reports of Todorov et al. we observe both an illumination-dependent shunt conductance, G_{sh}, as well as a crossover effect of the light and dark curves.[68] The change in shunt conductance with illumination indicates voltage-dependent collection efficiency problems that should be attempted to be solved in future work.[159] The crossover effect is caused by the change in diode properties under illumination preventing the curve to superpose the dark curve during illumination. The hypothesised explanation is that photogenerated carriers are trapped in interfaces creating a dipole moment that induces an interface transport barrier. This effect has also been reported to occur for the CdS/CZTSe interface which is attributed to negatively charged acceptor-like defect states in the CdS that causes an increase in the conduction band position which blocks the current.[160] This effect can temporarily be eliminated by light soaking which neutralises the defects through the photogeneration of holes.

Further observed non-ideal diode behaviours include a current-voltage scan direction hysteresis dependence as well as transient light degradation (see Figure 4.9). The hysteresis effect is not common in chalcogenide absorbers but has also been reported by Todorov et al. and has still not been fully investigated.[68] Hysteresis is however commonly observed in perovskite photovoltaics which originates from ionic migration, charge trapping and ferroelectric effects.[161]

All JV-curves of this work were made using reverse scans to better compare with both literature and our own results. Light degradation of the open-circuit voltage is observed to be around $\Delta V_{\mathrm{oc}} \approx 0.3$ V per minute that is measured independently of the scan direction. However, it has been shown that the device can retain its initial performance through annealing again as seen in Figure 4.8.

The influence of the MoO_x thickness was investigated where the thickness was varied between 15 nm (cells 1,4 and 7), 30 nm (cells 3, 6 and 9) and 45 nm (cells 2 and 5) (see Figure 4.10).

No apparent trend in the change of performance is observed when varying the thickness of the MoO_x. Todorov et al. reports an optimal MoO_x thickness of $\approx$ 20 nm.[68] This indicates that the properties of our MoO_x are less detrimental to the performance of our devices.

Brief attempts were made to include Spiro-MeOTAD instead of MoO_x as a HTL via. spin-coating. However, due to a very limited initial success and no theoretical benefit to this replacement, no further experiments were attempted.

Other computationally screened HTL were also briefly attempted without any ini-

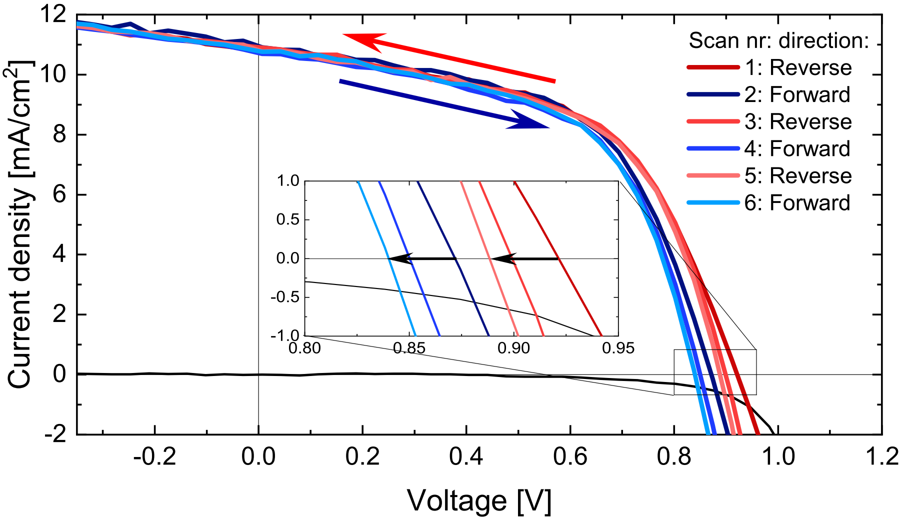

Figure 4.9: JV hysteresis and light degradation of a FTO/TiO$_2$/Se/MoO$_x$/Au device. A degradation of $\Delta V_{oc} \approx 0.3$ V per minute is measured independently of the scan direction.

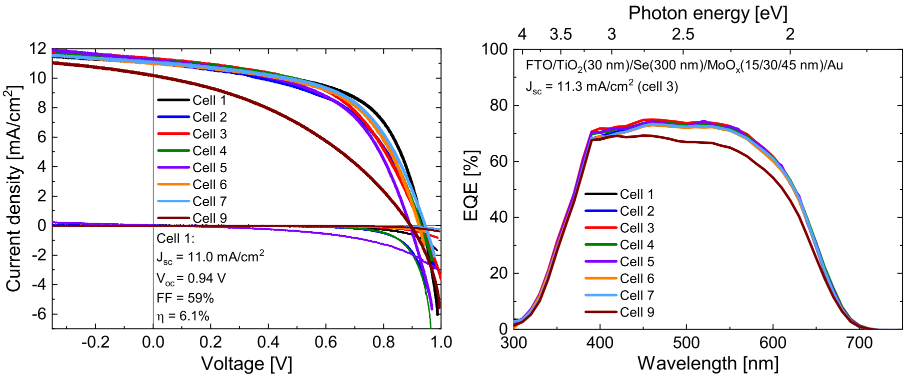

Figure 4.10: FTO/TiO$_2$(30 nm)/Te(1 nm)/Se(300 nm)/MoO$_x$(15/30/45 nm)/Au.

tial success. The PhD student Hadeel Moustafa from the Computational Atomic Scale Materials Design (CAMD) group at DTU Physics attempted to screen for potential HTL-candidates that would be suitable in conjunction with trigonal Se. The valence band offsets with respect to Se of BaO and YN were predicted to be 0 eV and 0.2 eV, respectively. Fabricating thin films of these two materials were attempted through reactive sputtering of metallic Y and Ba targets. Both metals are unstable under ambient conditions as they oxidise heavily. For Y this resulted in unsuccessful thin film formation due to the formation of stable yttria

Y_2O_3 which was confirmed through EDX-S analysis. BaO was not fully oxidised during the reactive sputtering which caused rapid oxidation after exposing the thin film to air causing large deformation in the film. Further investigations into the successful synthesises of BaO as a HTL are encouraged.

4.1.3 Replacing TiO_2 as an Electron-Transport Layer

Overall TiO_2 continued to give us massive issues with batch-to-batch reproducibility and unfortunately this meant that no greater PCE improvement was achieved during my PhD project. With poor reproducibility it was very difficult to statistically prove whether variations in the fabrication process resulted in any improvements to performance. Furthermore, the high temperature required for the 400 °C TiO_2 deposition prevented the possible inversion of the device since the melting point of Se is $\approx$ 220 °C.[67] This is a detrimental issue for the Si-Se monolithic tandem fabrication which requires the Si bottom-cell to be used as a substrate. Having the p-n junction situated at the opposite side of the illumination direction is expected to limit device performance and therefore finding a suitable ETL that can be deposited directly on Se is crucial.

For this reason other ETL were investigated as replacements for the TiO_2 that could be deposited at room temperature. A few suitable ETL replacements were attempted such as ZnO, ZnMgO, CdS and $SrTiO_3$.[112] ZnO and $Zn_{0.9}Mg_{0.1}O$ had already been successfully proven by Todorov et al. to increase device performance.[68] Including CdS was attempted by Rasmus Nielsen via chemical bath deposition during his Master project. Even though CdS has a non-ideal low bandgap of $\approx$2.4 eV, it was hoped that the CdS would allow for both inverting the device structure as well as protect the Se absorber from sputter damage.[96] Ultimately, it was possible to implement CdS but only when fabricated on FTO without inverting the architecture. For the inversion of the device it was discovered that the MoO_x was etched during the chemical bath deposition of the CdS which caused a delamination of the Se. The JV of the champion FTO/CdS/Se/MoO_x/Au device has been included in Figure 4.25.
$SrTiO_3$ was also briefly attempted by RF sputtering from a stoichiometric target. A batch was made with 45 nm $SrTiO_3$ but resulted in near zero PCE due to the deposited $SrTiO_3$ being highly insulating even without added oxygen during the sputtering giving a series resistance in the MΩ range. Further investigations into potentially combining a very thin $SrTiO_3$ with another ETL are yet to be conducted.

ZnO and ZnMgO were successfully implemented instead of TiO_2. No successfully inverted devices have yet been made and this still remains a high priority for future investigations.

ZnO as an ETL

ZnO was RF sputtered at room temperature using a stoichiometric ceramic ZnO target at a power of 40 W in a 5 mTorr inert Ar atmosphere. The ZnO was deposited without oxygen and is therefore expected to be oxygen deficient. The thickness of the MoO_x was again varied from 15 nm (cell 1, 4 and 7) and 30 nm (cell 3 and 6) to fully confirm whether it influenced the device performance or not. The performance results of this batch with 55 nm ZnO can be seen in Figure 4.11.

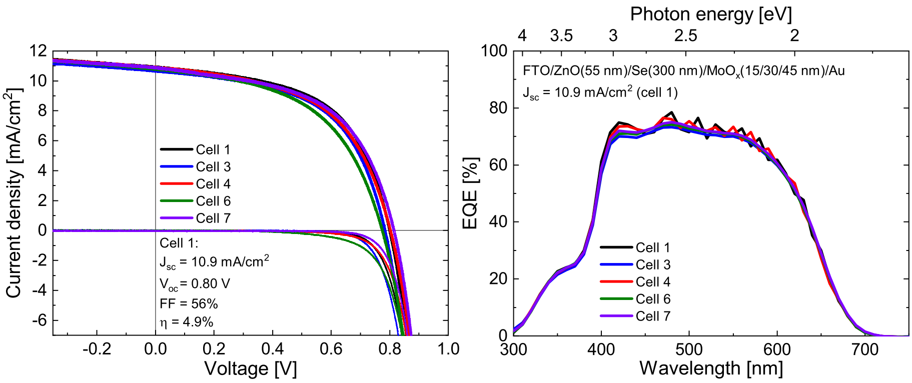

Figure 4.11: FTO/ZnO(55 nm)/Te(1 nm)/Se(300 nm)/MoO_x(15/30 nm)/Au.

The reproducibility of the batch was by far better than all previous batches made with TiO_2. This signifies the importance of using a stoichiometric target compared to a metallic target with reactive sputtering. The V_{oc} is $\approx$ 100 mV lower than the champion TiO_2 devices which indicates a greater conduction offset. The thickness of the MoO_x was yet again shown not to significantly influence the device performance. Some parasitic absorption from the ZnO ($E_g = 3.2$ eV) is clearly observed from the EQE where a short-wavelength shoulder is observed which limits the J_{sc} of these devices slightly. Notably no crossover of the dark and light curve is observed for these cells which indicates that the ZnO/Se interface is more pristine in which the photogenerated carriers do not induce a transport barrier. This may also be related to the mobility of the ZnO which is greater than for TiO_2. However, the worse band alignment of the conduction band with respect to Se results in a lower V_{oc}. Lastly it should be noted that no rollover effects were observed during aging experiments of these devices.

The cross-section of cell 7 (see Figure 4.12) shows large homogeneity and conformity of the thin film layers. The slight delamination of the Se from the ZnO is expected to be caused by the physical cracking of the device required for this cross-section image.

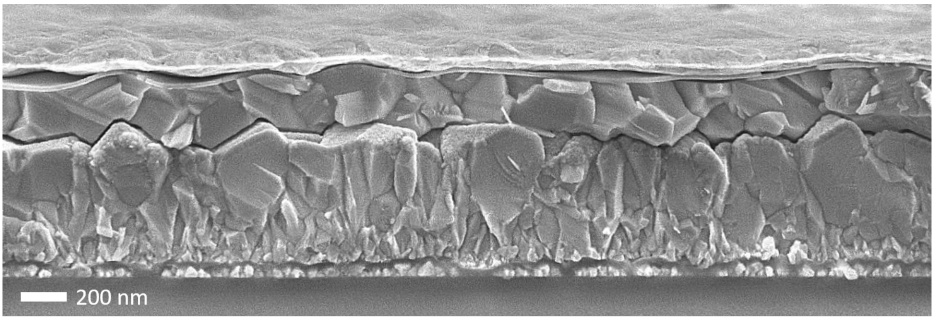

Figure 4.12: SEM cross-section of FTO/ZnO(55 nm)/Se(300 nm)/MoO_x(15 nm)/Au. SEM image taken by Rasmus Nielsen.

ZnMgO as an ETL

Even though ZnO provided significant reproducibility to our device fabrication the reduced V_{oc} was not optimal. Knowing that Todorov et al. had obtained 100 mV V_{oc} improvement by replacing TiO_2 with 60-85 nm ZnO/MgO RF co-sputtered $Zn_{0.9}Mg_{0.1}O$, we decided to buy a $Zn_{0.85}Mg_{0.15}O$ (99.95% purity) ceramic target from AJA International, which was the single target with the closest stoichiometric match we could find. We chose to go for a single ZnMgO target instead of also co-sputtering ZnO and MgO targets, as it was expected that tuning the right conditions for proper band alignment could be problematic. Todorov et al. report a large gradiant in both the bandgap (3.3-3.7 eV) and measured thickness (39-85 nm) of the deposited ZnMgO.[68] The fact that their reported champion device and batch had small active areas of only 0.023 cm^2 illustrates this potential issue. For comparison, our devices typically had contact areas of $\approx$ 0.4-0.5 cm^2.

The effect on the device performance by including the ZnMgO as an ETL was optimised mainly in terms of the thickness and oxygen flow. At this point in time Rasmus Nielsen had conducted an annealing study showing that the crystal Se grain size increases for 200 °C annealing compared to 190 °C. Therefore 200 °C annealing was performed for the Se crystallisation step of the fabrication for most device batches with ZnMgO.

The device performance and batch reproducibility was improved by adding some oxygen during deposition (1/30 SCCM O_2/Ar corresponding to 3.33% O_2) at 5 mTorr and room temperature. An example of such a batch can be seen in Figure 4.13. For this particular batch the Te thickness was altered between 0.5 nm (cells 1, 3 and 4) and 1 nm (cells 5, 6 and 8) to investigate the potential benefit of reducing the Te thickness. No obvious improvements were gained from this.

Even though the V_{oc} was still expected to be improved, obtaining a PCE of >5% for all devices of a batch was a great achievement that suddenly opened

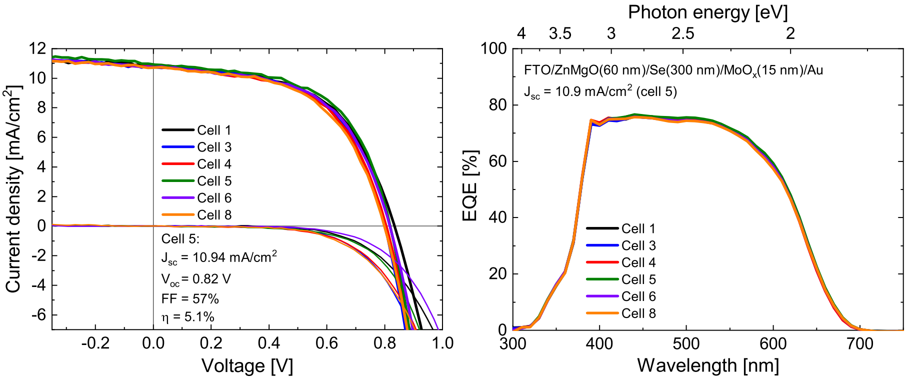

Figure 4.13: Reproducible batch of FTO/ZnMgO(60 nm)/Te(0.5-1 nm)/Se(300 nm)/MoO$_x$(15 nm)/Au with 3.33% O_2/Ar during ZnMgO deposition. The Te thickness was varied from 0.5-1 nm.

up the opportunity to further investigate the influence of certain parameters of the fabrication. This was especially an important milestone towards the tandem fabrication. The cross-section SEM image of cell 5 can be seen in Figure 4.14.

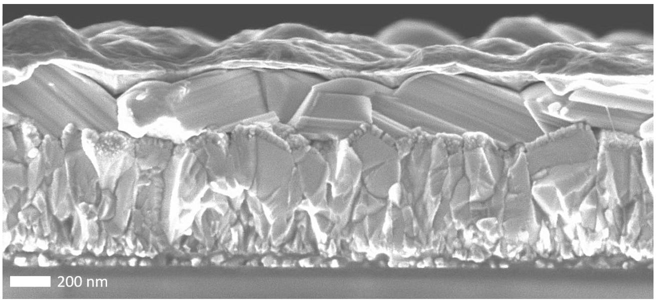

Figure 4.14: SEM cross-section of FTO/ZnMgO(60 nm)/Se(300 nm)/MoO$_x$(15 nm)/Au. SEM image taken by Rasmus Nielsen.

Knowing that decreasing the Te thickness had no major impact on performance, a batch was made to investigate the detrimental effects of increasing the Te thickness. This had already been reported to occur at 5 nm Te by Hadar et al.[71] where a significant reduction in especially the V_{oc} is expected. A batch was made where the Te thickness was increased from 1-5 nm (see Figure 4.15).

As expected the V_{oc} is reduced by around 100 mV by increasing the Te thickness. Further increasing the Te thickness is expected to further increase the Te/Se ratio which should further decrease the V_{oc}, but also increase the J_{sc} since the bandgap of the $\mathrm{Se}_{1-x}\mathrm{Te}_x$ alloy drops down towards the bandgap of 0.3 eV for Te.[66]

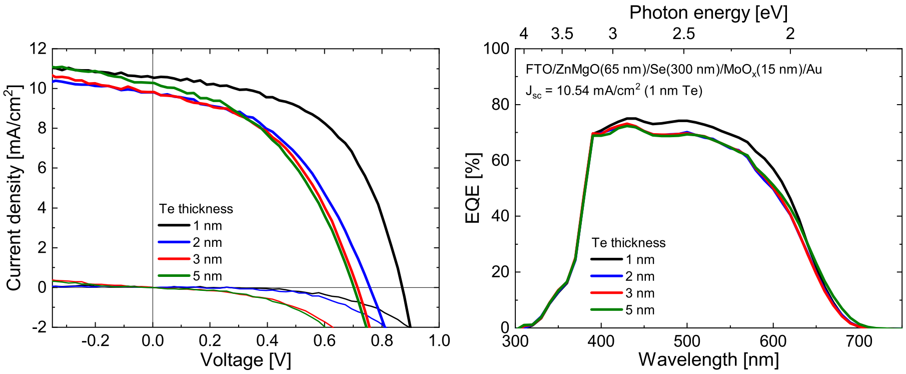

Figure 4.15: FTO/ZnMgO(65 nm)/Te(1-5 nm)/Se(300 nm)/MoO$_x$(15 nm)/Au.

Even though great reproducibility of some batches was demonstrated, the batch-to-batch reproducibility could vary tremendously. An illustration of this problem is shown in Figure 4.16 where the device performance is shown for the best cells from different batches with varying oxygen flows.

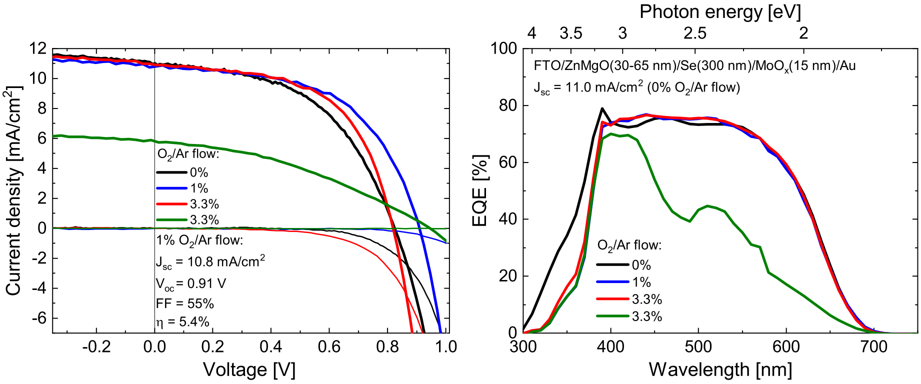

Figure 4.16: FTO/ZnMgO(30-65 nm)/Te(1 nm)/Se(300 nm)/MoO$_x$(15 nm)/Au from different batches with varying oxygen flows during the ZnMgO deposition (0%, 1% and 3.33% corresponding to 0/30, 0.3/30 and 1/30 SCCM O_2/Ar flows).

It was discovered that by reducing the oxygen flow from 3.33% to 1%, greater open-circuit voltages >900 mV and batch-to-batch reproducibility could be obtained. The reason for the poorer JV and EQE performance of the last 3.33% O_2/Ar flow cell is not fully understood. It is believed that the actual oxygen content of the ZnMgO may be more vulnerable to reproducibility issues for higher oxygen flows. If the ZnMgO becomes too oxidised it is expected that it will obtain a more insulating behaviour which will likely introduce a larger series resistance (which is also observed from the JV curve). Furthermore the oxygen deficiency is related to the intrinsic doping density of the ZnMgO and it is expected that the more oxidised the ZnMgO becomes, the less intrinsic n-type doping it has. With less doping the depletion region width is expected to become smaller which should influence the long-wavelength collection of the EQE (which is also observed from the EQE). These effects were observed only for the ZnMgO deposited with higher oxygen flows and illustrates our issues with reproducing similar oxygen conditions during sputter deposition over time. It was also observed that for some of the 3.33% O_2/Ar flow devices that behaved poorly, their cross-sectional SEM images showed pinholes. Furthermore, the tandem devices that were attempted with ZnMgO made with a high oxygen flow showed terrible adhesion of Se and therefore had macroscopic pinholes visible to the eye. It is most likely that the ZnMgO alters its surface energy with increased oxygen content, which affects both the Te deposition and subsequent Se growth. Further investigations into understanding this phenomenon could be beneficial.

Regardless, fabrication of ZnMgO with a flow of 1% O_2/Ar became a standard process and the thickness was settled around $\approx 60 - 65$ nm. No major improvements were obtained by reducing the ZnMgO thickness and due to many long-term reproducibility issues, it was decided that a thicker ETL was more likely to provide greater batch-to-batch reproducibility.
The annealing temperature for the crystallisation of Se was reevaluated and a batch of devices were made with 190 °C annealing (cells 2, 4 and 7) and 200 °C annealing (cells 3, 6 and 8) (see Figure 4.17).

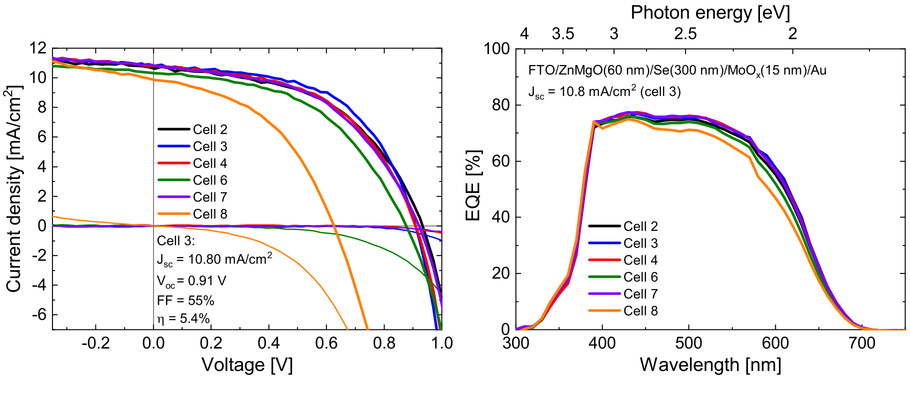

Figure 4.17: FTO/ZnMgO(60 nm)/Te(1 nm)/Se(300 nm)/MoO$_x$(25 nm)/Au with a Se crystallisation step of 190 °C annealing for cells 2, 4 and 7 and 200 °C annealing for cells 3, 6 and 8.

For some reason the cells made with the higher 200 °C annealing temperature resulted in both the best (cell 3) and the worst performing devices (cells 6 and 8) whereas 190 °C resulted in devices with similar performance. It is still uncertain why such a large variation is observed when the batch previously shown in Fig-

ure 4.13 was highly reproducible for 200 °C annealing. Though it is unlikely, the actual annealing temperature and/or the actual Se thickness may have changed over time. If the Se is thinner than expected then some reevaporation during annealing may result in either pinholes or a thinner Se thickness which could explain the larger deviation in performance for higher annealing temperatures. Potentially the surface of the ZnMgO may also have changed resulting in a variation in the Se growth similarly as observed for the variation in performance affected by the oxygen flow.
Regardless, cell 3 was the champion FTO/ZnMgO/Se/MoO_x/Au device of this project (and was also seen in Figure 4.16) and along with the cells annealed at 190 °C they all achieved >5% PCE with a V_{oc} greater than >900 mV. This provided us with a great baseline performance for further investigations of both bifacial and tandem devices. Here an annealing temperature of 190 °C was chosen to maintain reproducibility.

Overall including ZnMgO as an ETL instead of TiO_2 was deemed a success. Even though the champion PCE of 6.4% was not surpassed by the use of ZnMgO, the improvement of reproducibility within batches as well as from batch-to-batch of >5% PCE allowed for further investigations and understanding of the influence of some of the many fabrication parameters. Comparing these results with those reported by Todorov et al., their largest devices with active areas of 0.125 cm^2 (ours being 0.4-0.5 cm^2) achieved very similar device performances of $\approx$ 5% PCE with a V_{oc} of $\approx$ 925 mV and similar or lower J_{sc} and FF than our devices (found in their supplementary information).[68]

4.2 The Bifacial Selenium Single-Junction Solar Cell

Before the fabrication of a Se-Si tandem solar cell can be achieved, the top-cell needs to be semi-transparent such that the non-absorbed light below the bandgap of Se may transmit through to the Si bottom-cell. This requires the replacement of the Au metal contact with a transparent contact such as e.g. ITO. A solar cell which is semi-transparent on both sides is called a bifacial solar cell.

Prior to the ITO depositions of this work, a bachelor project by Magnus Strandgaard aimed to optimise the processing parameters of sputter deposited ITO thin films.[162] This work led to the fabrication of ITO thin films with resistivities of $\rho \approx 10^{-4}$ $\Omega\cdot$cm and transmissions over 80% (E_g = 3.7 eV) in the visible range. This was obtained for a pressure of 3-5 mTorr under a flow of 40/0.3 SCCM Ar/O_2 with a substrate temperature of 300 °C. The project also concluded that a substrate temperature of at least 100 °C was required to achieve low resistivities, which was proposed to be caused by the "activation of Sn-dopants".[162]

These processing parameters were replicated for the fabrication of the bifacial

Se-based solar cells. However, the low melting point of Se sets an upper thermal limit for the possible substrate temperature of the ITO deposition. To avoid the reevaporation of Se during ITO deposition, a substrate temperature of 100 °C was chosen. Attempts of varying the oxygen flow from 0-1 SCCM were made in collaboration with Rasmus Nielsen during his Master project [96], which resulted in an optimum resistivity of around $\rho \approx 4 \times 10^{-3}$ Ω·cm for a similar flow of 40/0.3 SCCM Ar/O_2 during deposition. The resistivity of the ITO thin films were an order of magnitude lower than those reported in the previous work. The transmission of these 200-300 nm ITO thin films were as expected with transmissions of $> 80\%$ in the visible range with $E_g = 3.7$ eV (see Figure S8 in Appendix B). Though the resistivity was less than optimal, attempts were still made to fabricate Se-based bifacial solar cells. These investigations led to the work which is shown in Paper I (see Appendix B). The main points will be conveyed in this section, but more details are available there.

A champion bifacial solar cell with a PCE of 5.2% from front-side illumination (through the n-type contact) and 2.7% PCE from back-side illumination (through the p-type contact) was achieved. The performance from front-side illumination is similar to the performance of devices with metal Au contacts. This indicates that the resistivity of the ITO is sufficiently low for a thickness of 200-300 nm and a contact area of ≈ 0.4 cm^2. The lower efficiency from back-side illumination is attributed to low carrier diffusion lengths and lifetimes in Se. This mandates that the carrier transport properties of Se are either improved or that the top-cell architecture is inverted for tandem fabrication. The bifacial performance was investigated as a function of the Se thickness. SCAPS (Solar Cell Capacitance Simulator) simulations were performed to compare and verify the performance trends from both illumination sides. This culminated in an estimated Se thickness optimum of around 300-500 nm for both illumination sides. A further discussion regarding the causes for this optimum will follow in Chapter 5.

Unsuccessful attempts were made to invert the bifacial architecture which resulted in a poor maximum PCE of only 0.5% and 0.1% from illumination of the ITO and FTO sides, respectively. The main complication of inverting the device architecture is expected to be caused by the damaging effects of sputter deposition directly into the p-n junction of the device. Efforts should be made to reduce the deposition damage onto Se. Some attempts were made by Rasmus Nielsen to introduce CdS as a protective buffer layer which purpose is to act as a diffusion barrier, shunt protection layer, sputter damage protection layer as well as functioning as an electron transport layer. However, the low bandgap of 2.4 eV will result in parasitic absorption if placed in front of the Se absorber. Attempts at inverting the structure with CdS as a protection layer were unfruitful, but a champion device of FTO/CdS/Se/MoO_x/Au obtained a PCE of 1.14% (JV included in Figure 4.25). The results of this work is under preparation in Paper II.

4.3 The Selenium-Silicon Tandem

The successful fabrication of well-performing bifacial Se devices opened up the possibility of using Se as a top-cell in a tandem device. The thin film photovoltaics group at DTU Risø study the kesterite absorber CZTS and have successfully reported a monolithically grown CZTS/Si tandem with a PCE of 3.9%.[163] Fortunately, it was possible to make a collaboration with the PhD student Alireza Hajijafarassar who was responsible for fabricating the Si bottom-cells. These Si bottom-cells were made as double-sided Tunnel Oxide Passivated Contact (TOPCon) structures. For the tandem fabrication of a CZTS/Si device, it is essential to protect the bottom-cell from a high temperature ($> 500\,°C$) sulfurisation step during the CZTS synthesis. Therefore, a thin layer of TiN (<25 nm) had been used as both a diffusion barrier and recombination layer.[164] For the fabrication of a monolithically grown Se-Si tandem, this TiN diffusion barrier may prove to be unnecessary since the highest processing temperature of the Se top-cell is $\approx$ 200 °C. Nevertheless, since the initial bottom-cells that we received included the TiN layer, it allowed us to attempt a Se top-cell with a TiO_2 ETL layer that is sputter deposited at 400 °C.

4.3.1 Fabrication Process

Monolithically grown Se-Si tandem devices were attempted with both TiO_2 and ZnMgO as the top-cell ETL on TOPCon Si bottom-cells with TiN. The bottom-cells were received from Alireza Hajijafarassar as wafers with a 5 nm TiN on p+Poly-Si on the frontside and SiN_x on n+Poly-Si on the backside. The SiN_x is a sacrificial layer whose main purpose is to facilitate a hydrogenation process that passivates the Poly-Si. This layer was kept on the bottom-cells until the final step of the tandem fabrication process where it was removed prior to the Ag back side contact deposition. The wafers were cut into 14x16 mm device sizes similar to the size used for the Se single-junction fabrication. Here a laser micromachining tool with a 30W 1064 nm time bandwidth (TBW) picosecond laser was used to cut through the wafers from the backside (the surface with SiN/n+ PolySi) in order to minimise damage to the p-n junction frontside. The layers of the Se top-cell were then deposited on the TiN and annealed in the same manner as explained in the previous sections of this chapter. Finally, the backside SiN_x was removed by etching with 2% diluted hydrogen fluoride (HF) which was carefully applied as droplets to the surface. It was especially this step that introduced a large variation in device performance. The SiN_x should ideally all be removed without accidentally applying HF to the sides of the bottom-cell or the front of the top-cell. Ag was subsequently sputter deposited onto the n+ Poly-Si. A schematic of the monolithically integrated three-terminal (MI-3T) Se-Si tandem device structure can be seen in Figure 4.18.

As can be seen from the schematic, it is possible to contact both the top-cell and bottom-cell independently making it a three-terminal (3T) tandem architecture.

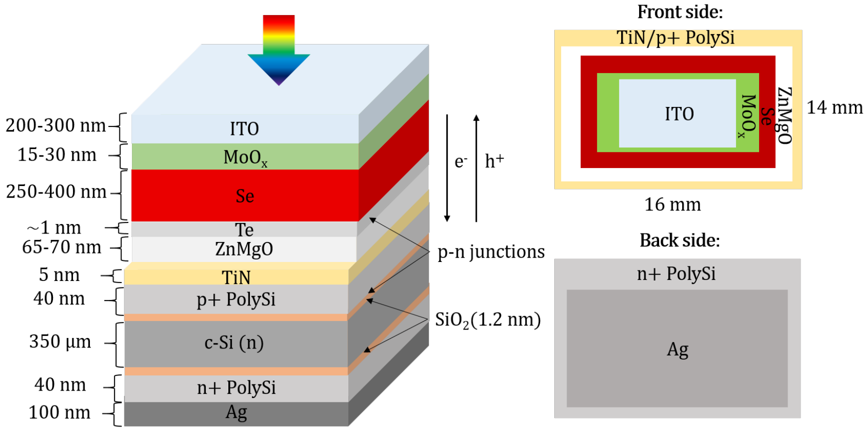

Figure 4.18: Schematic of the MI-3T tandem Se-Si solar cell architecture: Ag(100 nm)/n+ polySi(40 nm)/SiO$_2$(1.2 nm)/c-Si(n)(350 µm)/SiO$_2$(1.2 nm)/p+ polySi(40 nm)/TiN(5 nm)/ZnMgO(65-70 nm)/Te(1 nm)/Se(250-400 nm)/MoO$_x$(15-30 nm)/Au.

However, the resistivity of the recombination layer greatly influences the lateral transport of carriers. For a highly resistive 5 nm TiN this effect is detrimental inhibiting independent JV measurements of the subcells. However, the lateral transport in the Si bottom-cell is large enough to measure the EQE under short-circuit conditions. Thereby the EQE of the bottom- and top-cell was measured in the following manner.

The Si bottom-cell was contacted directly on the exposed TiN at the top and on the Ag at the bottom. The monochromatic light beam is then filtered through the entire Se top-cell to accurately measure the actual Si bottom-cell EQE response within the tandem. The EQE of the Se top-cell was measured by contacting the entire tandem stack (i.e. the ITO at the top and the Ag at the bottom) while applying a -0.5 V bias flooding the tandem (or more specifically the Si bottom-cell) with light through a +900 nm filter.

The TiN was later attempted replaced with a 40 nm ITO recombination layer that also allowed for the independent JV and EQE measurements of both the subcells.

A SEM cross-section was made on one of the initial Se-Si tandems made with TiN and TiO$_2$. This image can be seen in Figure 4.19.

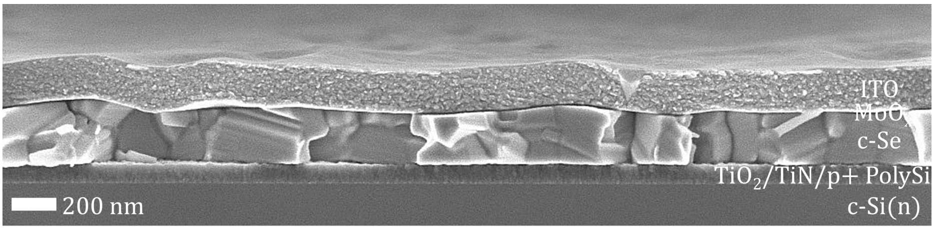

Figure 4.19: SEM cross-section of Se-Si tandem. Seen in image from bottom and up: c-Si(n)/p+ polySi(40 nm)/TiN(5 nm)/TiO$_2$(50 nm)/Se(250 nm)/MoO$_x$(15 nm)/ITO(200 nm). SEM image taken by Rasmus Nielsen.

4.3.2 TiN as the Recombination Layer

TiO$_2$ as an ETL

Initial attempts of making Se-Si tandems involved the use of TiO$_2$ as an ETL in the Se top-cell. A Si bottom-cell was measured in parallel as a reference in order to compare with the performance of the tandems. 200 nm ITO was sputter deposited onto both sides of the device. The SiN$_x$ of the bottom-cell was similarly HF etched from the backside. At the time Ag sputter deposition was not possible and therefore silver paste from Sigma Aldrich was applied to the n+ polysilicon of the tandems and to the backside ITO of the Si bottom-cell and left to dry overnight. These initial crude attempts of fabricating the Se-Si tandem resulted in poor reproducibility. The performance results of the best performing Se-Si tandem along with the Si bottom-cell can be seen in Figure 4.20. Here the current limiting subcell is the Se top-cell with a J_{sc} of 6.6 mA/cm^2.

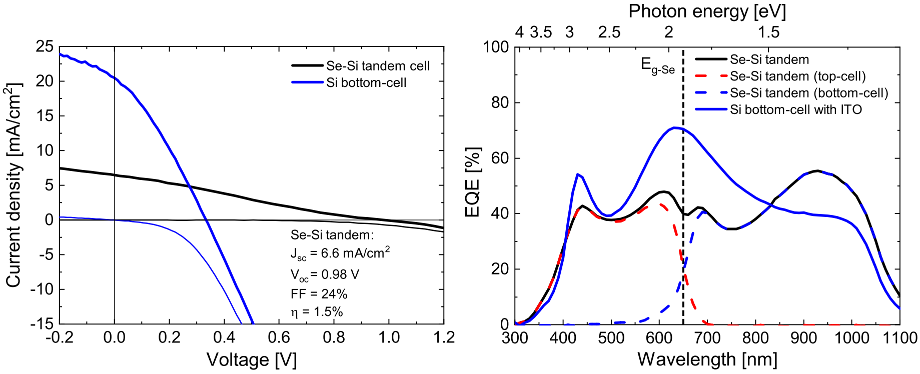

Figure 4.20: The champion Se-Si tandem with TiN and a top-cell configuration of TiO$_2$(50 nm)/Te(1 nm)/Se(200 nm)/MoO$_x$(25 nm)/ITO(200 nm). A Si bottom-cell with ITO and Ag was measured for reference.

The JV of both the tandem and Si bottom-cell show poor performance. Particularly the FF and V_{oc} of both are expected to be greater. The efficiencies of the bottom-cells should be around $\eta \approx 14-15\%$ with an open-circuit voltage of $V_{\mathrm{oc}} \approx 0.6$ V. The poor initial attempts of cutting the bottom-cell wafer, removing the SiN and contacting the Si bottom-cell resulted in a mere $\eta = 2.0\%$. However, it must be noted that the V_{oc} still exceeds that of all prior single-junction devices. Furthermore, the EQE of both the top- and bottom-cells looks promising with a Se top-cell EQE similar to the champion bifacial Se single-junction devices illuminated similarly from the ITO side. This again signifies the importance of inverting the device structure. The fringes in the EQE spectra match those seen for the transmission measurements of ≈ 200 nm ITO (see Figure S8 in Appendix B).

As seen from Figure 4.18, the active areas of the subcells are not equal. Due to a pyramid structure of the top-cell, its active area is only around 20% of the total device area (≈ 0.4 cm^2 compared to 2.24 cm^2). This has for the single-junction devices not been an issue since the lateral transport of the Se absorber is negligible. However, this is not the case for the Si bottom-cell. If carriers are generated outside the ITO area they have to travel far in the lateral direction which should result in a large series resistance and low FF of the device. This could be prevented by simply shadowing the area of the device without ITO during illumination measurements, but was unfortunately not a possibility with our equipment. Instead it was expected that by cleaving the sides of the sample, such that the total device area became equal to the active ITO area (≈ 0.4 cm^2), this effect could be prevented as well as potentially removing induced shunts at the edges from HF etching. Unfortunately, attempts at cracking the samples only resulted in similar or worse device performance indicating that the device limitations stem from some actual thin film layer properties of the device.

Relating the tandem device performance with the CZTS/Si tandem work by Alireza Hajijafarassar and Filipe Mesquita Alves Martinho, a similar current blocking mechanic seems to be present in the device.[163,164] Their work shows that if the TiN becomes oxidised, $\mathrm{Ti(O}_x\mathrm{N}_y)$, the Si obtains an ideal protection from diffusion of i.e. Cu at higher temperatures. However, the resistivity changes from 5×10^{-3} Ω·cm to 40 Ω·cm, which results in a large series resistance in the centre of the device. TiO_2 requires a significant oxygen flow at 400 °C during sputtering directly on the TiN. This process is in hindsight likely to oxidise the TiN. Furthermore, the TiO_2 had given us problems with the reproducibility of the single-junction fabrication and was therefore exchanged with ZnMgO (same architecture as depicted in Figure 4.18).

ZnMgO as an ETL

Exchanging the TiO_2 with ZnMgO resulted in reproducible tandem performance. The JV and EQE results of the champion batch can be seen in Figure 4.21.

The two best devices were cell 1 and cell 2 (the device performance of both can found in Table 4.2) with PCEs of 2.2% and 2.1%. A champion V_{oc} of 1.49 V is ob-

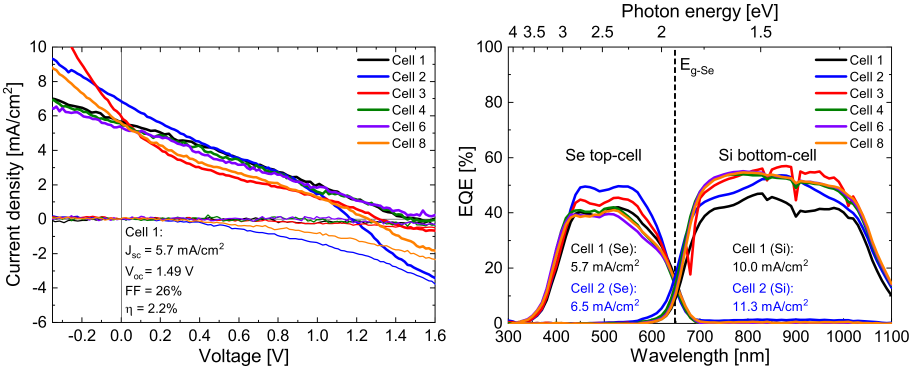

Figure 4.21: The champion tandem Se-Si batch with TiN as a recombination layer and ZnMgO as the top-cell ETL.

tained which matches an expected combined voltage of two well performing subcells placed in series connection, e.g. $V_{\mathrm{oc-tandem}} = V_{\mathrm{oc-bottom-cell}} + V_{\mathrm{oc-top-cell}} \approx 0.6\,\mathrm{V} + 0.9\,\mathrm{V} = 1.5$ V. Large parasitic transport losses are still observed during illumination indicated by low fill factors and roll-over effects and a large series resistance. Even though an increase in V_{oc} as well as reproducibility were obtained by including ZnMgO as an ETL, a large current barrier is still present in the device. This becomes especially apparent when comparing the tandem device performance with the device performance of individual top-cell and bottom-cell devices (see Figure 4.22). Here another Si bottom-cell is contacted with ITO and Ag in a similar manner as the tandem for comparison. The performance of the champion single-junction bifacial Se device, illuminated from the ITO side similarly as for the tandem, is also included.

The Si bottom-cell was in this case more efficiently contacted with a V_{oc} of 0.62 V yet a FF of only 55% indicating lateral transport losses from the non-optimal ITO. With a potential FF of ≈ 55% of the bottom-cell and ≈ 41% for the top-cell it become curious that the FF of the tandem remains only at ≈ 25%.
Still expecting the TiN to be the main culprit, attempts were made to Ar sputter away the potential native oxide surface of the TiN prior to the ZnMgO deposition as well as delay the oxygen flow during deposition for the first ≈ 3.5 nm out of the total 65 nm of ZnMgO to prevent oxidation of the TiN. Unfortunately, these attempts only resulted in worse device performance. An explanation for this could be due to a difference in the doping of the ZnMgO which may further cause a barrier at the recombination interface or alter the top-cell carrier separating junction and thereby decrease its collection efficiency.

Ultimately, it was decided to exchange the TiN with ITO. As long as the processing temperature of the top-cell does not exceed the needed 200 °C for the annealing step, the Si bottom-cell should not need the diffusion barrier protec-

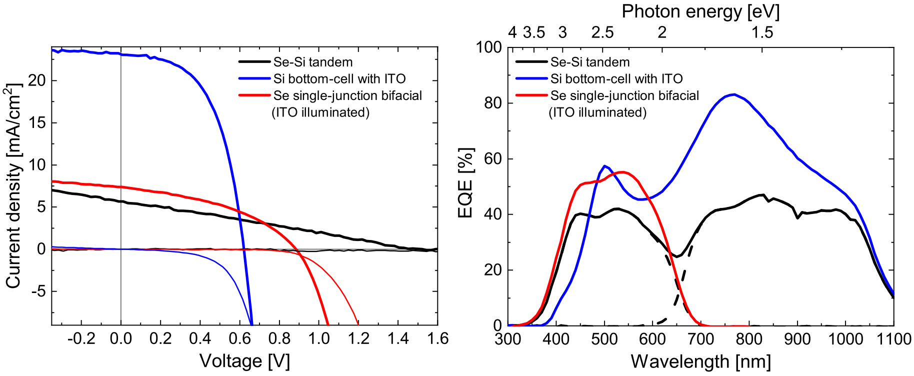

Figure 4.22: The champion tandem Se-Si device in comparison with the champion bifacial Se single-junction device illuminated from the ITO side as well as a Si bottom-cell contacted with ITO and Ag.

tion that the TiN provides. Ideally this should not only remove the current barrier causing parasitic transport losses but if the ITO has a resistivity low enough to allow for efficient lateral transport, then it should also allow for 3T JV measurements of the tandem device.

4.3.3 Exchanging the Recombination Layer with ITO

The TiN was replaced by a layer of 40 nm ITO sputter deposited onto the p+ polysilicon. With the increased resistivity of the recombination layer it became possible to independently directly measure both JV and EQE of the two subcells. The measurements of the champion device from this attempt can be seen in Figure 4.23. The top-cell EQE response was measured in a similar manner as for previous tandem cells with flooding of the Si bottom-cell, but in this case it was also possible to measure the EQE by directly contacting the top-cell from the two ITO contacts under short-circuit conditions. Fortunately, the two EQE measurements were near identical.

The performance of these tandems as well as their subcells were highly deteriorated with overall worse performance of all parameters. The performance of the subcells particularly indicate poor lateral transport by the ITO. A few potential issues could be the reason for the overall poor tandem performance and may require further investigations. The ITO may damage the p+ polysilicon during deposition. The ITO may have worse adhesion properties to the ZnMgO causing delamination. The active area of the bottom-cell and top-cell are not equal and may, due to the lack of shadowing during JV measurements, cause significant parasitic transport losses due to low lateral carrier conductivities. The ITO may have poor band alignment with both or either of the p+ PolySi and ZnMgO layers resulting in a Schottky barrier at this interface.

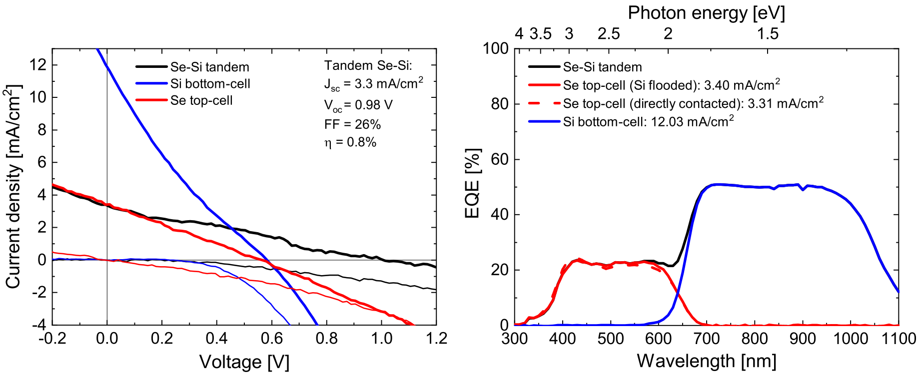

Figure 4.23: The champion tandem Se-Si batch with ITO as a recombination layer and ZnMgO as the top-cell ETL. The lower resistivity of the ITO allowed for 3T JV and EQE measurements in which case both individual subcells could be measured directly independently.

It could be beneficial to try to increase the recombination ITO layer to increase the lateral conductivity to further investigate the top-cell and bottom-cell performance as a function of further alterations to the fabrication process. Nevertheless, for these devices Suns-V_{oc} measurements were possible since no carrier movement is required to measure the open-circuit voltage as a function of illumination intensity. The measurements were made on a similar tandem from the same batch along with its subcells. The resulting JV and pseudo-JV curves are co-plotted in Figure 4.24 for comparison.

The pseudo-JV neglects the effect of parasitic series resistance transport losses. Whether these originate from poor transport material properties or poor band alignments remains unknown. The significant difference between the JV and pseudo-JV curves clearly shows the presence of a large detrimental series resistance which must originate from of one or multiple transport barriers within the device. The origins of this detrimental series resistance must be identified and eliminated before further tandem performance improvements can be achieved. The recombination layer is still suspected to be the major cause of this issue. Investigating the effect of increasing the ITO thickness or improving its resistivity ($\rho \approx 4 \times 10^{-3}$ Ω·cm) is encouraged.

Unfortunately, time was running out for me and my project and therefore I was not able to further optimise any single-junction or tandem device performance. I will therefore for the rest of this thesis focus on identifying and explaining some of the many limitations and potential issues of the Se-based devices with the hope that some of these results, discussions and conclusions may help or inspire further investigations and improvements of the Se-based single-junction and tandem devices.

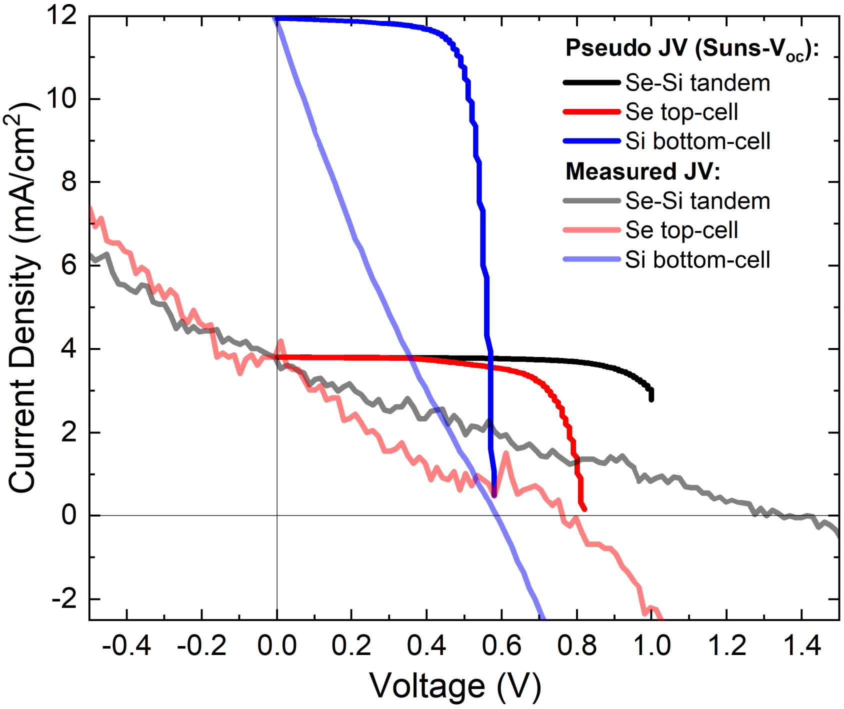

Figure 4.24: JV and pseudo-JV (from Suns-V_{oc} measurements) curves of a tandem Se-Si solar cell with ITO as a recombination layer and ZnMgO as the top-cell ETL. Both the top-cell and bottom-cells were also measured independently for comparison. The true V_{oc} of the tandem measured by Suns-V_{oc} was not obtainable since a voltage greater than 1 V could not be measured.

4.4 The Champion Devices

To conclude this chapter I would like to give an overview of some of the champion devices that were obtained during this project. Some of the champion devices with unique architectures have either not been reported before or have PCEs that are greater than those reported in literature with similar structures. The most significant of these I have tried to bundle together in the same JV plot for comparison (see Figure 4.25). The device performance of these devices along with some with similar architectures can be found in Table 4.2.

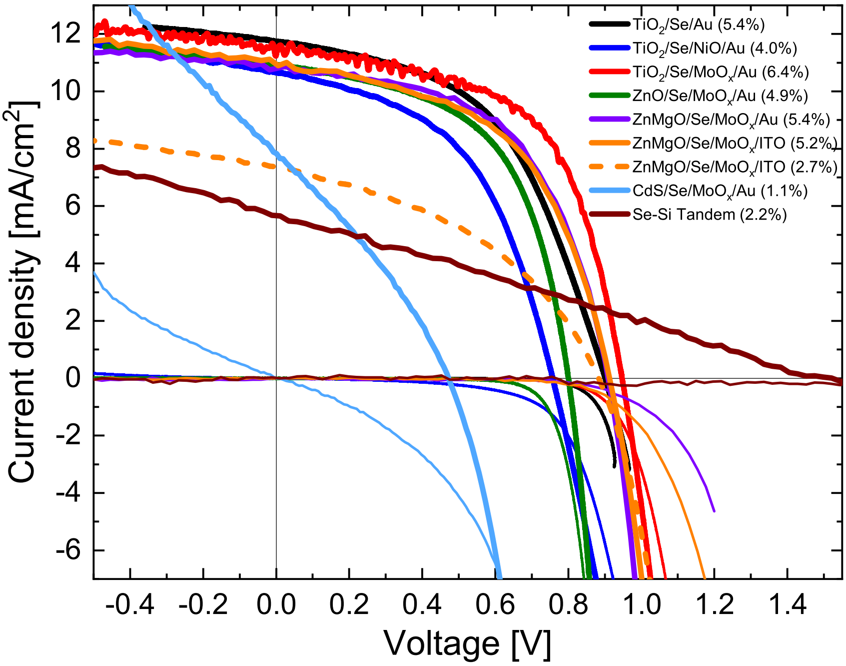

Figure 4.25: JV results of the champion Se-based solar cells of this PhD project. More details regarding the device architectures and performances can be found in Table 4.2.

Table 4.2: Champion Se-based solar cells of this PhD project. The thicknesses of the contacts FTO, Au and Ag used for the devices were all 500 nm, 30 nm and 100 nm respectively. All devices were fabricated with 1 nm Te prior to the Se deposition and have active areas corresponding to the Au/ITO area of about $\approx$ 0.4-0.5 cm^2. For the tandem devices the structure of the Si TOPCon bottom-cell is: n+ polySi(40 nm)/SiO$_2$(1.2 nm)/c-Si(n)(350 µm)/SiO$_2$(1.2 nm)/p+ polySi(40 nm). The values in parentheses are from the ITO/back illumination of the bifacial champion devices. The asterisk (*) denotes the device architectures that have either not been reported before or have a higher PCE than those reported in literature with similar structures (see Table 4.1).

Device architecture	**V$_{oc}$ (V)**	**J$_{sc}$ (mA/cm^2)**	**FF (%)**	**η (%)**
Monofacial Se single-junction:				
*FTO/TiO$_2$(30 nm)/Se(500 nm)/Au	0.90	11.7	51	5.4
FTO/TiO$_2$(30 nm)/Se(500 nm)/Au	0.83	**12.0**	42	4.2
*FTO/TiO$_2$(40 nm)/Se(300 nm)/NiO$_x$(25 nm)/Au	0.76	10.7	50	4.0
*FTO/TiO$_2$(35 nm)/Se(300 nm)/MoO$_x$(15 nm)/Au	**0.95**	11.3	**60**	**6.4**
*FTO/ZnO(55 nm)/Se(300 nm)/MoO$_x$(15 nm)/Au	0.80	10.9	56	4.9
FTO/ZnMgO(60 nm)/Se(500 nm)/MoO$_x$(25 nm)/Au	0.91	10.8	55	5.4
FTO/ZnMgO(60 nm)/Se(300 nm)/MoO$_x$(15 nm)/Au	**0.95**	10.5	55	5.5
*FTO/CdS($\approx$50 nm)/Se(300 nm)/MoO$_x$(15 nm)/Au	0.47	7.8	31	1.1
Bifacial Se single-junction:				
*FTO/ZnMgO(60 nm)/Se(300 nm)/MoO$_x$(25 nm)/ITO(300 nm)	**0.91 (0.88)**	11.0 **(7.4)**	**53 (41)**	**5.2 (2.7)**
FTO/ZnMgO(60 nm)/Se(500 nm)/MoO$_x$(25 nm)/ITO(300 nm)	0.87 (0.82)	**11.2** (6.3)	51 (38)	5.0 (2.0)
Tandem Se-Si:				
*Ag/Si TOPCon bottom-cell/TiN(5 nm)/TiO$_2$(50 nm)/Se(250 nm)/MoO$_x$(15 nm)/ITO(200 nm)	0.98	6.6	24	1.5
*Ag/Si TOPCon bottom-cell/TiN(5 nm)/ZnMgO(70 nm)/Se(400 nm)/MoO$_x$(30 nm)/ITO(300 nm)	**1.49**	5.7	26	**2.2**
Ag/Si TOPCon bottom-cell/TiN(5 nm)/ZnMgO(70 nm)/Se(400 nm)/MoO$_x$(30 nm)/ITO(300 nm)	1.18	**6.5**	**29**	2.1
*Ag/Si TOPCon bottom-cell/ITO(40 nm)/ZnMgO(65 nm)/Se(400 nm)/MoO$_x$(30 nm)/ITO(200 nm)	0.98	3.3	26	0.8

5 | Limitations of Selenium

This chapter seeks to describe measurements, calculations and estimations of the limitations of selenium itself and how they relate to current device performance limits and how to possibly break them. Measurements were made at Helmholtz-Zentrum Berlin (HZB) that resulted in the determination of intrinsic carrier transport properties of our thin film selenium such as its carrier lifetime, τ, mobility, μ, diffusion length, L_{diff} and acceptor density, n_{A}. Low photoluminescence signals were measured below 50 K which are likely related to bandgap defects that quench the photoluminescence signal, through non-radiative recombination. Likewise DFT calculations of the band structure of monocrystalline trigonal Se were performed by the group CAMD from DTU Physics that indicate large effective carrier masses and effective densities of states. Estimations and simulations were made to understand the present fundamental limits of the single-junction Se device performance and how they relate to the overall findings of this project.

5.1 Time-Resolved Terahertz-Spectroscopy of Selenium

Time-resolved Terahertz-Spectroscopy (TRTS) was performed at HZB on a sample of 200 nm c-Se on 1 nm Te on fused quartz (annealed at 190 °C for 2 minutes). PhD student Hannes Hempel at HZB was kind enough to perform both the measurements, the data treatment and plotting of the results. The TRTS setup used a 400 nm pump pulse, a THz probe pulse and an 800 nm sampling pulse.

The photoconductivity transient and mobility spectrum (of the sum of electron and hole mobility measured 500 ps after photoexcitation, $\mu_{\Sigma}(f, 500 \text{ ps})$) can be seen in Figure 5.1.

The transient photoconductivity $\Delta\sigma(t, f) = e\mu_{\Sigma}(f, t)\Delta n(t)$, where $\mu_{\Sigma}(f, t)$ is the sum of the electron and hole mobilities and $\Delta n(t)$ is the photoexcited charge carier concentration, exhibits two distinct decays which were modelled with a double exponential decay:

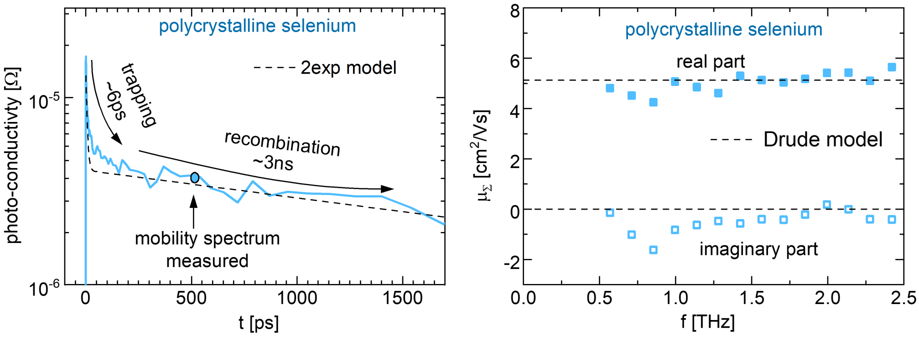

Figure 5.1: Time-Resolved Terahertz Spectroscopy (TRTS) measurements of a sample of c-Se(200 nm)/Te(1 nm)/quartz. The double exponential decay in photoconductivity is likely related to both the trapping and recombination of carriers. The lifetime and the sum DC-mobility of electrons and holes of c-Se is estimated to be $\tau \approx 3$ ns and $\mu_\Sigma \approx 5$ cm^2/Vs, respectively. With gratitude to Hannes Hempel for measuring and plotting the data.

$$\Delta\sigma(t) = \Delta\sigma_1 \exp\left(-\frac{t}{\tau_1}\right) + \Delta\sigma_2 \exp\left(-\frac{t}{\tau_2}\right) \tag{5.1}$$

The initial decay in photoconductivity has a time constant $\tau_1 \approx 6$ ps, which typically indicates the trapping of charge carriers into less-mobile states that causes a decrease in the average mobility $\mu(t)$ of the charge carriers.[165,166] The second decay has a time constant $\tau_2 \approx 3$ ns which is likely related to charge carrier recombination which causes a decay in the photoexcited charge carrier concentration $\Delta n(t)$.

The mobility exhibits an approximately constant real part of $\mu_\Sigma \approx 5$ cm^2/Vs and an imaginary part near zero. Usually the mobility of carriers in crystalline semiconductors exhibit a frequency-dependence that can be described by the Drude model of free charge carrier transport. However, the absence of frequency-dependence at 0.5 THz to 3 THz indicates that the scattering time is lower than $\tau_{\text{scat}} < 5$ fs (in accordance to Equation (2.24)). This is much shorter than for most other direct bandgap crystalline semiconductors (e.g. GaAs with $\tau_{\text{scat}} \approx 50-320$ fs).[167–169]

From the Drude model the DC-mobility at zero frequency is also ≈ 5 cm^2/Vs. This low mobility (compared to e.g. GaAs with $\mu >> 1000$ cm^2/Vs) is partially explained by the short scattering time (see equation 2.24).

The dark conductivity of c-Se has been reported to be of the order $\sigma \approx 10^{-5}$-10^{-6} Ω^{-1}cm^{-1}[105] which means that the hole mobility in this case is around $\mu_\text{h} \approx 10^{-3}$ cm^2/Vs (from $\sigma_\text{h} = e\mu n_\text{h}$, where $n_\text{h} = 9 \times 10^{15}$ cm^{-3} is calculated from CV measurements, see Section 2.2.4). The 4PP that was available to us was not able to measure such low conductivities and this measurement should ideally be made in future work to fully determine the individual mobility of holes and electrons. Such a low majority carrier mobility could potentially be detrimental to the performance of the device. If the hole mobility is in fact this low then the minority carrier mobility, namely the electron mobility will be $\mu_{\mathrm{e}} \approx 5\ \mathrm{cm}^2/\mathrm{Vs}$. From literature, a hole mobility at room temperature is found to be between 0.1-28 $\mathrm{cm}^2/\mathrm{Vs}$.[170] I would encourage further work to determine the conductivity of Se to clarify this.

Alternatively one can assume that the scattering time of both carriers is equal and use the calculated effective masses from DFT ($m_{\mathrm{C}} = 0.45 m_0$ and $m_{\mathrm{V}} = 3.4 m_0$, see Section 5.4) to obtain a scattering time of both carriers of approximately $\tau_{\mathrm{scat}} = 1.1$ fs in accordance with Equation (2.24). In this case the electron and hole mobilities will be $\mu_{\mathrm{e}} = 4.42\ \mathrm{cm}^2/\mathrm{Vs}$ and $\mu_{\mathrm{h}} = 0.58\ \mathrm{cm}^2/\mathrm{Vs}$.

It is important to note that the mobilities extrapolated from THz spectroscopy originate from short range transport of a few nm and are therefore not subject to transport barriers on larger scales. This may further reduce the measured mobility if measured across a greater distance where grain boundaries can affect both the lifetime and mobility. Performing Hall effect measurements would be beneficial to investigate this effect.

From the minority carrier electron lifetime and mobility, the diffusion coefficient and diffusion length is calculated to be $D_{\mathrm{e}} = \mu \frac{k_{\mathrm{B}} T}{e} \approx 0.11\ \mathrm{cm}^2/\mathrm{s}$ and $L_{\mathrm{e-diff}} = \sqrt{D_{\mathrm{e}} \tau} \approx 184$ nm, respectively.

Out of interest a sample of amorphous a-Se was measured in a similar manner. Here the mobility is further reduced to $\approx 0.6\ \mathrm{cm}^2/\mathrm{Vs}$ (see Figure 5.2). This is comparable to literature hole mobility values of $\approx 0.2\ \mathrm{cm}^2/\mathrm{Vs}$ measured by time of flight (TOF).[171]

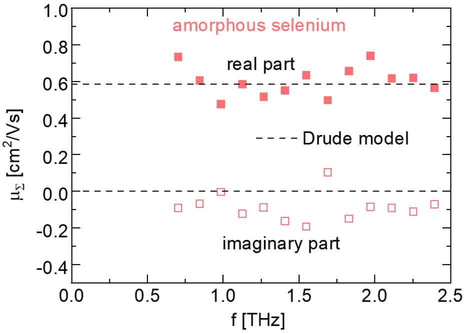

Figure 5.2: Time-Resolved Terahertz Spectroscopy (TRTS) measurements of a sample of a-Se(500 nm)/Te(1 nm)/quartz. The double exponential decay in photoconductivity is likely related to both the trapping and recombination of carriers. The sum DC-mobility of a-Se is estimated $\mu_\Sigma \approx 0.6$ cm^2/Vs. With gratitude to Hannes Hempel for measuring and plotting the data.

5.2 Photoluminescence

Steady-state photoluminescence (PL) was measured by the help of Sergiu Levcenco on different c-Se samples by use of a 532 nm diode laser which was dispersed through a ½-m grating monochromator to excite the sample. The PL signal was measured with a liquid-nitrogen-cooled InGaAs diode array and a thermoelectrically cooled CCD detector.[172] Neutral density filters were used to vary the excitation power density of the 100 µm diameter laser beam from 0.03-16 W/cm^2. The sample temperature was varied from 15 K to 55 K in a He closed cycle cryostat.

A PL signal could be obtained below the bandgap (1.95 eV) of all samples for temperatures below 50 K, but the signal was extremely low and even at the lowest excitation power densities, the signal degraded over time. In accordance with literature that have reported PL on monocrystalline selenium, PL signals can only be obtained for photon energies of $\approx$ 1.78-1.87 eV below temperatures of 50 K (down to 2 K) utilising a He-Ne laser (632.8 nm).[104,173,174] An excitation power of $\approx$ 0.37 W/cm^2 resulted in the highest signal to noise PL signal without diminishing the signal too rapidly. With an acquisition time of 5 seconds and a laser exposure time of 10 seconds, the PL signal was measured on a c-Se(200 nm)/Te(1 nm)/quartz sample as a function of time with a constant laser exposure of $\approx$ 0.37 W/cm^2 at 15 K (see Figure 5.3). After 37 minutes the signal degradation saturates and a similar PL signal is measured for 67 minutes and 97 minutes. Remeasuring the same spot after 30 minutes in the dark results in a similar PL signal indicating irreversible damage.

Comparing the PL signal with that found in literature for monocrystalline Se, our

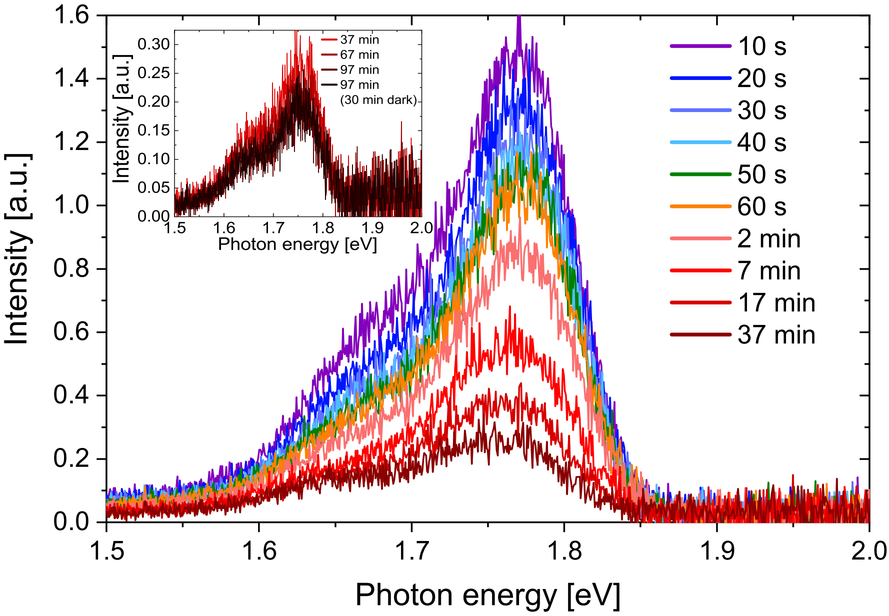

Figure 5.3: Photoluminescence of polycrystalline c-Se as a function of time with a constant 532 nm laser exposure of ≈ 0.37 W/cm^2 measured at 15 K. The signal diminishes considerably over time and remains low even after being kept in the dark for 30 minutes indicating irreversible damage.

PL signal for thin film polycrystalline Se is much wider and consists of two distinct peaks at around 1.65 eV and 1.775-1.8 eV. The reason for the extremely low PL signal as well as the PL peak position being situated below the bandgap is yet unknown, but potential explanations will be discussed at the end of this section. The reason for the PL signal degradation with constant excitation exposure is uncertain. Potentially the locally induced temperature gradient changes the c-Se morphology permanently or perhaps it could be inducing more detrimental defect states that further kill the signal through non-radiative recombination.

The degradation of the PL signal made it difficult to measure the signal as a function of temperature in the same 100 µm diameter spot size. In order to avoid the effect of degradation an experiment was thought out where a new spot was to be measured every time for just a 10 second laser exposure to investigate the homogeneity of the PL signal. 8 different spots located in a line with a ≈ 1 mm distance between each were measured at 16 K. This is illustrated in the schematic seen in Figure 5.4.

The PL signals of each spot for the homogeneity experiment is seen in Figure 5.5.

The peak intensities and positions match up indicating a homogeneous PL signal

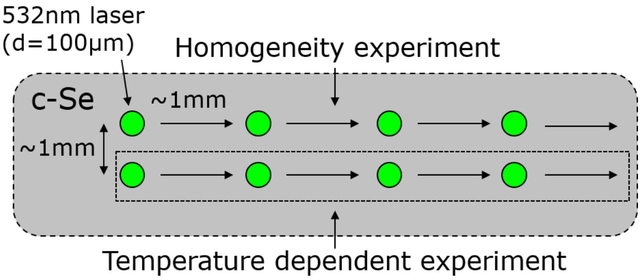

Figure 5.4: Illustration of the homogeneity and temperature dependence photoluminescence experiments.

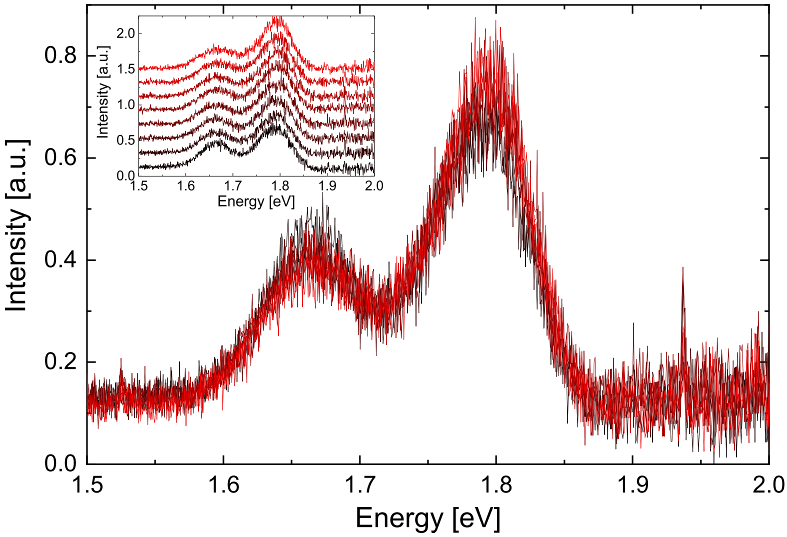

Figure 5.5: Photoluminescence investigation of the spatial homogeneity of the c-Se thin film. 8 spots were measured in a line with a ≈ 1 mm distance between each at 16 K.

within the measured area. Knowing that the PL signal intensity and position was fairly unaffected by the local position, a new linescan was made in a similar fashion ≈ 1 mm below the initial spot (as illustrated in Figure 5.4). In this case the temperature was varied from 16 K to 55 K to investigate the PL signals temperature dependence. A similar experiment was performed on a c-Se(1 µm)/TiO_2(35 nm)/FTO (annealed at 190 °C for 2 minutes) sample that more closely resembles our thin film c-Se in our fabricated devices. The resulting temperature dependent PL measurements can be seen in Figure 5.6.

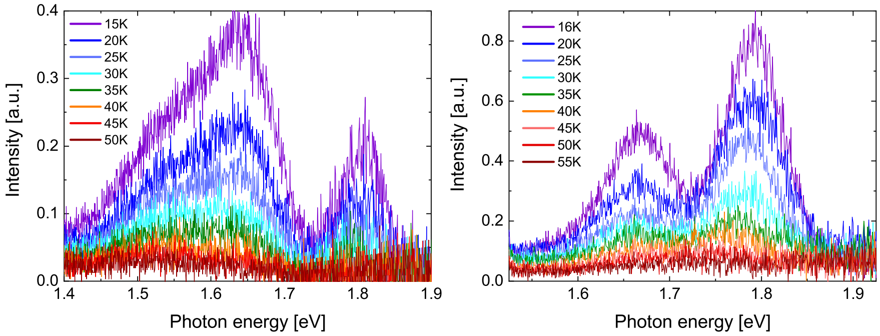

Figure 5.6: Temperature dependent photoluminescence measurements of the polycrystalline selenium of the samples c-Se(1 µm)/TiO_2(35 nm)/FTO (left) and c-Se(200 nm)/quartz (right).

A clear dependence of the PL signal is observed as a function of temperature where an observable signal is only measured above a temperature of 50 K, which is a similar effect to that reported for monocrystalline Se in literature.[173,174]

Noticeably, the peak intensities, widths and positions are highly dependent on either the substrate used or the c-Se thickness. This leads back to the three unanswered questions regarding the c-Se PL signal. 1. Why is the PL signal so low? 2. Why is the PL signal situated below the bandgap of 1.95 eV? (note that the bandgap is also expected to increase $\approx$ 0.1 eV for lower temperatures[175,176]) 3. How is this related to our low carrier lifetime of $\tau \approx 3$ ns measured with TRTS?

The answer to all three questions is likely the same, namely the existence of defect states inside the bandgap. For monocrystalline c-Se these defect states are from the PL signal identified to be 5 different energy levels that are situated near the band edges.[174] For polycrystalline c-Se we observe both wider and less energetic PL peaks that indicates more detrimental defects likely situated closer to the center of the bandgap. The low PL signal could in this manner be explained if the defects require some thermal energy to non-radiatively recombine the carriers. Reducing the temperature effectively freezes in the defects in such a way that the carriers are more likely to recombine either to or from the defects radiatively. The origin of the defects is yet to be identified, but are most likely related to be intrinsic Se vacancies/interstitials, O antisites/interstitials or Te antisites/interstitials. Potentially Se vacancies or interstitials could be caused by low formation energies of non-trigonal Se crystal structures that are not detected from our XRD or Raman measurements. The presence of some crystalline α-monoclinic and β-monoclinic Se states that contain Se_8 rings, instead of the trigonal chains, is plausible.[99–102,177] There is also a probability that some extrinsic foreign contamination elements below the XPS detection limit could be the cause.

The difference in PL signal observed from the two different samples (Figure 5.6) could be explained from a difference in the defect density in the c-Se related to intrinsic defects. The reason for this could be related to a variety of different parameters such as for instance the c-Se growth which vary by both the substrate material and the surface roughness of the two samples. Furthermore, the Se thickness is different, which with a fixed Te thickness of 1 nm changes the Te/Se ratio of the two samples to be $\approx 0.5\%$ (200 nm Se) and 0.1% (1 µm Se). The c-Se growth mechanic and Te/Se ratio are both likely to alter the possibility for the generation of defects related to either Se vacancies/interstitials, O antisites/interstitials or Te antisites/interstials in the crystal structure. There is also some possibility that the reported indirect bandgap of ≈ 1.85 eV may somehow influence the PL signal.[67] To further understand where the defect states are situated, it could be beneficial to further investigate c-Se with PL experiments where lower energy excitations are used to identify if defect states exist closer to the centre of the bandgap.

More investigations are required in order to identify the origins of both the low measured lifetime and low PL signal. To expand on this work, the origin and nature of the defects will be investigated simultaneously by PhD student Rasmus Nielsen and PostDoc Leopold Julian Scheffler (from Århus University) experimentally by use of deep-level transient spectroscopy (DLTS) and by PhD student Fabian Felix Bertoldo from DTU Physics CAMD through computational analysis. This combination of experimental and computational analysis has similarly resulted in valuable knowledge of the nature of the native defects of kesterite CZTSe, CZTS, CZGSe and AZTSe absorbers. Here a correlation between a low carrier lifetime, open-circuit voltage and external radiative efficiency (ERE) has also been found. This is specifically a very similar case for CZTS where a V_{oc}-deficit of ≈ 0.4 V caused by nonradiative-recombination corresponds to a ERE which is consistently below the detection limit of ca. $10^{-4}\%$. Through doping of the absorber up to 10^{20} cm^{-3}, some but not all of the V_{oc}-deficit can be regained.[178]

In short, even if we manage to fabricate the perfect transport-layers with minimal internal transport losses we have to obtain a detectable PL signal of c-Se at room temperature if c-Se is ever to reach the SQ-limit open-circuit ($V_{\mathrm{oc-SQ-limit}} \approx E_{\mathrm{g}} - 0.3$ V$= 1.65$ eV). A further discussion will follow later in Section 5.5.

5.3 Capacitance-Voltage Profiling

Capacitance-voltage (C-V) measurements were made with the help of Sergiu Levcenco using a HP 4284 LCR meter operated in R(resistance)-X(reactance) mode in the dark. The measurements were performed on well behaving FTO/TiO$_2$/Se/Au devices from frequencies of 1 kHz to 1 MHz with biases from -0.8 V to 0.4 V.[179] A simple equivalent circuit model consisting of a capacitor in parallel with a resistor (resistance of R_p) which are both in series with another resistor (resistance of R_s) was used to extract the capacitance, C (see Equations (5.2) and (5.3)).[180,181]

$$Z = R_\mathrm{s} + \frac{R_\mathrm{p}}{1 + (\omega R_\mathrm{p} C)^2} - i \frac{R_\mathrm{p}^2 C \omega}{1 + (\omega R_\mathrm{p} C)^2} \tag{5.2}$$

$$C = \frac{-\operatorname{Im}(Z)}{\left[(\operatorname{Re}(Z) - R_\mathrm{s})^2 + (-\operatorname{Im}(Z))^2\right] \omega} \tag{5.3}$$

The series resistance, R_s, is extrapolated from the Nyquist plot which can be directly plotted from the measured real and imaginary parts of the impedance. From the calculated capacitance, the CV density, n_CV, (corresponding to the doping density of the lightly doped side of the junction, e.g. the Se) and the distance from the p-n junction, $x_\mathrm{p-n}$, can be calculated in accordance to the Equations (2.16) and (2.17) shown in Section 2.2.4. The relative permittivity used is extrapolated from ellipsometry measurements of c-Se which yields a permittivity of $\epsilon_\mathrm{r} \approx 7.5$ at 1700 nm that is equivalent to that previously reported of $\epsilon_\mathrm{r} = 7.43$.[67] They are plotted as a function of the applied bias voltage. The corresponding plots can be seen in Figure 5.7.

The large variation in the calculated capacitance with frequency indicates that the used equivalent circuit model is too simple. It is expected that some series resistance or conductance related to either the Se or the TiO$_2$/FTO is frequency dependent giving greater deviations in the capacitance with increased frequency. The calculations for the measurement made at lower frequencies match up from which useful device parameters can be extracted. The acceptor density of our c-Se is calculated to be around $n_\mathrm{A} \approx 9 \times 10^{15}$ cm^{-3}. The intercept of $\mathrm{d}(C^{-2})/\mathrm{d}V_{dc}$ corresponds to a built-in voltage of $V_\mathrm{bi} \approx 0.45$ V which from Equation (2.13) gives us a depletion region width at zero bias of around $W \approx 200$ nm. This calculated depletion region width matches well with the calculated distance to the junction interface at zero bias as seen in Figure 5.7 (e).

The collection of carriers is related to the depletion region width and their diffusion length. With a diffusion length of around $L_\mathrm{diff} \approx 200$ nm and a depletion region width of around $W \approx 200$ nm one would expect an optimal Se thickness of around ≈ 400 nm. This fits nicely with our results of the optimum Se thickness of our bifacial devices of $\approx 300 - 500$ nm Se (see Figure 2 in Paper I in Appendix B).

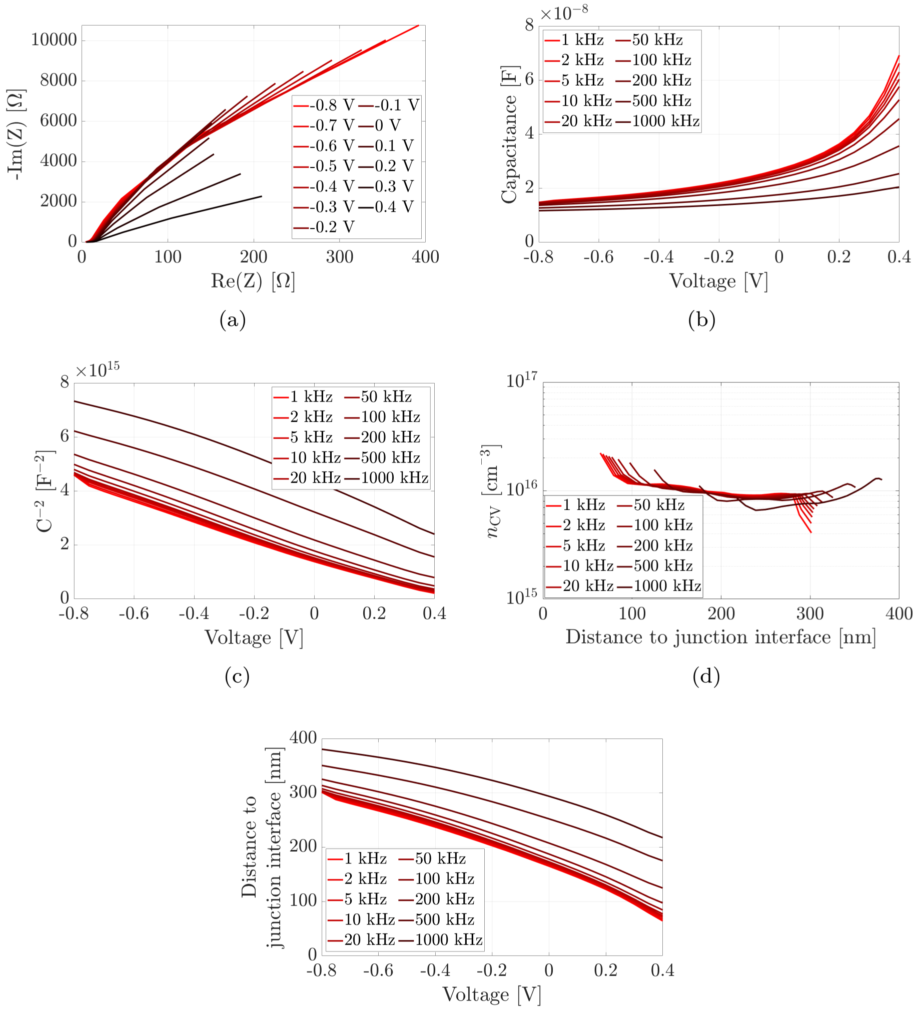

Figure 5.7: C-V measurements of a FTO/TiO$_2$(50 nm)/Se(>1 µm)/Au device with an active area of $A \approx 0.67$ cm^2. (a) Nyquist plots of the real and imaginary parts of the impedance, Z, as a function of the applied bias voltage. R_s is extrapolated to be ≈ 4-6 Ω. (b) The capacitance, C, is calculated from Equation (5.3) and plotted versus the voltage, V. (c) C^{-2} versus V. The intercept gives $V_{\mathrm{bi}} \approx 0.45$ V. (d) The CV density, n_{CV}, calculated from Equation (2.16) and the slope of (c), which is equivalent to the acceptor density of Se, $n_{\mathrm{A}} \approx 9 \times 10^{-15}$ cm^{-3}, as a function of the depth profiling calculated from Equation (2.17). (e) The depth profiling distance with respect to the p-n junction TiO$_2$/Se interface as a function of bias voltage.

5.4 Electronic Structure Calculations

In order to better understand and estimate the limitations of selenium as a photovoltaic absorber, electronic structure calculations were performed on monocrystalline hexagonal selenium at DTU Physics in the group of Computational Atomic scale Materials Design (CAMD) by Hadeel Moustafa, Carsten Wedel Jacobsen and Thomas Olsen. I thank all three for allowing me to show some of their calculations which have been highly useful for the estimation of the Se device performance limits. The Density Functional Theory (DFT) calculations were performed using the GPAW code where a newly set of python modules called Atomic Simulation Recipes (ASR) were employed. The band structure was computed using three different xc-functionals, namely PBE, HSE06 and G0W0. The calculations were made from the calculated anisotropic lattice constants, $a = 4.519$ Å and $c = 5.050$ Å, similar to the experimentally reported lattice constants $a = 4.374$ Å and $c = 4.951$ Å measured at room temperature.[67] The indirect bandgaps were calculated to be 1.03 eV, 1.76 eV and 2.46 eV for the PBE, HSE06 and G0W0 functions respectively. The direct bandgaps were similarly calculated to be 1.09 eV, 1.86 eV and 2.63 eV. Here the bandgaps calculated with HSE06 mostly resemble those that have been measured experimentally ($E_{\mathrm{g-ind}} = 1.85$ eV[67] and $E_{\mathrm{g-dir}} \approx 1.8 - 2$ eV[64,66,68])

The calculated Brillouin zone and band structure from PBE with and without spin-orbit coupling (SOC) can be seen in Figure 5.8.

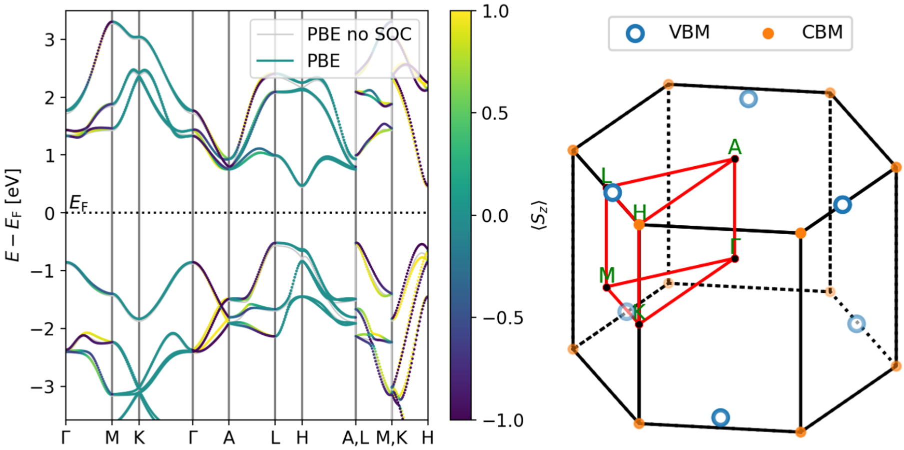

Figure 5.8: Calculated band structure and Brillouin zone for monocrystalline selenium by use of PBE. The electron density has been determined self consistently using 400 points distributed along the band path. The indirect bandgap is found for the L-H transition and the direct bandgap is found at H. Courtesy of Hadeel Moustafa, Carsten Jacobsen and Thomas Olsen.

The effective electron mass, m_{e}, is found from fitting the CBM to be 0.38 m_0, 0.39

m$_0$ and 0.18 m_0 for the x, y and z-directions, respectively. Similarly the effective hole mass, m_h, is found from fitting the VBM to be 2.38 m_0, 0.18 m_0 and 20.51 m_0. The large difference in the effective masses clearly shows the anisotropic conduction nature of the crystal structure. From the density of states (DOS) the effective DOS masses are found from a $E^{3/2}$ fit to the conduction and valence band edges in a 35 meV range to be $m_\mathrm{C} = 0.45\ m_0$ and $m_\mathrm{V} = 3.4\ m_0$. The reported effective density of states masses found in literature are in the range of 1.4-3.5 m_0.[67,182–184] The resulting effective density of states of the two bands are found to be $N_\mathrm{C} = 0.088$ nm^{-3} = 8.8×10^{19} cm^{-3} and $N_\mathrm{V} = 0.164$ nm^{-3} = 1.64×10^{20} cm^{-3} at 300 K in accordance to $N_\mathrm{C/V} = 2(2\pi m^*_\mathrm{e/h} k_\mathrm{B} T/h^2)^2$.[81] The large effective hole mass and density of states of the valence band relates to the rather flat plateau of the valence band structure at L-H and is consistent with DFT calculations from literature.[185] The high effective mass is problematic for the photovoltaic applications of the Se since it is inversely proportional to the mobility of the carriers, which we know from our THz measurements is also low ($\mu = q\tau_\mathrm{scat}/m^*$). Using the calculated effective masses in equation (2.24) one obtains an average scattering time of around $\tau_\mathrm{scat} \approx 1.1$ fs. If one assumes that the scattering time of both types of carriers are equal, then the electron and hole mobilities can independently be found from the sum carrier mobility of $\mu_\Sigma = 5$ cm^2/Vs to be $\mu_\mathrm{e} = 4.42$ cm^2/Vs and $\mu_\mathrm{h} = 0.58$ cm^2/Vs.

Knowing N_V and $n_\mathrm{A} \approx 9 \times 10^{15}$ cm^{-3} one can calculate the Fermi level position, E_F, relative to the valence band, E_V, which gives $E_\mathrm{F} - E_\mathrm{V} = k_\mathrm{B}T/q \ln(N_\mathrm{V}/n_\mathrm{A}) \approx$ 0.25 eV.[5] The discrepancy of ≈ 0.5 eV between this value and the one measured by UPS is likely related to Fermi level pinning to the surface for that measurement which causes band bending near the surface and therefore a surface Fermi level position which is not the same compared to the bulk.[134]

5.5 Estimating the Photovoltaic Limitations

The main limitations of the reported Se single-junction device performance is presently the open-circuit voltage, V_oc, and the fill factor, FF. The greatest measured values of these are as shown in Table 4.1 to be $V_\mathrm{oc} = 0.97$ V and FF = 63.4% for the champion device reported by Todorov et al.[68] From the physical properties that have been shown measured and derived in the previous sections we can begin to estimate and understand these present photovoltaic limitations. As recently demonstrated by the studies of Tress[186] and Solterfoht et al.[187] the achievable V_oc can be predicted, in the case of dominant non-radiative Shockley-Read-Hall (SRH) recombination, from the carrier lifetime in the following manner. The V_oc is given by:

$$eV_\mathrm{oc} = E_\mathrm{g} + k_\mathrm{B}T \ln\left(\frac{n_\mathrm{e} n_\mathrm{h}}{N_\mathrm{C} N_\mathrm{V}}\right) \tag{5.4}$$

where $k_\mathrm{B}T/e$ is the thermal voltage (25.7 mV), $n_\mathrm{e/h}$ are the density of electrons/holes in the conduction/valence band and $N_{\mathrm{C/V}}$ are the effective density of states in the conduction/valence band, respectively. At room temperature all donor and acceptors are almost completely ionized meaning that the hole density of p-type Se can reasonably approximated by $n_{\mathrm{h}} \approx n_{\mathrm{A}} \approx 9 \times 10^{15}$ cm^{-3} from our C-V measurements.[5]

The change in the electron density, $\mathrm{d}n_e/\mathrm{d}t$, in the conduction band is related to the generation rate, G, and the recombination rate, R, and can in the case of dominant SRH be approximated by (5.5).

$$\frac{dn_{\mathrm{e}}}{dt} = G - R = 0 \approx G - \frac{n_{\mathrm{e}}}{\tau_{\mathrm{SRH}}} \Rightarrow n_{\mathrm{e}} \approx G\tau \tag{5.5}$$

Here, the generation rate, G, is approximated by $J_{\mathrm{sc}}/(ed)$ where a maximum J_{sc} of ≈ 15.7 mA/cm^2 can for full collection be expected from a 500 nm Se thickness calculated from the absorption coefficient yielding $G \approx 2 \times 10^{21}$ cm^{-3}s^{-1} (see Figure 2 in Appendix B). Similar but slightly lower results are obtained if the $J_{\mathrm{sc}} = 12.0$ mA/cm^2 is used from the record current device with a Se thickness of $d \approx 500$ nm (see Figure 4.4 and Table 4.2). For this assumption to be valid, the lifetime must be SRH recombination dominated, τ_{SRH}.

This should be valid for our low carrier lifetime measured by THz spectroscopy of $\tau \approx 3$ ns where an excess photogenerated electron carrier density is calculated to be approximately $n_{\mathrm{e}} \approx 4.5 \times 10^{12}$ cm^{-3}. In this case a maximum achievable open-circuit voltage is around $V_{\mathrm{oc}} \approx 1.27$ V. That means that our V_{oc}-deficit can be estimated to be around $\Delta V_{\mathrm{oc}} \approx 1.65\,\mathrm{V} - 1.27\,\mathrm{V} = 0.38\,\mathrm{V}$.

This indicates that the intrinsic low carrier lifetime of our c-Se mainly limits the largest obtainable V_{oc}. Assuming that we can somehow improve the lifetime, then greater voltages should be achievable. Plotting the V_{oc} calculated from Equation (5.4) as a function of lifetime for our measured and calculated values for our c-Se one obtains the plot seen in Figure 5.9. Please note that this is only valid for dominant SRH recombination and therefore above a certain lifetime this assumption is no longer valid. With an increased lifetime, the diffusion length should increase as well from $L_{\mathrm{diff}} = \sqrt{D\tau} = \sqrt{\mu\tau k_{\mathrm{B}}T/e}$ if one assumes that the mobility remains the same $\mu \approx 5$ cm^2/Vs. The largest Se single-junction record $V_{\mathrm{oc}} = 970$ mV[68] is included for comparison to estimate how much V_{oc} can be achieved through the optimisation of the device architecture versus the intrinsic carrier lifetime of Se.

If our measurements and calculations are correct the V_{oc} of the device can optimised by $\approx$ 300 mV from further device architecture optimisations, which is likely mainly related to interface recombination effects, but then the remaining $\approx$ 380 mV can only be obtained through either somehow increasing the carrier lifetime or by doping the Se to obtain a larger doping density $n_A > 10^{16}$ cm^{-3}. However, even if all native defects of the Se are somehow removed and all surface and interface related recombination mechanics are minimised in order to fully

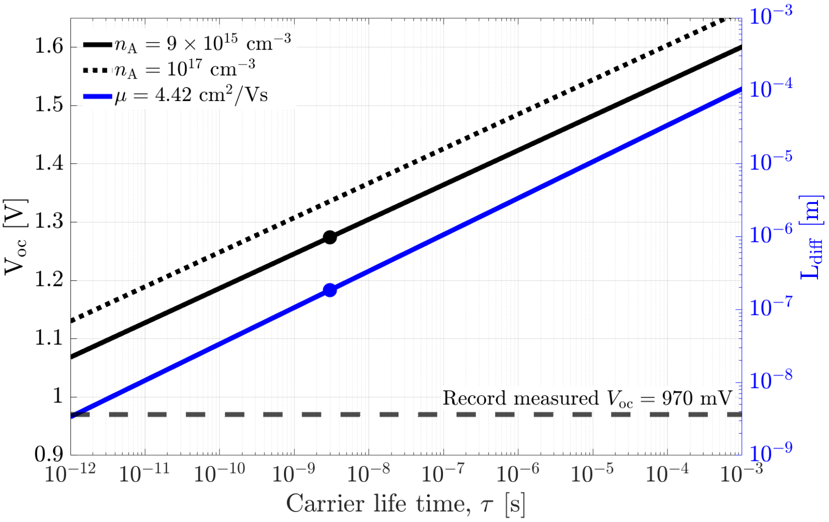

Figure 5.9: Open-circuit voltage, V_{oc}, and diffusion length, L_{diff}, estimation as a function of a SRH dominant carrier lifetime calculated from Equation (5.4) and Equation (5.5). Values used: $E_g = 1.95$ eV, $T = 300$ K, $J_{\text{sc}} = 12.0$ mA/cm^2, $d = 500$ nm, $n_h = n_A = 9 \times 10^{16}$ cm^{-3}, $N_C = 8.8 \times 10^{19}$ cm^{-3}, $N_V = 1.64 \times 10^{20}$ cm^{-3} and $\mu = 4.42$ cm^2/Vs. For a lifetime of $\tau = 3$ ns a maximum open-circuit voltage of $V_{\text{oc}}(\tau = 3\,\text{ns}) = 1.27$ V and a diffusion length of $L_{\text{diff}}(\tau = 3\,\text{ns}) = 184$ nm should be obtainable. An increased doping concentration of $n_A = 10^{17}$ cm^{-3} has been included as well assuming no resulting carrier lifetime losses.

eradicate SRH recombination, the radiative recombination rate will have an intrinsic limit. Comparing with other well studied direct bandgap semiconductors like e.g. Ge and GaAs, their lifetimes have been measured to be in the 10^{-6}-10^{-4} s and 10^{-9}-10^{-7} s range, respectively.[188,189] Furthermore, the radiative lifetime is affected by the doping level and above a certain threshold the lifetime is expected to drop due to Auger recombination and introduced defect states. For both Si and Ge this injection threshold level lies around 10^{17} cm^{-3}. Even if we are able to increase the doping density of Se to $n_A = 10^{17}$ cm^{-3} then a carrier lifetime in the order of 10^{-4}-10^{-3} s is required. For such an injection level, even Ge grown by Czochralski and floating zone methods has the largest measured lifetimes in the order of 10^{-5} s.[190]

Ultimately, this shows that another main limitation of Se as a photoabsorber is actually caused by its intrinsic bandstructure which causes the effective masses and density of states to be larger than most other well established photovoltaic semiconductors. To illustrate this point the same calculations were performed with the thought experiment that Se has a DOS similar to that of well known semiconductors such as GaAs, Ge and Si (see Figure 5.10).

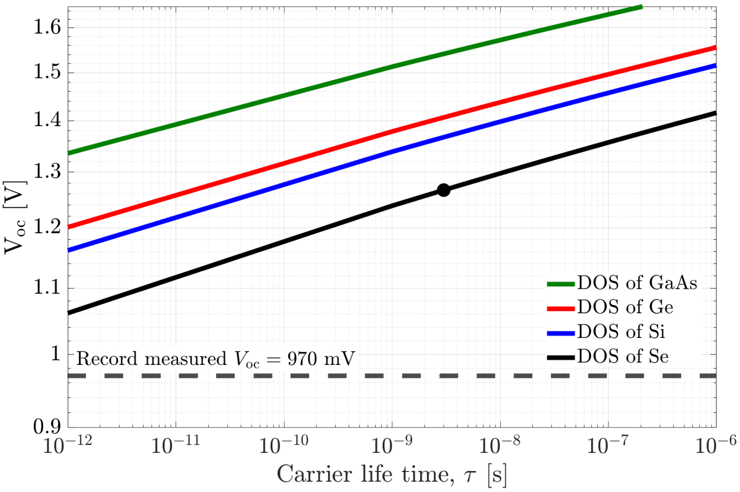

Figure 5.10: Illustration of the high DOS limitation on the V_{oc} of Se. The calculations were made with the same values as used for Figure 5.9 but also with the DOS of Se being replaced with those of GaAs, Ge and Si. GaAs: $N_C = 4.7 \times 10^{17}$ cm^{-3}, $N_V = 7.0 \times 10^{17}$ cm^{-3}. Ge: $N_C = 1.04 \times 10^{19}$ cm^{-3}, $N_V = 6.0 \times 10^{18}$ cm^{-3}. Si: $N_C = 2.8 \times 10^{19}$ cm^{-3}, $N_V = 1.04 \times 10^{19}$ cm^{-3}.[81,191]

This clearly illustrates that due to the high DOS of Se the V_{oc} is limited by 100-250 mV for the same lifetime compared to it having a lower DOS and that lifetimes of about 2-4 orders of magnitude higher are required to obtain a similar V_{oc}. However, it is important to note that the large DOS is likely related to the strong optical absorption of Se which translates into significant carrier generation and thereby a short distance required for carrier collection (when illuminating through the p-n junction).

Nevertheless, before completely dismissing Se as an efficient photovoltaic absorber, attempts should be made to remove the defects and try to increase the carrier lifetime. If the lifetime can be improved then ideally a PL signal should be obtainable at room temperature. One can calculate external radiative efficiency, ERE, (aka. the photoluminescence quantum yield or the external luminescence quantum efficiency) as a function of the voltage via Equation (5.6).[178,192]

$$V_{oc} = V_{oc}^{rad} + \frac{k_B T}{e} \ln(\text{ERE}) \tag{5.6}$$

where $V_{oc}^{rad} = 1.65$ eV. If one also combines Equation (5.4) and Equation (5.6) under the same SRH dominated carrier lifetime assumption with the same measured and calculated values, the plots seen in Figure 5.11 are obtained.

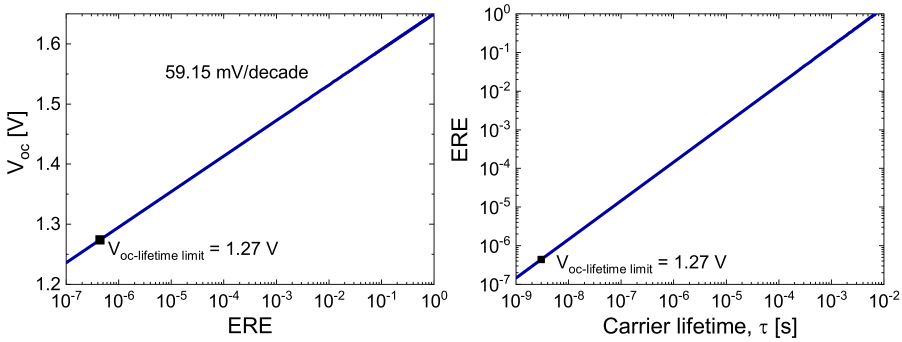

Figure 5.11: Left: Open-circuit voltage, V_{oc}, as a function of the external radiative efficiency, ERE, calculated from Equation (5.6). Right: ERE as a function of the carrier lifetime calculated from Equation (5.4) using the same values and assumptions.

With a detection limit of ca. ERE = 10^{-6} [178], one would therefore need to obtain a carrier lifetime increase of at least an order of magnitude higher in order to detect the PL signal at room temperature. To compare the ERE of our Se with that reported for other PV absorbers, some of the greatest ERE values have been shown to be 35.7% for GaAs [27], ≈ 5% for lead halide perovskites [193] and $1.5 - 3 \times 10^{-3}$% for CZTSe solar cells. [178,194,195] For CZTSe it has been reported that both the ERE and doping density could be increased through Li-doping without changing the lifetime significantly. [178]

If the carrier lifetime can be increased so should the diffusion length and the FF. As Todorov et al. points out, the main issues of the FF are the large ideality factor, $n > 2$, and shunt conductance, G_{sh}, under illumination, which are likely related to a severe recombination in the depletion region and a voltage-dependent collection efficiency due to a low carrier lifetime and diffusion length. [68]

A Suns-V_{oc} measurement was carried out on a champion single-junction ZnMgO/Se/MoO$_x$/Au device to investigate the pseudo fill factor neglecting the effects of these parasitic transport losses. The JV and pseudo-JV from the Suns-V_{oc} measurement obtained for 0.01-2 suns is shown in Figure 5.12.

Since no carrier movement occurs during the Suns-V_{oc} measurement, the parasitic transport losses have no effect on the carriers, showing that a pseudo fill factor of pFF = 80% and a pseudo-voltage pV_{oc} = 0.99 V can be obtained with an ideality factor of $n = 1.94$ at 1 sun. Calculating the ideal FF for this V_{oc} assuming an ideal diode $n = 1$ via. Equation (2.8) one obtains FF = 88%. If one could further optimise the collection efficiency via a more optimal device architecture and obtain a $V_{\mathrm{oc}} \approx 1.27$ one would be able to obtain FF = 90%. For comparison, the SQ-limit FF = 92% for the SQ-limit V_{oc} = 1.65 V.

Combining all of these findings and estimations for the potential improvements of the V_{oc}, FF and corresponding PCE (assuming either the short-circuit current

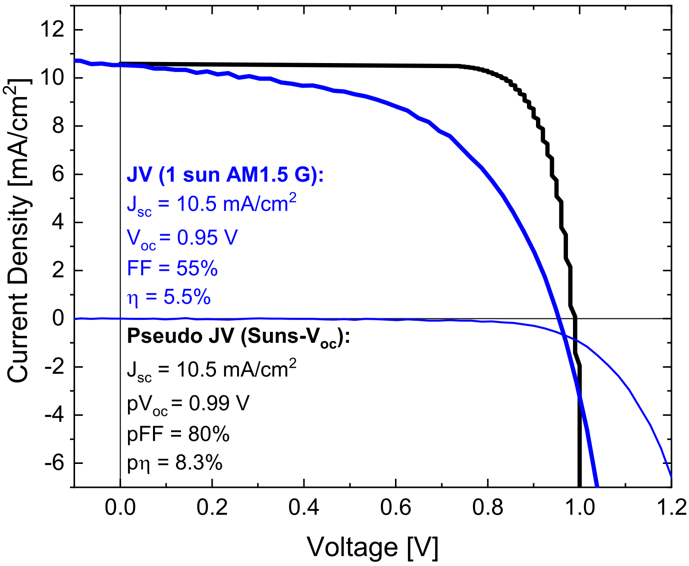

Figure 5.12: JV and pseudo-JV of the champion FTO/ZnMgO(60 nm)/Se(300 nm)/MoO$_x$(15 nm)/Au device.

density record $J_{\mathrm{sc}} = 12$ mA/cm^2 or the SQ-limit $J_{\mathrm{sc}} = 15.7$ mA/cm^2) one obtains the boxplots seen in Figure 5.13.

It should be noted that the parasitic transport losses, collection efficiency, diode ideality factor, doping and lifetime are all related and that these will likely all be affected by the change in the properties of both the device architecture layers and the Se layer itself. The figure and calculations are thereby mainly included as an illustration of some of the many issues that should be investigated and solved before Se can truly become an efficient top-cell photoabsorber for tandem applications.

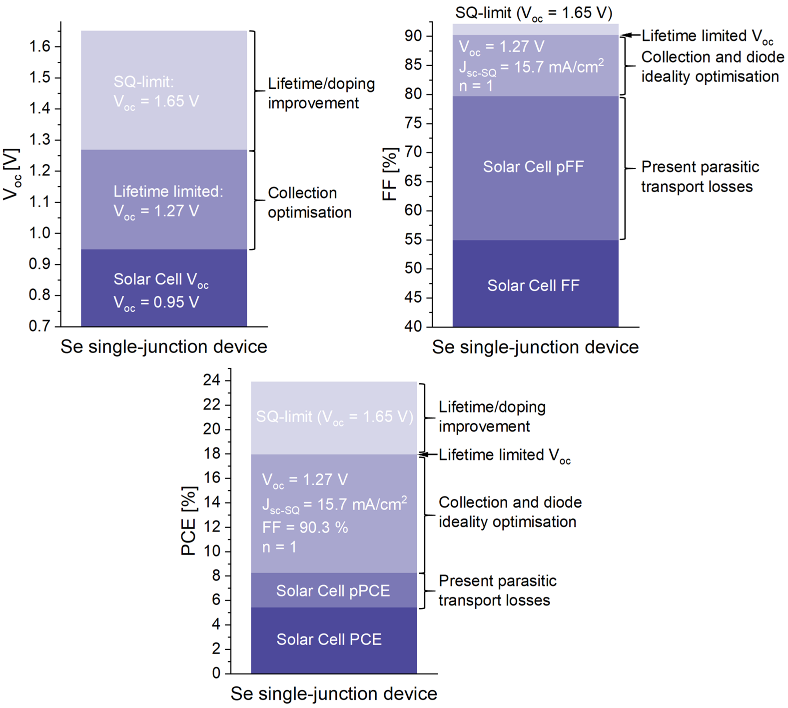

Figure 5.13: Estimation of the present main device performance limitations from measured and calculated properties of our polycrystalline thin film c-Se.

5.6 SCAPS Simulations

SCAPS (Solar Cell Capacitance Simulator) simulations were performed to investigate the device performance with respect to the inclusion of ideal and realistically assumed and measured properties of the device layer materials. SCAPS is a one dimensional solar cell simulation program developed at the Department of Electrons and Information Systems (ELIS) of the University of Grent, Belgium.

The simulation software functions by solving the one-dimensional Poisson's equation (that relates the charge to the electrostatic potential), the continuity equations for electrons and holes as well as the constitutive transport equations. The length of the total cell is divided into discrete intervals, where the value of the electrostatic potential and the concentrations of the electrons and holes (or the quasi fermi levels energies) are the unknowns of the equations. The equations are solved numerically for each interval using appropriate boundary conditions can provide a simulation of the bandbending and resulting collected photocurrent of the structure as a function of the applied bias.[196]

First of all the benefits of including MoO_x as a HTL was modelled via SCAPS simulations. Figure 5.14 shows a comparison of the SCAPS simulations of FTO/TiO_2(50 nm)/Se(400 nm)/MoO_x(15 nm)/Au devices with and without MoO_x with the similar device architecture champion devices of this work. For these SCAPS simulations realistic material property values were used that were either measured, calculated, found in literature or simply assumed. See Tables A.1, A.2 and A.3 for further details. All simulations include the measured absorption coefficient of c-Se shown in Figure 3.16.

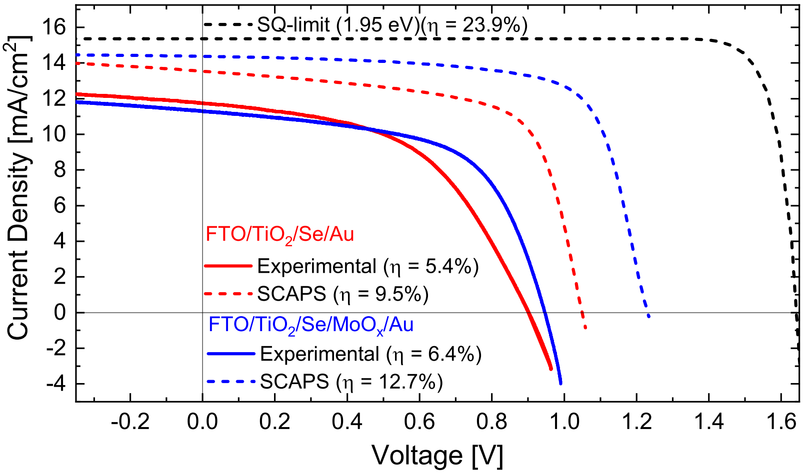

Figure 5.14: Comparison of JV curves from SCAPS simulations and device champions FTO/TiO_2(50 nm)/Se/MoO_x(15 nm)/Au with and without MoO_x. The material properties used for the SCAPS simulations can be found in Tables A.1, A.2 and A.3. The FTO and Au work functions used were $\phi = 4.4$ eV [97] and $\phi = 5.2$ eV [98], respectively.

The SCAPS simulations for both device architectures and materials agree nicely with the champion device performances. However, the improvements in the device performance for the devices with MoO_x does not fully match the simulated V_{oc} and FF improvements. The major difference is expected to be due to large interface recombination in the real devices. The lower J_{sc} is likely mostly attributed to parasitic absorption and reflection. It is evident that there is yet much room for improvement before the SQ-limit is reached.

From our previous estimations the main limiting factor for the performance of the Se-based solar cell devices is the low carrier lifetime and low mobility within Se itself. To further investigate this claim, SCAPS simulations were performed where both realistic and ideal parameter values for the Se absorber and the transport layers were included subsequently to try to further estimate how much the performance parameters can be improved through the optimisation of one or the other. A bifacial FTO/TiO_2(50 nm)/Se(50-1000 nm)/MoO_x(15 nm)/ITO device was assumed where both the Se thickness and illumination side was varied to further quantify how these are affected by improvements of the device qualities. The simulations were made in a fashion where both the transport layers and Se properties were initially assumed ideal. Thereby both the carrier lifetime and diffusion length were assumed to be very large ($\tau = 67\,\mu\text{s}$ and $L_{\text{diff}} = 21\,\mu\text{m}$) and the band alignment of the layers are aligned perfectly meaning that the conduction band and valence band of the Se at $E_{\text{C}} = -3.9$ eV and $E_{\text{V}} = -5.85$ eV perfectly match those of the ETL and HTL, respectively. No bulk or interface defects are introduced in the simulations. Next the realistic and non-ideal values (see Table A.1) are introduced for the Se alone while maintaining perfect transport layers and interfaces. Lastly, the realistic and non-ideal property values for the transport layers are also included. The results of the simulated device parameters as a function of Se thickness and illumination direction can be seen in Figure 5.15.

The simulations clearly indicate in the same way as our previous estimations that the largest device performance increase is to be achieved through the increase of the V_{oc} and FF which are mainly related to the optimisation of the carrier lifetime and carrier mobility of the Se, rather than the actual band alignment of transport layers. The poor carrier transport qualities of Se are especially detrimental to the performance when the illumination is opposite of the carrier separating p-n junction, resulting in a more narrow Se thickness optimum. As previously discussed the inversion of the architecture is for this reason highly recommended for tandem attempts. If the Se transport qualities can be improved this effect becomes less pronounced. If further device performance optimisations are achieved in future work it is important to note that an increasing optimum of the Se thickness up to around $\approx 1\,\mu\text{m}$ is to be expected in accordance with these simulations.

Comparing the simulation for the "realistic" $\text{TiO}_2/\text{Se}/\text{MoO}_x$ device with the present champion device performances, there is still major improvements to be made for the V_{oc} and FF. The simulations have not included interface recombination which is likely to be one of the main limiting factors of the current design architecture rather than actual band alignment. This is consistent with the findings of Todorov et al. that found from temperature-dependent V_{oc} measurements that the extrapolated V_{oc} at 0 K is 1.6 V which corresponds to a voltage loss of around ≈ 0.35 V (from the 1.95 eV bandgap) due to interface recombination.[68]

To conclude this chapter it is evident that the identification and removal of carrier defects is paramount. Both within Se itself and in the interfaces. This should improve both the carrier lifetime and mobility within Se as well as the reduction of interface recombination. Not only should this give rise to a detectable PL signal and an increased device performance, but it is also likely that non-ideal observations such as JV hysteresis, light degradation, cross-over and roll-over effects may be eliminated through this process.

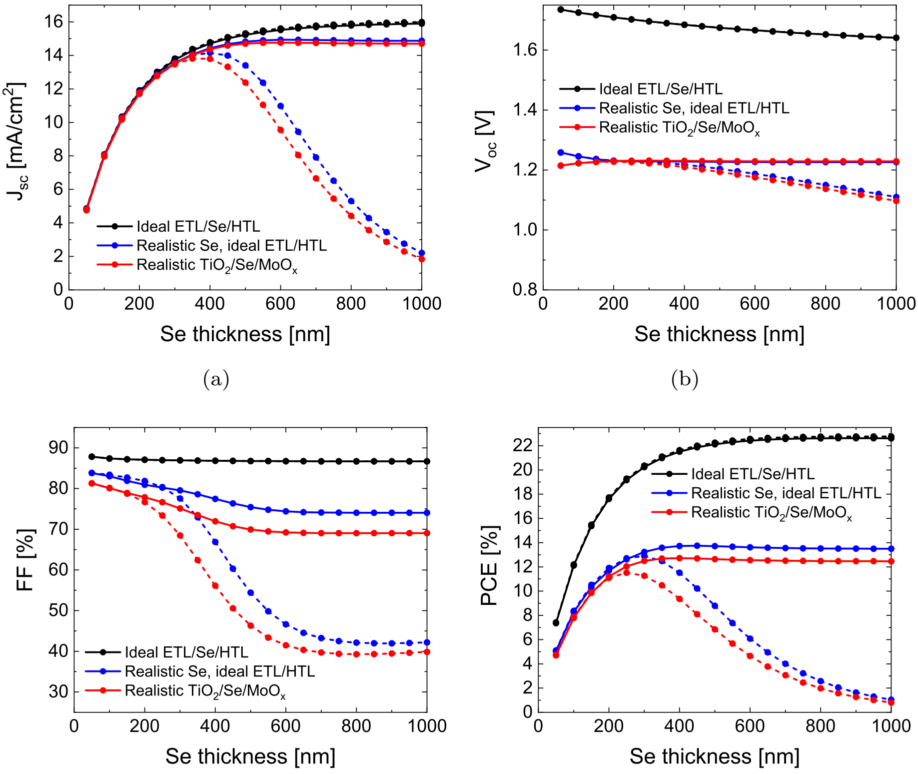

(a) (b)

(c) (d)

Figure 5.15: SCAPS simulations of the device performance parameters of FTO/TiO_2(50 nm)/Se(50-1000 nm)/MoO_x(15 nm)/ITO as a function of Se thickness and illumination direction. Solid lines: FTO/front illumination through the ETL/Se junction. Dashed lines: ITO/back illumination opposite of the ETL/Se junction. The transport layers and Se are subsequently assumed either ideal or realistic/non-ideal.

6 | Conclusion & Outlook

The aim of this project was to produce efficient top-cell Se-based solar cells for the purpose of integration into a monolithic Se-Si tandem photoelectrolysis device. This thesis has presented some of the many achievements and complications that was faced during this endeavour. A Se-Si tandem photoelectrolysis device was never realised but many unique and unpublished champion device structures were achieved, which most notably include the first monolithic tandem Se-Si photovoltaic device with a PCE of 2.2%, the first bifacial Se single-junction device with a state of the art PCE of 5.2% and 2.7% (depending on illumination direction) and a monofacial single-junction record of 6.4% that lies only 0.1% below the world record of 6.5%. All devices had active areas of around 0.4 cm^2 which is greater than most previously reported. The structure of the thesis was meant to reflect this progress and each chapter has focused on addressing relevant aspects along this journey.

Chapter 3 presented the typical Se single-junction architecture which included the physical role of each layer as well as how to fabricate them. The work required to adapt UHV equipment to accommodate the fabrication process was elaborated and a typical fabrication process was introduced. The importance of the crystallisation process of thin film Se was presented. The annealing conditions as well as the need for the Te nucleation layer heavily affects the morphology and grain size of the selenium. The morphology, crystallinity, photoabsorption and bandalignment of Se were measured and corresponds with those reported in literature. The elemental composition of the device layers were confirmed with XPS and ISS and the growth mechanics of Te were identified from ISS to correspond to an island or layer-plus-island formation.

Chapter 4 described the work from single-junction to tandem photovoltaic device fabrication and characterisation. These efforts culminated in a range of various champion devices that were either unique and unreported or obtained greater PCEs than those reported in literature with similar structures. The attempts of fabricating bifacial Se single-junction solar cells resulted in the work described in Paper I, from which an optimal Se absorber thickness is found to be around 300-500 nm. The illumination direction was found to heavily influence the performance of the device, which requires the inversion of the typical device architecture for future tandem incorporations. The reason for the poor Se-Si tandem device performance is yet unknown and requires further investigation. Potential explanations include the need for the inversion of the Se top-cell architecture as well as the presence of an unidentified detrimental series resistance somewhere in the device.

Chapter 5 presented some fundamental measured carrier transport properties of Se and how they relate to present device performance limitations. Low lifetimes are likely the result of intrinsic defects in Se that along with a low carrier mobility limits the diffusion length of the carriers. The optimum Se thickness of 300-500 nm coincides well with the extrapolated depletion region width and the diffusion length that were both found to be around 200 nm. Electronic structure calculations further indicated intrinsic carrier transport limitations which arise from large effective carrier masses and effective density of states that limit the mobility and ultimately the largest obtainable open-circuit voltage and fill factor of the devices. Finally, calculations and simulations were carried out to estimate the present device limitations and how they compare with the overall findings of this project. The greatest limiting factor is estimated to be the poor carrier transport qualities of our present crystalline Se which is plausibly followed by the presence of non-ideal interfaces that result in interface recombination.

Outlook

As the conclusions suggest, the main efforts to improve the Se device performance should be to identify and eliminate the likely presence of defects in both the crystalline Se as well as the device interfaces, that result in non-radiative recombination.

Towards these efforts it may be beneficial to optimise the Se crystal growth, which will require increased control of the pressure, atmosphere, temperature ramp rate, encapsulation and illumination conditions during annealing. Furthermore, investigations should be made to control the Te growth to improve its surface coverage and minimise its thickness. Alternatively, attempts should be made to replace or remove it entirely. Whether Te plays a beneficial or detrimental role in the junction is still uncertain and should be identified. Replacing the FTO with ITO will reduce the surface roughness which could improve the homogeneity of both the Te and Se growth. Optimising the single-junction device with an ITO substrate will also benefit Se-Si tandem fabrication since the Se top-cell is likely to be monolithically grown on an ITO recombination layer. The poor carrier transport qualities of Se dictate that the typical architecture must be inverted when integrated in tandem applications. This will likely be a priority whether or not the lifetime and mobility of the Se can be improved.

Combining all fabrication methods into one single vacuum chamber system would be ideal to limit contamination and oxidation of the device interfaces. This could likely improve and maintain reproducibility as well. Subsequent depositions to

Se should be as gentle as possible to avoid deposition damage that may introduce defects, which will ideally require the use of techniques such as thermal evaporation or atomic layer deposition. Lastly, it is encouraged that all the relevant properties of present and future attempted transport layers are frequently measured and calculated so that device reproducibility can be maintained. This includes the absorptivity, resistivity, bandalignment and doping of the layers.

Whether selenium will ever see the light of day as a commercial photovoltaic material is too early to determine. I would judge it similar to going back in time to 1954 to tell Daryl Chapin, Gerald Pearson and Calvin Fuller whether or not silicon could ever be commercially viable. Selenium devices presently face many limitations, but so did silicon photovoltaics at one point. The future of selenium will be determined by whether these limitations can be overcome or not and that will yet require much more research and work that I hope that some of these results might inspire.

A | SCAPS Material Properties

Table A.1: Material properties of trigonal selenium.

c-Se

Material property	**Value**	**Measured/calculated**	**Literature**	**Assumed**
Bandgap, E_{g}	1.95 eV	✓	✓ [64,67,68]	
Electron affinity, χ_{e}	3.9	✓	✓ [71]	
Relative dielectric permittivity, ϵ_{r}	7.43	✓	✓ [67]	
CB DOS, N_{C}	8.80×10^{19} cm^{-3}	✓	✓ [67]	
VB DOS, N_{V}	1.64×10^{20} cm^{-3}	✓	✓ [67]	
Electron thermal velocity, v_{e}	10^7 cm/s			✓
Hole thermal velocity, v_{h}	10^7 cm/s			✓
Electron mobility, μ_{e}	4.42 cm^2/Vs	✓		✓
Hole mobility, μ_{h}	0.58 cm^2/Vs	✓		✓
Shallow donor density, N_{D}	0 cm^{-3}	✓		
Shallow acceptor density, N_{A}	9×10^{15} cm^{-3}	✓	✓ [67]	
Carrier lifetime, τ	3 ns	✓		
Electron diffusion length, $L_{\mathrm{e-diff}}$	184 nm	✓		
Hole diffusion length, $L_{\mathrm{h-diff}}$	67 nm	✓		

Table A.2: Material properties of anatase TiO_2.

TiO_2

Material property	Value	Measured/calculated	Literature	Assumed
Bandgap, E_g	3.2 eV	✓	✓[112,197–200]	
Electron affinity, χ_e	4.2		✓[112,199]	
Relative dielectric permittivity, ϵ_r	31		✓[201]	
CB DOS, N_C	2.5×10^{19} cm^{-3}			✓
VB DOS, N_V	2.5×10^{19} cm^{-3}			✓
Electron thermal velocity, v_e	10^7 cm/s			✓
Hole thermal velocity, v_h	10^7 cm/s			✓
Electron mobility, μ_e	4 cm^2/Vs		✓[119,202]	
Hole mobility, μ_h	4 cm^2/Vs		✓[119,202]	
Shallow donor density, N_D	10^{19} cm^{-3}			✓
Shallow acceptor density, N_A	0 cm^{-3}			✓
Carrier lifetime, τ	1 μs			
Carrier diffusion length, L_diff	3.2 μm			✓

Table A.3: Material properties of MoO_x.

MoO_x

Material property	**Value**	**Measured/calculated**	**Literature**	**Assumed**
Bandgap, E_g	3.5 eV	✓		
Electron affinity, χ_e	2.3 eV		✓ [122,203,204]	
Relative dielectric permittivity, ϵ_r	4.6	✓	✓ [205]	
CB DOS, N_C	2.5×10^{19} cm^{-3}			✓
VB DOS, N_V	2.5×10^{19} cm^{-3}			✓
Electron thermal velocity, v_e	10^7 cm/s			✓
Hole thermal velocity, v_h	10^7 cm/s			✓
Electron mobility, μ_e	50 cm^2/Vs			✓
Hole mobility, μ_h	50 cm^2/Vs			✓
Shallow donor density, N_D	10^{19} cm^{-3}			✓
Shallow acceptor density, N_A	0 cm^{-3}			✓
Carrier lifetime, τ	1 μs			✓
Carrier diffusion length, L_diff	11 μm			✓

B | Paper I

Semi-transparent selenium solar cells as a top-cell for tandem photovoltaics

Tomas H. Youngman, Rasmus Nielsen, Andrea Crovetto, Brian Seger, Ole Hansen,
Ib Chorkendorff, Peter C. K. Vesborg

Under review at Solar RRL

Semi-transparent selenium solar cells as a top-cell for tandem photovoltaics

*Tomas H. Youngman, Rasmus Nielsen, Andrea Crovetto, Brian Seger, Ole Hansen, Ib Chorkendorff, Peter C. K. Vesborg**

Tomas H. Youngman, Rasmus Nielsen, Prof. Brian Seger, Prof. Ib Chorkendorff, Prof. Peter C. K. Vesborg
Surfcat, DTU Physics, Technical University of Denmark, DK-2800 Kongens Lyngby, Denmark.
E-mail: Peter.Vesborg@fysik.dtu.dk

Dr. Andrea Crovetto
Department of Structure and Dynamics of Energy Materials, Helmholtz-Zentrum Berlin für Materialien und Energie, 14019 Berlin, Germany.

Prof. Ole Hansen
DTU Nanolab, National Center for Nano Fabrication and Characterization, Technical University of Denmark, DK-2800, Kgs. Lyngby, Denmark.

Keywords: photovoltaic devices, selenium, solar cells, tandem photovoltaics, bifacial

Trigonal selenium (Se) is an elemental, direct bandgap (1.95 eV) semiconductor with a low processing temperature, which could be a suitable top absorber for tandem solar cell applications. For incorporation in tandem architectures, both sides of the Se cell should be semi-transparent. However, all reported Se solar cells have metallic back contacts. To demonstrate the potential feasibility of Se as a wide-bandgap absorber for tandems, we report bifacial single-junction selenium solar cells with device areas above 0.4 cm^2 using FTO on the n-type contact side and ITO on the p-type contact side. When illuminating through the n-type contact the bifacial cell power conversion efficiency (PCE) is 5.2%, similar to a standard monofacial cell. The efficiency is lower (2.7%) when illuminating through the p-type contact, which is attributed to low carrier diffusion lengths and lifetimes in selenium. This suggests inverting the typical single-junction device structure when incorporating it into a tandem device.

In recent years silicon-based photovoltaics have achieved major cost reductions. The two main cost-reduction drivers of silicon-based solar cells has been to increase the cell efficiency as well as reduce the total system processing cost. The silicon-based solar cells are now approaching their theoretical Shockley-Queisser (SQ) efficiency limit for a single absorber with a 1.1 eV bandgap (29.4%).[1] Simultaneously, the cell cost has become only a minor fraction of the total system cost.[2,3] Therefore, further improvements of cell efficiency or reduction of cell cost does not significantly affect the levelized cost of energy (LCOE). A way to overcome the single-absorber SQ-limit is to use a tandem solar cell architecture which introduces a wide-bandgap (>1.6 eV) absorber cell on top of a smaller bandgap absorber cell. A suitable small bandgap absorber could be (1.12 eV) silicon.[4,5] Tandem cells have the potential to offer large efficiency improvements and in turn a lower LCOE as a result.[6]

Selenium (Se) is a suitable wide-bandgap absorber with a reported direct bandgap of 1.83 eV to 2 eV for its crystalline trigonal allotrope.[7,8] Selenium is an inexpensive single-element semiconductor with a low toxicity and a low melting point (220 ^{o}C), which offers potential for a low cost fabrication process. We report a bandgap of 1.95 eV for our trigonal Se which in conjunction with Si in a Se-Si tandem has the SQ-efficiency limit of ≈37% or ≈44% for a 2-terminal (2T) or 3-terminal (3T) design, respectively.[9] For a 2T design, ≈41% should be obtainable with a $E_g \approx 1.4$ eV top-cell absorber (e.g. GaAs with $E_g = 1.42$ eV).[5] In order to let the light with energies below the bandgap of the Se transmit through the top-cell stack, it must be semi-transparent on both sides. If light is able to pass through both sides of the device it is called a bifacial solar cell. Making bifacial single-junction Se solar cells is key to understanding the limitations of both the Se absorber and the device architecture itself, which is crucial knowledge to possess before incorporating it into a tandem device.

Selenium was demonstrated as the very first photovoltaic material by Charles Fritts in 1883 with a power-conversion efficiency (PCE) of <1%, just ten years after Willoughby Smith discovered its photoconductivity.[10,11] However, due to the success of the c-Si technology and the fact that the bandgap of Se is too large for use as a single-absorber cell, only limited efforts have been made to further develop selenium for photovoltaic purposes. In 1985, Nakada et al. achieved a PCE of 5.0% with a single junction selenium solar cell which was recently surpassed by Todorov et al. in 2017 with a PCE of 6.5% for a contact area of 0.023 cm^2.[12,13] Others have since reported insights into the further improvement of the selenium solar cells by tuning the annealing conditions for the selenium crystallization.[14,15] Most recently, the structure architecture has been adapted with organic electron- and hole-transport layers that have been shown to improve the stability of the devices and it has been demonstrated to function with a 3.9% PCE in the inverted structure.[16,17]

In this study, we report the first bifacial selenium solar cell with state of the art performance above 5% PCE from front-side illumination (through n-type contact) and 2.7% PCE from back-side illumination (through the p-type contact) for devices with contact areas above 0.4 cm^2. For these contact area sizes, we show better bifacial cell performance than any reported monofacial cells of similar size. By replacing the back-side Au contact with ITO we demonstrate similar device performances from front-side illumination and simultaneously allow for back-side illumination. These are important steps towards future scalability of selenium devices as well as future tandem investigations where light with photon energies below the top-cell bandgap has to transmit through the cell.

Cells were fabricated by using physical vapour deposition techniques with a similar cell architecture of FTO/ZnMgO/Te/Se/MoO$_x$/(Au or ITO) as reported by Todorov et al. (see Figure S1).[13] All layers were deposited at room temperature unless otherwise stated. ZnMgO (≈60 nm) was deposited on commercial FTO(500 nm)/SLG substrates from a $Zn_{0.85}Mg_{0.15}O$ stoichiometric target by use of RF magnetron sputtering in a 5 mTorr 30/0.3 sccm Ar/O$_2$ atmosphere for 3 hours. Te (≈1 nm) was thermally evaporated under vacuum with a rate of ≈0.25 Å/s for 40 seconds at ≈390-400 ^{o}C. Se (100-750 nm) was thermally evaporated under vacuum with rates of ≈20-30 nm/min at ≈85-95 ^{o}C. MoO$_x$ (≈15-25 nm) was deposited by use of DC magnetron sputtering in a 5 mTorr 30/5 sccm Ar/O_2 atmosphere for 6-8 minutes. For monofacial devices, Au (≈30 nm) was deposited with DC magnetron sputtering under a 5 mTorr 30 sccm Ar atmosphere for 6 minutes. For bifacial devices, ITO (≈200-300 nm) was deposited with RF magnetron sputtering at 100 ^{o}C in a 3 mTorr 41/0.3 sccm Ar/O_2 atmosphere for 2.5-4.5 hours. Devices were annealed in air at ≈190 ^{o}C for 2-4 minutes (depending on Se thickness) in a small home-made aluminum mini-oven after each Se, MoOx and Au/ITO deposition step. Devices that were not annealed in this manner performed worse (i.e. leaving out a single of the annealing steps was detrimental). It is believed that each annealing step during the fabrication process helps to alleviate potential sputter damage of the Se absorber. The increased annealing time seems to increase the size of the Se crystal grains, which also increases the roughness of the film (see Figure S2). For Se thicknesses below <300 nm Se, the larger roughness increases the risk of shunting. Better performance was observed for such devices if they were annealed for 2 minutes instead of 4 minutes during each annealing step.

Figure 1 shows the current-voltage (J-V) and external quantum efficiency (EQE) performance of both monofacial and bifacial devices with varying Se thickness.

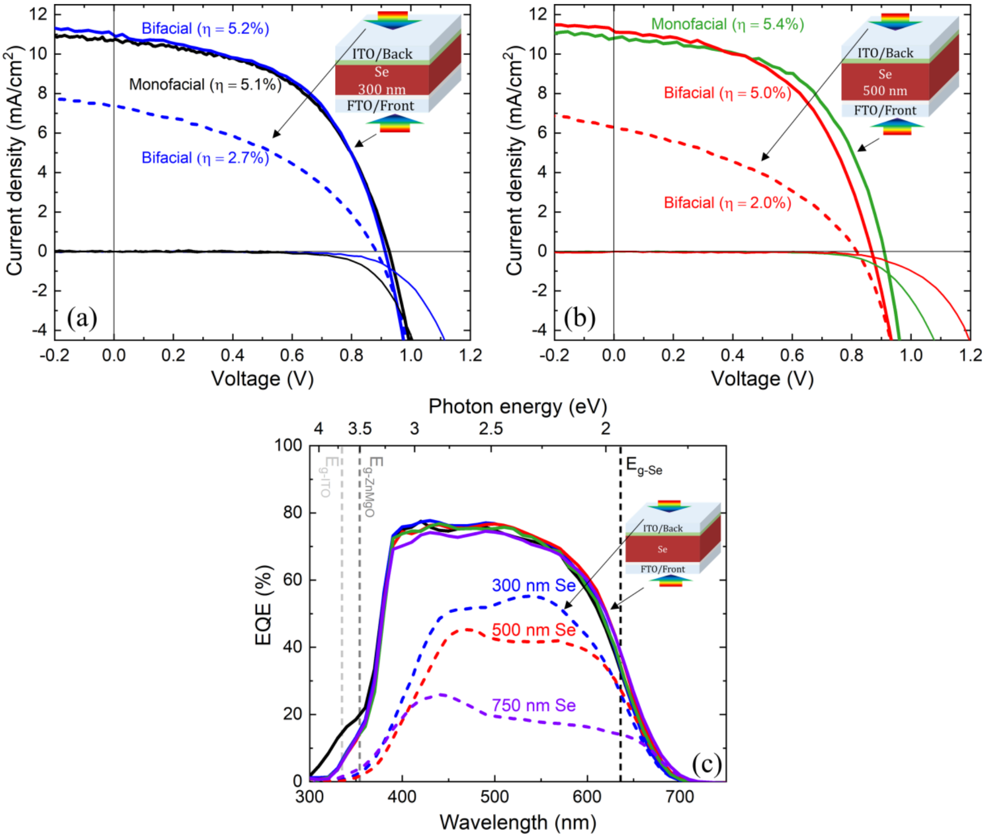

Figure 1. (a), (b) Measured current-voltage (J-V) characteristics of monofacial and bifacial cells in the dark (thin lines) and under 100 mW/cm^2 AM1.5G solar irradiation. (a) 300 nm thick Se cells. (b) 500 nm thick Se cells. (c) External quantum efficiency (EQE) measurements of the same devices as well as a bifacial device with 750 nm Se shown in purple. EQE scans were made with a step size of 10 nm. Monofacial FTO/ZnMgO/Se/MoO$_x$/Au devices are shown as black and green. Bifacial FTO/ZnMgO/Se/MoO$_x$/ITO devices measured with front illumination are shown as blue, red and purple. Bifacial back illumination is shown with dashed lines of the corresponding colour. The EQE shows a bandgap of Se of ≈1.9 eV for all devices.

The monofacial and bifacial cells show similar device performance with front-side illumination indicating no inhibition of performance by replacement of Au with ITO. When comparing the 300 nm and 500 nm Se devices there seems to be no major difference in the JV-performance parameters for front-side illumination. However, it is noticeable that with back-side illumination a lower collected current and fill factor is observed compared to front-side illumination. This difference is likely related to the position of the charge carrier-separating junction at the n-type ZnMgO and p-type Se interface as was confirmed by device simulations

(Figure S6). This p-n junction is closest to the front-side of the device and therefore back-side illumination performance is more dependent on the diffusion length of the photoexcited carriers. It has previously been reported that trigonal Se thin films, annealed under similar conditions, exhibit low lifetimes which results in a low diffusion length.[18] Therefore it is expected that the bifacial cells under back-side illumination will generate a higher current for thinner Se cells as is also seen from the EQE in Figure 1 (c). The direct transmission of the bifacial devices as a function of Se thickness is shown in Figure S3.

Since longer wavelength photons penetrate deeper on average, this diffusion length limitation becomes especially apparent from the shape of the EQE spectra (see Figure 1(c)) where an optimum ≈77% collection is observed for low wavelengths from front-side illumination of all devices. For back-side illumination there is low collection efficiency for shorter wavelengths and greater collection efficiency for the longer wavelengths, that are absorbed (on average) closer to the ZnMgO/Se interface. For the champion 300 nm bifacial cell an optimum ≈55% collection efficiency is observed around 550 nm wavelength for back-side illumination.

Table 1 summarizes the device characteristics of the champion devices.

Table 1. JV-characteristics of champion bifacial and monofacial selenium-based solar cells. The values in parentheses are from ITO/back illumination.

Device type	Se thickness	J_{sc} (mA/cm^2)	V_{oc} (V)	FF (%)	PCE (%)
Bifacial	300 nm	10.96 (7.40)	0.91 (0.88)	52.6 (41.4)	5.2 (2.7)
Monofacial	300 nm	10.67	0.93	51.7	5.1
Bifacial	500 nm	11.16 (6.34)	0.87 (0.82)	51.4 (37.9)	5.0 (2.0)
Monofacial	500 nm	10.78	0.91	55.0	5.4

The change in the JV-characteristics was investigated as a function of selenium thickness for bifacial cells for both front- and back-illumination. The results are shown in **Figure 2**.

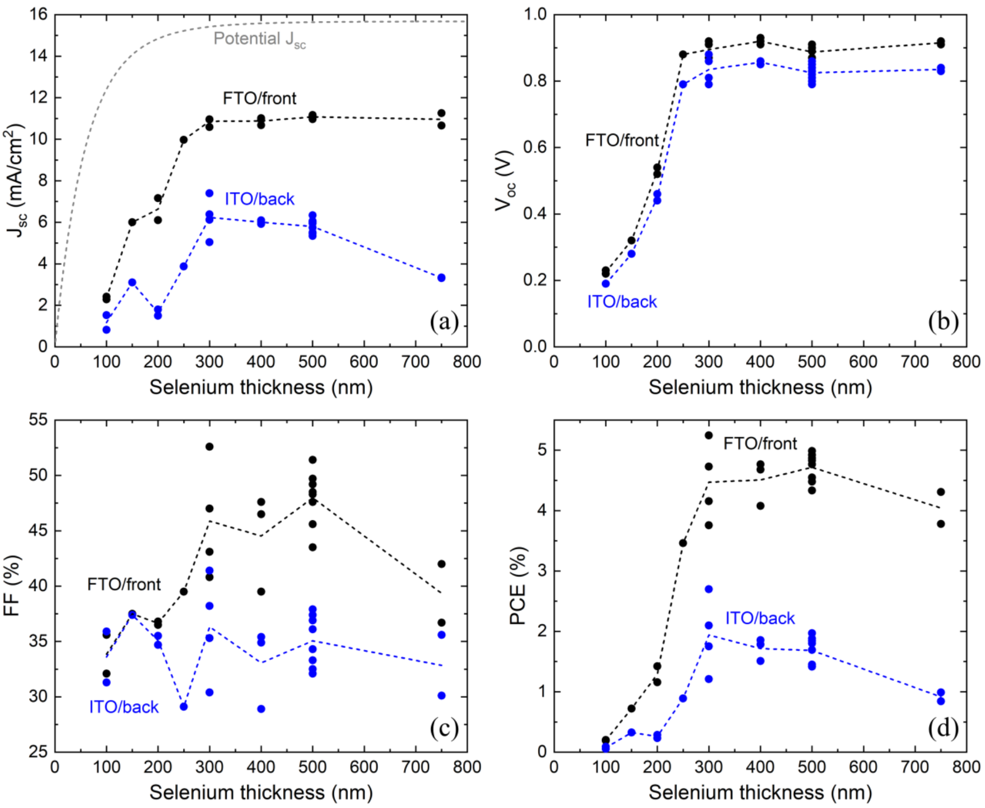

Figure 2. Statistics and mean-line trends for photovoltaic parameters of selenium-based solar cells as a function of selenium thickness. (a) Short-circuit current, J_{sc}, with calculated potential J_{sc} from combined total transmission and total reflection data of Se on quartz, where all non-transmitted and non-reflected light is assumed to be both absorbed and collected from the AM1.5G spectrum above the direct bandgap of 1.95 eV (see Figure S4). (b) Open-circuit voltage, V_{oc}. (c) Fill factor, FF. (d) Power conversion efficiency, PCE.

As expected from the potential J_{sc} curve in Figure 2 (a), a maximum current is obtained above a certain selenium thickness threshold (around 300 nm Se for our devices) for front-side illumination. The discrepancy between the largest measured J_{sc} and the potentially collected J_{sc}, is mainly related to reflection and a non-ideal long wavelength shoulder shape of the EQE (as seen in Figure 1 (c)). For back-side illumination, an optimum J_{sc} is observed around 300 nm Se thickness, which as discussed previously relates to the position of the charge carrier-separating junction. The junction position being opposite side of the illumination side, gives rise to an optimum ratio between photon absorption and electron-hole pair collection efficiency, since the former will increase with the absorber thickness and the latter will decrease.

The V_{oc} trend is similar for both illumination sides and remains around 20-100 mV lower for back-side illumination compared to front-side illumination for all Se thicknesses. The V_{oc} decreases significantly below a Se thickness of 250 nm. This is attributed to either a large Se roughness, as seen from SEM images in Figure S2, and/or a large surface recombination rate at the contacts.

The FF seems to have an optimum for cells with a Se thickness around 300-500 nm. This optimum is expected due to a trade-off between the series and shunt resistance, R_s and R_{sh}, which should both increase with increasing Se thickness. The FF is rather unaffected by the Se thickness for back-side illumination. The general low FF of the devices is mainly related to the non-ideal JV-diode behavior of the devices (see Figure S5). The FF should increase from both illumination sides for thinner Se thicknesses, but since the V_{oc} decreases, so does the FF.

The culmination of these characteristic trends is seen in the PCE, where an optimum is found for both illumination sides around 300-500 nm Se.

One-dimensional SCAPS (a Solar Cell Capacitance Simulator) simulations of the JV-characteristics of a bifacial Se solar cell with ideal transport layers as a function of Se thickness and illumination side are shown in Figure S6.[19] The trends of the simulated JV-characteristics match well with the experimental ones, where an optimal Se thickness was found to be ≈300-500 nm for FTO/front illumination and ≈250 nm for ITO/back illumination.

To investigate the long-term durability of our real bifacial device architecture, we measured the aging effects of the JV-curve of the champion bifacial cell after a period of 9 weeks being at room temperature under ambient conditions without encapsulation. The results are shown in Figure S6. A loss in J_{sc} and FF is recovered after reannealing at 190 °C for 4 minutes.

In summary, we have fabricated selenium-based bifacial solar cells with a champion device of 300 nm Se with a PCE of 5.2% and 2.7% from front-side- and back-side illumination, respectively. It was shown how the performance from back-side illumination is more strongly dependent on the architecture of the device and also in particular the selenium thickness. This is an important step towards a future Se incorporated tandem, where it will be advantageous to invert the typical single-junction device structure before/when incorporating it into the tandem device. It must be noted that the overall low performance of the Se solar cell, is to be further improved before one can expect any useful tandem performance. The limitations of the Se solar cell performance are currently mainly expected to be related to low charge carrier lifetimes and diffusion lengths in the fabricated films of Se. Extensive studies on improving the Se crystal quality and reducing native defects is encouraged.

Experimental Section

Materials: Se(99.999+%) and Te(99.9999%) pellets as well as FTO-coated glass substrates (≈7 Ω/sq) were purchased from Sigma-Aldrich. Zn0.85Mg0.15O (99.95+%), Mo (99.98%), Au(99.99%) and ITO 90/10 wt% (99.99%) targets were purchased from AJA International.

Device fabrication: FTO-coated glass was cut into 14x16 mm substrate sizes. The substrates were cleaned by ultrasonication with Triton X-100, acetone and isopropanol for 15 minutes each. The substrates were rinsed with deionized water and dried with nitrogen gas. All layers were deposited at room temperature unless otherwise is stated. A layer of ZnMgO (≈60 nm) was deposited by RF magnetron sputtering from a stoichiometric Zn0.85Mg0.15O target for 3 hours (rate of ≈0.33 nm/min) at 5 mTorr with an inlet flow of 30/0.3 sccm Ar/O2. Te (≈1 nm) was deposited by thermal evaporation for 40 seconds (rate of ≈0.25 Å/s) at a pressure of ≈10^{-8} mTorr and a resistively heated boat temperature of ≈390-400 °C. Subsequently Se (100-750 nm) was thermally evaporated at a rate of ≈20-30 nm/min at a pressure of ≈10^{-7} mTorr and at a resistively heated boat temperature of ≈85-95 °C. MoOx (≈15-25 nm) was deposited by DC magnetron sputtering from a Mo target for 6-8 minutes (rate of ≈2.5-3 nm/min) at 5 mTorr with an inlet flow of 30/5 sccm Ar/O2. For monofacial devices Au (≈30 nm) was deposited with DC magnetron sputtering for 6 minutes (rate of ≈5 nm/min) at 5 mTorr with an inlet flow of 30 sccm Ar. For bifacial devices ITO (≈200-300 nm) was deposited with RF magnetron sputtering at 100 ^{o}C from a stoichiometric ITO (90/10 wt%) target for 2.5-4.5 hours (depending on both the position of the ITO target and the deposited ITO film thickness) (rate of 1.1 nm/min or 2.2 nm/min depending on target position in vacuum chamber) at 3 mTorr with an inlet flow of 41/0.3 Ar/O2 atmosphere.

Devices were annealed at ≈190 ^{o}C for 2-4 minutes (depending on Se thickness) in a small home-made aluminum minioven after each Se, MoOx and Au/ITO deposition step.

Film and device characterization: The thickness of ZnMgO, MoO_x and ITO was measured by use of a spectroscopic ellipsometer VASE (J.A. Woollam) with the thin films being deposited on substrates of silicon. The thickness of Te, Se and Au was estimated from the measured rate of a quartz crystal microbalance (QCM). The thickness of Se and Au compares well with the observed thickness seen with scanning electron microscope (SEM) images (see Figure S1)**.** SEM images were made with with a Supra 40 VP SEM from Zeiss. An InLens detector was used for the cross-sectional images.

Ultraviolet-visible (UV-Vis) transmission spectra were measured with a UV-2600 spectrophotometer from Shimadzu in the 300-1000 nm wavelength range at room temperature.

Total transmission and total reflection were measured in a double-beam Cary 7000 spectrophotometer. Total transmission (the sum of direct and diffuse transmission) was measured by collecting the light transmitted over a ~2π sr solid angle using an integrating sphere. Similarly, total reflection (the sum of mirror and diffuse reflection) was measured by collecting the light reflected over a ~2π sr solid angle using an integrating sphere, with an incidence angle close to normal. The absorption coefficient, α, was then derived from the transmission, T, by use of the equation: $\alpha = A/d$, where A is the absorbance $A = -\log_{10}(T)$ and the d is the thickness.

EQE spectra were measured from 300-800 nm in steps of 10 nm without bias voltage with a QEXL from PV Measurements. A Si photodiode was used for calibration. J-V measurements were made in air at room temperature under 100 mW/cm^2 AM1.5G solar irradiation with a Keithley 2561A source meter with a 4-terminal sensing setup. The light intensity was calibrated by use of a reference Si solar cell from Orion and a shutter controlled the incident light. All scans were made in reverse. Even with a calibrated light intensity, a spectral mismatch from the solar simulator as well as internal reflection from outside the active area of the solar cells can result in overstated J_{sc} for wide-bandgap absorbers. Therefore, all measured J-V curves were adjusted down to match the measured J_{sc} from the EQE measurements.[13]

Supporting Information
Supporting Information is available from the Wiley Online Library or from the author.

Acknowledgements
This work was supported by the Villum Foundation V-SUSTAIN grant (9455) to the Villum Center for the Science of Sustainable Fuels and Chemicals.

Received: ((will be filled in by the editorial staff))
Revised: ((will be filled in by the editorial staff))
Published online: ((will be filled in by the editorial staff))

References

[1] A. Richter, M. Hermle, S.W. Glunz, Reassessment of the limiting efficiency for crystalline silicon solar cells, IEEE J. Photovoltaics. 3 (2013) 1184–1191. https://doi.org/10.1109/JPHOTOV.2013.2270351.

[2] G. Kavlak, J. McNerney, J.E. Trancik, Evaluating the causes of cost reduction in photovoltaic modules, Energy Policy. 123 (2018) 700–710. https://doi.org/10.1016/j.enpol.2018.08.015.

[3] M.A. Green, Commercial progress and challenges for photovoltaics, Nat. Energy. 1 (2016) 15015. https://doi.org/10.1038/nenergy.2015.15.

[4] M.A. Green, Photovoltaic technology and visions for the future, Prog. Energy. 1 (2019)

013001. https://doi.org/10.1088/2516-1083/ab0fa8.

[5] G.E. Eperon, M.T. Hörantner, H.J. Snaith, Metal halide perovskite tandem and multiple-junction photovoltaics, Nat. Rev. Chem. 1 (2017). https://doi.org/10.1038/s41570-017-0095.

[6] Z. Li, Y. Zhao, X. Wang, Y. Sun, Z. Zhao, Y. Li, H. Zhou, Q. Chen, Cost Analysis of Perovskite Tandem Photovoltaics, Joule. 2 (2018) 1559–1572. https://doi.org/10.1016/j.joule.2018.05.001.

[7] A.K. Bhatnagar, K.V. Reddy, V. Srivastava, Optical energy gap of amorphous selenium: Effect of annealing, J. Phys. D. Appl. Phys. 18 (1985) L149–L153. https://doi.org/10.1088/0022-3727/18/9/001.

[8] S. Tutihasi, I. Chen, Optical properties and band structure of trigonal selenium, Phys. Rev. 158 (1967) 623–630. https://doi.org/10.1103/PhysRev.158.623.

[9] P. Tockhorn, P. Wagner, L. Kegelmann, J.C. Stang, M. Mews, S. Albrecht, L. Korte, Three-Terminal Perovskite/Silicon Tandem Solar Cells with Top and Interdigitated Rear Contacts, ACS Appl. Energy Mater. 3 (2020) 1381–1392. https://doi.org/10.1021/acsaem.9b01800.

[10] W.G. Adams, R.E. Day, The Action of Light on Selenium. [Abstract], Proc. R. Soc. London. 25 (1876) 113–117. https://doi.org/10.2307/113462.

[11] C.E. Fritts, On a new form of selenium photocell Am. J. Sci., vol. 26, no. 156, pp. 465–472, Dec. 1883., Am. J. Sci. 26 (1883) 465–472.

[12] T. Nakada, A. Kunioka, Polycrystalline Thin-Film TiO2_Se Solar Cells, Jpn. J. Appl. Phys. 24 (1985) L536–L538.

[13] T.K. Todorov, S. Singh, D.M. Bishop, Y.S. Lee, T.S. Gershon, P.D. Antunez, R.A. Haight, Ultrathin, record-performance solar cells with high band gap from the world's oldest photovoltaic material, Nat. Commun. (2017). https://doi.org/10.1038/s41467-017-00582-9.

[14] I. Hadar, T. Bin Song, W. Ke, M.G. Kanatzidis, Modern Processing and Insights on Selenium Solar Cells: The World’s First Photovoltaic Device, Adv. Energy Mater. 1802766 (2019) 1–9. https://doi.org/10.1002/aenm.201802766.

[15] J. Wu, Z. Zhang, C. Tong, D. Li, A. Mei, Y. Rong, Y. Zhou, H. Han, Y. Hu, Two-Stage Melt Processing of Phase-Pure Selenium for Printable Triple-Mesoscopic Solar Cells, ACS Appl. Mater. Interfaces. 11 (2019) 33879–33885. https://doi.org/10.1021/acsami.9b09572.

[16] W. Liu, A.A. Said, W.J. Fan, Q. Zhang, Inverted Solar Cells with Thermally Evaporated Selenium as an Active Layer, ACS Appl. Energy Mater. (2020). https://doi.org/10.1021/acsaem.0c00680.

[17] W. Liu, F. Yu, W. Fan, Q. Zhang, Improved stability and efficiency of polymer-based selenium solar cells through the usage of tin(iv) oxide in the electron transport layers and the analysis of aging dynamics, Phys. Chem. Chem. Phys. 22 (2020) 14838–14845. https://doi.org/10.1039/d0cp02367a.

[18] M. Zhu, F. Hao, L. Ma, T.-B. Song, C.E. Miller, M.R. Wasielewski, X. Li, M.G. Kanatzidis, Solution-Processed Air-Stable Mesoscopic Selenium Solar Cells, ACS Energy Lett. 1 (2016) 469–473. https://doi.org/10.1021/acsenergylett.6b00249.

[19] M. Burgelman, P. Nollet, S. Degrave, Modelling polycrystalline semiconductor solar cells, Thin Solid Films. 361 (2000) 527–532. https://doi.org/10.1016/S0040-6090(99)00825-1.

Semitransparent selenium solar cells are reported with a champion state-of-the art performance efficiency of 5.2%, when illuminating through the carrier-separating junction and 2.7% when illuminating from the opposite side of the device. Varying the Se thickness shows a narrow optimal selenium thickness of approximately 300-500 nm for both illumination directions. Inverting the typically reported architecture is encouraged for tandem fabrication.

Selenium bifacial solar cells

*Tomas H. Youngman, Rasmus Nielsen, Andrea Crovetto, Brian Seger, Ole Hansen, Ib Chorkendorff, Peter C. K. Vesborg**

Semi-transparent selenium solar cells as a top-cell for tandem photovoltaics

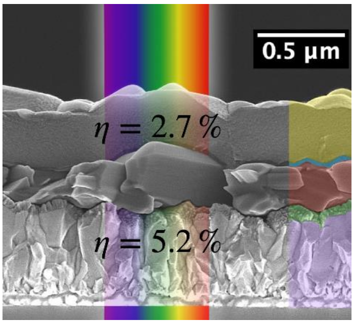

Supporting Information

Semi-transparent selenium solar cells as a top-cell for tandem photovoltaics

*Tomas H. Youngman, Rasmus Nielsen, Andrea Crovetto, Brian Seger, Ole Hansen, Ib Chorkendorff, Peter C. K. Vesborg**

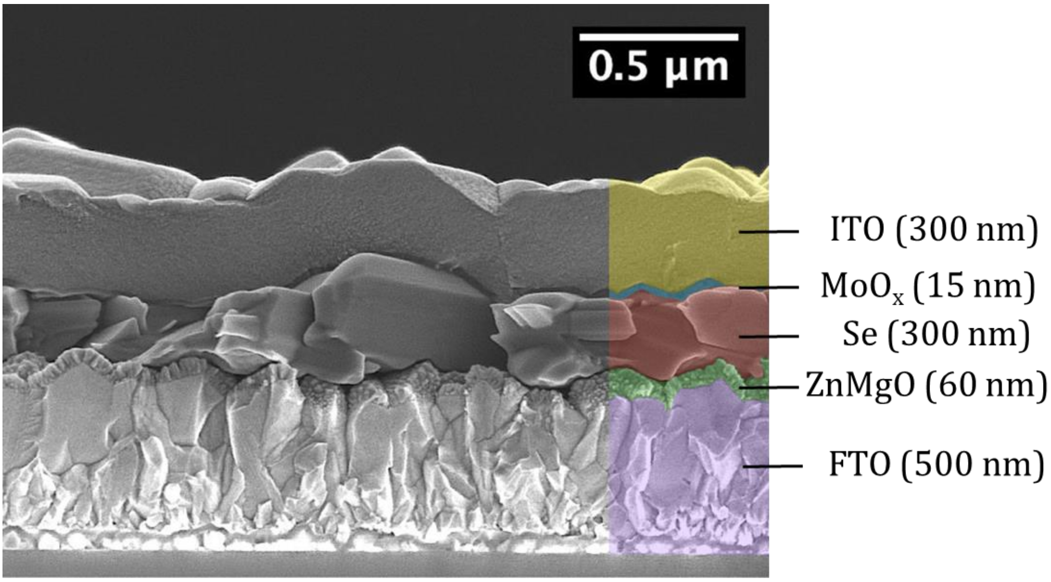

Figure S1. Cross-sectional SEM image of the bifacial FTO/ZnMgO/Se/MoO$_x$/ITO illustrating the layers of the device.

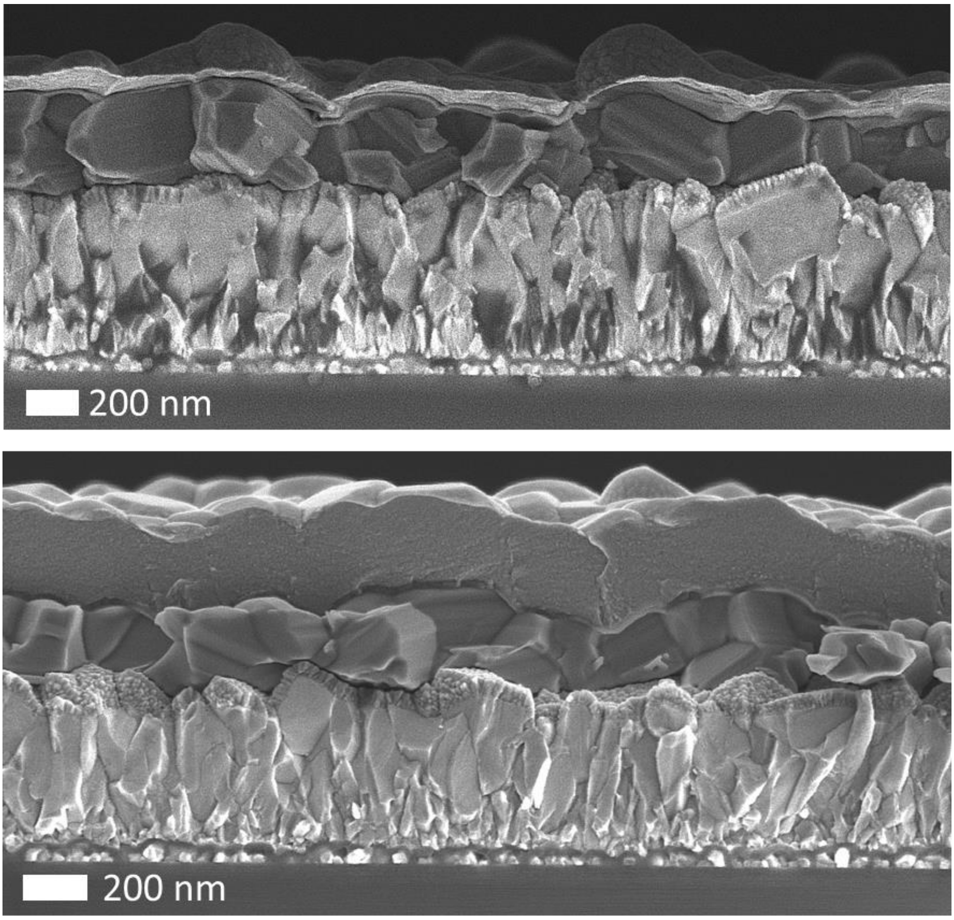

Figure S2. Cross-sectional SEM image of a monofacial FTO/ZnMgO/Se/MoO$_x$/Au (top image) and bifacial FTO/ZnMgO/Se/MoO$_x$/Au/ITO device (bottom image).

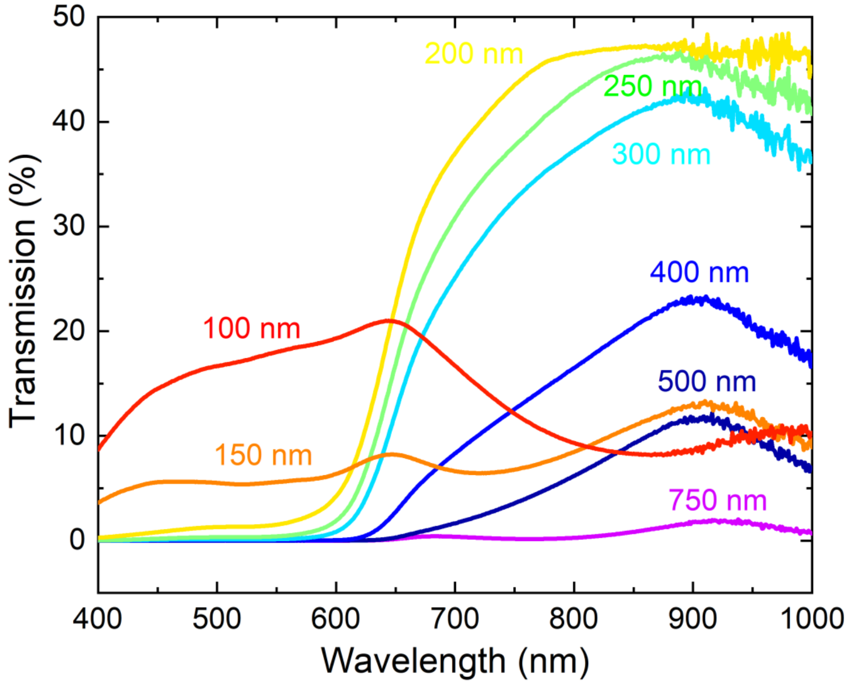

Figure S3. Direct transmission UV-Vis measurements of FTO/ZnMgO/Se/MoO_x/ITO bifacial cells as a function of Se thickness.

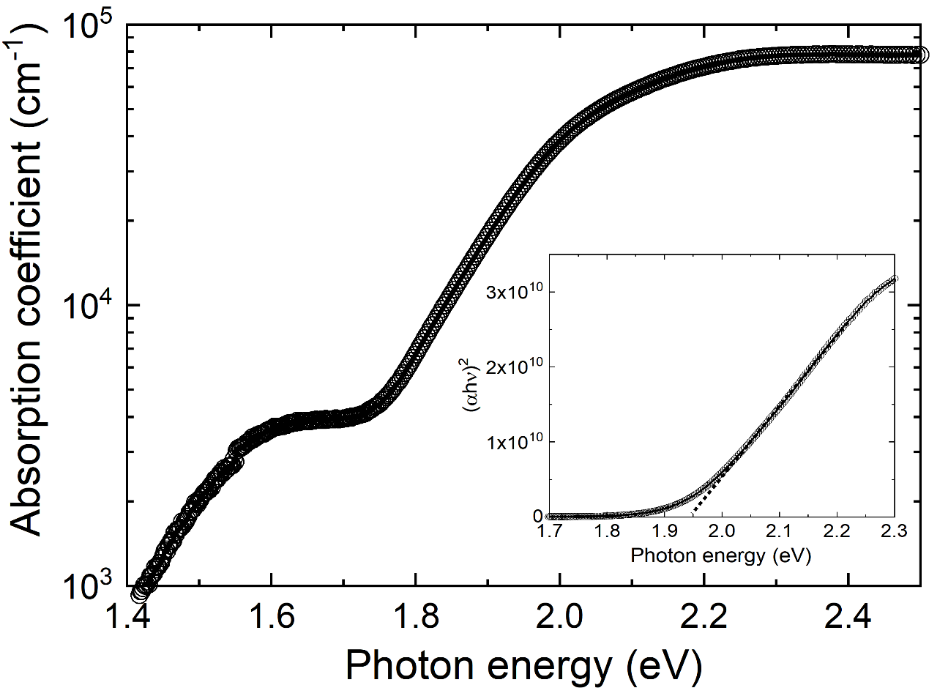

Figure S4. Absorption coefficient and Tauc plots of 300 nm Se on 1 nm Te on quartz (annealed at 190 °C for 4 minutes). The plots are calculated from the combined total transmission and total reflection data and the direct optical bandgap is extrapolated from the Tauc plot to be 1.95 eV.

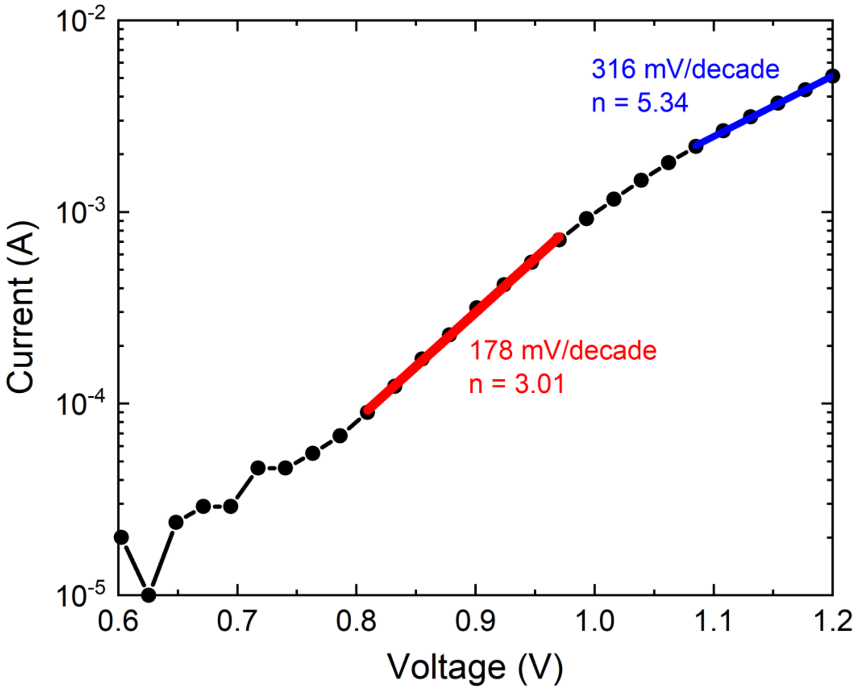

Figure S5. $Log_{10}(I)$ as a function of voltage for the dark IV measurement of the champion 300 nm bifacial device. The ideality factor, n, is calculated from the slope of the natural logarithm linear fit of the blue and red lines.

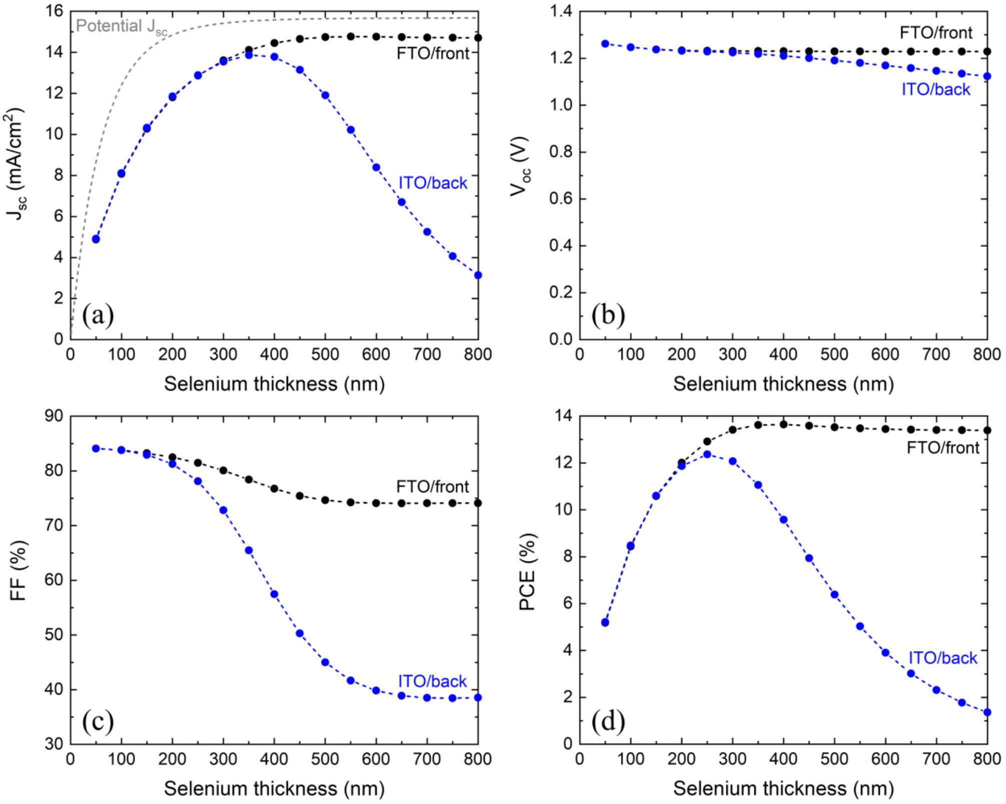

Figure S6. One-dimensional SCAPS (a Solar Cell Capacitance Simulator) simulations for an ideal FTO/ETL/Se/HTL/ITO bifacial cell architecture for photovoltaic parameters as a function of selenium thickness.[19] (a) Short-circuit current, J_{sc}, with calculated potential J_{sc} from total transmission data of Se on quartz, where all non-transmitted and non-reflected light is assumed to be both absorbed and collected from the AM1.5G spectrum above the direct bandgap of 1.95 eV (see Figure S4). (b) Open-circuit voltage, V_{oc}. (c) Fill factor, FF. (d) Power conversion efficiency, PCE. Further details about these simulations are provided in the section below.

SCAPS simulation details

SCAPS (Solar Cell Capacitance Simulator) is a one dimensional solar cell simulation program developed at the Department of Electrons and Information Systems (ELIS) of the University of Grent, Belgium.[19] A simple simulation was done with an ideal architecture of TCO/ETL/Se/HTL/TCO, where the TCOs (transparent conducting oxides) represent ideal ITO and FTO layers and the ETL (electron transport layer) and HTL (hole transport layer) represent ideal transport layers instead of our ZnMgO and MoO_x, respectively, in our real architecture. Realistic values for the material parameters of Se with low lifetimes ($\tau = 3$ ns), carrier mobilities ($\mu = 2.5$ cm^2/Vs) and diffusion lengths ($L = 140$ nm) were assumed. From these chosen values, we get a reasonable fit with our experimental data. The band alignment of the ideal transport layers (i.e. the ETL, HTL and TCOs) were set to match the Se for ideal collection of carriers. The ETL and HTL were set to have bandgaps of >3 eV to avoid parasitic absorption and ensure selective electron/hole transport. For ideal as well as realistic band bending the donor and acceptor levels of the ETL and HTL were set to 10^{18}-10^{19} cm^{-3}. The simulations were in this manner done to simulate the current device performance limitations of the Se absorber itself as a function of both the absorber thickness and the illumination side as illustrated in Figure S5.

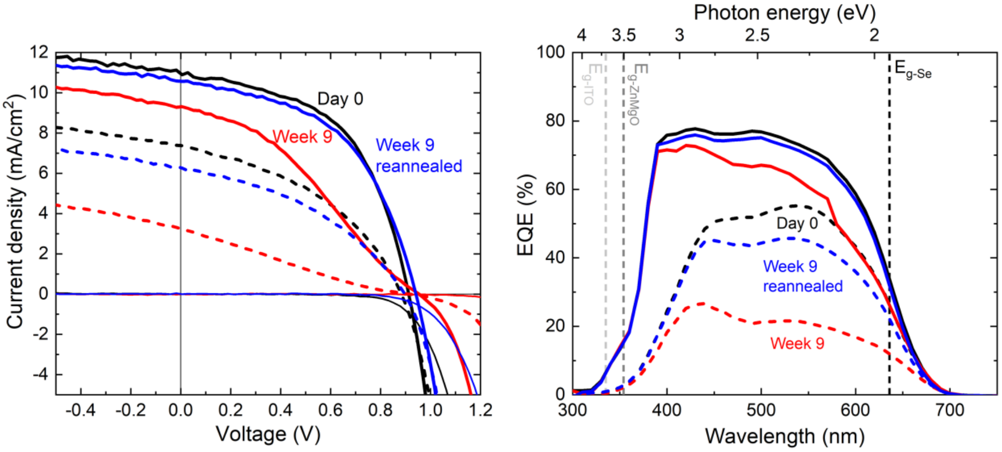

Figure S7. JV and EQE of bifacial 300 nm Se champion device before and after long-term aging of 9 weeks at room temperature under ambient conditions without encapsulation. The cell was annealed again at 190 ^{o}C for 4 minutes (after the week 9 measurement) and retained similar performance as that on day 0. Solid lines: FTO/front illumination. Dashed lines: ITO/back illumination.

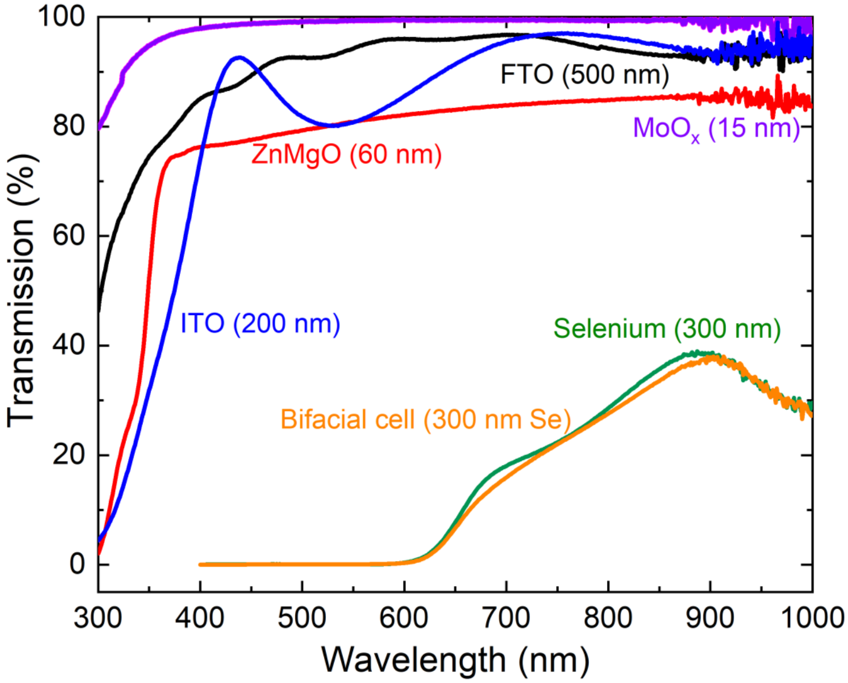

Figure S8. Direct transmission of all fabricated layers of the bifacial selenium solar cell.

References

[1] W. Steffen, J. Rockström, K. Richardson, T. M. Lenton, C. Folke, D. Liverman, C. P. Summerhayes, A. D. Barnosky, S. E. Cornell, M. Crucifix, J. F. Donges, I. Fetzer, S. J. Lade, M. Scheffer, R. Winkelmann, and H. J. Schellnhuber, "Trajectories of the Earth System in the Anthropocene," *Proceedings of the National Academy of Sciences of the United States of America*, vol. 115, no. 33, pp. 8252–8259, 2018.

[2] J. R. Petit, J. Jouzel, D. Raynaud, J. M. Barnola, I. Basile, M. Bender, J. Chappellaz, M. Davis, G. Delaygue, M. Delmotte, V. M. Kotlyakov, M. Legrand, V. Y. Lipenkov, C. Loriu, L. Pepin, C. Ritz, E. Saltzman, and M. Stievenard, "Climate and atmospheric history of the past 420,000 years from the Vostok ice core, Antarctica," *The Future of Nature: Documents of Global Change*, pp. 348–358, 2013.

[3] C. P. Morice, J. J. Kennedy, N. A. Rayner, and P. D. Jones, "Quantifying uncertainties in global and regional temperature change using an ensemble of observational estimates: The HadCRUT4 data set," *Journal of Geophysical Research Atmospheres*, vol. 117, no. 8, pp. 1–22, 2012.

[4] T. F. Stocker, D. Qin, G. K. Plattner, M. M. Tignor, S. K. Allen, J. Boschung, A. Nauels, Y. Xia, V. Bex, and P. M. Midgley, *Climate change 2013 the physical science basis: Working Group I contribution to the fifth assessment report of the intergovernmental panel on climate change.* 2013.

[5] P. Würfel, *Physics of Solar Cells: From Principles to New Concepts.* 2007.

[6] Q. Ma, "NASA GISS: Science Briefs: Greenhouse Gases: Refining the Role of Carbon Dioxide," 1998.

[7] P. Tans and R. Keeling, "Trends in Atmospheric Carbon Dioxide," 2019.

[8] D. Lüthi, M. Le Floch, B. Bereiter, T. Blunier, J. M. Barnola, U. Siegenthaler, D. Raynaud, J. Jouzel, H. Fischer, K. Kawamura, and T. F. Stocker, "High-resolution carbon dioxide concentration record 650,000-800,000 years before present," *Nature*, vol. 453, no. 7193, pp. 379–382, 2008.

[9] J. Zscheischler, S. Westra, B. J. Van Den Hurk, S. I. Seneviratne, P. J. Ward, A. Pitman, A. Aghakouchak, D. N. Bresch, M. Leonard, T. Wahl,

and X. Zhang, “Future climate risk from compound events,” *Nature Climate Change*, vol. 8, no. 6, pp. 469–477, 2018.

[10] H. Ritchie and M. Roser, “"Energy". Published online at OurWorldInData.org.,” 2020.

[11] B. Bereiter, S. Eggleston, J. Schmitt, C. Nehrbass-Ahles, T. F. Stocker, H. Fischer, S. Kipfstuhl, and J. Chappellaz, “Revision of the EPICA Dome C CO2 record from 800 to 600-kyr before present,” *Geophysical Research Letters*, vol. 42, no. 2, pp. 542–549, 2015.

[12] C. P. Morice, J. J. Kennedy, N. A. Rayner, and P. D. Jones, “Quantifying uncertainties in global and regional temperature change using an ensemble of observational estimates: The HadCRUT4 data set,” *Journal of Geophysical Research Atmospheres*, vol. 117, no. 8, pp. 1–22, 2012.

[13] UNFCCC. Conference of the Parties (COP), “Paris Climate Change Conference-November 2015, COP 21,” tech. rep., 2015.

[14] J. Rogelj, D. Shindell, K. Jiang, S. Fifita, P. Forster, V. Ginzburg, C. Handa, H. Kheshgi, S. Kobayashi, E. Kriegler, L. Mundaca, R. Seferian, and M. Vilarino, “Mitigation Pathways Compatible With 1.5°C in the Context of Sustainable Development,” in *Global warming of 1.5°C. An IPCC Special Report [...]*, 2018.

[15] M. E. Boot-Handford, J. C. Abanades, E. J. Anthony, M. J. Blunt, S. Brandani, N. Mac Dowell, J. R. Fernández, M. C. Ferrari, R. Gross, J. P. Hallett, R. S. Haszeldine, P. Heptonstall, A. Lyngfelt, Z. Makuch, E. Mangano, R. T. Porter, M. Pourkashanian, G. T. Rochelle, N. Shah, J. G. Yao, and P. S. Fennell, “Carbon capture and storage update,” *Energy and Environmental Science*, vol. 7, no. 1, pp. 130–189, 2014.

[16] V. Smil, “Energy Transitions: Global and National Perspectives,” 2017.

[17] BP, “Statistical Review of World Energy, 2020 | 69th Edition,” *Bp*, 2020.

[18] N. S. Lewis and D. G. Nocera, “Powering the planet: Chemical challenges in solar energy utilization,” 2006.

[19] P. C. Vesborg and T. F. Jaramillo, “Addressing the terawatt challenge: Scalability in the supply of chemical elements for renewable energy,” *RSC Advances*, vol. 2, no. 21, pp. 7933–7947, 2012.

[20] R. Perez and M. Perez, “A Fundamental Look At Supply Side Energy Reserves For The Planet,” *The International Energy Agency SHC programme Solar Update*, vol. 62, no. April 2009, pp. 4–6, 2015.

[21] F. Creutzig, P. Agoston, J. C. Goldschmidt, G. Luderer, G. Nemet, and R. C. Pietzcker, “The underestimated potential of solar energy to mitigate climate change,” *Nature Energy*, vol. 2, no. 9, 2017.

[22] Z. W. She, J. Kibsgaard, C. F. Dickens, I. Chorkendorff, J. K. Nørskov, and T. F. Jaramillo, “Combining theory and experiment in electrocatalysis: Insights into materials design,” *Science*, vol. 355, no. 6321, 2017.

[23] G. Kopp and J. L. Lean, “A new, lower value of total solar irradiance: Evidence and climate significance,” *Geophysical Research Letters*, vol. 38, no. 1, pp. 1–7, 2011.

[24] “National Renewable Energy Laboratory (NREL), Solar Spectral Irradiance: Air Mass 1.5. Available at: https://rredc.nrel.gov/solar/ spectra/am1.5/,” 2021.

[25] W. Shockley and H. J. Queisser, “Detailed balance limit of efficiency of p-n junction solar cells,” *Journal of Applied Physics*, 1961.

[26] J.-f. Guillemoles, T. Kirchartz, D. Cahen, and U. Rau, “Guide for the perplexed to the Shockley – Queisser model for solar cells,” vol. 13, no. August, 2019.

[27] M. A. Green and A. W. Ho-Baillie, “Pushing to the Limit: Radiative Efficiencies of Recent Mainstream and Emerging Solar Cells,” *ACS Energy Letters*, vol. 4, no. 7, pp. 1639–1644, 2019.

[28] A. Polman, M. Knight, E. C. Garnett, B. Ehrler, and W. C. Sinke, “Photovoltaic materials: Present efficiencies and future challenges,” *Science*, vol. 352, no. 6283, 2016.

[29] M. A. Green, “Photovoltaic technology and visions for the future,” *Progress in Energy*, vol. 1, no. 1, p. 013001, 2019.

[30] M. A. Green, “The path to 25% silicon solar cell efficiency: History of silicon cell evolution,” *Progress in Photovoltaics: Research and Applications*, 2009.

[31] M. A. Green, E. D. Dunlop, J. Hohl-Ebinger, M. Yoshita, N. Kopidakis, and X. Hao, “Solar cell efficiency tables (version 56),” *Progress in Photovoltaics: Research and Applications*, vol. 28, no. 7, pp. 629–638, 2020.

[32] F. Lafond, A. G. Bailey, J. D. Bakker, D. Rebois, R. Zadourian, P. McSharry, and J. D. Farmer, “How well do experience curves predict technological progress? A method for making distributional forecasts∗,” 2017.

[33] International Renewable Energy Agency, “Renewable Power Generation Costs in 2019,” tech. rep., 2020.

[34] G. Barbose, N. Darghouth, D. Millstein, M. Spears, R. Wiser, M. Buckley, R. Widiss, and Lawrence Berkeley National Laboratory, “Tracking the Sun VIII: The Installed Price of Residential and Non- Residential Photovoltaic Systems in the United States,” *LBNL Technical Report*, 2016.

[35] G. Kavlak, J. McNerney, and J. E. Trancik, “Evaluating the causes of cost reduction in photovoltaic modules,” *Energy Policy*, vol. 123, pp. 700–710, 2018.

[36] H. H. Fang, S. Adjokatse, S. Shao, J. Even, and M. A. Loi, “Long-lived hot-carrier light emission and large blue shift in formamidinium tin triiodide perovskites,” *Nature Communications*, vol. 9, no. 1, 2018.

[37] A. Lenert, D. M. Bierman, Y. Nam, W. R. Chan, I. Celanović, M. Soljačić, and E. N. Wang, "A nanophotonic solar thermophotovoltaic device," *Nature Nanotechnology*, vol. 9, no. 2, pp. 126–130, 2014.

[38] T. Trupke, M. A. Green, and P. Würfel, "Improving solar cell efficiencies by up-conversion of sub-band-gap light," *Journal of Applied Physics*, vol. 92, no. 7, pp. 4117–4122, 2002.

[39] J. Lee, P. Jadhav, P. D. Reusswig, S. R. Yost, N. J. Thompson, D. N. Congreve, E. Hontz, T. Van Voorhis, and M. A. Baldo, "Singlet exciton fission photovoltaics," *Accounts of Chemical Research*, vol. 46, no. 6, pp. 1300–1311, 2013.

[40] A. J. Nozik, "Quantum dot solar cells," in *Physica E: Low-Dimensional Systems and Nanostructures*, 2002.

[41] A. Luque, A. Martí, and C. Stanley, "Understanding intermediate-band solar cells," *Nature Photonics*, vol. 6, no. 3, pp. 146–152, 2012.

[42] H. Cotal, C. Fetzer, J. Boisvert, G. Kinsey, R. King, P. Hebert, H. Yoon, and N. Karam, "III-V multijunction solar cells for concentrating photovoltaics," 2009.

[43] Z. J. Yu, J. V. C. Iii, and Z. C. Holman, "tandem photovoltaic modules in the United States," *Nature Energy*, vol. 3, no. September 2018, pp. 747–753, 2020.

[44] C. D. Bailie and M. D. McGehee, "High-efficiency tandem perovskite solar cells," *MRS Bulletin*, vol. 40, no. 8, pp. 681–685, 2015.

[45] G. E. Eperon, M. T. Hörantner, and H. J. Snaith, "Metal halide perovskite tandem and multiple-junction photovoltaics," *Nature Reviews Chemistry*, vol. 1, no. 12, 2017.

[46] P. Tockhorn, P. Wagner, L. Kegelmann, J. C. Stang, M. Mews, S. Albrecht, and L. Korte, "Three-Terminal Perovskite/Silicon Tandem Solar Cells with Top and Interdigitated Rear Contacts," *ACS Applied Energy Materials*, vol. 3, no. 2, pp. 1381–1392, 2020.

[47] S. Essig, C. Allebé, T. Remo, J. F. Geisz, M. A. Steiner, K. Horowitz, L. Barraud, J. S. Ward, M. Schnabel, A. Descoeudres, D. L. Young, M. Woodhouse, M. Despeisse, C. Ballif, and A. Tamboli, "Raising the one-sun conversion efficiency of III-V/Si solar cells to 32.8% for two junctions and 35.9% for three junctions," *Nature Energy*, vol. 2, no. 9, 2017.

[48] M. Yamaguchi, K. H. Lee, K. Araki, and N. Kojima, "A review of recent progress in heterogeneous silicon tandem solar cells," *Journal of Physics D: Applied Physics*, vol. 51, no. 13, 2018.

[49] A. Al-Ashouri, E. Köhnen, B. Li, A. Magomedov, H. Hempel, P. Caprioglio, J. A. Márquez, A. B. M. Vilches, E. Kasparavicius, J. A. Smith, N. Phung, D. Menzel, M. Grischek, L. Kegelmann, D. Skroblin, C. Gollwitzer, T. Malinauskas, M. Jošt, G. Matič, B. Rech, R. Schlatmann, M. Topič, L. Korte,

A. Abate, B. Stannowski, D. Neher, M. Stolterfoht, T. Unold, V. Getautis, and S. Albrecht, “Monolithic perovskite/silicon tandem solar cell with >29% efficiency by enhanced hole extraction,” *Science*, vol. 370, no. 6522, pp. 1300–1309, 2020.

[50] A. R. Jeong, S. B. Choi, W. M. Kim, J. K. Park, J. Choi, I. Kim, and J. H. Jeong, “Electrical analysis of c-Si/CGSe monolithic tandem solar cells by using a cell-selective light absorption scheme,” *Scientific Reports*, vol. 7, no. 1, pp. 1–10, 2017.

[51] M. G. Walter, E. L. Warren, J. R. McKone, S. W. Boettcher, Q. Mi, E. A. Santori, and N. S. Lewis, “Solar water splitting cells,” *Chemical Reviews*, vol. 110, no. 11, pp. 6446–6473, 2010.

[52] J. Brillet, J. H. Yum, M. Cornuz, T. Hisatomi, R. Solarska, J. Augustynski, M. Graetzel, and K. Sivula, “Highly efficient water splitting by a dual-absorber tandem cell,” *Nature Photonics*, vol. 6, no. 12, pp. 824–828, 2012.

[53] J. Barber, “Photosynthetic energy conversion: Natural and artificial,” *Chemical Society Reviews*, vol. 38, no. 1, pp. 185–196, 2009.

[54] B. Seger, I. E. Castelli, P. C. K. Vesborg, K. W. Jacobsen, O. Hansen, and I. Chorkendorff, “2-Photon tandem device for water splitting: comparing photocathode first versus photoanode first designs,” *Energy Environ. Sci.*, vol. 7, no. 8, pp. 2397–2413, 2014.

[55] M. F. Weber and M. J. Dignam, “Splitting water with semiconducting photoelectrodes-Efficiency considerations,” *International Journal of Hydrogen Energy*, 1986.

[56] B. Seger, O. Hansen, and P. C. K. Vesborg, “A Flexible Web-Based Approach to Modeling Tandem Photocatalytic Devices,” *Solar RRL*, vol. 1, no. 1, p. e201600013, 2017.

[57] W. Smith, “Effect of light on selenium during the passage of an electric current,” *Nature*, 1873.

[58] P. W. G. Adams and R. E. Day, “On the action of light on Selenium,” *Nature*, vol. 13, no. 334, p. 407, 1876.

[59] A. Einstein, “On a Heuristic Point of View about the Creation and Conversion of Light, translated from german by Haar, T.,” *Annalen der Physik*, 1905.

[60] C. E. Fritts, “On a new form of selenium cell, and some electrical discoveries made by its use,” *American Journal of Science*, 1883.

[61] D. M. Chapin, C. S. Fuller, and G. L. Pearson, “A new silicon p-n junction photocell for converting solar radiation into electrical power [3],” *Journal of Applied Physics*, vol. 25, no. 5, pp. 676–677, 1954.

[62] P. John, “The Silicon Solar Cell turns 50,” *NREL Report*, 2004.

[63] T. Nakada and A. Kunioka, “Polycrystalline Thin-Film TiO2_Se Solar Cells,” *Japanese Journal of Applied Physics*, vol. 24, no. 7, pp. L536–L538, 1985.

[64] A. K. Bhatnagar, K. V. Reddy, and V. Srivastava, “Optical energy gap of amorphous selenium: Effect of annealing,” *Journal of Physics D: Applied Physics*, vol. 18, no. 9, pp. L149–L153, 1985.

[65] S. Tutihasi and I. Chen, “Optical properties and band structure of trigonal selenium,” *Physical Review*, vol. 158, no. 3, pp. 623–630, 1967.

[66] I. Hadar, X. Hu, Z. Z. Luo, V. P. Dravid, and M. G. Kanatzidis, “Nonlinear Band Gap Tunability in Selenium-Tellurium Alloys and Its Utilization in Solar Cells,” *ACS Energy Letters*, vol. 4, no. 9, pp. 2137–2143, 2019.

[67] O. Madelung, “Semiconductors: Data Handbook; Ix - VIy compounds,” in *Semiconductors: Data Handbook 3rd Ed.*, pp. 424–428, 2004.

[68] T. K. Todorov, S. Singh, D. M. Bishop, O. Gunawan, Y. S. Lee, T. S. Gershon, K. W. Brew, P. D. Antunez, and R. Haight, “Ultrathin high band gap solar cells with improved efficiencies from the world’s oldest photovoltaic material,” *Nature Communications*, 2017.

[69] A. A. Yaroshevsky, “Abundances of chemical elements in the Earth’s crust,” *Geochemistry International*, vol. 44, no. 1, pp. 48–55, 2006.

[70] H. Ullah, G. Liu, B. Yousaf, M. U. Ali, S. Irshad, Q. Abbas, and R. Ahmad, *A comprehensive review on environmental transformation of selenium: recent advances and research perspectives*, vol. 41. 2019.

[71] I. Hadar, T. B. Song, W. Ke, and M. G. Kanatzidis, “Modern Processing and Insights on Selenium Solar Cells: The World’s First Photovoltaic Device,” *Advanced Energy Materials*, vol. 1802766, pp. 1–9, 2019.

[72] J. Wu, Z. Zhang, C. Tong, D. Li, A. Mei, Y. Rong, Y. Zhou, H. Han, and Y. Hu, “Two-Stage Melt Processing of Phase-Pure Selenium for Printable Triple-Mesoscopic Solar Cells,” *ACS Applied Materials & Interfaces*, vol. 11, no. 37, pp. 33879–33885, 2019.

[73] W. Liu, A. A. Said, W. J. Fan, and Q. Zhang, “Inverted Solar Cells with Thermally Evaporated Selenium as an Active Layer,” *ACS Applied Energy Materials*, 2020.

[74] W. Liu, F. Yu, W. Fan, and Q. Zhang, “Improved stability and efficiency of polymer-based selenium solar cells through the usage of tin(iv) oxide in the electron transport layers and the analysis of aging dynamics,” *Physical Chemistry Chemical Physics*, vol. 22, no. 26, pp. 14838–14845, 2020.

[75] S. A. Campbell, *Fabrication Engineering at the Micro- and Nanoscale.* No. 10, 2008.

[76] G. Sauerbrey, “Verwendung von Schwingquarzen zur Wägung dünner Schichten und zur Mikrowägung,” *Zeitschrift für Physik*, vol. 155, no. 2, pp. 206–222, 1959.

[77] Standford Research Systems, “Quartz Crystal Microbalance Theory and Calibration The QCM oscillator,” *Technical Reports*, vol. 408, no. 408, pp. 744–9040, 2004.

[78] D. R. Lide, “CRC Handbook of Chemistry and Physics, 84th Edition, 2003-2004,” *Handbook of Chemistry and Physics*, vol. 53, p. 2616, 2003.

[79] Yves Huttel, *Gas-Phase Synthesis of Nanoparticles Edited by Yves Huttel.* 2017.

[80] J. T. Gudmundsson and D. Lundin, *Introduction to magnetron sputtering.* 2019.

[81] Donald A. Neamen, *Semiconductor Physics and Devices, Fourth Edition.* 2013.

[82] M. A. Green, “Accuracy of analytical expressions for solar cell fill factors,” *Solar Cells*, 1982.

[83] D. Abou-Ras, T. Kirchartz, and U. Rau, *Advanced Characterization Techniques for Thin Film Solar Cells: Second Edition*, vol. 1-2. 2016.

[84] R. A. Sinton and A. Cuevas, “A quasi-steady-state open-circuit voltage method for solar cell characterization,” *16th European Photovoltaic Solar Energy Conference*, no. May, pp. 1–4, 2000.

[85] J. Heath and P. Zabierowski, “Capacitance Spectroscopy of Thin-Film Solar Cells,” *Advanced Characterization Techniques for Thin Film Solar Cells: Second Edition*, vol. 1-2, pp. 93–119, 2016.

[86] I. Chorkendorff and J. W. Niemantsverdriet, *Concepts of Modern Catalysis and Kinetics.* 2003.

[87] C. D. Wagner, W. M. Riggs, L. E. Davis, J. F. Moulder, and G. E. Muilenberg, *Handbook of X-ray electron spectroscopy: A reference book of standard data for use in X-ray photoelectron spectroscopy.* 1979.

[88] H. H. Brongersma, M. Draxler, M. de Ridder, and P. Bauer, “Surface composition analysis by low-energy ion scattering,” *Surface Science Reports*, vol. 62, no. 3, pp. 63–109, 2007.

[89] P. Brüner, T. Grehl, and H. H. Brongersma, “Low-energy ion scattering (LEIS),” *Characterization of Nanoparticles: Measurement Processes for Nanoparticles*, pp. 419–439, 2019.

[90] J. Goldstein, D. Newbury, D. Joy, C. Lyman, P. Echlin, E. Lifshin, L. Sawyer, and J. Michael, *Scanning Electron Microscopy and X-ray Microanalysis*, vol. 1. 2003.

[91] Y. Waseda, E. Matsubara, and K. Shinoda, *X-Ray Diffraction Crystallography; Introduction, examples and solved problems.* 2011.

[92] J. Tauc, “Optical properties and electronic structure of amorphous Ge and Si,” *Materials Research Bulletin*, vol. 3, no. 1, pp. 37–46, 1968.

[93] H. Hempel, C. J. Hages, R. Eichberger, I. Repins, and T. Unold, "Minority and Majority Charge Carrier Mobility in Cu2ZnSnSe4 revealed by Terahertz Spectroscopy," *Scientific Reports*, vol. 8, no. 1, pp. 1–9, 2018.

[94] P. Kužel, F. Kadlec, and H. Němec, "Propagation of terahertz pulses in photoexcited media: Analytical theory for layered systems," *Journal of Chemical Physics*, vol. 127, no. 2, 2007.

[95] H. Hempel, A. Redinger, I. Repins, C. Moisan, G. Larramona, G. Dennler, M. Handwerg, S. F. Fischer, R. Eichberger, and T. Unold, "Intragrain charge transport in kesterite thin films - Limits arising from carrier localization," *Journal of Applied Physics*, vol. 120, no. 17, 2016.

[96] R. Nielsen, "Synthesis of New Carrier-selective Transport Materials for Tandem Solar Cell Applications (Master's Thesis). Retrieved from https://orbit.dtu.dk/en/projects/large-bandgap-photovoltaic-devices-and-tandem-integration-with-si," 2020.

[97] M. G. Helander, M. T. Greiner, Z. B. Wang, W. M. Tang, and Z. H. Lu, "Work function of fluorine doped tin oxide," *Journal of Vacuum Science & Technology A: Vacuum, Surfaces, and Films*, vol. 29, no. 1, p. 011019, 2011.

[98] S. Rentenberger, A. Vollmer, E. Zojer, R. Schennach, and N. Koch, "UV/ozone treated Au for air-stable, low hole injection barrier electrodes in organic electronics," *Journal of Applied Physics*, vol. 100, no. 5, 2006.

[99] P. Unger and P. Cherin, "Coordination and thermal motion in crystalline selenium and tellurium," in *The Physics of Selenium and Tellurium* (W. C. Cooper, ed.), p. 223, New York,: Pergamon Press, 1969.

[100] G. Abdullaev, Y. Asadov, and K. Mamedov, "The growth of alpha and beta-red monoclinic selenium crystals and an investigation of some of their physical properties," in *The Physics of Selenium and Tellurium* (W. C. Cooper, ed.), p. 179, New York: Pergamon Press, 1969.

[101] K. E. Murphy, M. B. Altman, and B. Wunderlich, "The monoclinic-to-trigonal transformation in selenium," *Journal of Applied Physics*, vol. 48, no. 10, pp. 4122–4131, 1977.

[102] B. W. Corb, W. D. Wei, and B. L. Averbach, "Atomic models of amorphous selenium," *Journal of Non-Crystalline Solids*, 1982.

[103] M. Zhu, G. Niu, and J. Tang, "Elemental Se: Fundamentals and its Optoelectronic Applications," *Journal of Materials Chemistry C*, 2019.

[104] J. Stuke, "Recent progress in the physics of selenium and tellurium," in *The Physics of Selenium and Tellurium*, 1969.

[105] J. Mort, "Acoustoelectric current saturation in trigonal selenium," *Physical Review Letters*, 1967.

[106] Y. Ma, B. Tang, W. Lian, C. Wu, X. Wang, H. Ju, C. Zhu, F. Fan, and T. Chen, “Efficient defect passivation of Sb2Se3 film by tellurium doping for high performance solar cells,” *Journal of Materials Chemistry A*, vol. 8, no. 14, pp. 6510–6516, 2020.

[107] R. Tang, X. Wang, W. Lian, J. Huang, Q. Wei, M. Huang, Y. Yin, C. Jiang, S. Yang, G. Xing, S. Chen, C. Zhu, X. Hao, M. A. Green, and T. Chen, “Hydrothermal deposition of antimony selenosulfide thin films enables solar cells with 10% efficiency,” *Nature Energy*, pp. 1–9, 2020.

[108] Z. Li, X. Liang, G. Li, H. Liu, H. Zhang, J. Guo, J. Chen, K. Shen, X. San, W. Yu, R. E. Schropp, and Y. Mai, “9.2%-Efficient Core-Shell Structured Antimony Selenide Nanorod Array Solar Cells,” *Nature Communications*, vol. 10, no. 1, pp. 1–9, 2019.

[109] Y. Zhou, L. Wang, S. Chen, S. Qin, X. Liu, J. Chen, D. J. Xue, M. Luo, Y. Cao, Y. Cheng, E. H. Sargent, and J. Tang, “Thin-film Sb2Se3 photovoltaics with oriented one-dimensional ribbons and benign grain boundaries,” *Nature Photonics*, vol. 9, no. 6, pp. 409–415, 2015.

[110] X. Liu, J. Chen, M. Luo, M. Leng, Z. Xia, Y. Zhou, S. Qin, D. J. Xue, L. Lv, H. Huang, D. Niu, and J. Tang, “Thermal evaporation and characterization of Sb2Se3 thin film for substrate Sb2Se3/CdS solar cells,” *ACS Applied Materials and Interfaces*, vol. 6, no. 13, pp. 10687–10695, 2014.

[111] C. Griffiths and H. Sang, “the Growth of Selenium Single-Crystal Films,” *The Physics of Selenium and Tellurium*, vol. 3, no. 0001, pp. 135–154, 1969.

[112] M. F. Mohamad Noh, C. H. Teh, R. Daik, E. L. Lim, C. C. Yap, M. A. Ibrahim, N. Ahmad Ludin, A. R. B. Mohd Yusoff, J. Jang, and M. A. Mat Teridi, “The architecture of the electron transport layer for a perovskite solar cell,” *Journal of Materials Chemistry C*, vol. 6, no. 4, pp. 682–712, 2018.

[113] K. Tennakone, G. R. R. A. Kumara, K. Tennakone, G. R. R. A. Kumara, K. Tennakone, and V. P. S. Perera, “Nanoporous n-TiO2/selenium/p-CuCNS photovoltaic cell,” pp. 4–9, 1998.

[114] D.-C. Nguyen, S. Tanaka, H. Nishino, K. Manabe, and S. Ito, “3-D solar cells by electrochemical-deposited Se layer as extremely-thin absorber and hole conducting layer on nanocrystalline TiO2 electrode.,” *Nanoscale research letters*, vol. 8, no. 1, p. 8, 2013.

[115] K. Wang, Y. Shi, H. Zhang, Y. Xing, Q. Dong, and T. Ma, “Selenium as a photoabsorber for inorganic-organic hybrid solar cells,” *Physical Chemistry Chemical Physics*, vol. 16, no. 42, pp. 23316–23319, 2014.

[116] S. Ito, N. Kitagawa, T. Shibahara, and H. Nishino, “Electrochemical Deposition of Te and Se on Flat TiO2 for Solar Cell Application,” *International Journal of Photoenergy*, vol. 2014, pp. 1–5, 2014.

[117] M. Zhu, F. Hao, L. Ma, T.-B. Song, C. E. Miller, M. R. Wasielewski, X. Li, and M. G. Kanatzidis, "Solution-Processed Air-Stable Mesoscopic Selenium Solar Cells," *ACS Energy Letters*, vol. 1, no. 2, pp. 469–473, 2016.

[118] M. Zhu, Y. Deng, W. Liu, and X. Li, "Preparation of Se-based solar cell using spin-coating method in ambient condition," *Chinese Physics B*, vol. 27, no. 1, pp. 0–4, 2018.

[119] S. I. Seok, "Exploring wide bandgap metal oxides for perovskite solar cells Exploring wide bandgap metal oxides for perovskite solar cells," vol. 022401, no. October 2018, 2019.

[120] Z. Yin, Q. Zheng, S. C. Chen, D. Cai, L. Zhou, and J. Zhang, "Bandgap tunable Zn1-xMgxO thin films as highly transparent cathode buffer layers for high-performance inverted polymer solar cells," *Advanced Energy Materials*, vol. 4, no. 7, pp. 1–6, 2014.

[121] R. García-Hernansanz, E. García-Hemme, D. Montero, J. Olea, A. del Prado, I. Mártil, C. Voz, L. G. Gerling, J. Puigdollers, and R. Alcubilla, "Transport mechanisms in silicon heterojunction solar cells with molybdenum oxide as a hole transport layer," *Solar Energy Materials and Solar Cells*, vol. 185, no. May, pp. 61–65, 2018.

[122] Y. Yang, N. D. Pham, D. Yao, H. Zhu, P. Yarlagadda, and H. Wang, "Inorganic p-type semiconductors and carbon materials based hole transport materials for perovskite solar cells," *Chinese Chemical Letters*, vol. 29, no. 8, pp. 1242–1250, 2018.

[123] A. L. Cauduro, R. Dos Reis, G. Chen, A. K. Schmid, C. Méthivier, H. G. Rubahn, L. Bossard-Giannesini, H. Cruguel, N. Witkowski, and M. Madsen, "Crystalline Molybdenum Oxide Thin-Films for Application as Interfacial Layers in Optoelectronic Devices," *ACS Applied Materials and Interfaces*, vol. 9, no. 8, pp. 7717–7724, 2017.

[124] Y. Nakayama, K. Morii, Y. Suzuki, H. Machida, S. Kera, N. Ueno, H. Kitagawa, Y. Noguchi, and H. Ishii, "Origins of Improved Hole-Injection Efficiency by the Deposition of MoO3 on the Polymeric Semiconductor Poly(dioctylfluorene-alt-benzothiadiazole)," *Advanced Functional Materials*, 2010.

[125] T. Minami, "Transparent conducting oxide semiconductors for transparent electrodes," *Semiconductor Science and Technology*, vol. 20, no. 4, 2005.

[126] A. E. Delahoy and S. Guo, "Transparent Conducting Oxides for Photovoltaics," *Handbook of Photovoltaic Science and Engineering*, vol. 32, no. March 2007, pp. 716–796, 2011.

[127] N. R. Armstrong, P. A. Veneman, E. Ratcliff, D. Placencia, and M. Brumbach, "Oxide contacts in organic photovoltaics: Characterization and control of near-surface composition in indium-tin oxide (ITO) electrodes," *Accounts of Chemical Research*, vol. 42, no. 11, pp. 1748–1757, 2009.

[128] Y. Li, Z. Liu, Q. Li, Z. Liu, and L. Zeng, "Recovery of indium from used indium-tin oxide (ITO) targets," *Hydrometallurgy*, vol. 105, no. 3-4, pp. 207–212, 2011.

[129] T. H. Youngman, "Fabrication and characterisation of wide-bandgap selenium-based solar cells for tandem device applications (Master's Thesis). Retrieved from https://findit.dtu.dk/en/catalog/2409669892," 2018.

[130] D. a. Young, "Phase diagrams of the elements," *Lawrence Livermore Laboratory*, p. 64, 1975.

[131] Y. Qu, Z. Zhang, S. Jiang, X. Wang, Y. Lai, Y. Liu, and J. Li, "Confining selenium in nitrogen-containing hierarchical porous carbon for high-rate rechargeable lithium–selenium batteries," *Journal of Materials Chemistry A*, vol. 2, no. 31, p. 12255, 2014.

[132] "FIZ Karlsruhe - Leibniz-Institut für Informatonsinfrastruktur, Inorganic Crystal Structure Database (ICSD), https://icsd.fiz-karlsruhe.de/."

[133] C. R. Stanley, "The Physics of Selenium and Tellurium," *Physics Bulletin*, 1970.

[134] A. Crovetto and O. Hansen, "Solar Energy Materials and Solar Cells What is the band alignment of Cu 2 ZnSn (S , Se) 4 solar cells ?," *Solar Energy Materials and Solar Cells*, vol. 169, no. March, pp. 177–194, 2017.

[135] R. L. Erickson and D. P. Smith, "Oscillatory cross sections in low-energy ion scattering from surfaces," *Physical Review Letters*, vol. 34, no. 6, pp. 297–299, 1975.

[136] J. C. Tully, "Neutralization of ions at surfaces," *Physical Review B*, vol. 16, no. 10, pp. 4324–4334, 1977.

[137] D. Goebl, D. Roth, D. Primetzhofer, R. C. Monreal, E. Abad, A. Putz, and P. Bauer, "Quasi-resonant neutralization of He+ ions at a germanium surface," *Journal of Physics Condensed Matter*, vol. 25, no. 48, 2013.

[138] D. Goebl, B. Bruckner, D. Roth, C. Ahamer, and P. Bauer, "Low-energy ion scattering: A quantitative method?," *Nuclear Instruments and Methods in Physics Research, Section B: Beam Interactions with Materials and Atoms*, vol. 354, pp. 3–8, 2015.

[139] D. P. Woodruff, "Neutralisation effects in low energy ion scattering," *Nuclear Instruments and Methods*, 1982.

[140] W. Yu, J. L. Sullivan, and S. O. Saied, "XPS and LEISS studies of ion bombarded GaSb, InSb and CdSe surfaces," *Surface Science*, vol. 352-354, pp. 781–787, 1996.

[141] A. Kramer, M. L. Van de Put, C. L. Hinkle, and W. G. Vandenberghe, "Tellurium as a successor of silicon for extremely scaled nanowires: a first-principles study," *npj 2D Materials and Applications*, vol. 4, no. 1, pp. 1–8, 2020.

[142] K. A. Lozovoy, A. G. Korotaev, A. P. Kokhanenko, V. V. Dirko, and A. V. Voitsekhovskii, “Kinetics of epitaxial formation of nanostructures by Frank–van der Merwe, Volmer–Weber and Stranski–Krastanow growth modes,” *Surface and Coatings Technology*, vol. 384, no. October 2019, 2020.

[143] T. Nakada and A. Kunioka, “Efficient ITO / Se Heterojunction Solar Cells,” *Japanese Journal of Applied Physics*, vol. 23, no. 8, pp. L587–L589, 1984.

[144] H. Ito, M. Oka, T. Ogino, A. Takeda, and Y. Mizushima, “Selenium Thin-Film Solar cell,” *Japanese Journal of Applied Physics*, vol. 23, no. 6, 1984.

[145] S. Kashiwaya, J. Morasch, V. Streibel, T. Toupance, W. Jaegermann, and A. Klein, “The Work Function of TiO2,” *Surfaces*, vol. 1, no. 1, pp. 73–89, 2018.

[146] R. Brendel, M. Hirsch, R. Plieninger, and J. H. Werner, “Ouantum Efficiencv Analvsis of Thin-Layer Silicon Solar Cells,” *IEEE Transactions on Electron Devices*, vol. 43, no. 7, pp. 1104–1113, 1996.

[147] W. J. Yang, Z. Q. Ma, X. Tang, C. B. Feng, W. G. Zhao, and P. P. Shi, “Internal quantum efficiency for solar cells,” *Solar Energy*, vol. 82, no. 2, pp. 106–110, 2008.

[148] J. R. Manders, S. W. Tsang, M. J. Hartel, T. H. Lai, S. Chen, C. M. Amb, J. R. Reynolds, and F. So, “Solution-processed nickel oxide hole transport layers in high efficiency polymer photovoltaic cells,” *Advanced Functional Materials*, vol. 23, no. 23, pp. 2993–3001, 2013.

[149] Z. Liu, A. Zhu, F. Cai, L. M. Tao, Y. Zhou, Z. Zhao, Q. Chen, Y. B. Cheng, and H. Zhou, “Nickel oxide nanoparticles for efficient hole transport in p-i-n and n-i-p perovskite solar cells,” *Journal of Materials Chemistry A*, vol. 5, no. 14, pp. 6597–6605, 2017.

[150] L. Trotochaud, S. L. Young, J. K. Ranney, and S. W. Boettcher, “Nickel-Iron oxyhydroxide oxygen-evolution electrocatalysts: The role of intentional and incidental iron incorporation,” *Journal of the American Chemical Society*, vol. 136, no. 18, pp. 6744–6753, 2014.

[151] D. A. Corrigan and S. P. Maheswari, “Catalysis of the Oxygen Evolution Reaction By Trace Iron Impurities in Thin Film Nickel Oxide Electrodes.,” *Electrochemical Society Extended Abstracts*, vol. 85-1, pp. 934–935, 1985.

[152] D. Bae, B. Seger, P. C. Vesborg, O. Hansen, and I. Chorkendorff, “Strategies for stable water splitting: Via protected photoelectrodes,” *Chemical Society Reviews*, vol. 46, no. 7, pp. 1933–1954, 2017.

[153] P. C. Vesborg, B. Seger, and I. Chorkendorff, “Recent development in hydrogen evolution reaction catalysts and their practical implementation,” *Journal of Physical Chemistry Letters*, vol. 6, no. 6, pp. 951–957, 2015.

[154] B. Seger, T. Pedersen, A. B. Laursen, P. C. Vesborg, O. Hansen, and I. Chorkendorff, "Using TiO2 as a conductive protective layer for photocathodic H2 evolution," *Journal of the American Chemical Society*, vol. 135, no. 3, pp. 1057–1064, 2013.

[155] A. L. Fernandes Cauduro, Z. E. Fabrim, M. Ahmadpour, P. F. Fichtner, S. Hassing, H. G. Rubahn, and M. Madsen, "Tuning the optoelectronic properties of amorphous MoOx films by reactive sputtering," *Applied Physics Letters*, vol. 106, no. 20, 2015.

[156] M. Ahmadpour, A. L. Fernandes Cauduro, C. Méthivier, B. Kunert, C. Labanti, R. Resel, V. Turkovic, H. G. Rubahn, N. Witkowski, A. K. Schmid, and M. Madsen, "Crystalline molybdenum oxide layers as efficient and stable hole contacts in organic photovoltaic devices," *ACS Applied Energy Materials*, vol. 2, no. 1, pp. 420–427, 2019.

[157] X. Li, W. C. Choy, F. Xie, S. Zhang, and J. Hou, "Room-temperature solution-processed molybdenum oxide as a hole transport layer with Ag nanoparticles for highly efficient inverted organic solar cells," *Journal of Materials Chemistry A*, vol. 1, no. 22, pp. 6614–6621, 2013.

[158] R. Saive, "S-Shaped Current-Voltage Characteristics in Solar Cells: A Review," *IEEE Journal of Photovoltaics*, vol. 9, no. 6, pp. 1477–1484, 2019.

[159] S. S. Hegedus and W. N. Shafarman, "Thin-film solar cells: Device measurements and analysis," *Progress in Photovoltaics: Research and Applications*, vol. 12, no. 2-3, pp. 155–176, 2004.

[160] M. Neuschitzer, Y. Sanchez, S. Lõpez-Marino, H. Xie, A. Fairbrother, M. Placidi, S. Haass, V. Izquierdo-Roca, A. Perez-Rodriguez, and E. Saucedo, "Optimization of CdS buffer layer for high-performance Cu2ZnSnSe4 solar cells and the effects of light soaking: Elimination of crossover and red kink," *Progress in Photovoltaics: Research and Applications*, 2015.

[161] G. E. Eperon, R. D. Johnson, H. J. Snaith, and P. G. Radaelli, "Non-ferroelectric nature of the conductance hysteresis in CH 3 NH 3 PbI 3 perovskite-based photovoltaic devices," vol. 173502, no. 2015, 2017.

[162] M. Strandgaard, "Development of contact materials for conversion of solar energy (Bachelor Thesis). Retrieved from https://findit.dtu.dk/en/catalog/2436419316," no. June, 2018.

[163] F. Martinho, A. Hajijafarassar, S. Lopez-Marino, M. Espíndola-Rodríguez, S. Engberg, M. Gansukh, F. Stulen, S. Grini, S. Canulescu, E. Stamate, A. Crovetto, L. Vines, J. Schou, and O. Hansen, "Nitride-Based Interfacial Layers for Monolithic Tandem Integration of New Solar Energy Materials on Si: The Case of CZTS," *ACS Applied Energy Materials*, vol. 3, no. 5, pp. 4600–4609, 2020.

[164] A. Hajijafarassar, F. Martinho, F. Stulen, S. Grini, S. López-Mariño, M. Espíndola-Rodríguez, M. Döbeli, S. Canulescu, E. Stamate, M. Gansukh, S. Engberg, A. Crovetto, L. Vines, J. Schou, and O. Hansen, "Monolithic thin-film chalcogenide–silicon tandem solar cells enabled by a diffusion barrier," *Solar Energy Materials and Solar Cells*, vol. 207, no. September 2019, p. 110334, 2020.

[165] M. Ziwritsch, S. Müller, H. Hempel, T. Unold, F. F. Abdi, R. Van De Krol, D. Friedrich, and R. Eichberger, "Direct Time-Resolved Observation of Carrier Trapping and Polaron Conductivity in BiVO4," *ACS Energy Letters*, vol. 1, no. 5, pp. 888–894, 2016.

[166] P. Parkinson, H. J. Joyce, Q. Gao, H. H. Tan, X. Zhang, J. Zou, C. Jagadish, L. M. Herz, and M. B. Johnston, "Carrier lifetime and mobility enhancement in nearly defect-free core-shell nanowires measured using time-resolved terahertz spectroscopy," *Nano Letters*, vol. 9, no. 9, pp. 3349–3353, 2009.

[167] Z. Mics, A. D'Angio, S. A. Jensen, M. Bonn, and D. Turchinovich, "Density-dependent electron scattering in photoexcited GaAs," *International Conference on Infrared, Millimeter, and Terahertz Waves, IRMMW-THz*, pp. 38–40, 2013.

[168] S. Funk, G. Acuna, M. Handloser, and R. Kersting, "Probing the momentum relaxation time of charge carriers in ultrathin layers with terahertz radiation," *Optics Express*, vol. 17, no. 20, p. 17450, 2009.

[169] C. L. Tang, F. W. Wise, and M. J. Rosker, "Intraband relaxation dynamics of photo-excited carriers in GaAs and related compounds," *Conference on Solid State Devices and Materials*, vol. 2, no. 4, pp. 157–159, 1986.

[170] H. Mell and J. Stuke, "Magnetoconductivity of Trigonal Selenium Single Crystals," *Physica Status Solidi (B)*, vol. 24, no. 1, pp. 183–193, 1967.

[171] S. Kasap, C. Koughia, J. Berashevich, R. Johanson, and A. Reznik, "Charge transport in pure and stabilized amorphous selenium: re-examination of the density of states distribution in the mobility gap and the role of defects," *Journal of Materials Science: Materials in Electronics*, vol. 26, no. 7, pp. 4644–4658, 2015.

[172] B. Teymur, S. Levcenco, H. Hempel, E. Bergmann, J. A. Márquez, L. Choubrac, I. G. Hill, T. Unold, and D. B. Mitzi, "Optoelectronic and material properties of solution-processed Earth-abundant Cu2BaSn(S, Se)4 films for solar cell applications," *Nano Energy*, vol. 80, no. August 2020, 2021.

[173] H. J. Queisser and J. Stuke, "Photoluminescence of trigonal selenium," *Solid State Communications*, vol. 5, no. 1, pp. 75–78, 1967.

[174] H. Zetsche and R. Fischer, "Photoluminescence of Trigonal Crystals," *J. Phys. C: Solids*, vol. 30, pp. 2–5, 1969.

[175] J. W. Slotboom and H. C. de Graaff, “Measurements of bandgap narrowing in Si bipolar transistors,” *Solid State Electronics*, 1976.

[176] H. Ünlü, “A thermodynamic model for determining pressure and temperature effects on the bandgap energies and other properties of some semiconductors,” *Solid State Electronics*, 1992.

[177] A. Mooradian and G. Wright, “The raman spectrum of trigonal, alpha-monoclinic and amorphous selenium,” in *The Physics of Selenium and Tellurium*, pp. 269–276, Pergamon Press Inc., 1969.

[178] S. Kim, J. A. Márquez, T. Unold, and A. Walsh, “Upper limit to the photovoltaic efficiency of imperfect crystals from first principles,” *Energy and Environmental Science*, vol. 13, no. 5, pp. 1481–1491, 2020.

[179] S. Levcenko, J. Just, A. Redinger, G. Larramona, S. Bourdais, G. Dennler, A. Jacob, and T. Unold, “Deep Defects in Cu2ZnSn (S,Se)4 Solar Cells with Varying Se Content,” *Physical Review Applied*, vol. 5, no. 2, pp. 1–10, 2016.

[180] E. Kask, M. Grossberg, R. Josepson, P. Salu, K. Timmo, and J. Krustok, “Materials Science in Semiconductor Processing by admittance and photoluminescence spectroscopy,” vol. 16, pp. 992–996, 2013.

[181] G. Larramona, S. Levcenko, S. Bourdais, A. Jacob, C. Choné, B. Delatouche, C. Moisan, J. Just, T. Unold, and G. Dennler, “Fine-Tuning the Sn Content in CZTSSe Thin Films to Achieve 10.8% Solar Cell Efficiency from Spray-Deposited Water-Ethanol-Based Colloidal Inks,” *Advanced Energy Materials*, vol. 5, no. 24, 2015.

[182] W. E. Spear, “The hole mobility in selenium,” *Proceedings of the Physical Society*, vol. 76, no. 6, pp. 826–832, 1960.

[183] D. J. Olechna and R. S. Knox, “Energy-band structure of selenium chains,” *Physical Review*, 1965.

[184] A. Mukherjee, D. Vasileska, and A. H. Goldan, “Hole transport in selenium semiconductors using density functional theory and bulk Monte Carlo,” *Journal of Applied Physics*, vol. 124, no. 23, 2018.

[185] M. Hirayama, R. Okugawa, S. Ishibashi, S. Murakami, and T. Miyake, “Weyl Node and Spin Texture in Trigonal Tellurium and Selenium,” *Physical Review Letters*, vol. 114, no. 20, pp. 1–5, 2015.

[186] W. Tress, “Perovskite Solar Cells on the Way to Their Radiative Efficiency Limit – Insights Into a Success Story of High Open-Circuit Voltage and Low Recombination,” *Advanced Energy Materials*, vol. 7, no. 14, 2017.

[187] M. Stolterfoht, C. M. Wolff, J. A. Márquez, S. Zhang, C. J. Hages, D. Rothhardt, S. Albrecht, P. L. Burn, P. Meredith, T. Unold, and D. Neher, “Visualization and suppression of interfacial recombination for high-efficiency large-area pin perovskite solar cells,” *Nature Energy*, vol. 3, no. 10, pp. 847–854, 2018.

[188] E. Gaubas and J. Vanhellemont, "Dependence of carrier lifetime in germanium on resisitivity and carrier injection level," *Applied Physics Letters*, vol. 89, no. 14, pp. 1–4, 2006.

[189] R. J. Nelson and R. G. Sobers, "Minority-carrier lifetimes and internal quantum efficiency of surface-free GaAs," *Journal of Applied Physics*, vol. 49, no. 12, pp. 6103–6108, 1978.

[190] E. Gaubas and J. Vanhellemont, "Comparative Study of Carrier Lifetime Dependence on Dopant Concentration in Silicon and Germanium," *Journal of The Electrochemical Society*, vol. 154, no. 3, p. H231, 2007.

[191] S. Sze and K. N. Kwok, "Physics of Semiconductor Devices, 3rd Edition," *John Wiley & Sons, Inc*, 2007.

[192] M. G. Abebe, A. Abass, G. Gomard, L. Zschiedrich, U. Lemmer, B. S. Richards, C. Rockstuhl, and U. W. Paetzold, "Rigorous wave-optical treatment of photon recycling in thermodynamics of photovoltaics: Perovskite thin-film solar cells," *Physical Review B*, vol. 98, no. 7, pp. 1–12, 2018.

[193] Z. Liu, L. Krückemeier, B. Krogmeier, B. Klingebiel, J. A. Márquez, S. Levcenko, S. Öz, S. Mathur, U. Rau, T. Unold, and T. Kirchartz, "Open-Circuit Voltages Exceeding 1.26 v in Planar Methylammonium Lead Iodide Perovskite Solar Cells," *ACS Energy Letters*, vol. 4, no. 1, pp. 110–117, 2019.

[194] A. Cabas-Vidani, S. G. Haass, C. Andres, R. Caballero, R. Figi, C. Schreiner, J. A. Márquez, C. Hages, T. Unold, D. Bleiner, A. N. Tiwari, and Y. E. Romanyuk, "High-Efficiency (LixCu1−x)2ZnSn(S,Se)4 Kesterite Solar Cells with Lithium Alloying," *Advanced Energy Materials*, vol. 8, no. 34, pp. 1–8, 2018.

[195] S. Li, M. A. Lloyd, H. Hempel, C. J. Hages, J. A. Márquez, T. Unold, R. Eichberger, B. E. McCandless, and J. B. Baxter, "Relating Carrier Dynamics and Photovoltaic Device Performance of Single-Crystalline Cu2ZnSnSe4," *Physical Review Applied*, vol. 11, no. 3, pp. 1–13, 2019.

[196] M. Burgelman, P. Nollet, and S. Degrave, "Modelling polycrystalline semiconductor solar cells," *Thin Solid Films*, vol. 361, pp. 527–532, 2000.

[197] A. Haque, A. D. Sheikh, X. Guan, and T. Wu, "Metal Oxides as Efficient Charge Transporters in Perovskite Solar Cells," vol. 1602803, pp. 1–23, 2017.

[198] J. ichi Fujisawa, T. Eda, and M. Hanaya, "Comparative study of conduction-band and valence-band edges of TiO2, SrTiO3, and BaTiO3 by ionization potential measurements," *Chemical Physics Letters*, vol. 685, pp. 23–26, 2017.

[199] F. Ongul, "Solution-processed inverted organic solar cell using V2O5 hole transport layer and vacuum free EGaIn anode," *Optical Materials*, vol. 50, pp. 244–249, 2015.

[200] J. Robertson, "Band offsets, Schottky barrier heights, and their effects on electronic devices," *Journal of Vacuum Science & Technology A: Vacuum, Surfaces, and Films*, vol. 31, no. 5, p. 050821, 2013.

[201] M. N. Solovan, P. D. Maryanchuk, V. V. Brus, and O. A. Parfenyuk, "Electrical and optical properties of TiO 2 and TiO 2:Fe thin films," *Inorganic Materials*, vol. 48, no. 10, pp. 1026–1032, 2012.

[202] A. K. Chandiran, M. Abdi-Jalebi, M. K. Nazeeruddin, and M. Grätzel, "Analysis of electron transfer properties of ZnO and TiO2 photoanodes for dye-sensitized solar cells," *ACS Nano*, vol. 8, no. 3, pp. 2261–2268, 2014.

[203] P. Agarwala and D. Kabra, "A review on triphenylamine (TPA) based organic hole transport materials (HTMs) for dye sensitized solar cells (DSSCs) and perovskite solar cells (PSCs): Evolution and molecular engineering," *Journal of Materials Chemistry A*, vol. 5, no. 4, pp. 1348–1373, 2017.

[204] V. Shrotriya, G. Li, Y. Yao, C. W. Chu, and Y. Yang, "Transition metal oxides as the buffer layer for polymer photovoltaic cells," *Applied Physics Letters*, 2006.

[205] L. Lajaunie, F. Boucher, R. Dessapt, and P. Moreau, "Strong anisotropic influence of local-field effects on the dielectric response of α-MoO3," *Physical Review B - Condensed Matter and Materials Physics*, vol. 88, no. 11, pp. 1–9, 2013.